N O T I C E

THIS DOCUMENT HAS BEEN REPRODUCED FROM
MICROFICHE. ALTHOUGH IT IS RECOGNIZED THAT
CERTAIN PORTIONS ARE ILLEGIBLE, IT IS BEING RELEASED
IN THE INTEREST OF MAKING AVAILABLE AS MUCH
INFORMATION AS POSSIBLE

NASA

QCGAT MIXER COMPOUND
EXHAUST SYSTEM DESIGN AND
STATIC RIG MODEL TEST REPORT

by W. L. Blackmore, and C. E. Thompson

AIRESEARCH MANUFACTURING COMPANY OF ARIZONA
A DIVISION OF THE GARRETT CORPORATION
P.O. BCX 5217
PHOENIX, ARIZONA 85010

Prepared for

NATIONAL AERONAUTICS AND SPACE ADMINISTRATION

NASA Lewis Research Center
Cleveland, Ohio   44135

Contract NAS 3-20585

FOREWORD

Design and analysis of the AiResearch QCGAT mixer exhaust system was conducted at the AiResearch Engineering facilities at Phoenix, Arizona. Data reduction of performance and acoustical measurements were also conducted at the AiResearch facilities.

The testing performed on the 35-percent scale model exhaust nozzles for the QCGAT engine program was conducted at the FluiDyne Engineering Corporation's facilities at the FluiDyne Medicine Lake Aerodynamic Laboratory, Minneapolis, Minnesota.

PRECEDING PAGE BLANK NOT

TABLE OF CONTENTS

TABLE OF CONTENTS (Contd)

TABLE OF CONTENTS (Contd)

LIST OF FIGURES

LIST OF FIGURES (Contd)

LIST OF FIGURES (Contd)

LIST OF FIGURES (Contd)

LIST OF FIGURES (Contd)

LIST OF FIGURES (Contd)

LIST OF FIGURES (Cont'd

LIST OF FIGURES (Contd)

LIST OF FIGURES (Contd)

LIST OF TABLES

LIST OF TABLES

LIST OF TABLES

1.0 SUMMARY

1.1 Objectives

The objective of the NASA QCGAT (Quiet Clean General Aviation Turbofan) engine mixer-nozzle exhaust system scale-model program was to develop a mixer compound nozzle exhaust system to meet the proposed performance and exhaust jet-noise goals for the AiResearch QCGAT Engine.

1.2 Scope

This report covers the period from the preliminary optimization to the engine cycle matching of the selected full-scale exhaust system. A preliminary mixer nozzle optimization computer program, based on state-of-the-art techniques, defined the initial mixer configuration geometry. The initial aerodynamic contours of the mixer and fan duct were determined with a radial-equilibrium-flow analysis program. The mixer lobe designs were analyzed with an advanced 3-D viscous compressible flow program. Several lobe modifications were studied based on the results of the flow analysis. The configurations were also analyzed in terms of relative mixing efficiency, using a turbulent mixing-model program. Based on the flow analysis, three mixer compound configurations and a standard compound nozzle were selected for scale-model testing. Three mixing duct length variations were also selected. Model hardware was fabricated and tested. Performance and acoustic data were recorded at the sea-level static takeoff and cruise design point conditions. A final mixer exhaust system was selected and the scale-model mixer system was tested at selected off-design conditions in order to generate the performance maps. The performance maps were then used in an engine cycle sizing analysis to obtain the optimum areas for the overall flight regime.

1.3 Test Results

The program goals were exceeded with a cruise total specific fuel consumption (TSFC) reduction of 3.2 percent; a sea level static takeoff turbine inlet temperature reduction of 11.7°K (21.1°F); and a projected flyover jet noise reduction of 5.1 EPNdb. Performance results in terms of thrust coefficient and mixing efficiency are summarized in Table 1-1. Proposed performance goals were exceeded at both the sea-level-static point and the cruise design point. Mixer nozzle pressure losses derived from the cold-flow testing yielded the same order of ranking as predicted by the 3-D viscous analysis, but were lower in absolute level than the predicted values.

The tested performance of the short parallel mixer compound exhaust system (Configuration II) results in an increase in engine net thrust at cruise of 5.4 percent and an improvement in TSFC of 5.4 percent, relative to the reference coannular nozzle system, when sized to hold the reference nozzle cruise cycle match.

Far-field acoustic measurements were made during the hot-flow model testing. A summary of the measured noise levels of the tested configurations is presented in Table 1-2. Configuration II, the short parallel mixer compound exhaust system with the long mixing duct, had the lowest noise level at both the sea-level-static takeoff and cruise-design-point pressure ratio settings.

TABLE 1-1. SCALE MODEL TEST PERFORMANCE SUMMARY.

Model No.	Mixer-Compound	Configuration	Sea-Level Static 298°K(77°F)		Cruise M = 0.8 Alt = 12,192 m (40,000 ft)	
			C_{FT}	η_{mix}%	C_{FT}	η_{mix}%
Design Goals	—	—	0.9756	75.0	0.9940	75.0
Test Goals	—	X/D = 0.750	0.9782	75.0	1.0005	75.0
I	Compound	X/D = 0.752	0.9897	30.5	0.9940	--
II	Short Parallel	X/D = 0.752	0.9932	89.0	1.0050	72.1
III	Long Parallel	X/D = 0.752	0.9902	37.1	1.0032	60.8
IV	Long Radial	X/D = 0.752	0.9918	51.4	1.0075	65.5
V	Short Parallel	X/D = 0.501	0.9902	62.6	1.0068	76.2
VI	Short Parallel	X/D = 0.626	0.9908	75.6	1.0066	92.2

3

TABLE 1-2.   SUMMARY OF QCGAT MIXER NOZZLE
ACOUSTIC TEST RESULTS.

Nozzle Configuration		Maximum Tone Corrected Perceived Noise Level* $(PNdB_t)$			
		1.4 Nozzle Press. Ratio		2.4 Nozzle Press. Ratio	
		Absolute	Delta Relative to Config. I	Absolute	Delta Relative to Config. I
I	Standard Compound	136.8	0	155.7	0
II	Short Parallel	132.7	-4.1	152.0	-3.7
III	Long Parallel	135.8	-1.0	153.7	-2.0
IV	Long Radial	137.6	0.8	153.5	-2.2
V	Short Parallel	134.2	-2.6	152.4	-3.3
VI	Short Parallel	134.7	-2.1	152.7	-3.0

*As measured at FluiDyne Test Facility for microphone array 2.44m
(8 ft) radius from source, at 0.26, 0.35, 0.52, 0.70, 0.37, 0.4
radians (15, 20, 30, 40, 50, and 60 degrees) from exhaust center-
line.

4

SECTION II

INTRODUCTION

2.0 INTRODUCTION

2.1 Background

The NASA QCGAT (Quiet Clean General Aviation Turbofan) engine program seeks to demonstrate that large turbofan design concepts can be successfully applied to turbofan engines with sea-level thrust below 22.241 kN (5000 pounds). The program goals are to improve the environmental characteristics of civil aircraft by alleviating noise as well as pollution near airports, thereby assisting in reducing current growth restraints to civil aviation, and also providing engines with reduced fuel consumption.

This program requires the design of a full-scale co-annular reference-exhaust nozzle and mixer-compound exhaust nozzle systems. Scale-model testing of several mixer design candidates has been accomplished to meet the program requirement.

2.2 Scope

Mixer designs for cold- and hot-model testing were accomplished with extensive use of computer programs for analysis of the mixer-compound nozzle system. A major effort of the QCGAT program was the analytical design approach utilized in selecting and analyzing the mixer configurations to be tested. Also included in the design effort and analysis was the fan-bypass duct, the reference co-annular exhaust nozzle, and the baseline compound nozzle.

2.3 Purpose

This report covers the analytical techniques used in the design effort in producing the test models as well as presenting the data obtained from the tests to compare with the predicted results.

The test results are then used with the design techniques to predict the full-scale engine performance and noise levels.

2.4 Test Report

Included as an attachment to this report is the FluiDyne Engineering Corporation Report No. 1123 titled "Hot/Cold Flow Model Tests to Determine Static Performance of 35% Scale QCGAT Exhaust Nozzles".

This research was conducted for AiResearch under subcontract as approved by NASA for accomplishment of the model testing.

5/6

SECTION III

ANALYSIS AND DESIGN

3.0 ANALYSIS AND DESIGN

3.1 Design Approach

The QCGAT mixer-exhaust system design analysis utilized the latest analytical technology. The exhaust system was sized and performance predictions were made with an advanced version of the compound flow analysis computer program. The mixer-lobe geometry was initially selected with an empirical parametric optimization analysis and the preliminary end-wall contours were analyzed with conventional radial-equilibrium flow analysis. The mixer-lobe design was then refined with use of an analysis method which solves the 3-dimensional compressible Navier-Stokes equations. Various contour changes were then analyzed to reduce the end-wall curvature, and reduce losses due to 3-dimensional diffusion and secondary flows. The impact of lobe design and mixing-duct contour on the mixing process was evaluated with a three-dimensional viscous recirculating-flow mixing analysis.

The reference coannular exhaust system was scaled from the AiResearch Model TFE731-3 engine reference nozzles. The nozzles were analyzed with a conventional radial-equilibrium-flow solution and boundary-layer calculations. The flow in the bypass duct and standard compound-core duct was analyzed with standard boundary layer and radial-equilibrium techniques.

3.2 Preliminary Prediction of the QCGAT Mixer-Compound-Exhaust System Performance and Off-Design Matching Characteristics

Over the past several years, compound-flow analysis has been developed into an industry-accepted performance prediction procedure (ref. 1, 2, and 3). AiResearch has extended the prediction procedures for coannular-unmixed, partially-mixed, or forced-mixing exhaust systems. The semi-empirical analysis is based on a fundamental understanding of the flow processes and proper loss-bookkeeping procedures. The nomenclature used in the analysis is summarized in Figure 3-1. The exhaust system is broken into specific calculation stations, i.e.,

- o Rating stations
- o Bypass and core ducts
- o Flow splitter plane
- o Inlet or mixing plane
- o Mixing duct
- o Minimum plane
- o Exit plane

7
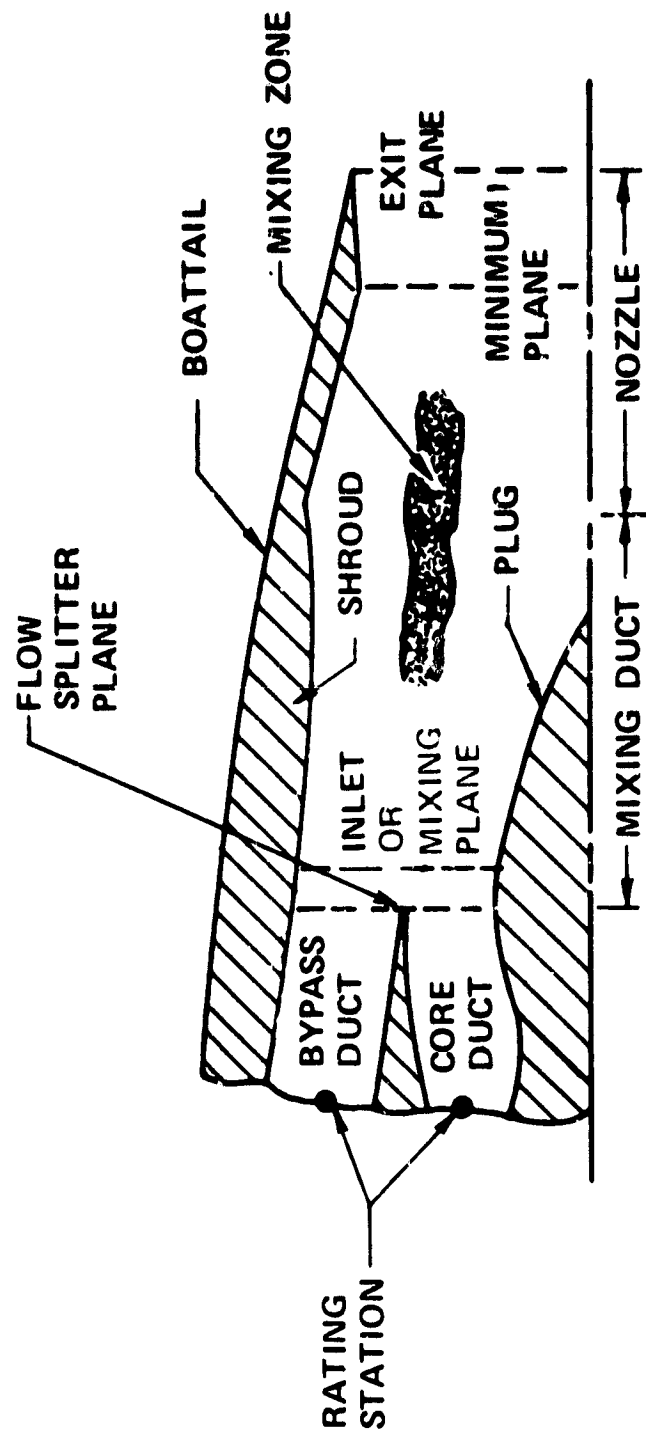
Figure 3-1. Compound Flow Analysis Calculation Stations and Nomenclature.

8

At each prime calculation station, flow coefficients are assigned as in a normal, separate, flow exhaust system. However, the splitter flow coefficients are assigned in a unique manner (see Figures 3-2 and 3-3), i.e., the splitter flow coefficient is defined as a function of the ratio of the total pressures. This flow coefficient correlation method (see Figure 3-3) has proved successful for coannular, partially mixed, and fully mixed systems.

A total pressure-loss bookkeeping procedure was established which would accommodate the losses of the various types of mixed flow exhaust systems (Figure 3-4). The losses are assigned independently to each gas stream and have been separated such that the local total pressure is used at each of the calculation stations.

The solution boundary conditions are summarized in Figure 3-5. The Kutta condition, or static pressure balance, is applied where the gas streams merge, i.e., at the splitter or inlet calculation station. The compound-choking criteria, developed by Bernstein, et al (ref. 1) is applied at the exit and minimum calculation stations.

The compound-flow analysis procedure is used for system design point sizing as well as predicting exhaust system component performance maps for new systems. The flow coefficients and total pressure losses for geometrically similar systems may be used to successfully predict the performance and matching characteristics of a new exhaust system. Table 3-1 presents a comparison between analytically predicted results and engine test data for a TFE731 engine compound-nozzle system (ref. 4). The agreement between predicted and tested results is excellent. Small discrepancies still exist in estimating the engine back pressure and exit area. However, the deviations are well within those experienced with some standard coannular-exhaust systems when first run on the engine.

The AiResearch compound-flow analysis procedure has been used to size and predict the performance of the QCGAT-compound and mixer-compound exhaust systems.

3.2.1 Pressure Loss Estimates

The QCGAT duct pressure loss estimates used in the preliminary design optimization are presented in Table 3-2. The loss estimates are based on the AiResearch compound-nozzle tests and the 1976 IR&D mixer (see Figure 3-6) cold-flow model test data (ref. 6). The pressure loss of a lobed mixer duct cannot be estimated from friction losses alone, such as:

$$\frac{\Delta P_T}{P_T} = \int_o^L \frac{\gamma M^2}{2} \frac{4\bar{\delta}}{D_h} \, dL \tag{1}$$

$$A'_{S2} = C_{DS2}A_{S2}$$

$$A'_{IN} = \Sigma A'_{S}$$

$$A'_{S1} = C_{DS1}A_{S1}$$

$$A'_{MIN} = \Sigma C_{DE}A_{MIN}$$

$$A'_{EXIT} = \Sigma C_{DE}A_{EXIT}$$
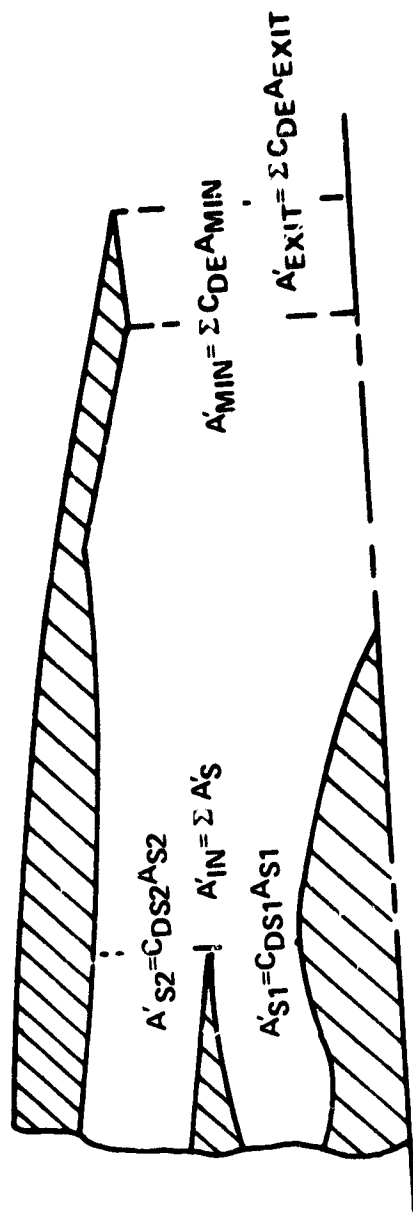
WHERE:
$$C_{DS1} = f(P_{TR1}, P_{TR2})$$
$$C_{DS2} = f(P_{TR1}, P_{TR2})$$
$$C_{DE1} = f(P_{TR1}, P_{\infty})$$
$$C_{DE2} = f(P_{TR2}, P_{\infty})$$

Figure 3-2. Compound Flow Analysis Effective Flow Areas.
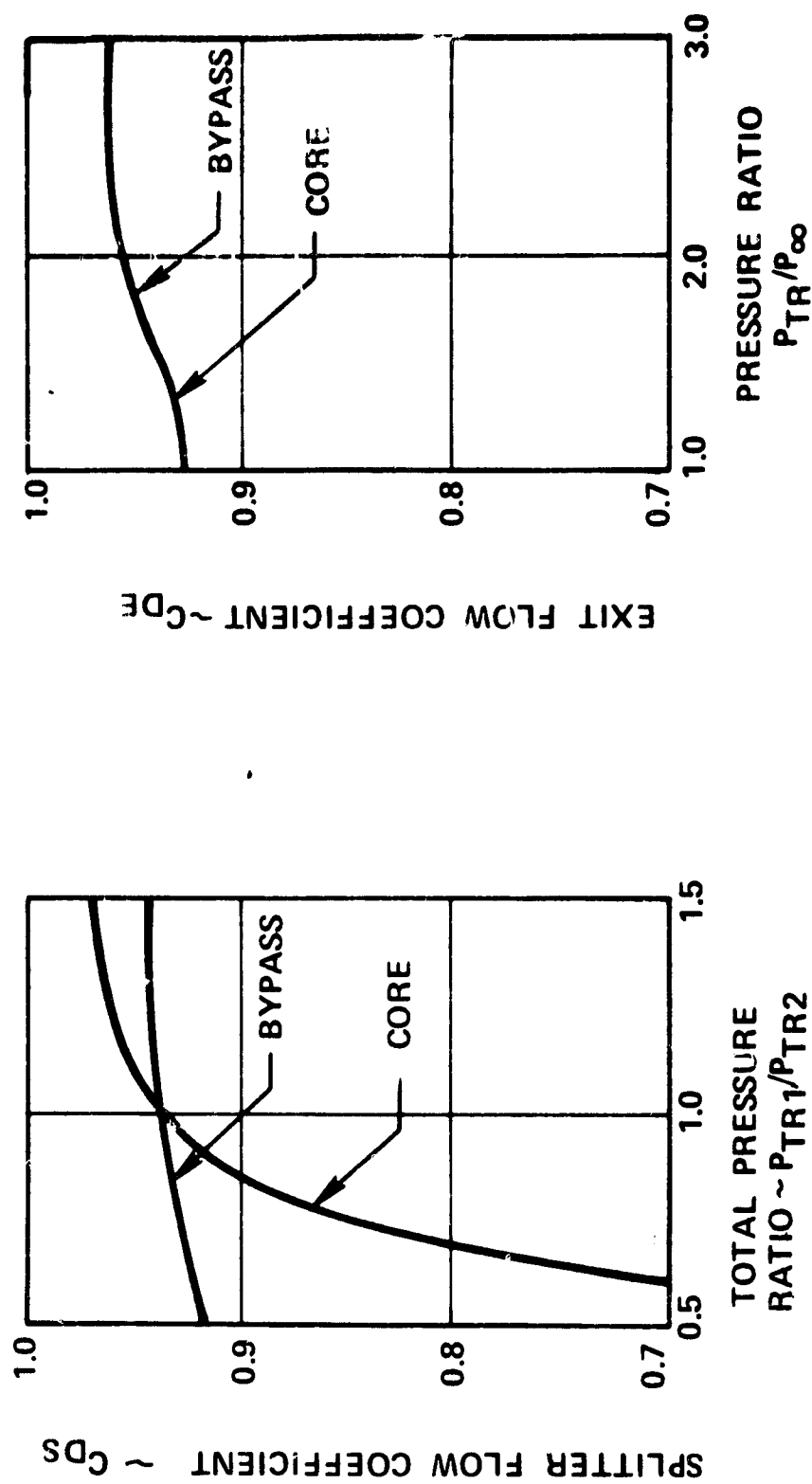
Figure 3-3. Compound Flow Analysis Typical Flow Coefficients.

11

$$\frac{\Delta P}{P_T}\Big)_{CORE} = \frac{\Delta P}{P_T}\Big)_1 + \frac{\Delta P}{P_T}\Big)_{PLUG}$$

$$\frac{\Delta P}{P_T}\Big)_{BYPASS} = \frac{\Delta P}{P_T}\Big)_2 + \frac{\Delta P}{P_T}\Big)_{SHROUD}$$

$$\frac{\Delta P}{P_T}\Big)_{MIX} = f(P_{T1}, P_{T2}, T_{T1}, T_{T2}, W_1, W_2, P_S, \eta_{MIX})$$
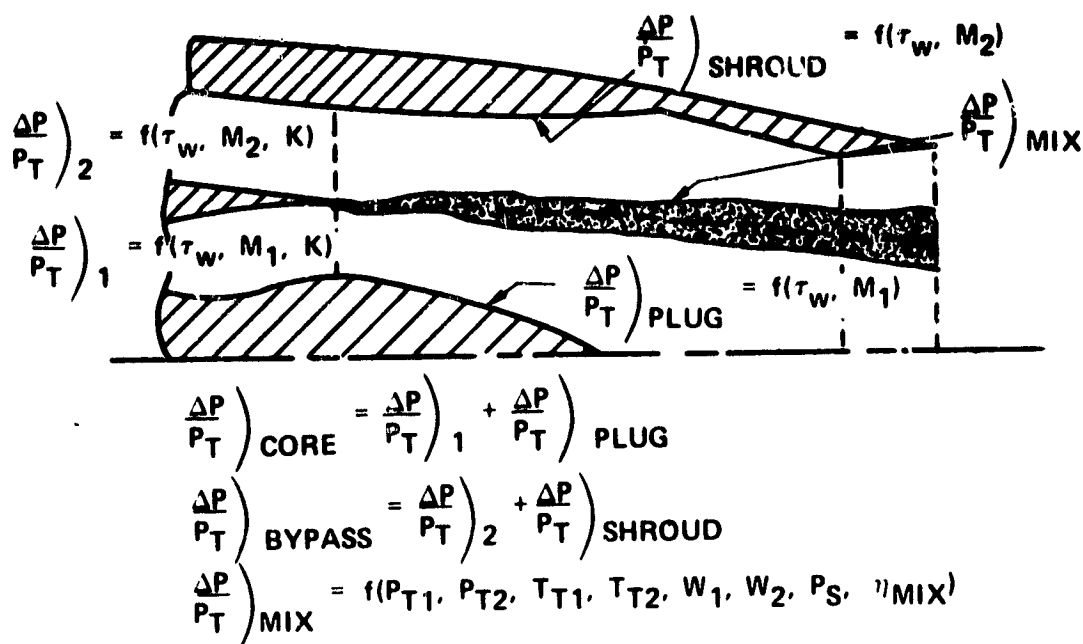
Figure 3-4. Compound Flow Analysis Total Pressure Losses.
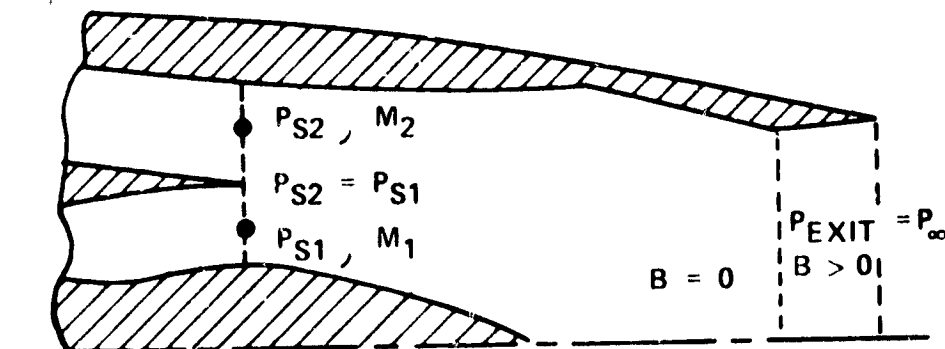
- SPLITTER MATCHING CRITERIA
  KUTTA CONDITION APPLIED, I.E., $P_{S1} = P_{S2}$
  INLET MACH NUMBER LIMIT, I.E., $M_1 \leq 1.0$, $M_2 \leq 1.0$
- COMPOUND NOZZLE CHOKING CRITERIA
  COMPOUND UNCHOKED $P_{EXIT} = P_\infty$ $B > 0$
  COMPOUND CHOKED $B = 0$

  WHERE: $B = \sum\limits_{i=1}^{n} \frac{A_i}{\gamma_i}\left(\frac{1}{M_i^2} - 1\right)$

Figure 3-5. Compound Flow Analysis Boundry Conditions.

12
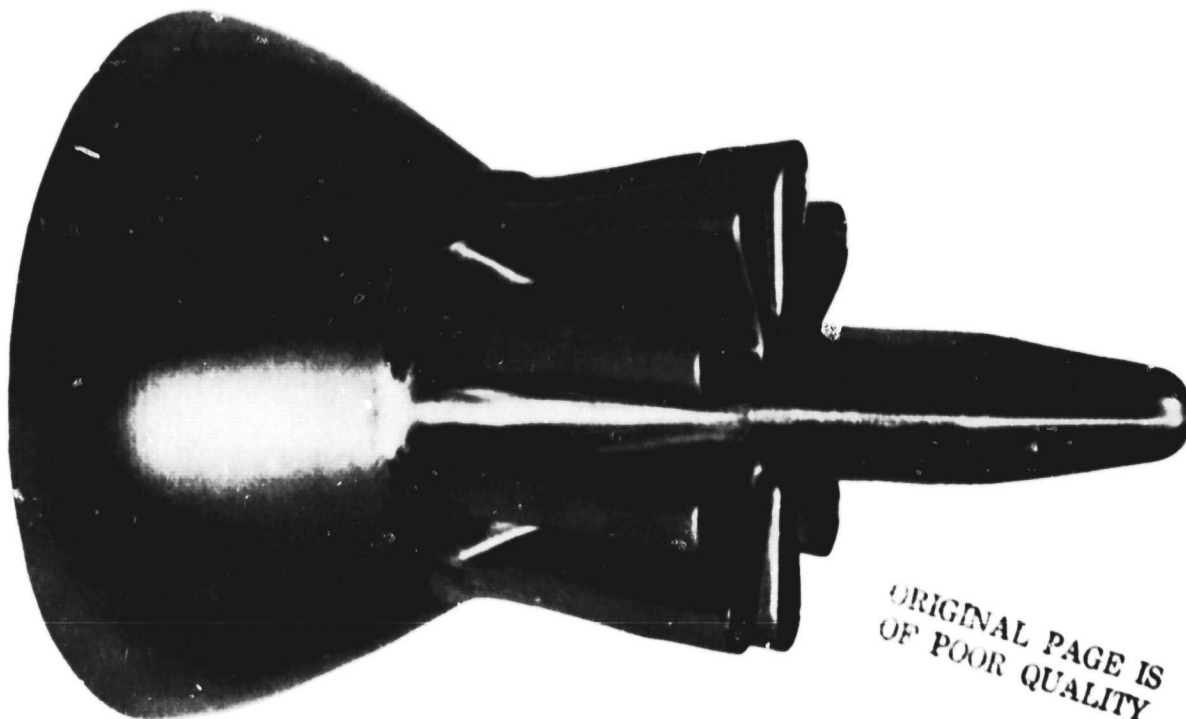
NUMBER OF LOBES	N = 9
TAPER RATIO	TR = 1.18
ASPECT RATIO	AR = 2.39
PENETRATION RATIO	PEN = 0.72
SPACING RATIO	SR = 0.78
MIXING DUCT LENGTH RATIO	X/D = 0.80

Figure 3-6.   AiResearch 1976 IR&D Mixer Compound Core.

13

MP-64487

TABLE 3-1. CYCLE MATCH CHANGES DUE TO A COMPOUND NOZZLE
RELATIVE TO A COANNULAR AT SLS TAKEOFF THRUST.

Parameter	Analytical Predictions	Engine Test
$\Delta N_1/N_1$	-1.7%	-1.9%
$\Delta N_2/N_2$	-0.2%	-0.0%
$\Delta T_{4.1}$	+1.8°K (+3°F)	+4.8°K (+8°F)
$\Delta P_{T5.2}/P_{T5.2}$	+0.6%	+2.8%
$\Delta P_{T14.0}/P_{T14.0}$	0.0%	0.0%
$\Delta TSFC/TSFC$	-1.5%	-0.6%

NOTES:

N_1 - low-rotor speed

N_2 - high-rotor speed

$T_{4.1}$ - turbine inlet total temperature

$P_{T5.2}$ - core-nozzle supply, total pressure

$P_{T14.0}$ - bypass-nozzle supply, total pressure

TSFC   - thrust specific fuel consumption

TABLE 3-2. QCGAT MIXER-COMPOUND EXHAUST SYSTEM
PRESSURE LOSS ESTIMATES.

Flight Condition	$\frac{\Delta P}{P_T}$ Core	$\frac{\Delta P}{P_T}$ Bypass	$\frac{\Delta P}{P_T}$ Mix
Design Point M = 0.8 Alt = 12,192m (40K ft)	0.0248	0.0297	0.0044
S.L.S. Takeoff 298°K (77°F) Day	0.0161	0.0241	0.0031

In order to account for the secondary flow losses and other unknown losses, a ratio of the test-data loss to the analytical friction loss was formed:

$$K_R = \frac{\Delta P/P_T\big)_{\text{Test Data}}}{\frac{\Delta P}{P_T}\big)_{\substack{\text{Analytical} \\ \text{Friction}}}} \tag{2}$$

The loss ratio for the 1976 IR&D mixer (see Figure 3-6) was three to one (KR = 3.0). Thus, the preliminary QCGAT mixer analytical-loss estimate was calculated using the standard friction loss and a loss ratio of three (K_R = 3.0). In the off-design calculations, the design point loss is scaled with the corrected flow i.e.,

$$\frac{\Delta P}{P_T} = K \left(\frac{W_\gamma \overline{\theta}}{\delta}\right)^2 \tag{3}$$

The QCGAT mixer off-design loss scalars are presented in Table 3-3.

The mixing-duct loss estimate is comprised of two basic elements; a mixing-duct-shroud friction loss, and an empirical flow mixing loss correlation. The mixing loss is computed by simultaneous solution of the momentum and continuity equations for a presumed thermal-mixing efficiency. The mixing-duct shroud-friction loss is computed from standard-duct friction loss analysis.

3.2.2 QCGAT Flow Coefficients

The design point and sea-level-static flow coefficient estimates for the QCGAT exhaust system preliminary design are summarized in Table 3-4. The exhaust system exit-flow coefficients used in the QCGAT preliminary design were obtained from scale model cold-flow rig test data (see Figure 3-7). Mixer-compound systems have flow coefficients which are lower than standard compound nozzles. However, the characteristic shape is the same as shown in Figure 3-7. Comparison of the compound-flow analysis to the Model ATF3 Turbofan engine hot-flow mixer test data (ref. 5) has verified that the exit flow-coefficient dependence on thermal mixing can be adequately accounted for by proper mixing loss accounting. Thus the cold-exit-flow coefficients are used for both hot-and cold-flow predictions.

15

TABLE 3-3. QCGAT MIXER-COMPOUND EXHAUST SYSTEM OFF-DESIGN LOSS SCALARS.

$$\frac{\Delta P}{P_T} = K \left(\frac{W\sqrt{\theta}}{\delta}\right)^2$$

Loss	K		$\frac{W\sqrt{\theta}}{\delta}$	
	s^2/kg^2	(sec^2/lb^2)	kg/s	(lbs/sec)
Core	5.54×10^{-5}	(1.14×10^{-5})	20.2	(44.5)
Bypass	10.70×10^{-6}	(2.20×10^{-6})	41.8	(92.1)
Mixing Duct	21.39×10^{-7}	(4.40×10^{-7})	62.6	(138.0)

TABLE 3-4. QCGAT EXHAUST SYSTEM PERFORMANCE INTERNAL FLOW COEFFICIENTS.

Flight Condition	$C_{D_{S1}}$	$C_{D_{S2}}$	$C_{D_{E1}}$	$C_{D_{E2}}$
Design Point M = 0.8 Alt = 12,192m(40K ft)	0.9330	0.9355	0.9540	0.9547
S.L.S. Takeoff 298°K (77°F) Day	0.9300	0.9350	0.9340	0.9350

16
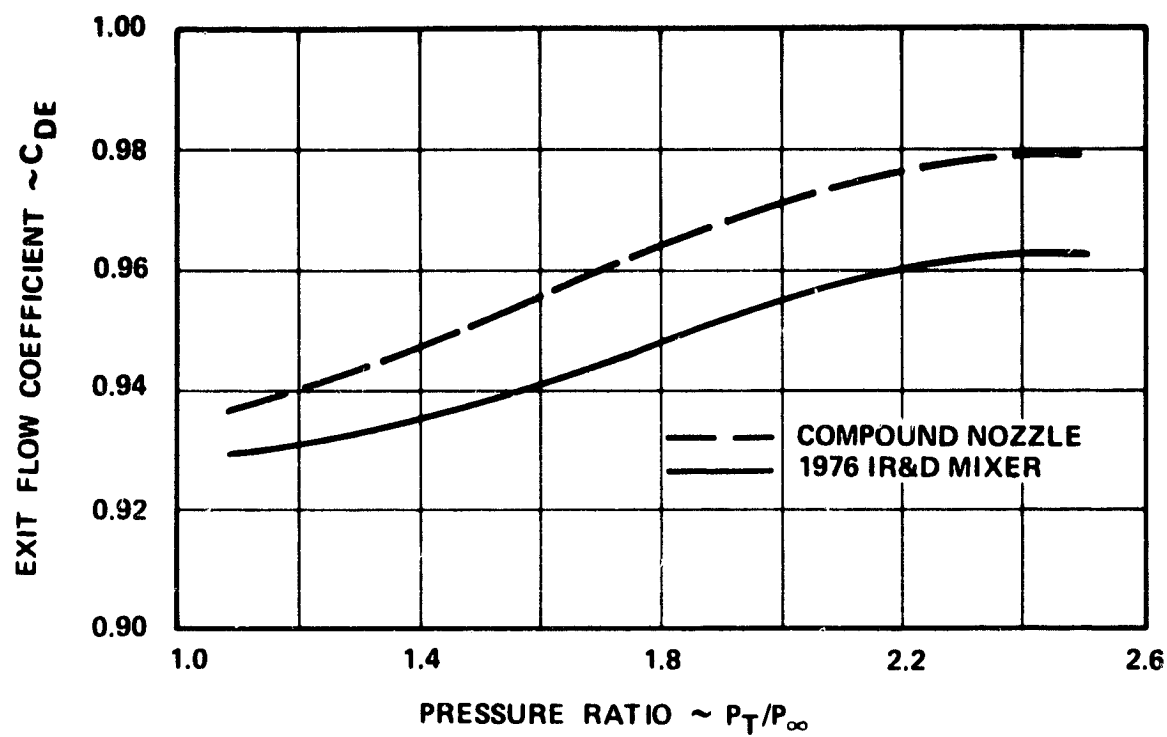
Figure 3-7. Mixed and Partially Mixed Exhaust System Exit Flow Coefficients.

A unique splitter-plane flow-coefficient correlation has been developed. The standard flow-coefficient definition is still used, i.e.,

$$C_D = W_{actual}/W_{ideal} \qquad (4)$$

However, the ideal flow is based on the local static pressure at the splitter plane. A single value curve results when the splitter flow coefficients are correlated against the total pressure split. The AiResearch 1976 IR&D mixer flow coefficients shown in Figure 3-8 were used for the QCGAT preliminary design.

3.2.3 Exhaust System Area Sizing

Optimizing the cycle performance at the cruise and SLS operating conditions was the main design consideration for selecting the QCGAT exhaust system areas. The engine cycle was initially optimized with a separate-flow coannular-exhaust system, then a mixer-compound exhaust system was sized to hold the same cruise match. Cycle off-design studies were then conducted and the exhaust system areas were modified, thus trading design-point performance for better off-design performance.

3.2.3.1 Minimum and Exit Area Sizing

Design-point flow conditions (W, P_T, T_T) were specified for each stream in addition to the appropriate pressure losses and thermal mixing efficiency. Only the exit boundary condition is applied while the exit area and/or minimum area are varied. A total-pressure deviation function is plotted versus exit and/or minimum area as shown in Figure 3-9. The cycle match area corresponds to a deviation function of zero. The QCGAT design-point match area is 2603.2 cm^2 (403.5 in^2) while the SLS-takeoff match point area is 2649.0 cm^2 (410.6 in^2). (Note that later cycle optimization analysis set the exit area at 2619.3 cm^2 (406 in^2) as discussed in Section 3.2.5). If the design point is compound choked, then the exit area may be increased to either optimize thrust or to trade off the design-point thrust for a closer compound unchoked secondary design-point cycle match. However, the exit and minimum plane areas were set equal for the QCGAT design.

3.2.3.2 Inlet and Mixing Plane Areas

Once the minimum and exit plane areas were sized, an inlet area study was conducted. Again, only the exit boundary condition was applied while the exit area was held constant and the inlet area was varied. The performance versus inlet area study is presented in Figure 3-10. The inlet area sizing criteria were based on maximizing internal thrust while remaining within a
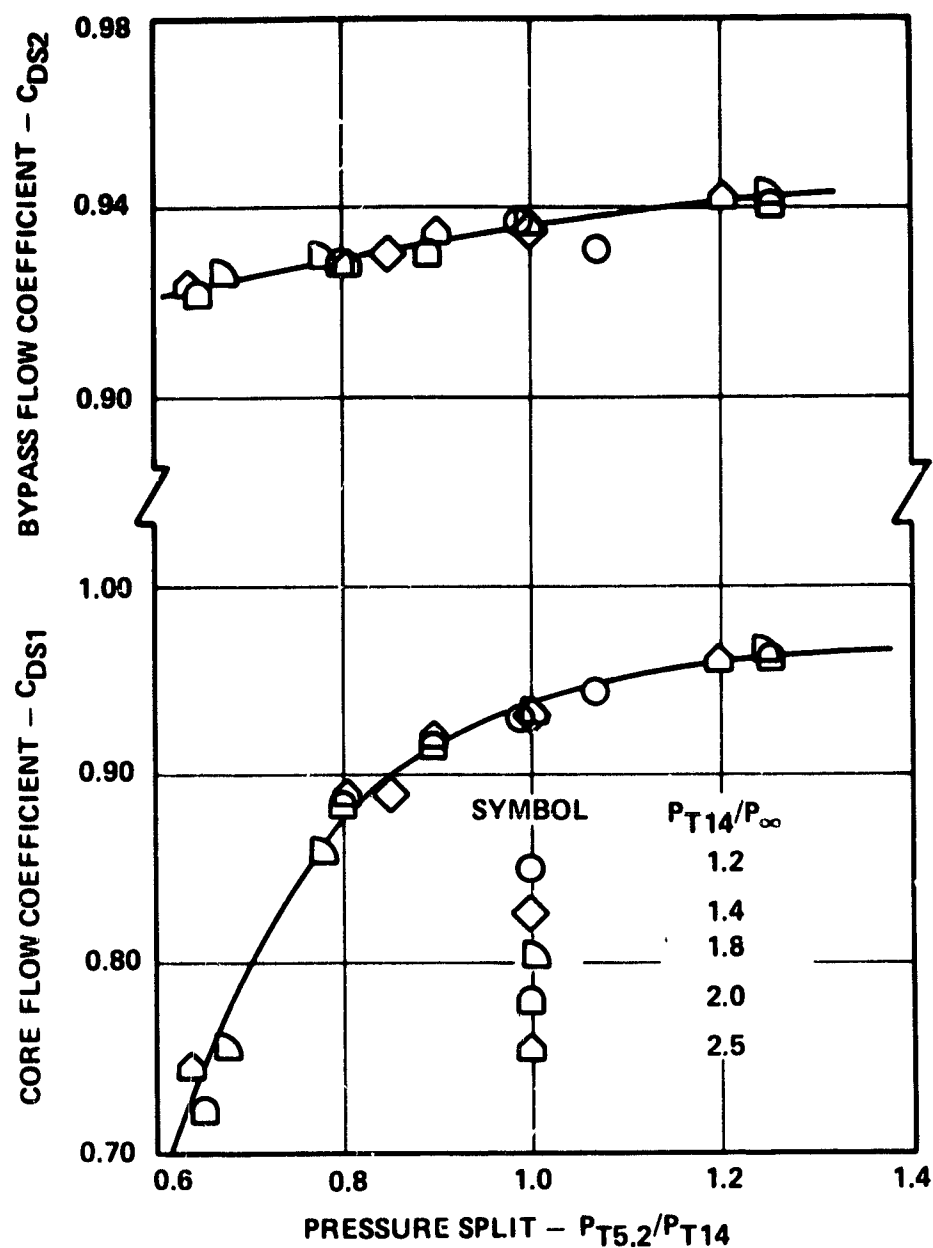
Figure 3-8.   AiResearch 1976 IR&D Mixer Compound Splitter Flow Coefficients.

Figure 3-9. QCGAT Exit Area Sizing.
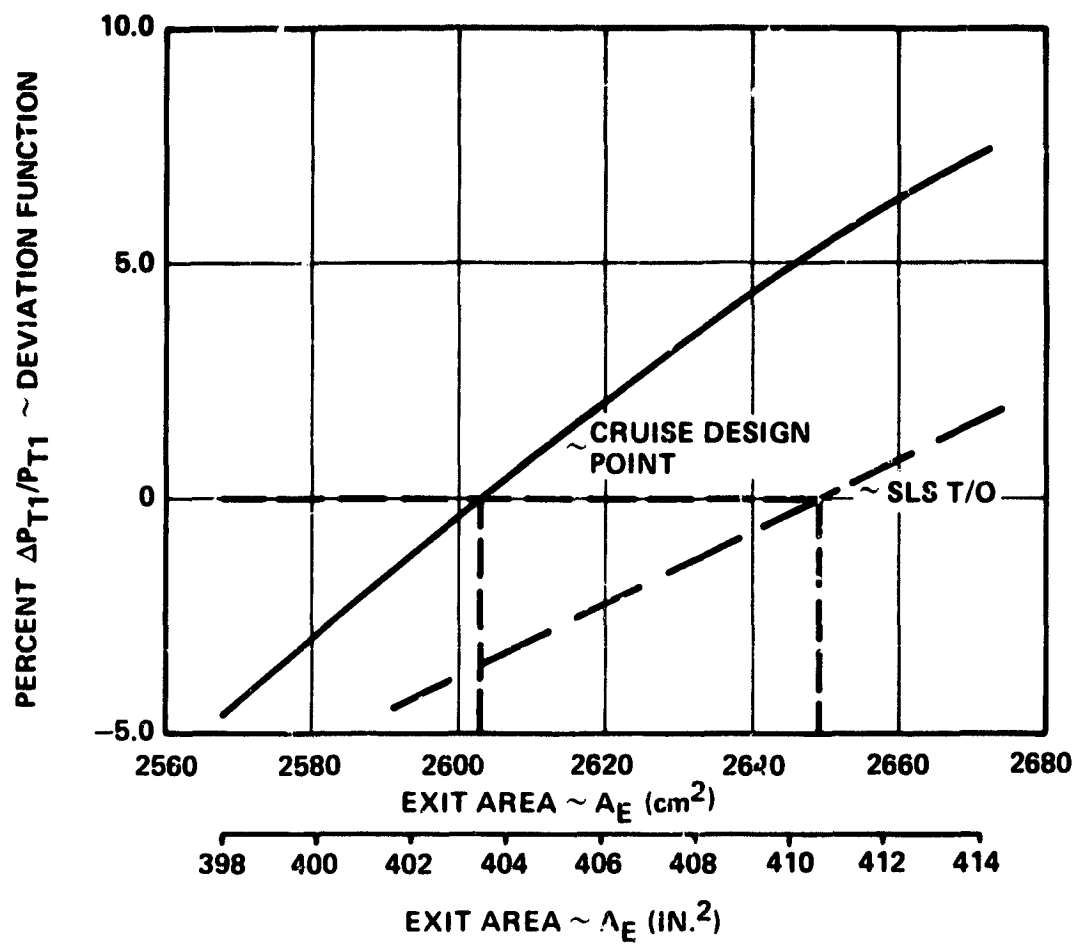
NOTE: A_E (CRUISE) = 2603.2 cm^2 (403.5 IN.^{2})
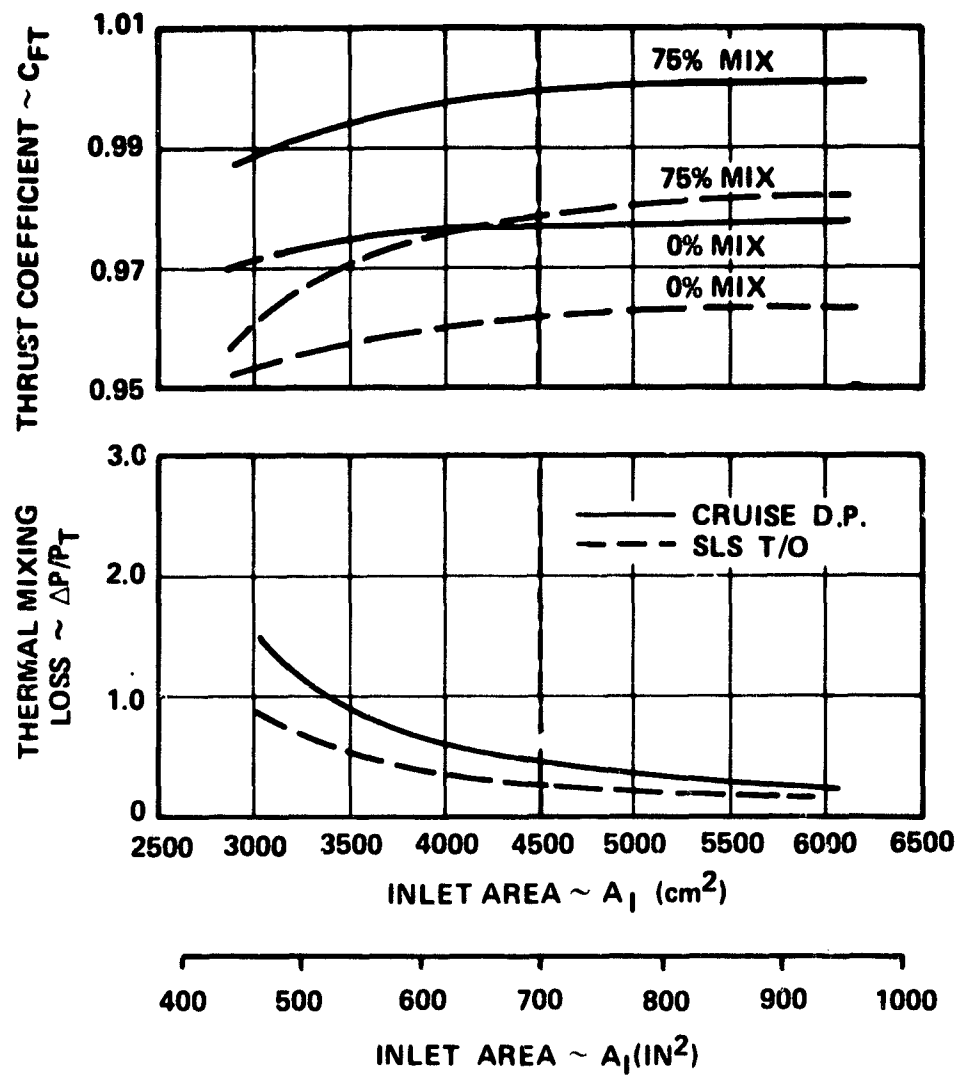
A_E (SLS-T/O) = 2649.0 cm^2 (410.6 IN.^{2})

Figure 3-10. QCGAT Inlet Area Sizing.

practical nacelle size for drag considerations. Characteristically, the thrust-coefficient curves level off with increasing inlet area. Therefore, the evident trade-off guideline of size versus performance is the point where the internal performance begins to level off. Above that point, external drag would become dominant. Therefore, a nozzle inlet area of 4516.1 cm^2 (700 in^2) appeared to be the optimum choice for QCGAT.

The mixing loss variation with inlet area, as shown in Figure 3-10, also indicates that the 4516.1 cm^2 (700 in^2) is a good choice. The rate of change of the mixing-duct inlet Mach numbers also appears to be leveling off at 4516.1 cm^2 (700 in^2) as shown in Figure 3-11. It is important to minimize the inlet Mach numbers since they directly set the loss levels, mixing rate, and mixer-lip noise generation. Examination of the required splitter area, Figure 3-11, indicates that both the sea level and cruise design point nozzle demand areas could be held equal if the inlet area was set at 4032.3 cm^2 (625 in^2). However, 4032.3 cm^2 (625 in^2) would result in higher Mach numbers with increased losses and increased mixer generated noise. Thus, the sea level static takeoff areas were allowed to deviate. A final area iteration was conducted in conjunction with the engine cycle deck to optimize the engine design and off-design performance as discussed in Section 3.2.5.

3.2.4 Thrust Coefficient Prediction

Thrust coefficients are predicted using compound-flow analysis. Empirical correlations for pressure losses are required as defined previously in Section 3.2.2. In addition, a throat-efficiency correlation is also required for the calculations. The throat-efficiency relationship was developed from boundary layer theory and is expressed as:

$$C_F = \frac{C_S \ (mV+PA)_{exit} - P_\infty A_{exit}}{F_{ID}} \tag{5}$$

$$C_S = 1.0 - 0.12088 \ (D_{HE})^{-0.5} \ (R_{e_D})^{-0.211} \left(\frac{L}{D}\right)^{0.789} \left(1+\frac{\gamma-1}{2} \ M^2\right)^{-0.632}$$

22
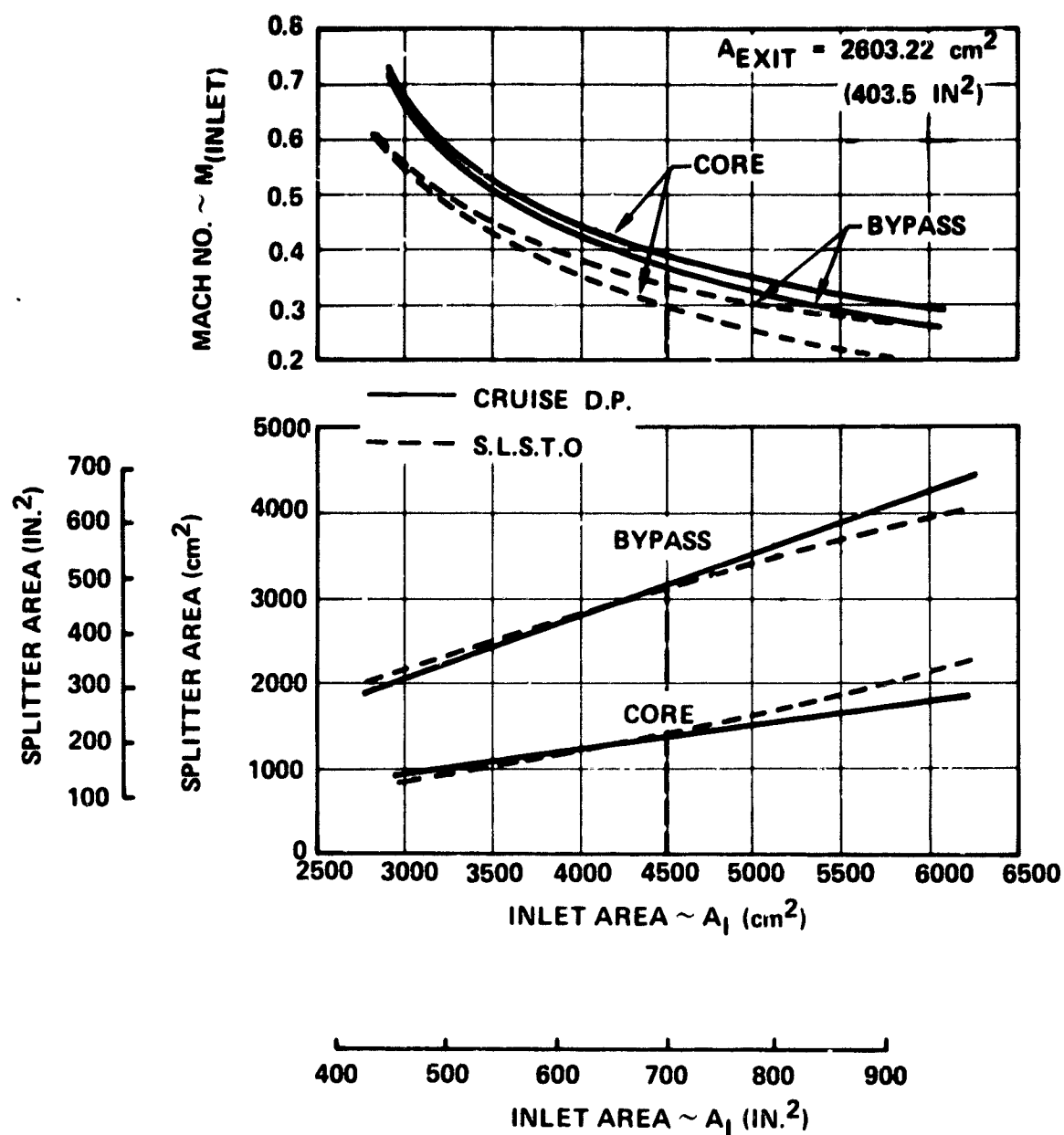
Figure 3-11. QCGAT Splitter Area and Mach Number Versus Inlet Area.

The thrust gain due to thermal mixing is calculated from a solution of the continuity and momentum equations. Based on the Frost-mixing efficiency correlation, as discussed later in Section 3.3.2, a mixing efficiency of 0.75 was chosen for the QCGAT predictions. This level appears to be the maximum obtainable for realistic geometries. The predicted thrust coefficients at the cruise design point and at sea level static takeoff as a function of η_{mix} are shown in Figure 3-12. With an η_{mix} of 0.75, the predicted cruise design point thrust coefficient is 1.001 and the sea-level value is 0.974. Since the design-point thrust coefficient exceeds the proposal target value of 0.994, and since this level had not been previously demonstrated by AiResearch; the design-point thrust coefficient in the cycle deck was maintained at 0.994.

3.2.5 Performance and Matching Characteristic Maps

With the exhaust system geometry and loss characteristics defined, the off-design performance and matching characteristics were computed. Component maps can be generated provided the temperatures, mixing efficiency, and fuel-air ratios are known. Currently, constant values based on an average from the flight mission study are used. The averaged values are as follows:

$$T_{T1} = 758.4°K \ (1365.2°R)$$

$$T_{T2} = 306.6°K \ (551.9°R)$$

$$\eta_{mix} = 0.75$$

Initial maps sized to the cruise design-point condition were transmitted to the performance group where off-design engine match characteristics were studied. Based on the off-design engine match studies, the exhaust system exit area was resized to 2619.3 cm^2 (406.0 in^2). The performance maps were then scaled to the revised exit area using the compound-flow analysis scaling routine.

The predicted QCGAT exhaust system matching-characteristic maps are presented in Figure 3-13 as core-corrected flow and bypass-corrected flow versus core-pressure ratio for lines of constant bypass-pressure ratio. The thrust-coefficient map is presented in Figure 3-14 as thrust coefficient versus core-pressure ratio for lines of constant bypass-pressure ratio.
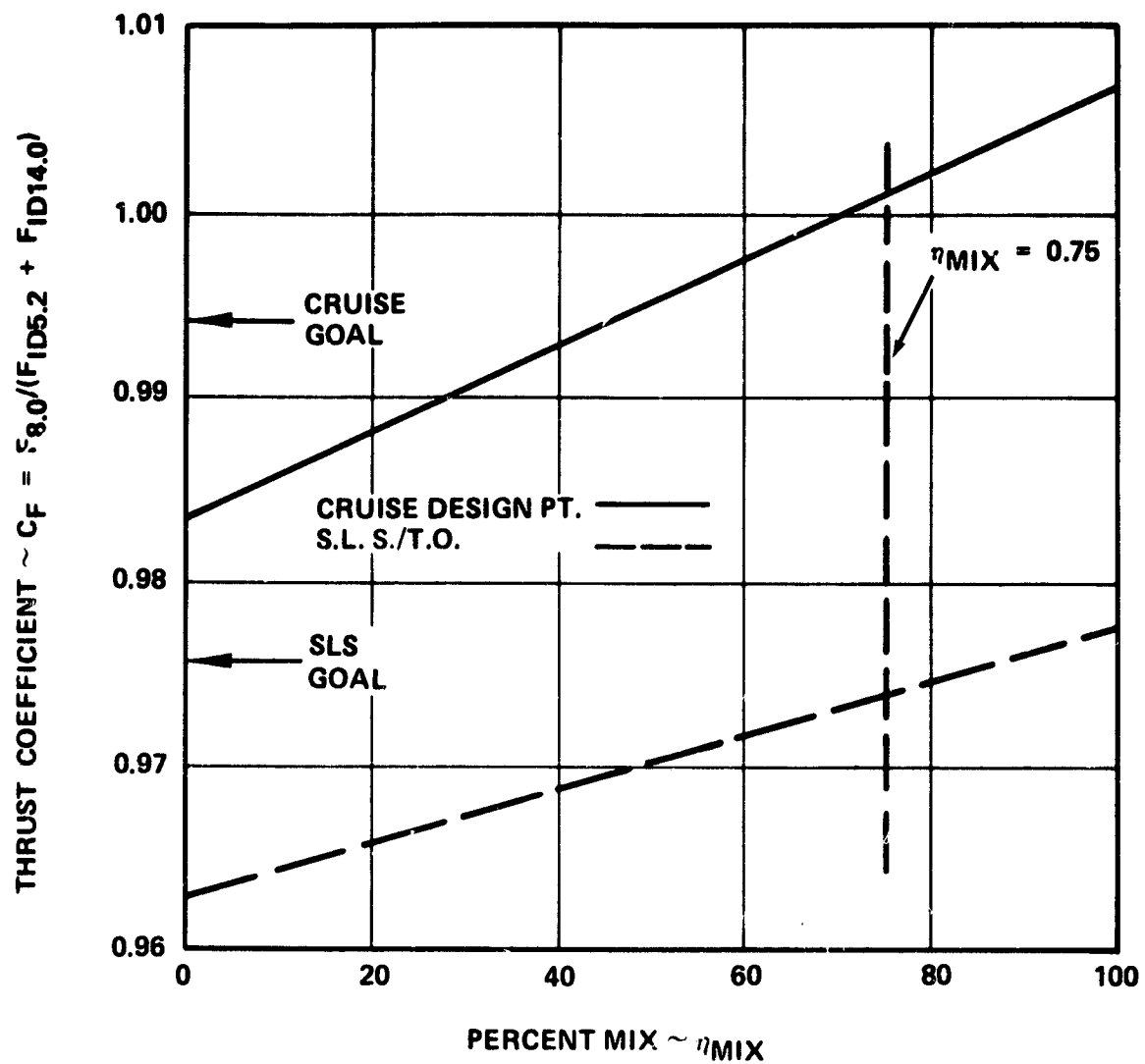
Figure 3-12. Thrust Coefficient Versus Percent Mixing.
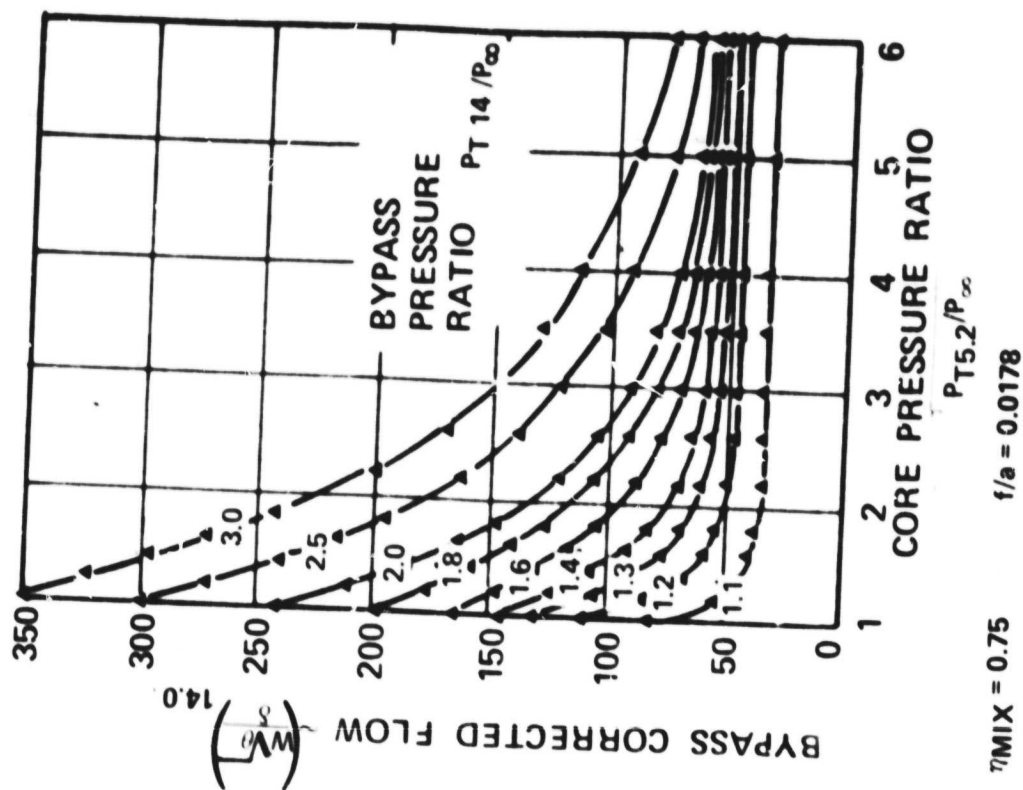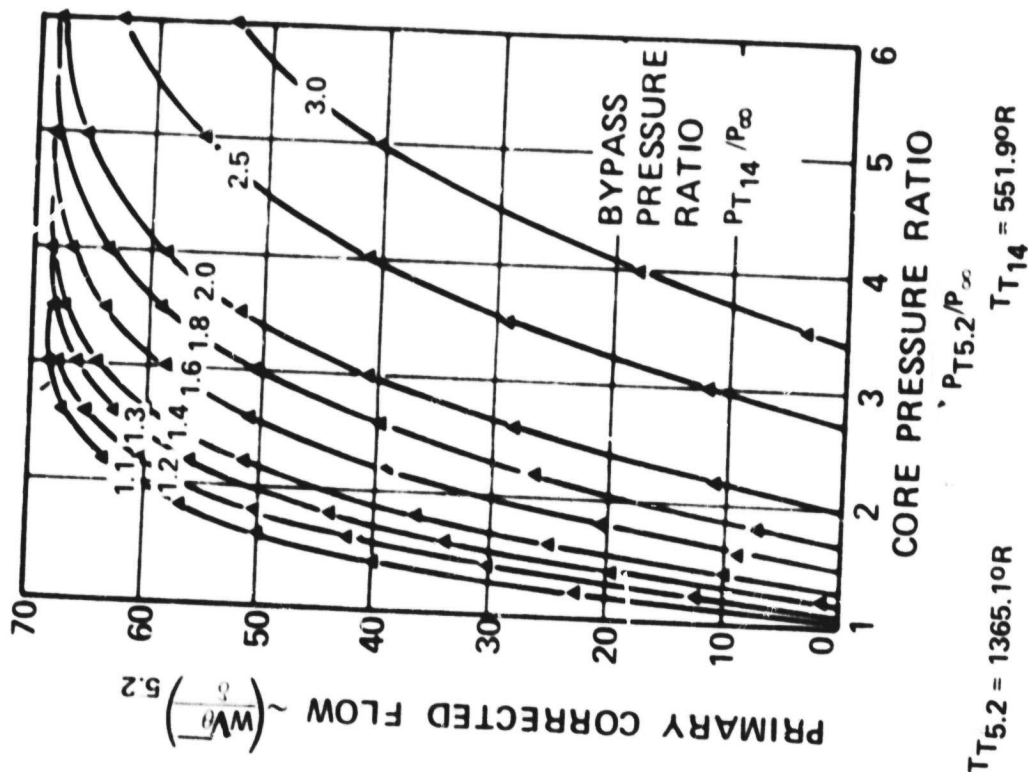
Figure 3-13. QCGAT Compound Nozzle Exhaust System Performance Cycle Matching Characteristics.

26
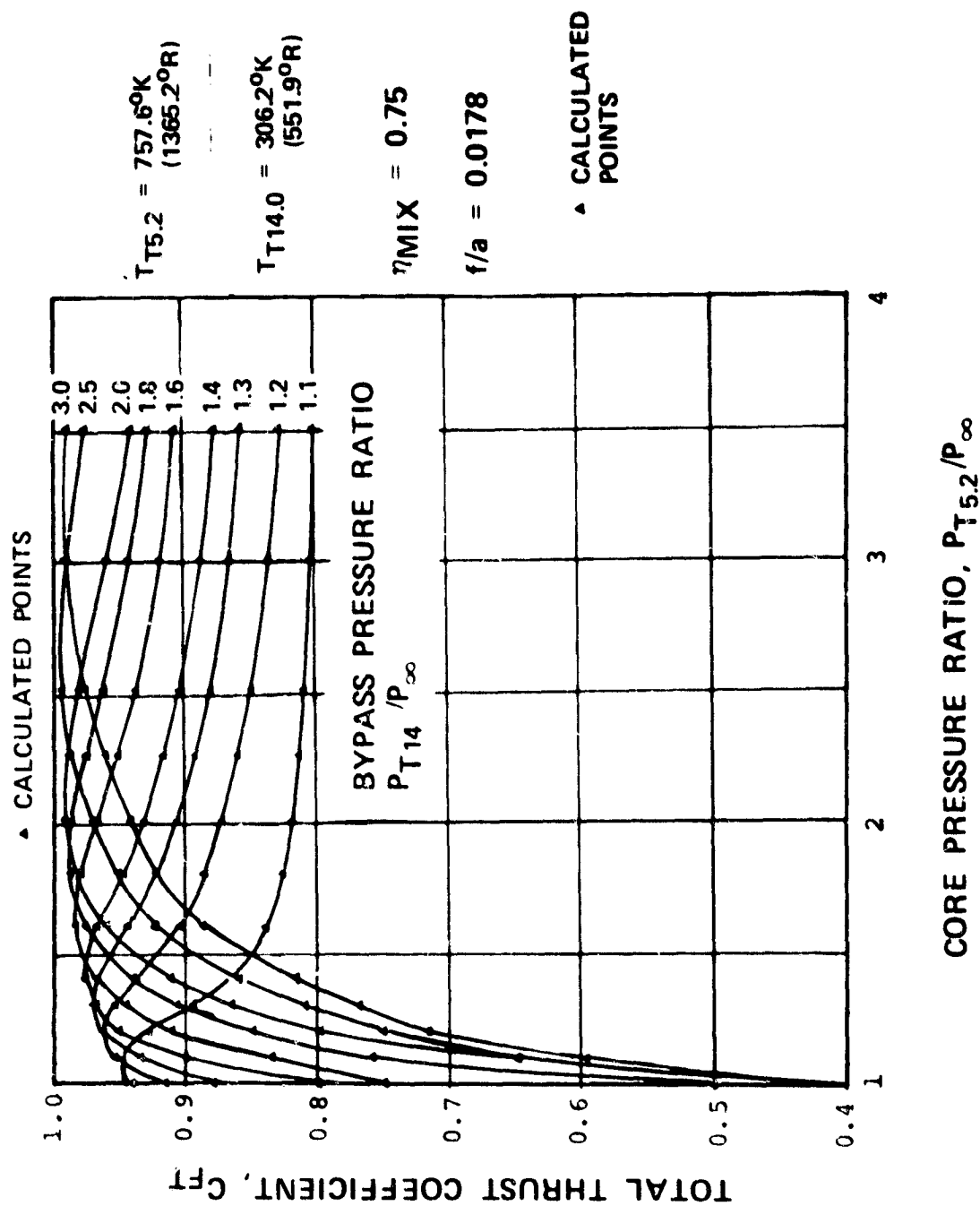
Figure 3-14. QCGAT Compound Nozzle Exhaust System Performance Total
Thrust Coefficient.

3.3 Preliminary Mixer Design Selection and Optimization

A preliminary mixer design optimization computer program was developed to perform preliminary parametric studies of mixer exhaust-system geometry effects on overall performance. The program was based on state-of-the-art techniques involving empirical and semi-empirical equations for pressure loss, thermal mixing, and peak velocity decay. Mixer geometry parameters studied are defined in Figure 3-15.

3.3.1 Mixer Lobe Total Pressure Loss Correlations

Several sources of pressure loss were included in the analysis: an empirical mixer loss factor which is a function of the mixer equivalent hydraulic diameter, the turning loss through the mixer lobes, the flow-mixing loss for an assumed η_{mix}, and the skin friction loss for the mixing duct and plug.

The mixer-loss factor is based on empirical studies conducted by Postlewaite (ref. 7) and by Frost (ref. 8). The mixer-loss factor can be correlated as a function of the equivalent hydraulic diameter as shown in Figure 3-16. The AiResearch data (ref. 6) falls on the data line of Postlewaite, therefore Postlewaite's data was used in the analysis. The mixer-loss-factor is defined as the ratio of the mixer-nozzle loss to the analytical loss of a circular convergent nozzle of equivalent length and exit area. The pressure loss of the convergent nozzle is calculated in the analysis by using standard skin friction calculations, i.e.,

$(\Delta P/P = \frac{\gamma}{2}M^2 4 f\ L/D)$. This loss correlation provides losses

consistent with the loss ratio (K_R) discussed in Section 3.2.1.

A turning loss was included in the analysis since a varying plug-crown radius requires various degrees of core-flow turning relative to the base circular nozzle. The bypass stream has the flexibility of designing large radius ratio turns; therefore, bypass turning loss was considered negligible. The degree of turning was based on the difference between the mean-exit radius and the mean-inlet radius of an equivalent-area-annulus duct. The offset-loss factor shown in Figure 3-17, is a function of the radius change divided by the mixer length. A loss correlation, Curve A, was obtained from diffuser-duct offset data, and was initially used in the analysis. Since the turning losses were a significant loss in the analysis, an additional check on turning losses was made. A second loss estimate, Curve B, was derived from circular duct bend losses and the diffusion loss incurred in turning flows. Use of Curve B had little impact on the optimization results.

28
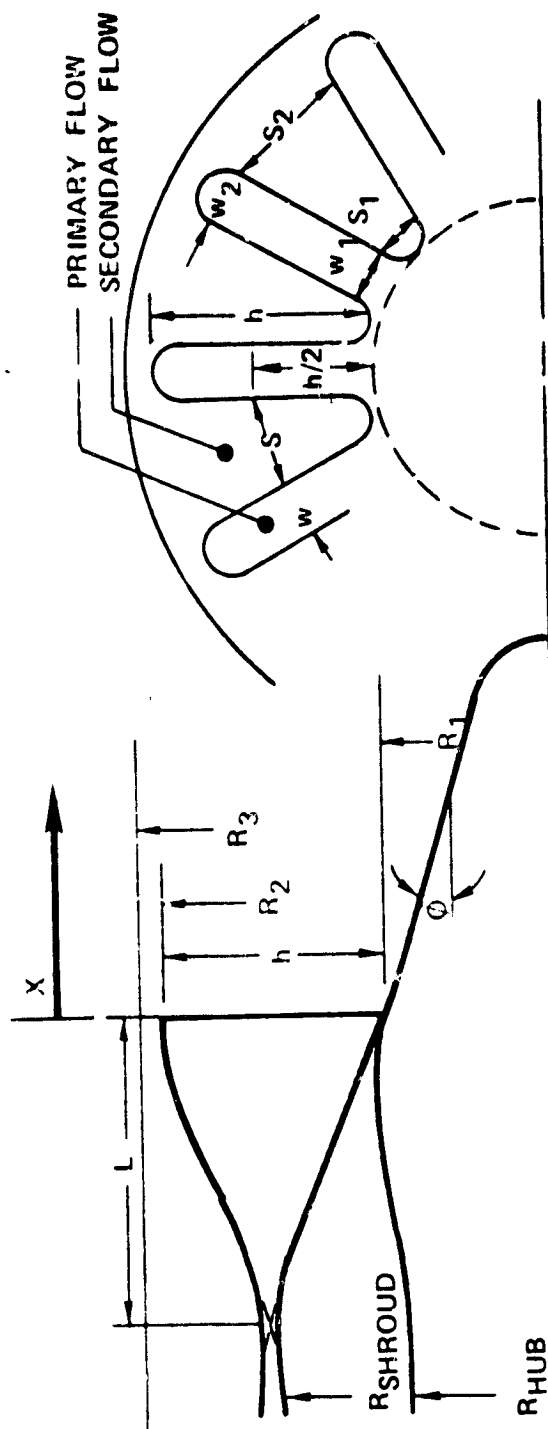
MIXER GEOMETRY SPECIFIED BY:

PENETRATION RATIO	PEN = $h/(R_3 - R_1)$
LOBE ASPECT RATIO	AR = h/w
SPACING RATIO	SR = S/w
NUMBER OF LOBES	N
LOBE TAPER RATIO	TR = w_2/w_1
PLUG HALF ANGLE	ϕ
PLUG RADIUS	R_1
MIXER LENGTH	L
MIXING DUCT LENGTH	X
MIXING DUCT DIA.	$D = 2R_3$

D_E = DIAMETER OF EQUIVALENT AREA CIRCLE

D_H = HYDRAULIC DIAMETER

D_{HE} = EQUIVALENT HYDRAULIC DIAMETER (D_H/D_E)

Figure 3-15. Mixer Design Analysis - Nomenclature.

29
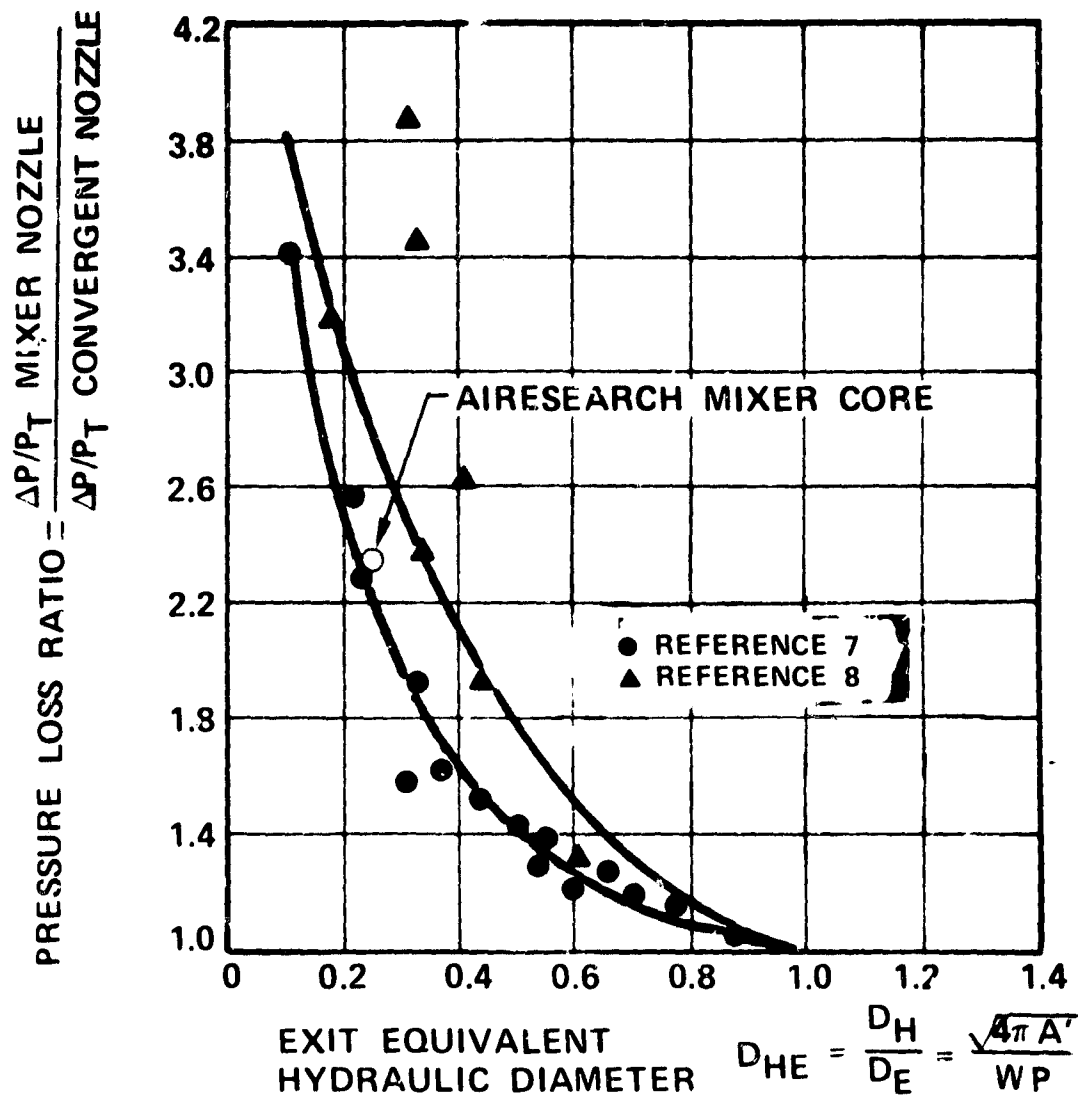
Figure 3-16. Total Pressure Loss Ratio Due to Mixer.
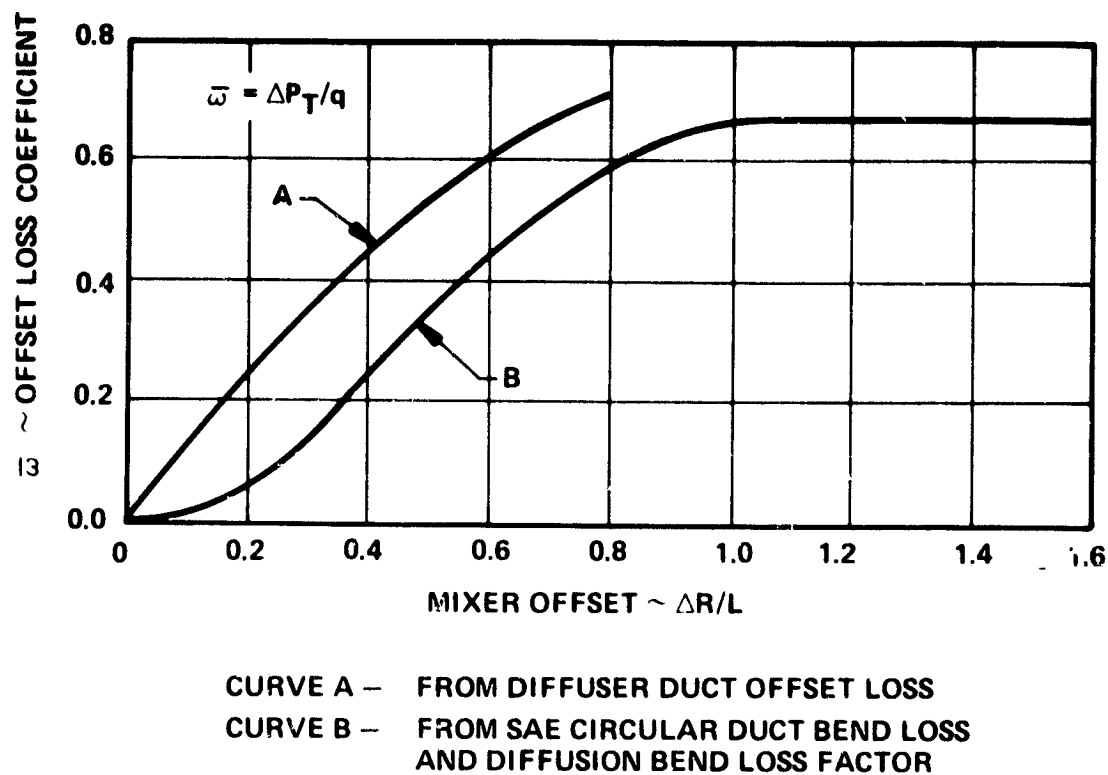
Figure 3-17. Total Pressure Loss Due to Offset Ratio.

The centerbody plug and mixing duct friction losses are calculated in the analysis using the standard friction-loss calculations. The mixing-duct and centerbody-plug lengths are calculated in the program as a function of other parameters with an assumed plug angle of 0.26 radians (15°).

3.3.2 Criteria for Mixing Duct Length Selection

Mixing of streams with different velocities occurs within two distinctive zones. The mixing process is described in Figure 3-18. Zone I is single element decay of the high-velocity streams and the velocity decay is fairly rapid. Zone II is called the coalescing core region and decay becomes linear and much slower than in Zone I. The peak velocity decay term is defined as the local peak velocity difference relative to the initial (mixing plane) velocity difference of the two flow streams. The velocity decay rate can be used to establish the required mixing duct length. Because of the slow velocity decay of Zone II, the practical mixing duct length is set at the end of Zone I which is represented by the characteristic length Z_C (ref. 9, 10, and 11).

The mixing duct characteristic length, Z_C, is defined as:

$$Z_C = 12[1+1/4 \ (s/w)^{2/3}](s/w)^{1/3} \ f_1(D_{HE}, \ TR) f_2(R/s, \ AR, \ VR) f_3(VR) \quad (6)$$

where:
$$s = (s_1 + s_2)/2 \qquad w = (w_1 + w_2)/2 \qquad VR = V_B/V_C$$

$$R/s = \frac{R_1 + h/2}{s}$$

$$f_1(D_{HE}, TR) = \left[1 + \frac{2.67(1/D_{HE} - 1)}{1 + 5(1 - 1/TR)^8} \right]^{-1}$$

$$f_2(R/s, AR, VR) = [1 + 0.33 * R/s * TR^3 * R^2]^{-1}$$

$$f_3(VR) = (1 - VR)^{-1.25}$$
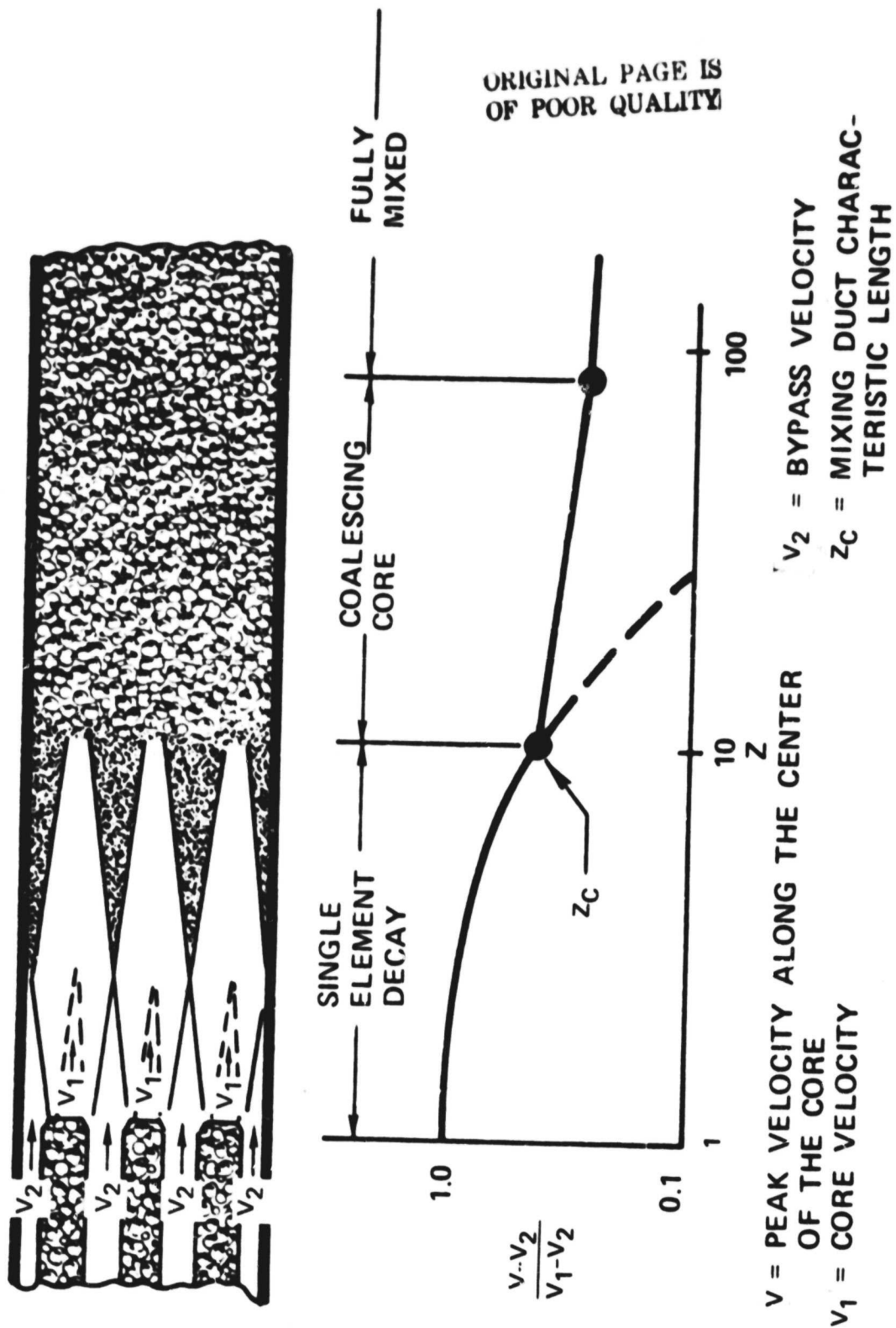
Figure 3-18. Peak Velocity Decay Characteristics.

$$\frac{v - v_2}{v_1 - v_2}$$

v = PEAK VELOCITY ALONG THE CENTER
    OF THE CORE

v_1 = CORE VELOCITY

v_2 = BYPASS VELOCITY

z_c = MIXING DUCT CHARAC-
       TERISTIC LENGTH

FULLY
MIXED

COALESCING
CORE

SINGLE
ELEMENT
DECAY

33

For calculating the thermal mixing characteristic length, the average spacing ratio was selected. However, for a conservative estimate of the peak-velocity-decay characteristic length, the maximum spacing ratio at the tip of the lobes (S_2/W_2) was used. The mixing duct length is determined from the characteristic length as defined by the following equation:

$$X = Z_C^{1/b} * C_D * \sqrt{4/\pi \, A_{Lobe}} * \sqrt{1+M_{core}} \qquad (7)$$

$$\text{where:} \quad b = 1 + \frac{1}{3[(\frac{1}{VR})^2 - 1]}$$

The peak velocity decay is a function of the mixing length characteristic, lobe geometry, and velocity ratio as defined below:

$$(V - V_B)/(V_C - V_B) = [1 + (0.15 \, Z_V)^a]^{-1/a} \qquad (8)$$

$$\text{where:} \qquad a = 4 \, (2 - 1/TR)[1 + 8/3 \, (1/D_{HE} - 1)]$$

$$Z_V = Z_C * f_4 \, (VR)$$

$$f_4 \, (VR) = (1 - VR)^{1.25}/(1 + VR)$$

$$s = s_2 \qquad w = w_2$$

3.3.3 Frost Mixing Correlation

The analysis used a semi-empirical thermal mixing correlation derived by Frost (ref. 8) which is shown in Figure 3-19. The mixing effectiveness is correlated as a function of mixer and mixing duct geometry by the interface function, $f = \sqrt{C_D} \, (CP/D)(X/D)$. From the definition of equivalent hydraulic diameter the function can be redefined in the following manner:

34

$$f = \frac{\sqrt{C_D} \, (CP)(X)}{D^2}$$

WHERE:
C_D = FLOW COEFFICIENT
CP = CONTACT PERIMETER
X = MIXING DUCT LENGTH
D = MIXING DUCT DIAMETER

INTERFACE FUNCTION f

MIXING EFFICIENCY η_{MIX}
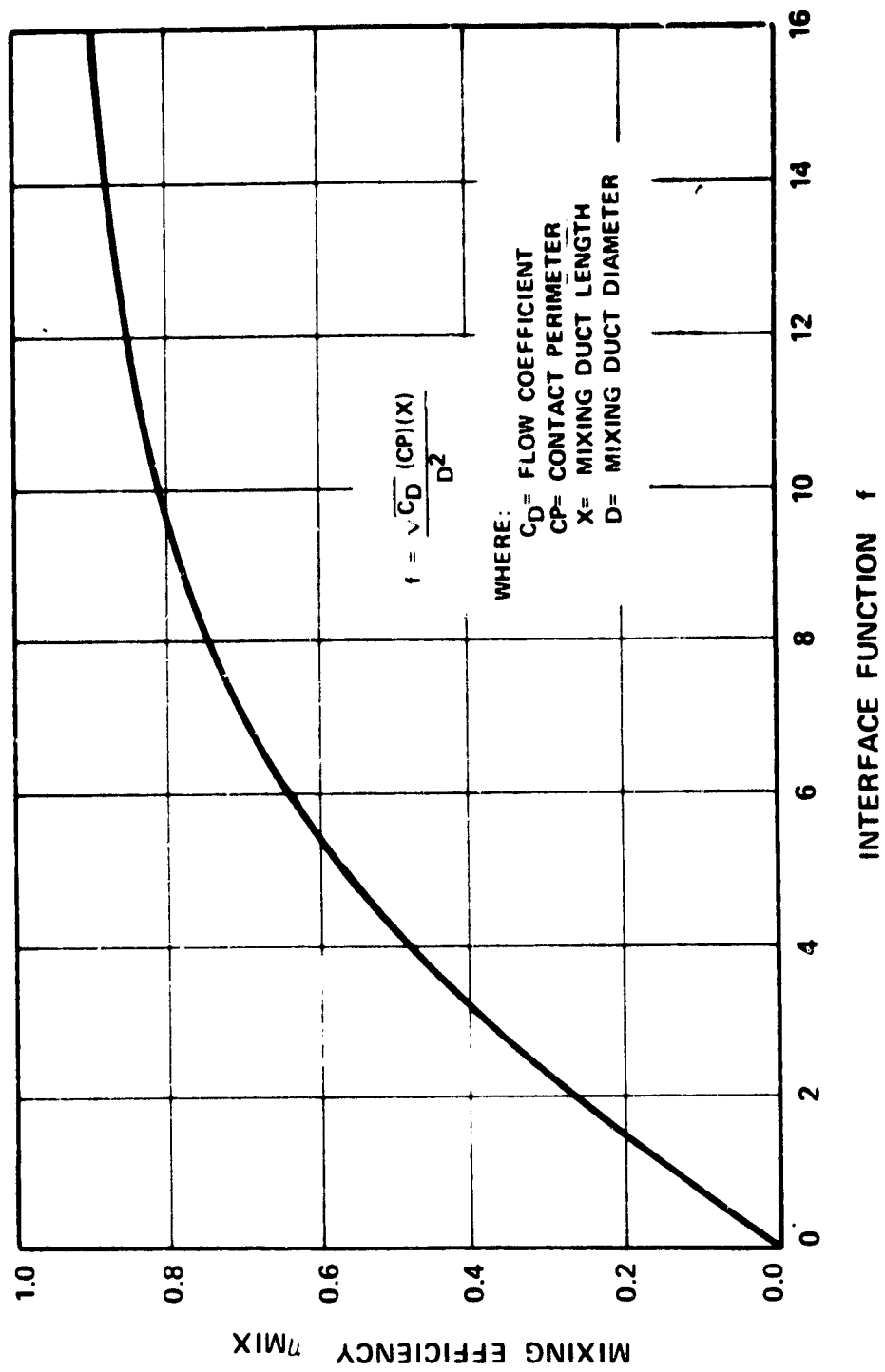
Figure 3-19. Frost Mixing Correlation.

35

$$f = \sqrt{C_D}\,(CP/D)\,(X/D) \qquad\qquad (9)$$

$$= \frac{\sqrt{C_D}}{D}\,CP\left(\frac{\pi D_E}{\pi D_E}\right)\,\left(\frac{X}{D}\right) = \frac{\sqrt{C_D}\,\pi D_E}{D}\left(\frac{CP}{\pi D}\right)\left(\frac{X}{D}\right)$$

$$\text{since } D_{HE} \qquad = \frac{\sqrt{4\pi A}}{CP} = \frac{\pi D_E}{CP}$$

$$f = \frac{\sqrt{C_D}\,\pi D_E}{D}\left(\frac{1}{D_{HE}}\right)\left(\frac{X}{D}\right)$$

Since D_E/D varies with bypass ratio, the equivalent hydraulic diameter (D_{HE}), or the duct length (X), may be altered to maintain the same degree of mixing efficiency. It follows that an increase in the mixing efficiency must be accompanied by a decrease in the equivalent hydraulic diameter or the mixing duct length must increase.

3.3.4 Parametric Design Studies

The various losses, mixing efficiency, mixing duct length calculations, and peak-velocity-decay predictions were used in a parametric study to optimize the QCGAT mixer design. The following parameters were varied:

N ∿	Number of Lobes	8, 9, 10, 12, 16
TR ∿	Lobe Taper Ratio	1, 2, 3, 4
AR ∿	Lobe Aspect Ratio	1, 2, 3, 4, 6

The exhaust system areas used in the study were determined from the compound-flow analysis and were held constant. Penetration ratio was computed as a function of the above parameters and the mixing plane areas. It was assumed that each configuration would maintain the cycle match point; thus, the thrust coefficient changes are directly related to the losses as shown in Table 3-5.

The initial parametric plots are shown in Figures 3-20, 3-21, and 3-22 for aspect ratios of 2, 3, and 4 respectively. Each plot presents the thrust coefficient change as a function of lobe penetration for varying taper ratio and a given lobe number. All parameters are plotted versus a delta gross-thrust coefficient. The results clearly indicate that a taper ratio of 1.0 (parallel core lobe walls) is, in all cases, the optimum choice for the ranges of parameters studied. More detailed results for a taper ratio of 1.0 are presented in Figures 3-23, 3-24, and 3-25 for lobe

36

TABLE 3-5. QCGAT CRUISE DESIGN POINT THRUST SENSITIVITIES.

Core pressure loss sensitivity	$\Delta C_{F_{core}} = 0.50 \ (\Delta P/P_{T_{core}} + \Delta P/P_{T_{plug}})$
Bypass pressure loss sensitivity	$\Delta C_{F_{bypass}} = 0.49 \ (\Delta P/P_{T_{bypass}} + \Delta P/P_{T_{mix}})$
Mixing efficiency sensitivity	$\Delta C_{F_{total}} = 0.0235 \ \eta_{mix}$
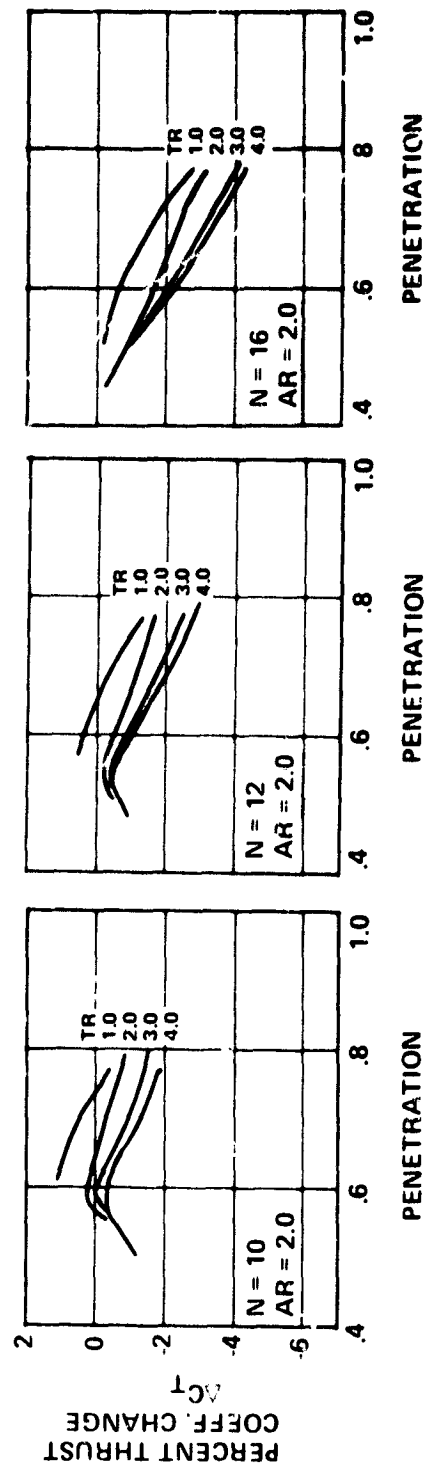
Figure 3-20. Parametric Plots of Various Taper Ratios for an Aspect Ratio of 2.0.

NOTE: MAXIMUM PENETRATION SET BY MINIMUM LOBE TIP-TO-SHROUD SPACING OF S/2.

38
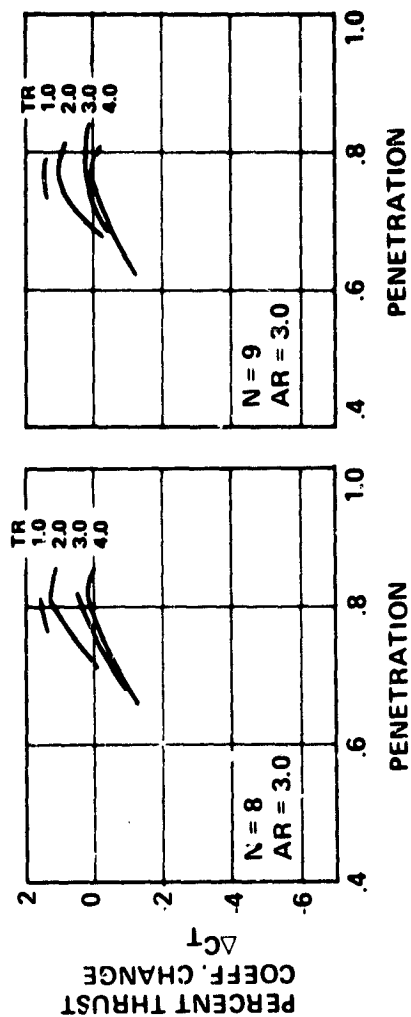
ASPECT RATIO = 3.0

NOTE: MAXIMUM PENETRATION SET BY MINIMUM LOBE
TIP-TO-SHROUD SPACING OF S/2.
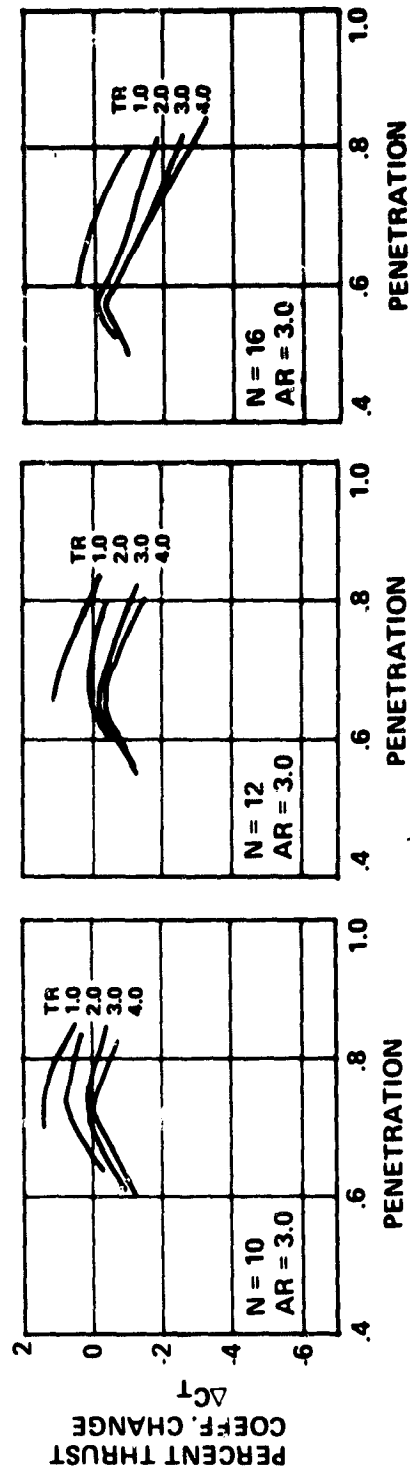
Figure 3-21. Parametric Plots of Various Taper Ratios
or an Aspect Ratio of 3.0.
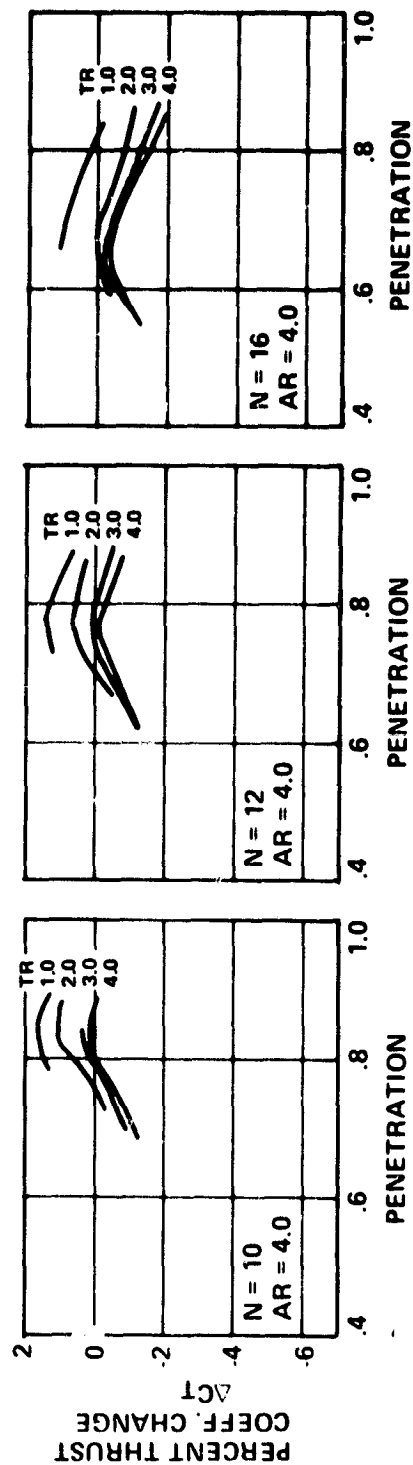
Figure 3-22. Parametric Plots of Various Taper Ratios for an Aspect Ratio of 4.0.
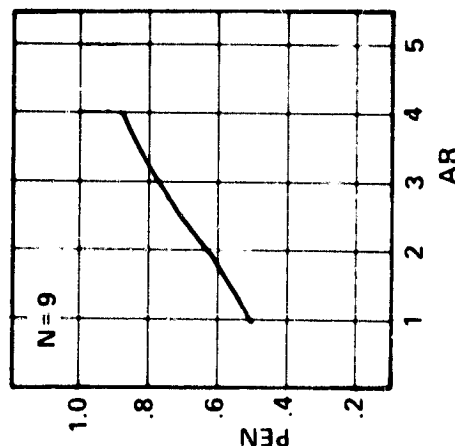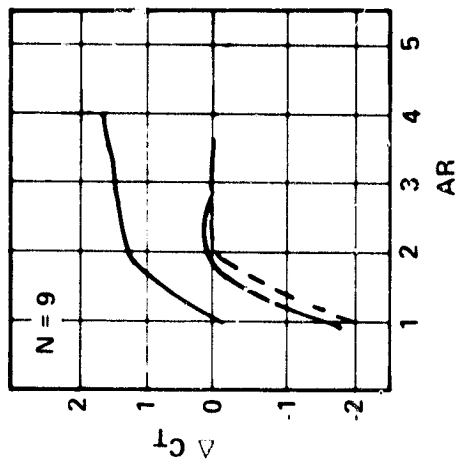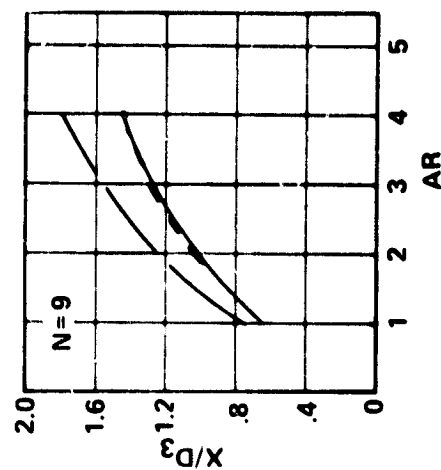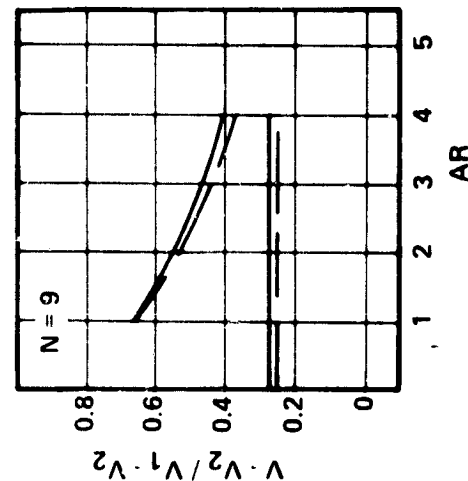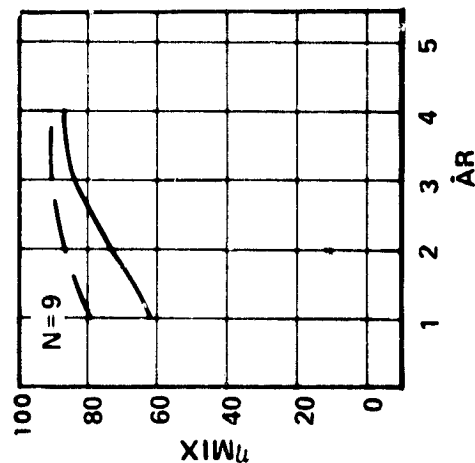
Figure 3-23. Detailed Results for a Taper Ratio of 1.0 and 9 Lobes.

41
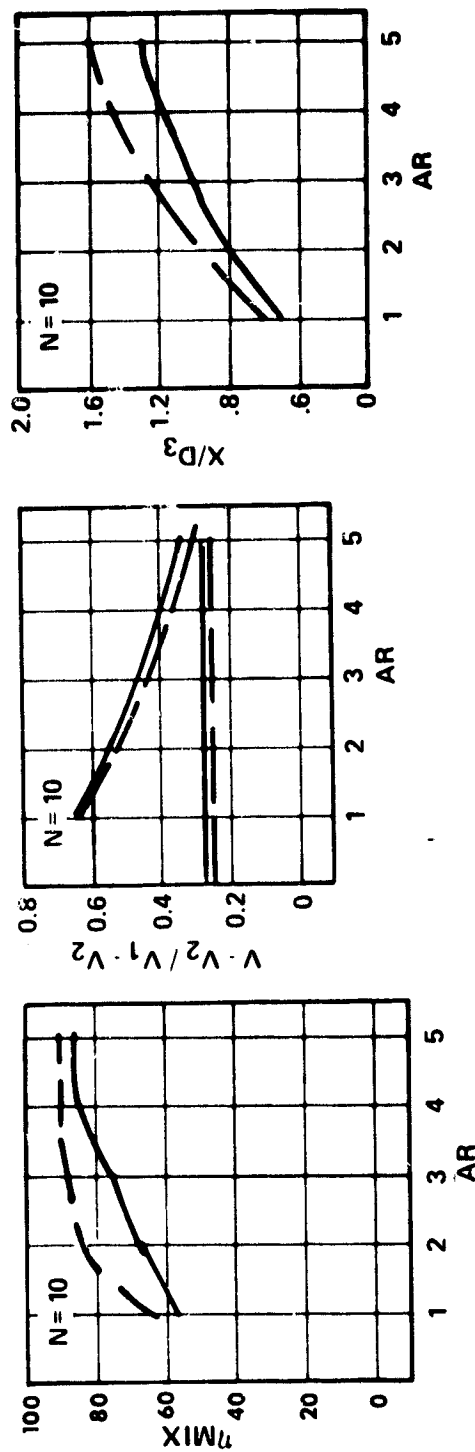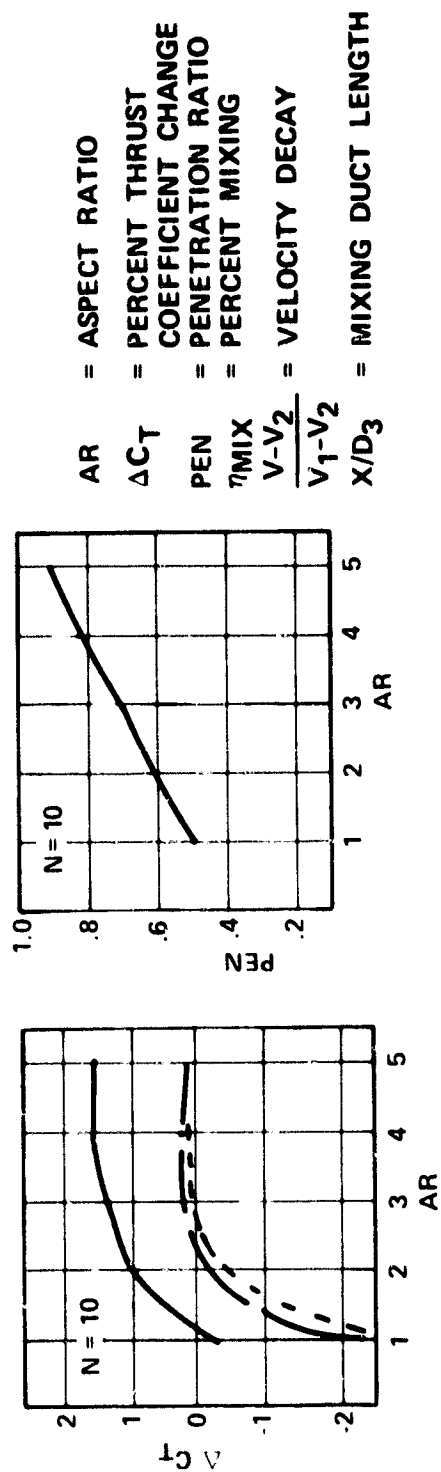
Figure 3-24. Detailed Results for a Taper Ratio of 1.0 and 10 Lobes.

42
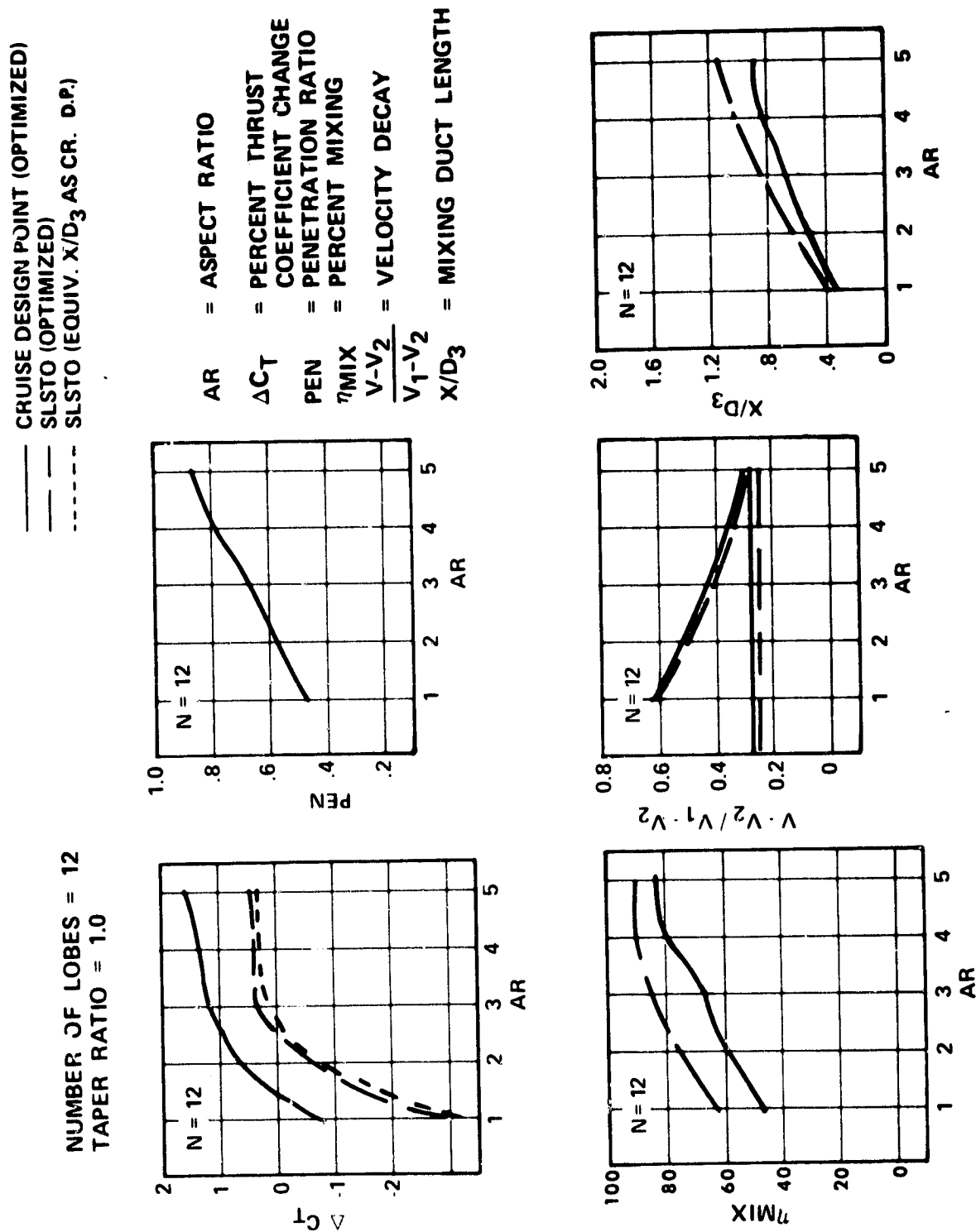
Figure 3-25. Detailed Results for a Taper Ratio of 1.0 and 12 Lobes.

43

numbers of 9, 10, and 12, respectively. The peak thrust coefficient for the taper ratio of 1.0 (Figures 3-20, 3-21, and 3-22) is plotted versus aspect ratio. The other results presented are: penetration ratio, mixing efficiency, velocity decay, and mixing length. In Figure 3-26 the results from Figures 3-23, 3-24, and 3-25, which were considered to be within practical application limits, are cross-plotted versus lobe number for lines of constant aspect ratio. One of the design requirements was to achieve 75-percent thermal mixing, shown by a dashed line on the mixing efficiency plot. The points of intersection with the lines of constant aspect ratio then determined the design length requirement and the resultant thrust and velocity parameters as shown by the dashed lines on the other plots.

3.3.5 Preliminary Mixer Configuration Selection

Referring back to Figure 3-26 the dashed lines represent a thermal mixing efficiency of 0.75. The selected design took into consideration performance, weight, length, and acoustics. Delta thrust coefficient for a 0.75 η_{mix} was fairly constant within the aspect ratio range of 2 to 4, which meant the length and velocity decay would determine the selected design. As shown by the mixing length plot (Figure 3-26), mixing length decreases with increasing aspect ratio for a given η_{mix}. Peak velocity at the mixing duct exit also decreases with increasing aspect ratio for constant η_{mix}. For minimum noise the peak velocity ratio should be minimized. For minimum weight the mixing duct length should be minimized. Thus, an aspect ratio of 3.5 and lobe number of 12 was chosen for the preliminary design. The higher aspect ratio of 4 was not chosen because it was felt the lobes would be difficult to fill and thus, higher than predicted losses would result.

A summary of the selected preliminary design parameters are compared to the proposal values in Table 3-6.

3.3.6 Gas Path Preliminary Design

A radial-equilibrium flow analysis was used to establish the preliminary gas path design for the mixer compound exhaust system. This analysis was also used to establish the final gas path controls for the bypass duct, reference nozzles, and baseline compound nozzles. The computerized analysis solves the equilibrium equations in an axisymmetrical flow field. The boundary-layer blockage is estimated simultaneously with the free-stream flow-field calculation based on an empirical Mach-number-dependent correlation. Further flow solution details are presented in the following sections.

44
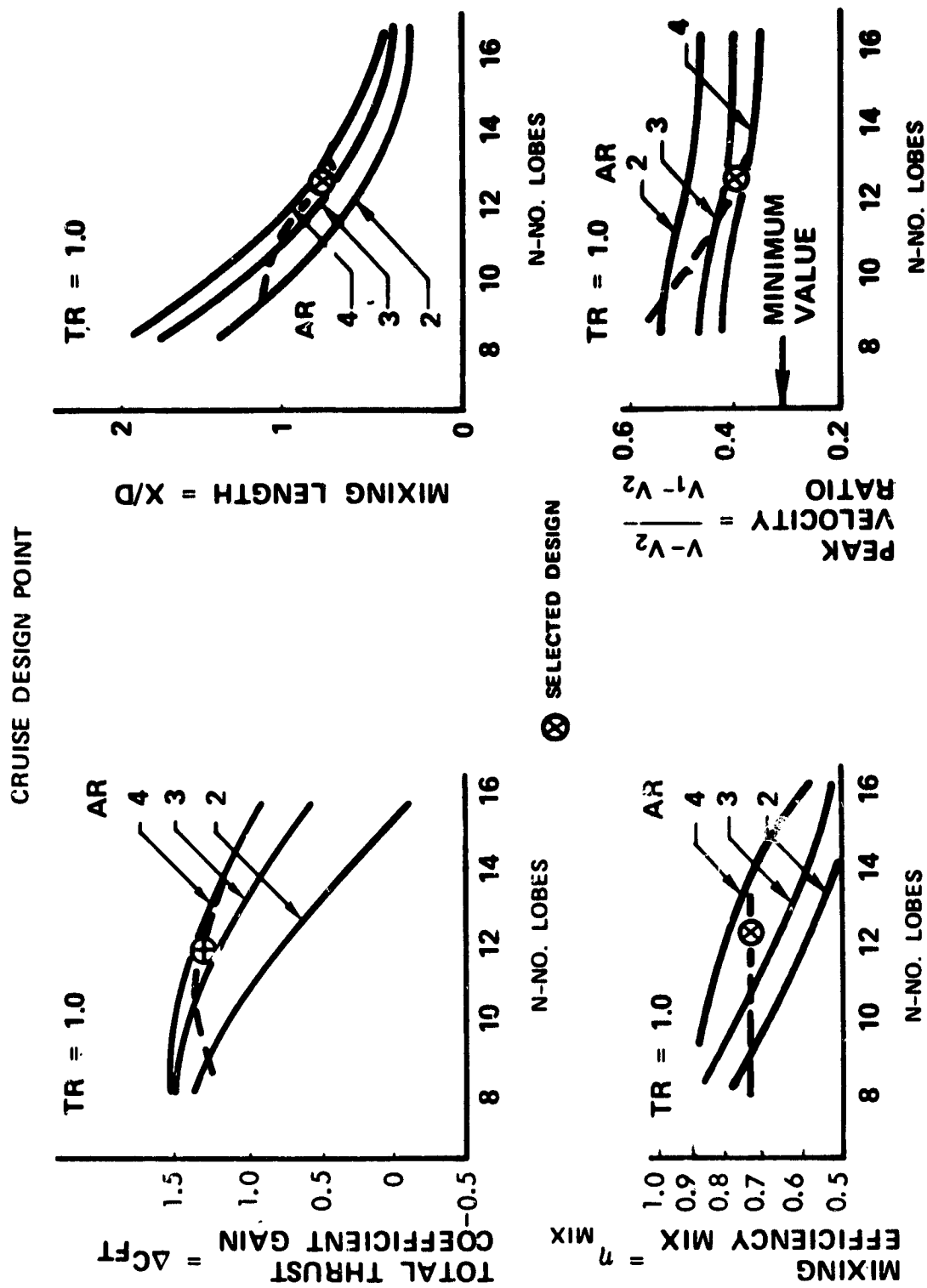
Figure 3-26. Effect of Lobe Number at Cruise Design Point.

45

TABLE 3-6.   DESIGN PARAMETER SELECTION.

Design Parameter		Proposal Design	Preliminary Design
Number of lobes	N	9	12
Taper ratio	TR	2.0	1.0
Aspect ratio	AR	2.8	3.5
Penetration ratio	PEN	0.84	0.77
Spacing ratio	SR	1.00	1.05
Mixing duct length ratio	X/D	0.70	0.75

3.3.6.1 Bypass Duct Radial Equilibrium Flow Analysis

A preliminary loss-optimization analysis of the bypass duct indicated that the diffusion loss was predominant and that minimum diffusion would yield minimum overall loss. The duct diffuser was designed to diffuse the flow to an average Mach number of 0.362 at the end of the oil cooler. A constant-area passage was maintained from oil-cooler exit to nozzle inlet. The diffuser area ratio (AR) of 1.32 and the length ratio of 3.82 are quite conservative, as shown in Figure 3-27. The estimated duct loss including struts is 1.5 percent with an additional 0.5-percent total-pressure loss for the air/oil cooler (ref. 12). The final design flow path and calculated Mach numbers are presented in Figure 3-28.

3.3.6.2 Reference Nozzle

The QCGAT reference performance nozzle was designed along the same guidelines as the 731 reference nozzles. The exit areas of 794.1 cm^2 (123.08 in^2) for the core and 1775.9 cm^2 (275.28 in^2) for the bypass are required to maintain the QCGAT cycle match. The core-nozzle-throat angle was set at 0.09 radian (5°) and was faired into the core customer connect flange at the engine station 237.37 as shown in Figure 3-29. A 0.16-radian (9°) bypass nozzle hub angle was chosen to blend tangent to the bypass duct contour at engine station 241.0. The bypass exit plane axial location was determined by a spacing ratio requirement of 0.25 based on Garrett reference nozzle experience where spacing ratio is defined by:

$$SR = L/2R \qquad\qquad (10)$$

where   L = Axial distance between core exit and bypass exit
          R = Core exit radius

The bypass exit radius was set based on the required bypass nozzle area being perpendicular to the core nozzle. The radial-equilibrium flow analysis resulted in Mach number and boundary layer thickness distributions very similar to the existing TFE731-3 reference nozzles. Since the geometries are very similar and the flow analysis does not indicate any significant flow differences, the QCGAT reference nozzles will produce the performance presented in Figure 3-30.

3.3.6.3 Baseline Compound Nozzle Design

The compound nozzle was designed such that the same centerbody and mixing duct could be used for the baseline compound nozzle and the mixer compound nozzle. The first step in setting the gas path was to lay out a preliminary turbine diffuser and centerbody. The diffusion rate was established to provide maximum diffusion without

47
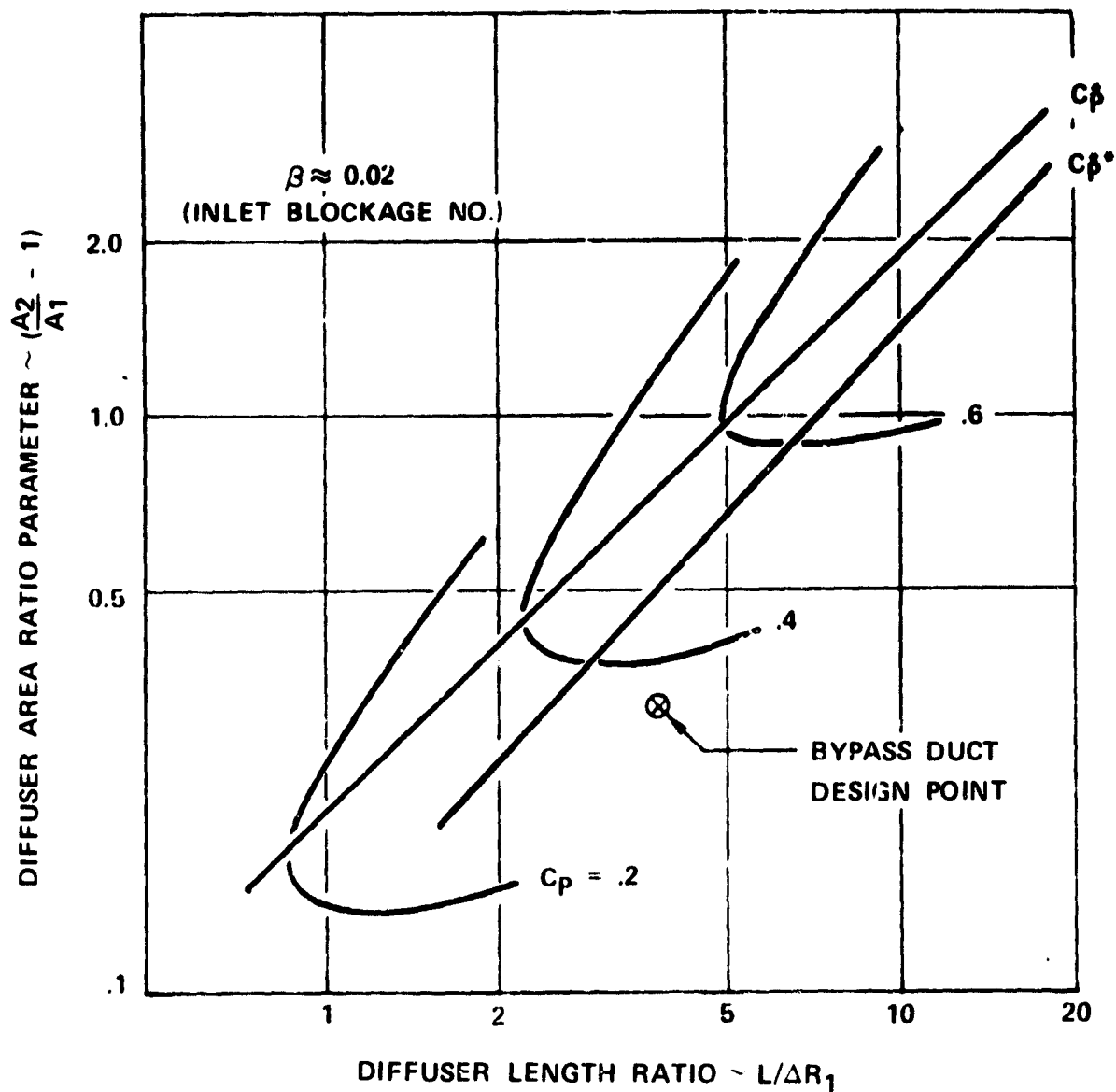
C$_\beta$ = LOCUS OF MAXIMUM PRESSURE RECOVERY COEFFICIENT AT
PRESCRIBED NON-DIMENSIONAL LENGTH.

C$_p$** = LOCUS OF MAXIMUM PRESSURE RECOVERY COEFFICIENT
AT PRESCRIBED AREA RATIO.

Figure 3-27. QCGAT Bypass Duct Diffuser.
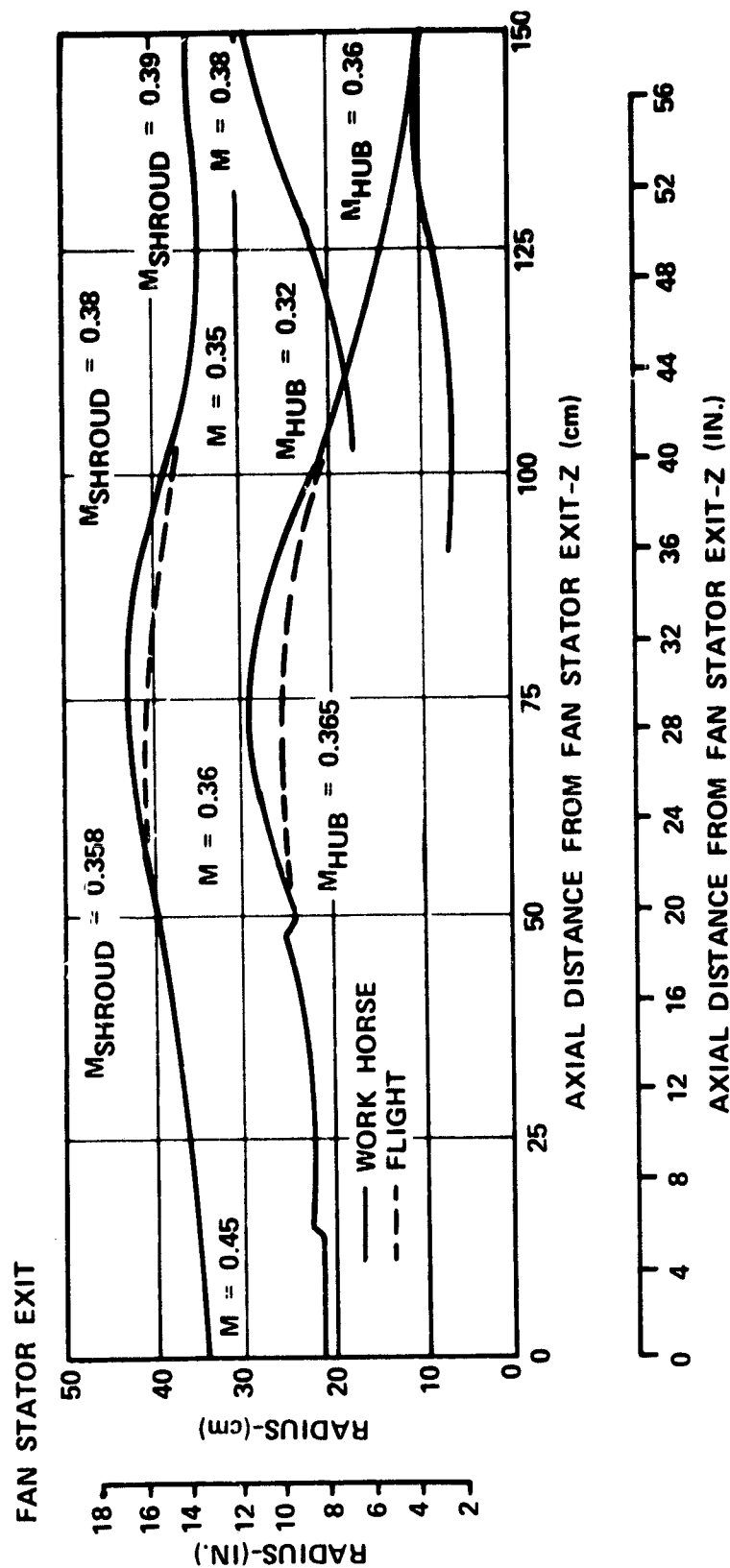
Figure 3-28.   QCGAT Flight Versus Workhouse Bypass
Duct Contours and Mach Numbers.

49
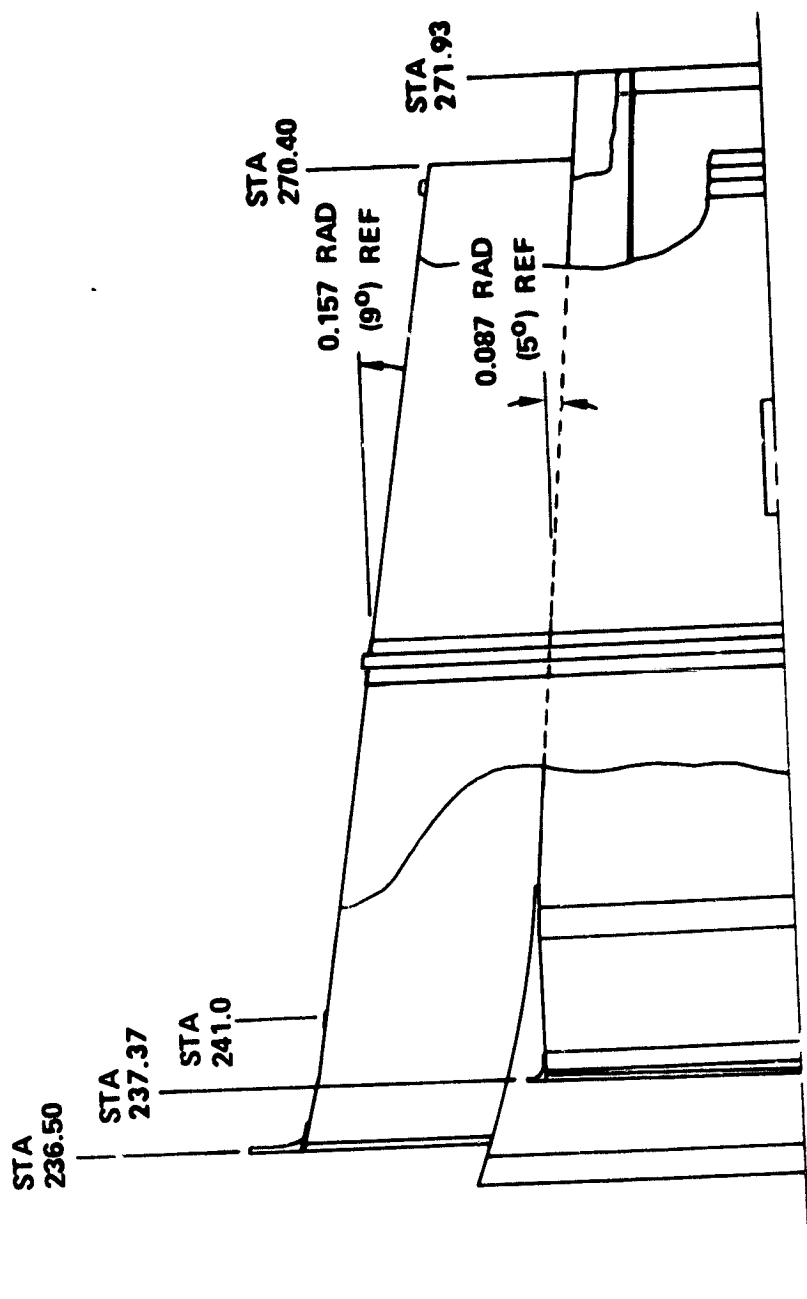
Figure 3-29. Reference Nozzle.

STA 236.50

STA 237.37

STA 241.0

STA 270.40

STA 271.93

0.157 RAD (9°) REF

0.087 RAD (5°) REF
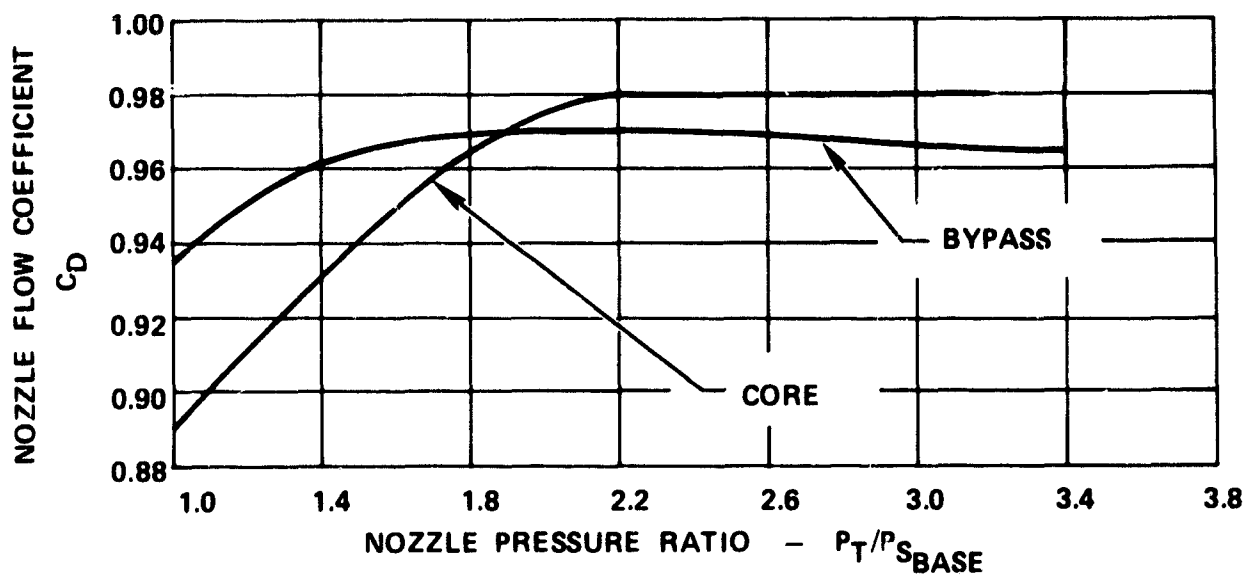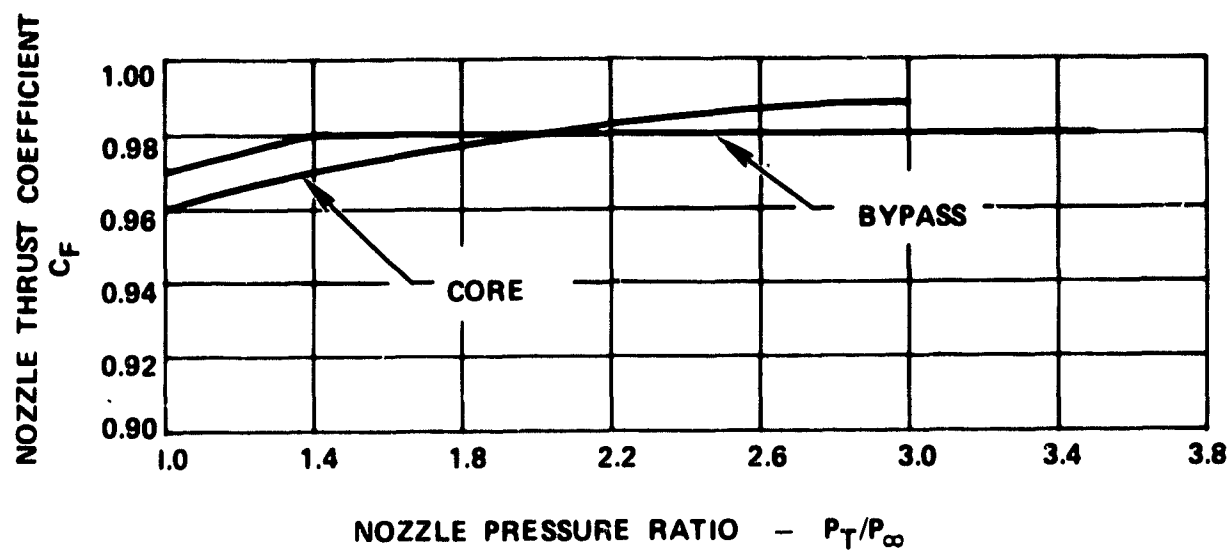
Figure 3-30. QCGAT Reference Nozzle Predicted
Performance Characteristics.

flow separation following the guidelines established in Ref. 13. The radial equilibrium flow analysis was then used to analyze the contours. Based on the solution results appropriate contour changes were made until a satisfactory core and bypass splitter design was obtained. A drawing of the compound nozzle splitter is presented in Figure 3-31. The core area distribution, calculated wall Mach numbers, and estimated boundary layer displacement thicknesses are presented in Figures 3-32 through 3-34. The bypass area distribution, calculated wall Mach numbers, and estimated boundary layer displacement thicknesses are presented in Figures 3-35 through 3-37.

3.3.6.4 Mixer Compound Preliminary Design

Because the lobe side-wall boundary-layer blockages are neglected in the first solution, the mixer-compound contours were analyzed through two types of iterations of the radial-equilibrium flow analysis. The mixer initial one-dimensional flow contours were input along with the hub and shroud contour definitions from the customer connecting flange upstream to the turbine rotor exit and fan stator exit. The mixer lobe was input as radially distributed annulus blockage. The mixer apogee and perigee contours were varied until satisfactory area, Mach number, and displacement thickness distributions were obtained. The boundary-layer blockage on the mixer-lobe sidewalls was estimated and added to the radial blockage distribution, and the contour was again modified until acceptable distributions were obtained. The preliminary design mixer apogee and perigee contours are presented in Figure 3-38. The calculated mixer core area, Mach number, and displacement distributions are presented in Figures 3-39 through 3-41, and the corresponding bypass data are presented in Figures 3-42 through 3-44.

3.4 Detailed Mixer Design and Flow Analysis

A three-dimensional viscous-flow analysis method solution was used to define the empirically optimized design and provide guidance for developing alternate designs. A solution to the three-dimensional compressible Navier-Stokes equations developed for cascade flows (ref. 14, 15, and 16) was used to analyze the core and bypass flow through the mixer lobes. A separate three-dimensional mixing program developed for combustors (ref. 17, 18, and 19) was used to analyze the flow in the mixing duct. The lobe analysis results were input as inlet conditions to the mixing duct. The main lobe design criteria were:

o   Minimize the loss through the mixer lobes

o   Minimize pressure and velocity gradients across the lobe exit at the mixing plane

o   Minimize the length of the mixer configuration

52
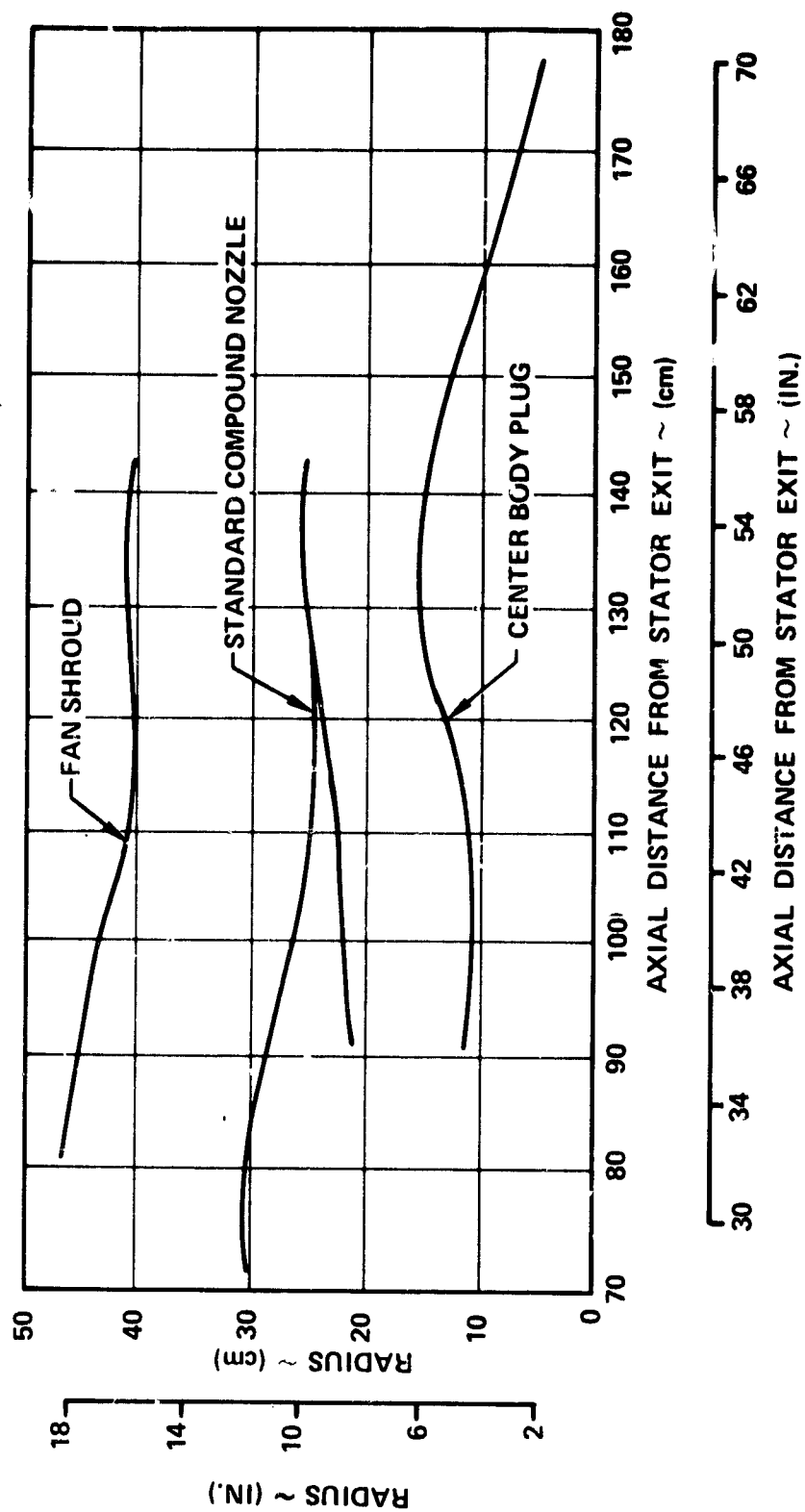
Figure 3-31. QCGAT Compound Nozzle.
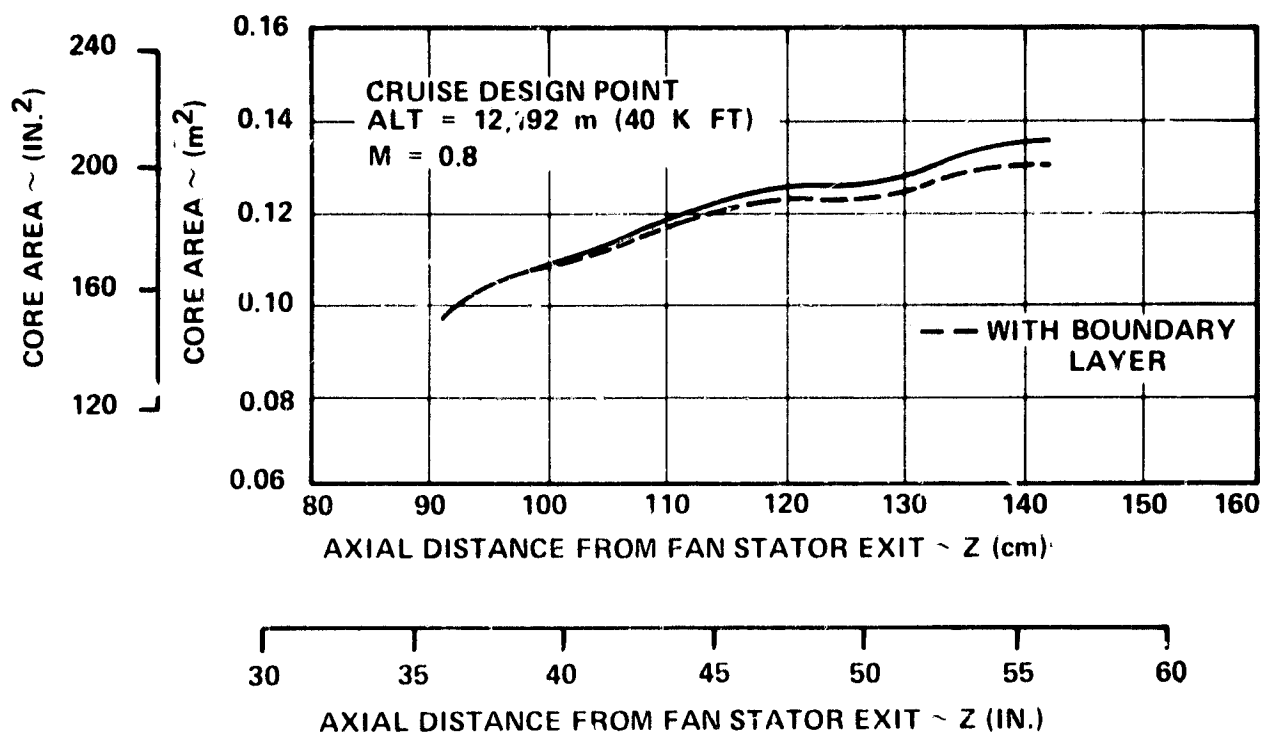
Figure 3-32. QCG⁷T Compound Splitter Core Duct
Area Distribution.

CRUISE DESIGN POINT
ALT = 12,192 m (40 K FT)
M = 0.8
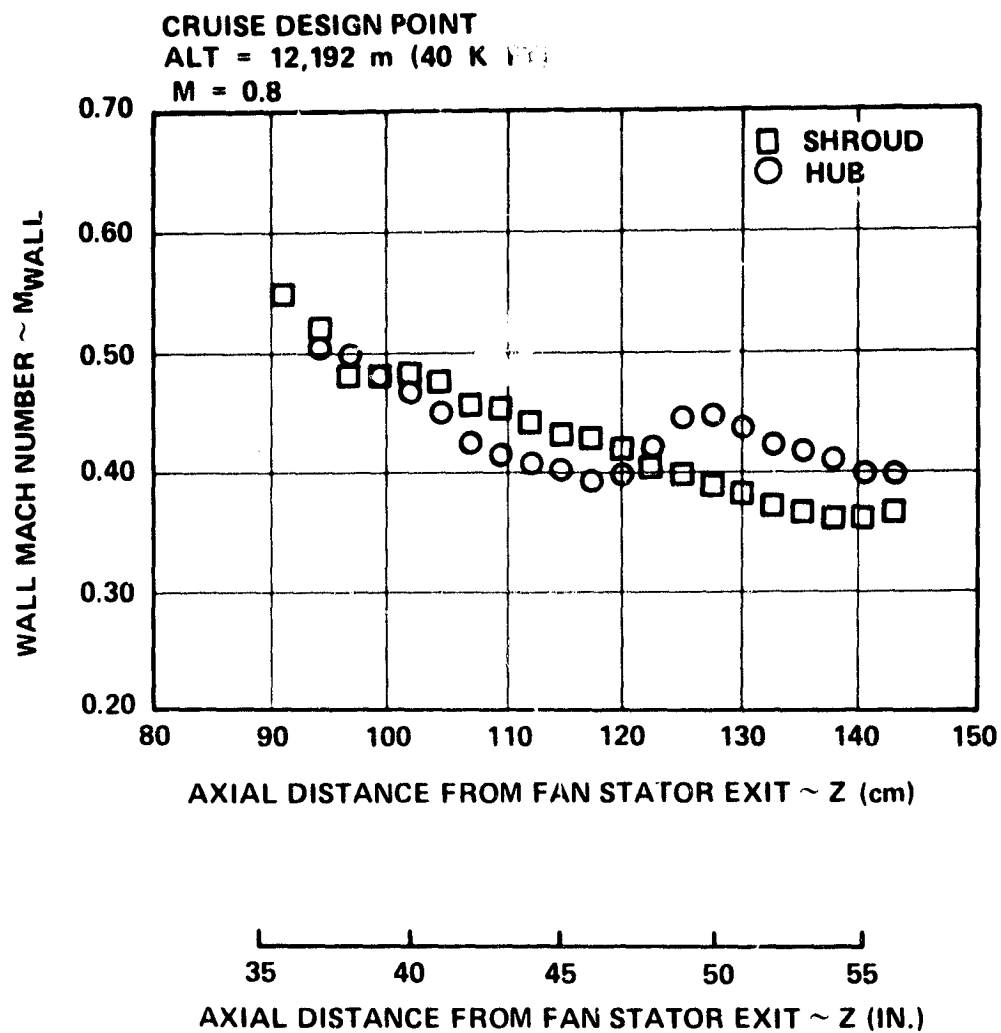
Figure 3-33. QCGAT Compound Splitter Core Duct Mach Number.

55
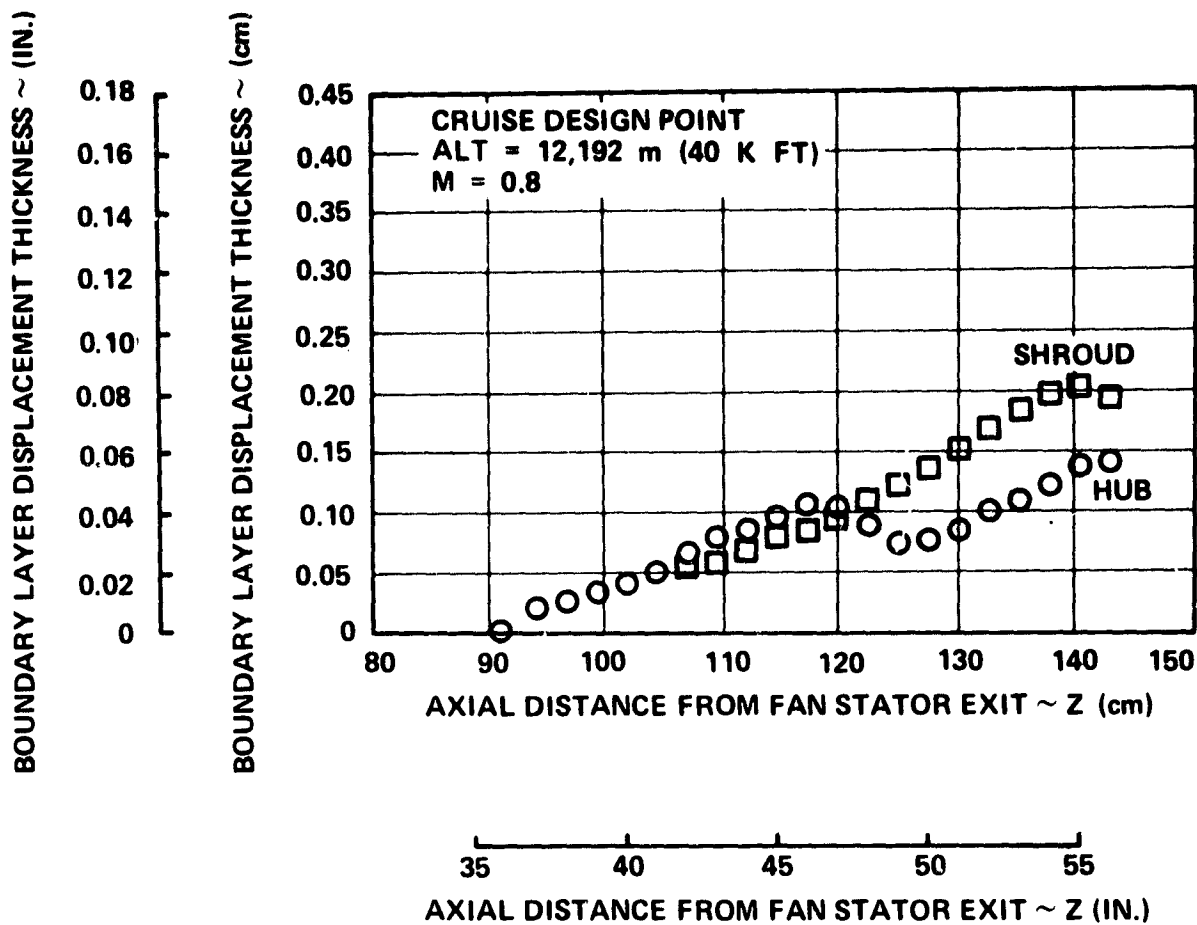
Figure 3-34. QCGAT Compound Splitter Core Duct Boundary Layer Thickness.

CRUISE DESIGN POINT
ALT = 12,192 m (40 K FT)
M = 0.8
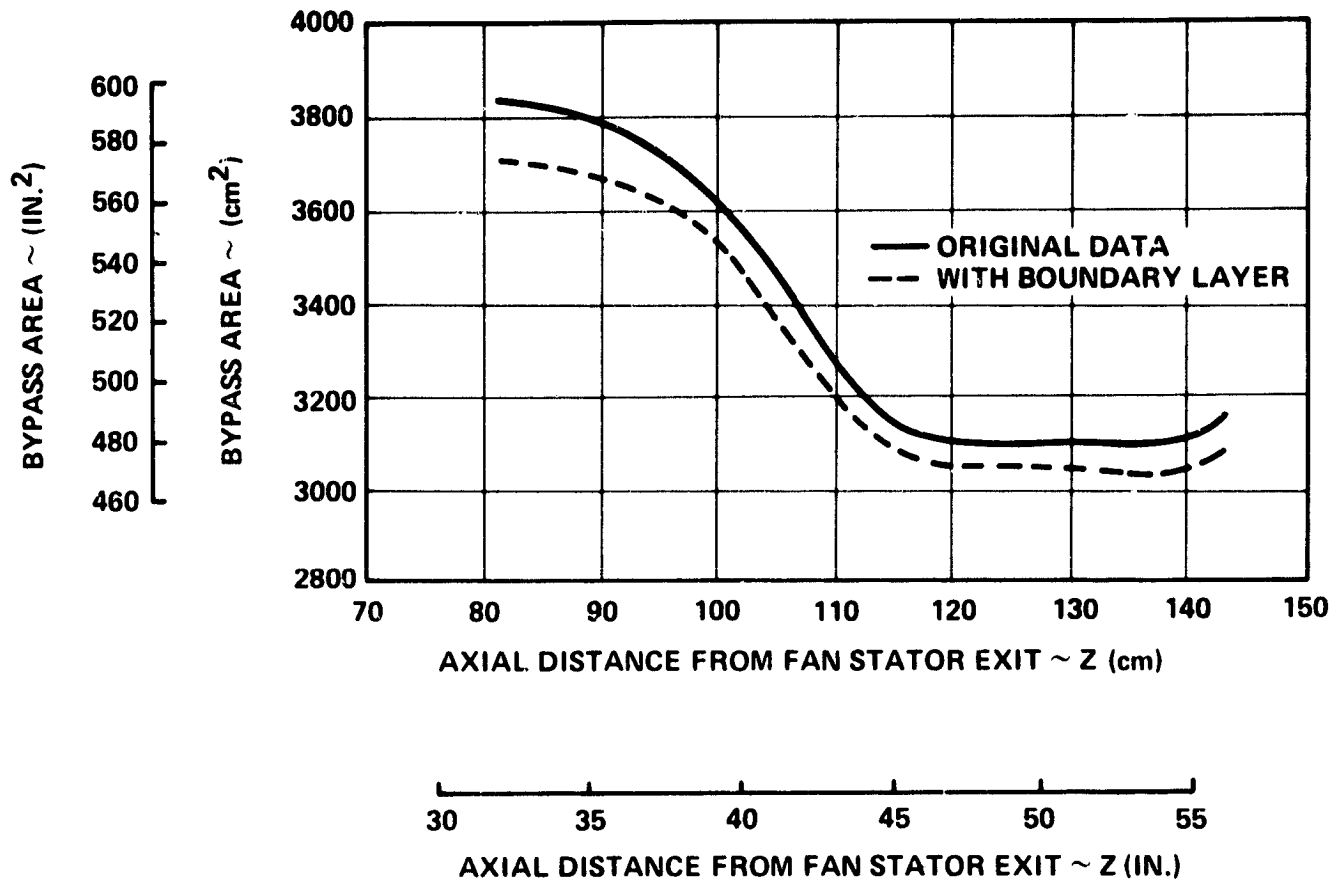
Figure 3-35.   QCGAT Compound Splitter Bypass Duct Area Distribution.

57
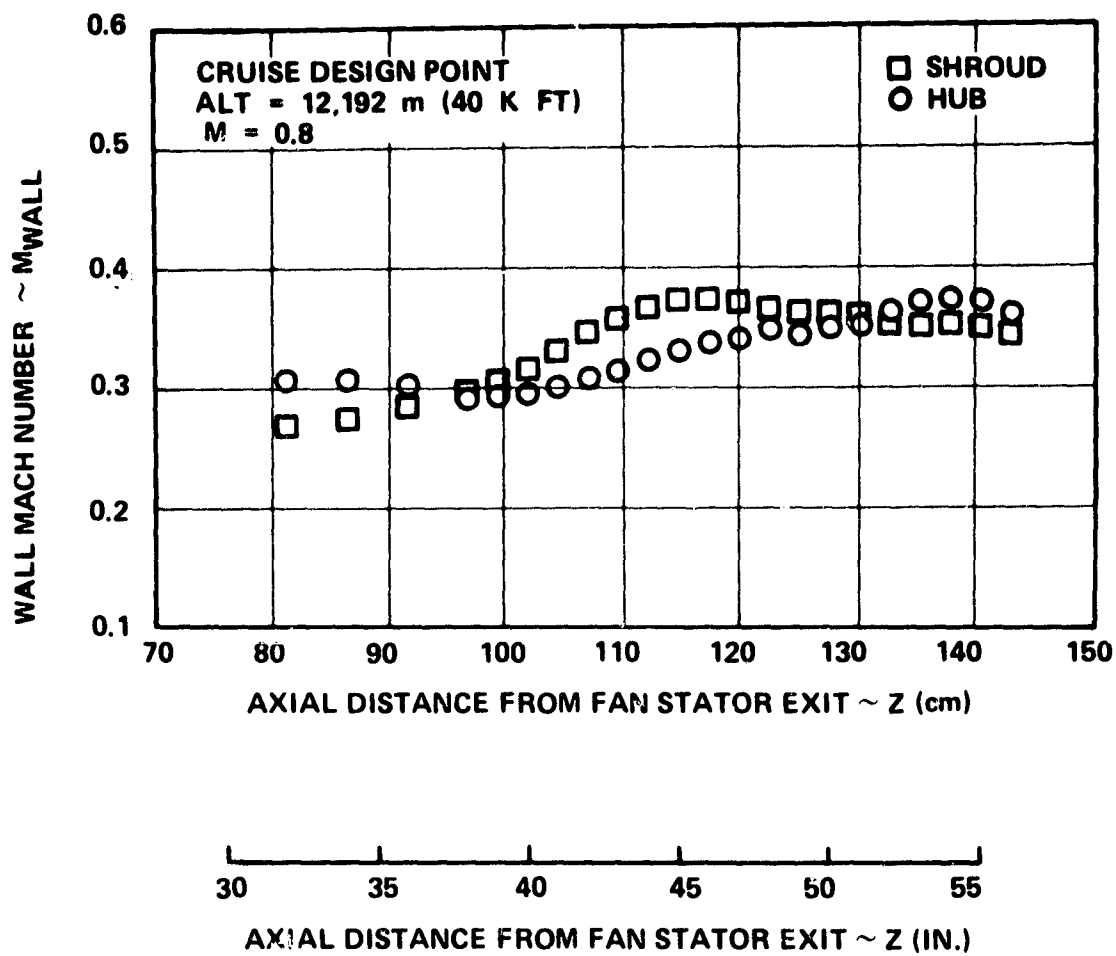
Figure 3-36. QCGAT Compound Splitter Bypass Duct Mach Number.

58
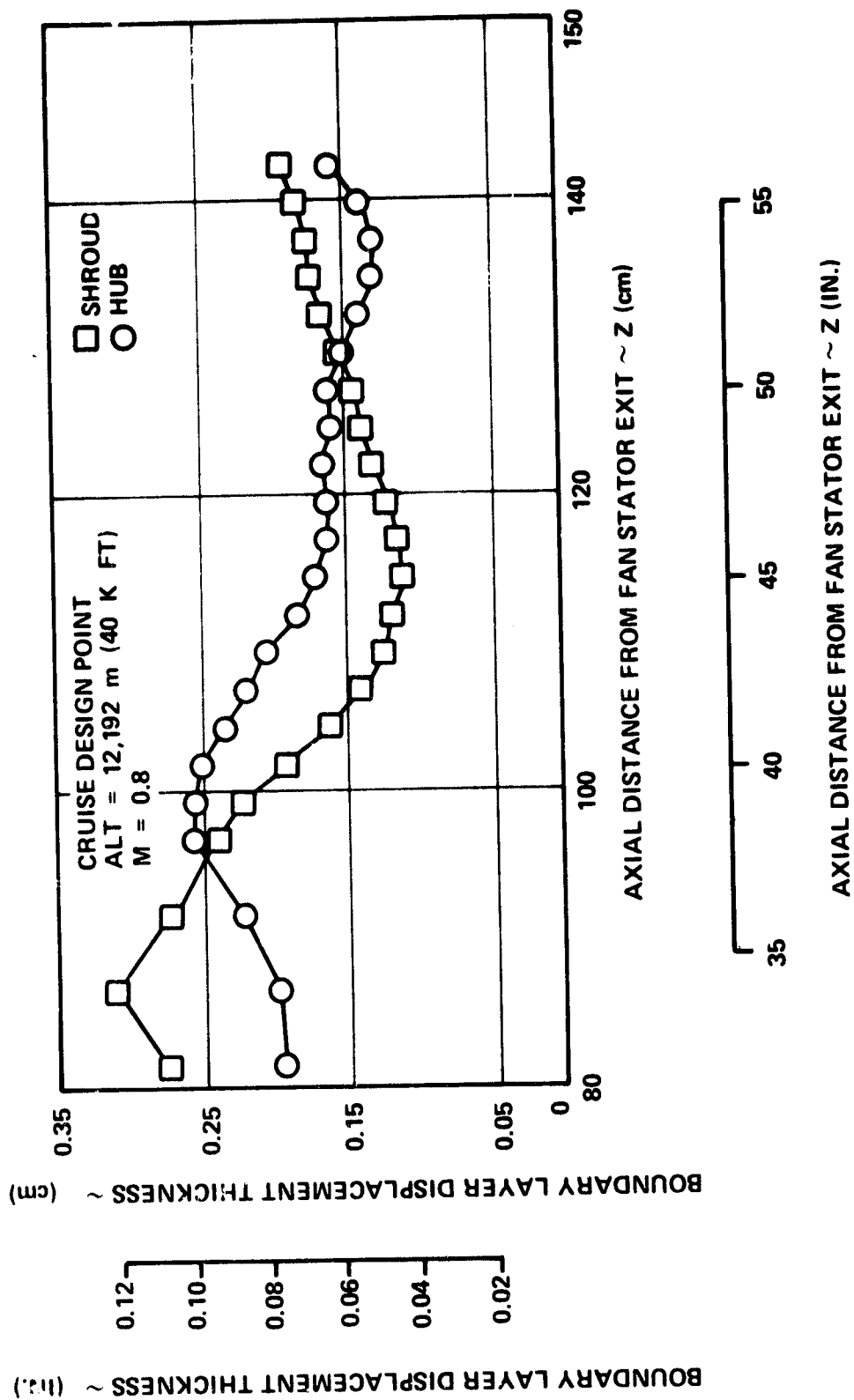
Figure 3-37. QCGAT Compound Splitter Bypass Duct Boundary Layer Thickness.

59
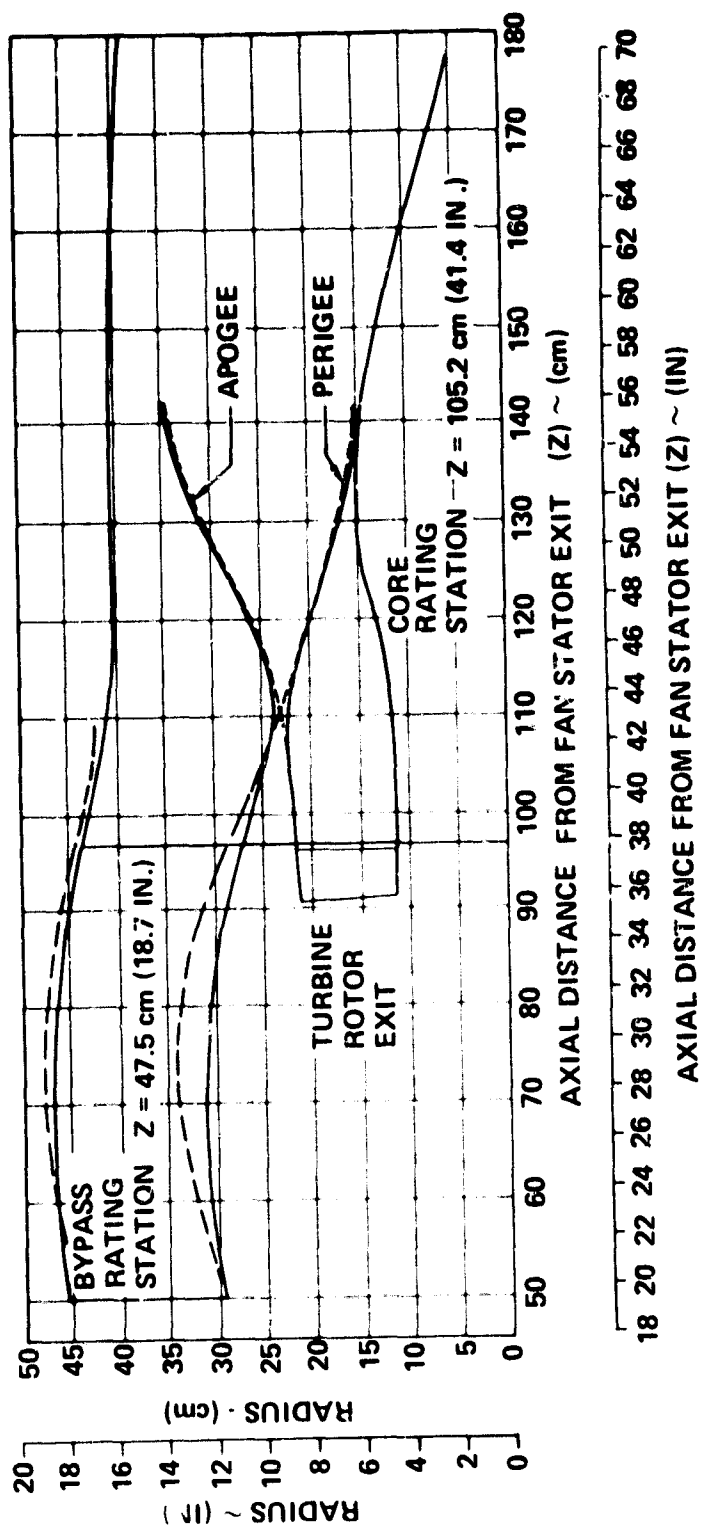
Figure 3-38. Preliminary Design Mixer Apogee and Perigee Contours.
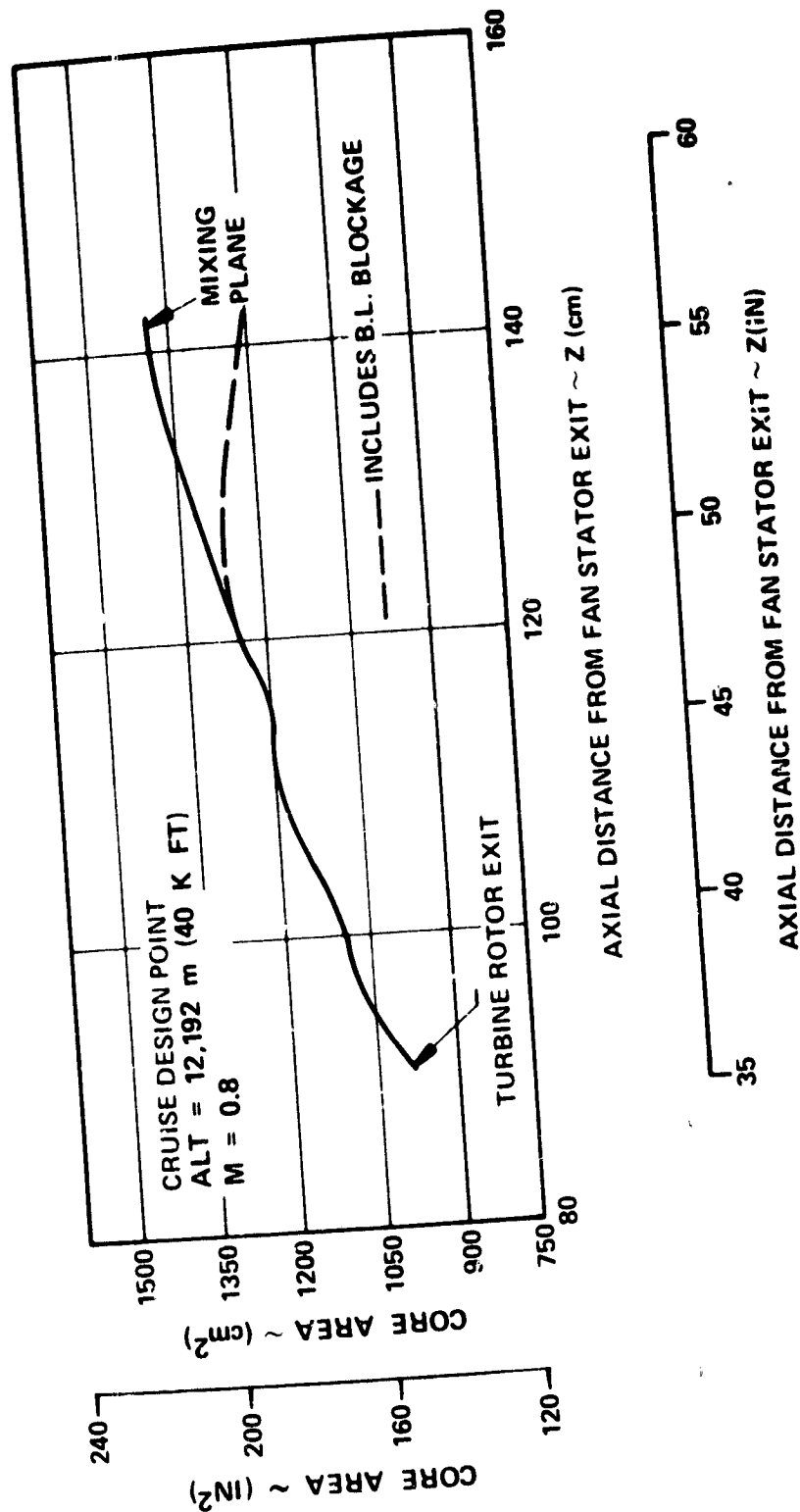
Figure 3-39. QCGAT Mixer Compound Nozzle--Core Duct Area Distribution.
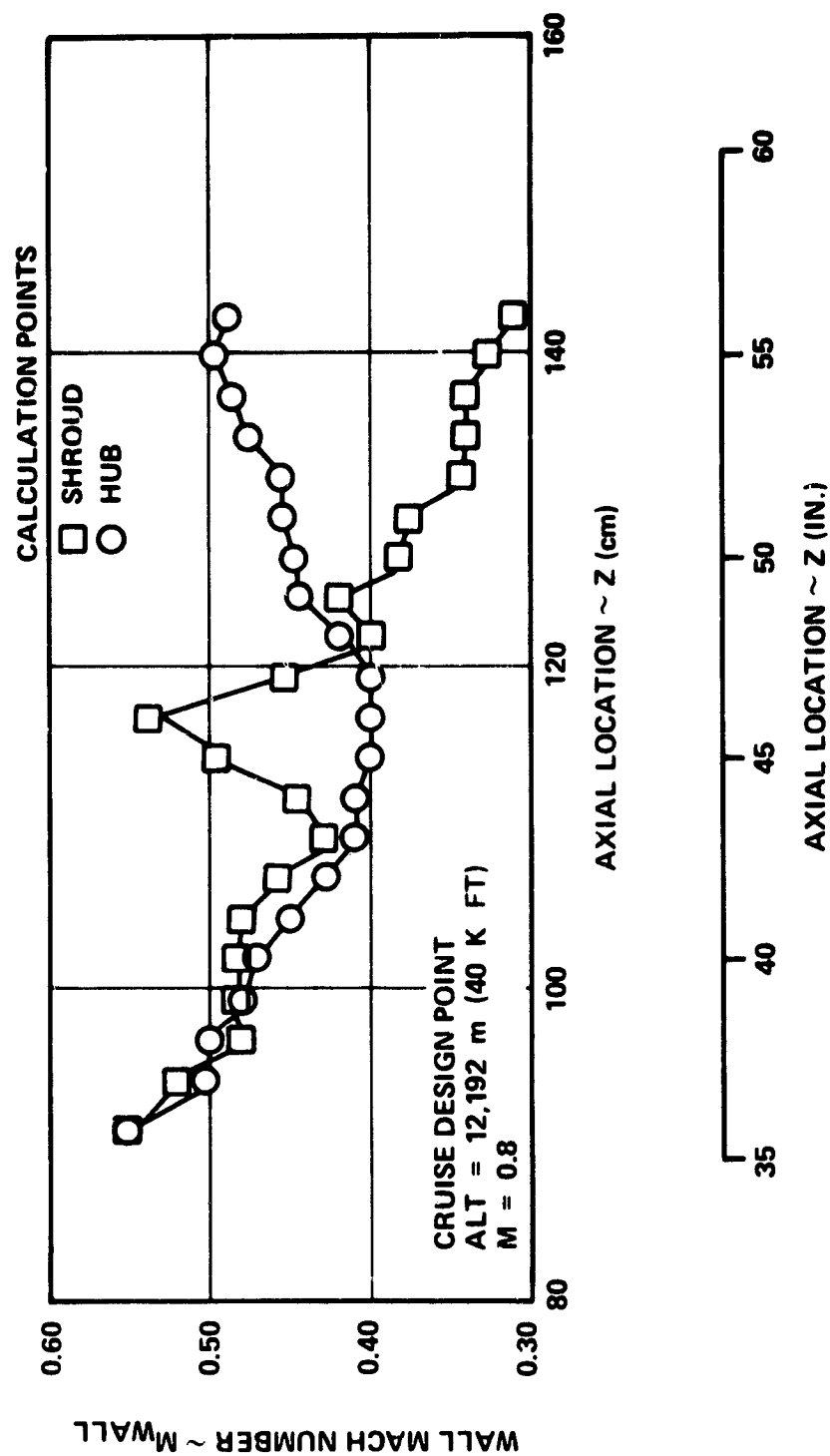
Figure 3-40. QCGAT Mixer Compound Nozzle Core Duct Mach Numbers.

62
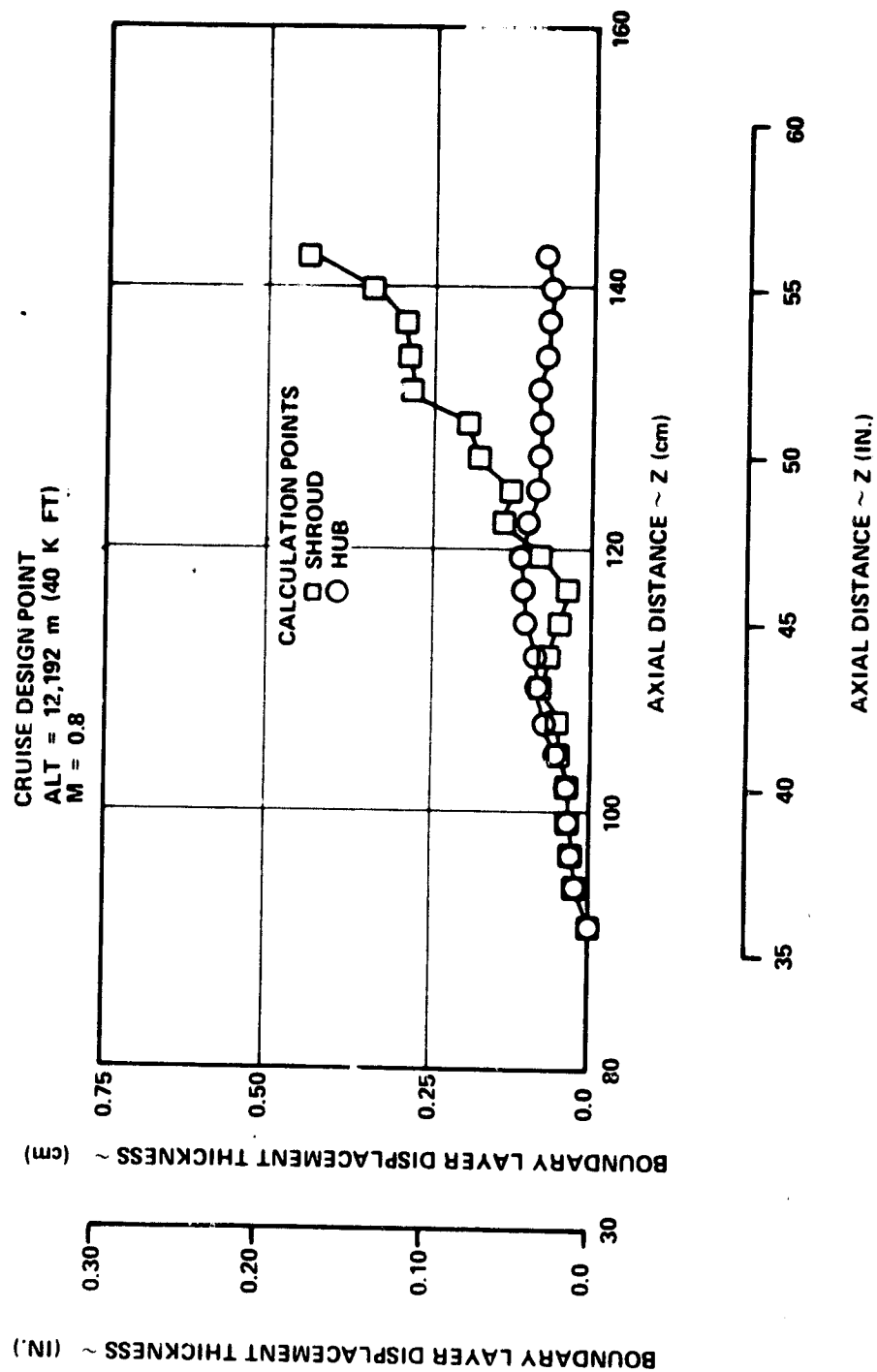
Figure 3-41. QCGAT Mixer Compound Nozzle Core Duct Boundary Layer Thickness.

63
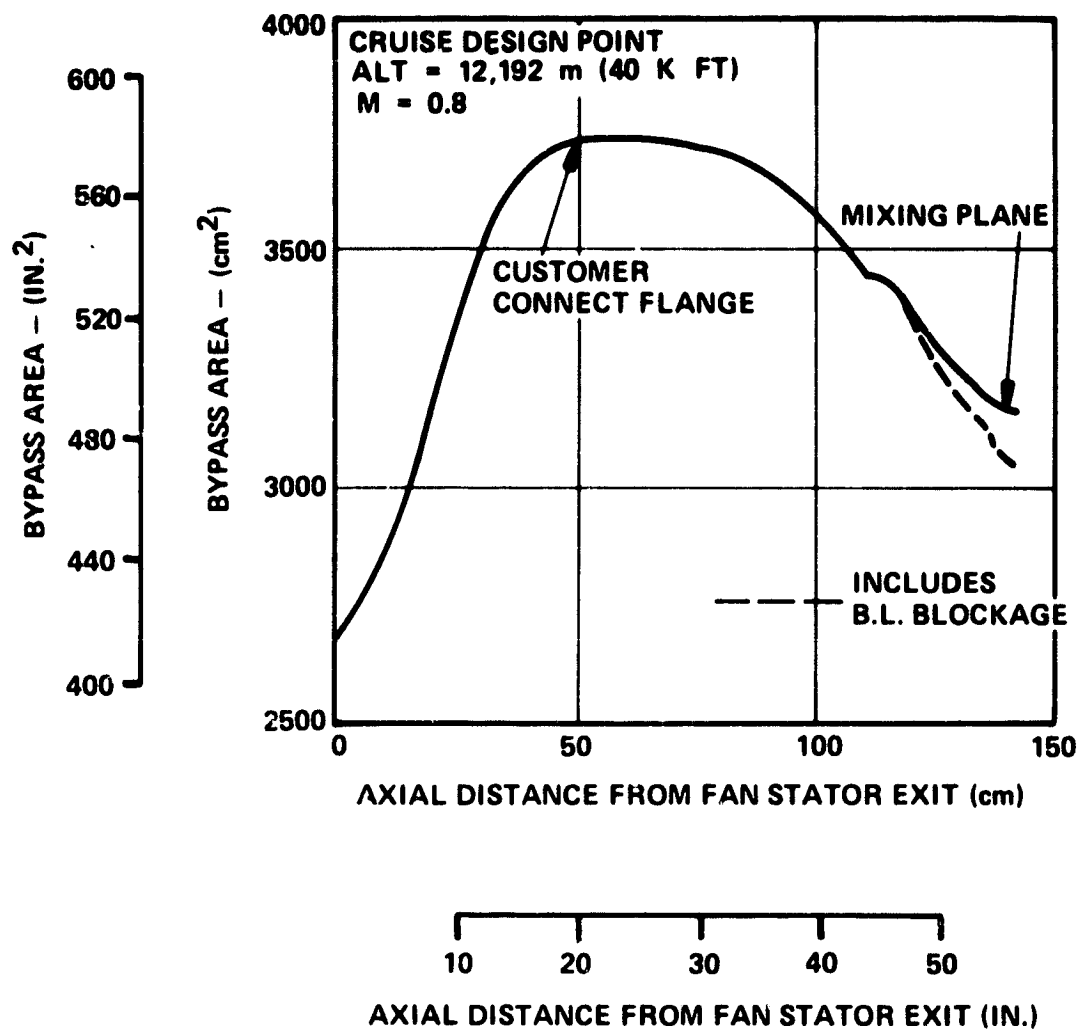
Figure 3-42. QCGAT Mixer Compound Nozzle Bypass Duct Area Distribution.
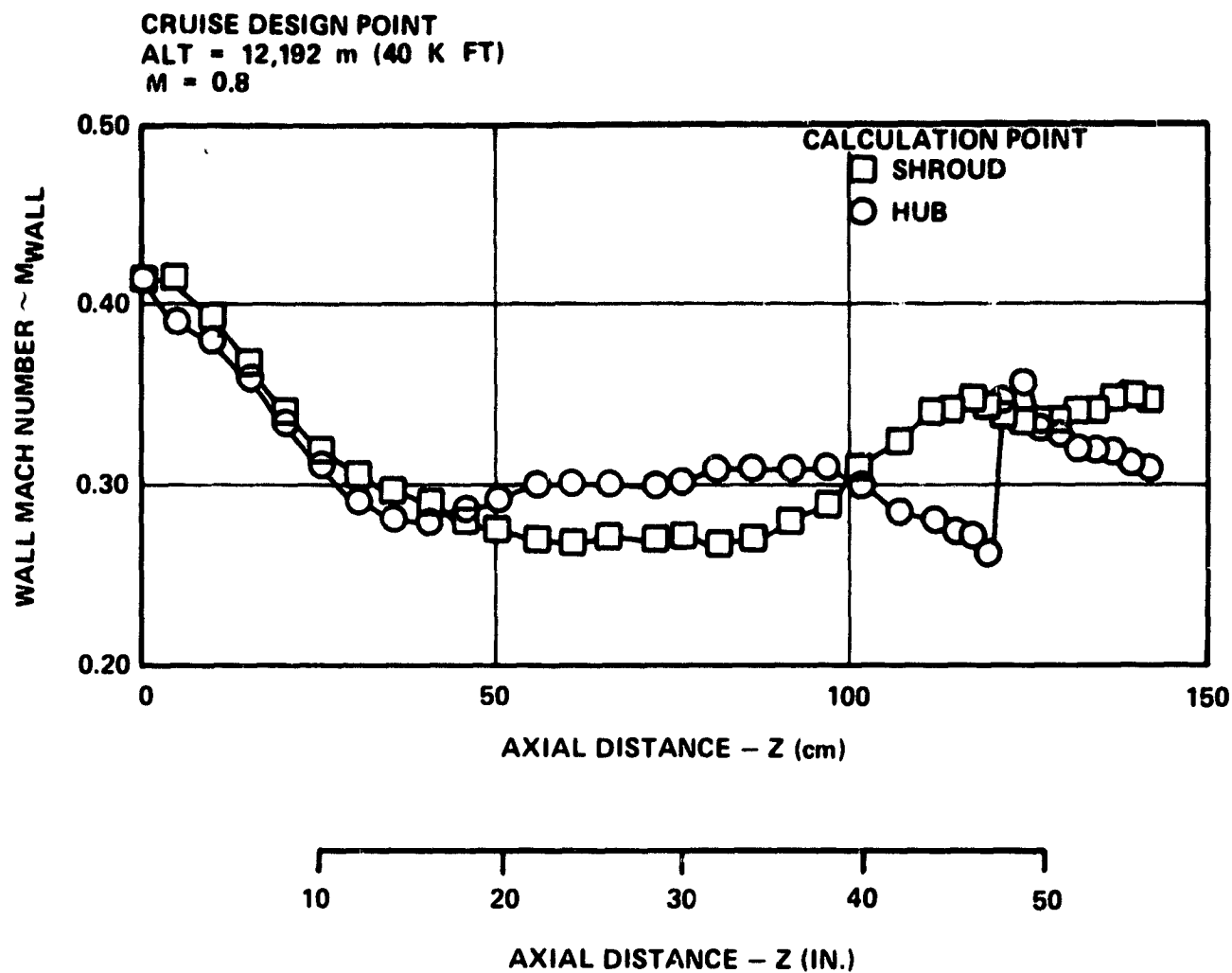
Figure 3-43. QCGAT Mixer Compound Nozzle Bypass
Duct Mach Numbers.
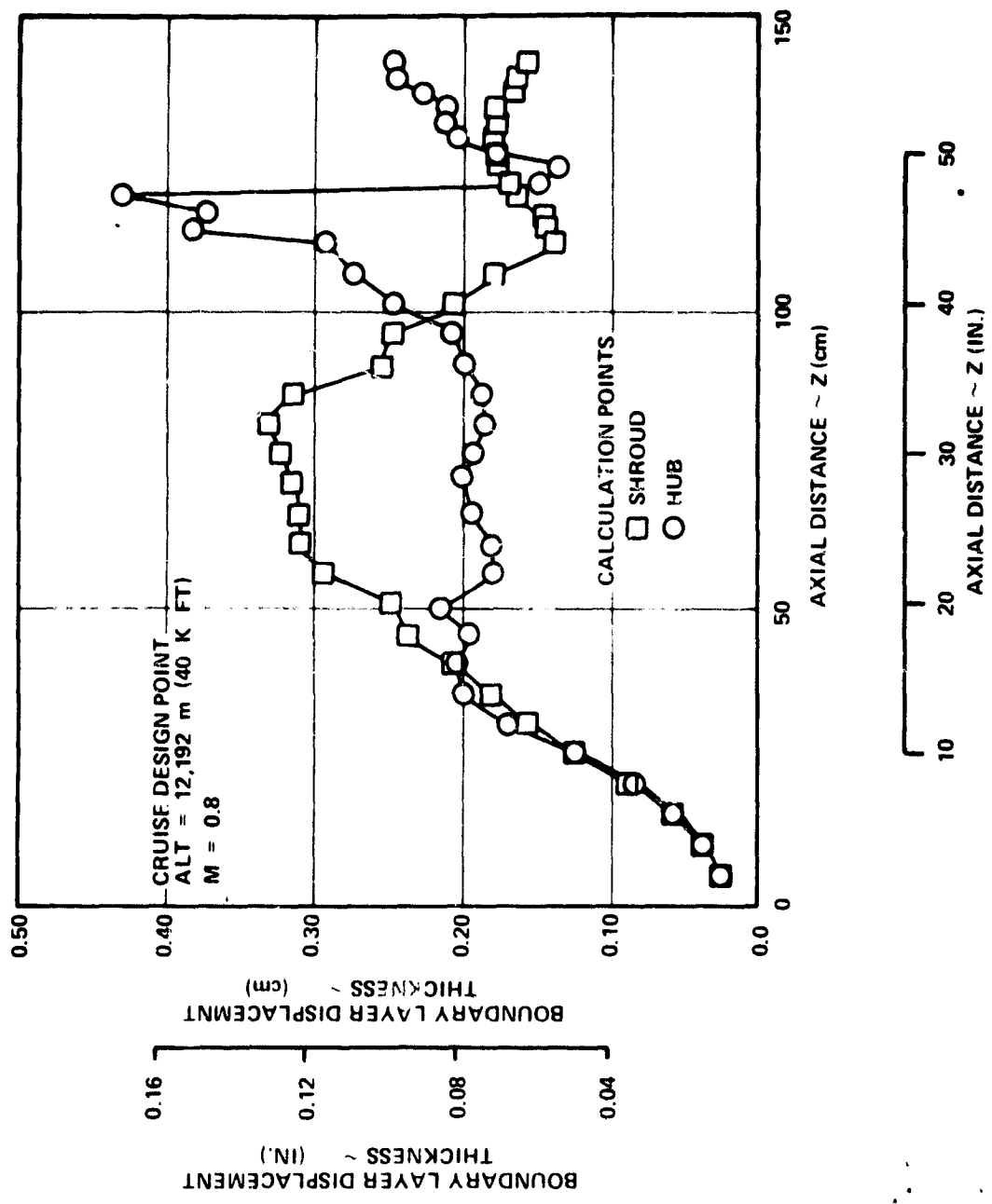
Figure 3-44. QCGAT Mixer Compound Nozzle Bypass Duct Boundary Layer Thickness.

The mixing duct design criteria are:

o   Minimize mixing-duct-exit peak velocity and temperature

o   Minimize mixing-duct-exit velocity, pressure and
     temperature gradients

o   Minimize mixing-duct length

3.4.1 Mixer-Lobe Three-Dimensional Viscous Compressible Flow Analysis

Mixer-lobe flow paths are usually analyzed with a radial-equilibrium flow analysis as described in 3.3.6.4. Unfortunately, radial-equilibrium-type-flow analysis cannot adequately account for the secondary flows and corner losses generated by forced mixers. AiResearch has successfully predicted these types of flow fields using a numerical solution to the 3-D compressible Navier-Stokes equations. The analysis is based on an equation-splitting technique. One of the split equations is solved by a numerical matching method while the other is solved by a relaxation method. The two equations are cross-coupled by an iterative process between the relaxation and matching solutions. This method was used to analyze the QCGAT mixer-lobe design (ref. 14, 15, and 16).

3.4.2 Mixer-Lobe Design Procedure and Geometric Definition

The initial geometry definition analyzed with the 3-D viscous program was based on the empirical mixer optimization study and the radial-equilibrium flow solutions. The core and bypass streams are analyzed separately. The program analyzes a single lobe passage which corresponds to the open lobe section in the stream. When the core stream was analyzed, the shroud wall is decreased slightly which truncates the tip of the lobe. This is necessary since the lobe blockage approaches 100 percent as it nears the wall, and the program calculations cannot negotiate the extremely blunt region followed by an infinitesimal flow area. In the bypass stream the same truncation is applied to the hub wall.

The 3-D viscous analysis of the preliminary mixer-lobe design showed undesirable velocity distributions and higher-than-desired losses. Flow problems were thought to be due to excessive end-wall curvature or excessive hub-to-shroud diffusion gradients. Six alternate geometries were analyzed in detail in an attempt to reduce the losses and improve the velocity distributions. The lobe length, taper ratio, aspect ratio, and end-wall curvature were changed (Table 3-7). The three main lobe shapes; parallel, radial, and modified radial, with the hub and shroud walls at the mixing plane, are compared as shown in Figure 3-45. The core lobes are symmetric about the zero-radian (0°) line and

TABLE 3-7. MIXER LOBE DESIGN COMPARISON.

Core Lobe Configuration	Geometric Parameters				
				L	
	TR	AR	PEN	cm	(IN.)
Short Parallel	1.0	3.5	0.77	39.82	(15.68)
Long Parallel	1.0	3.5	0.77	49.98	(19.68)
Short Radial	1.8	3.14	0.73	39.82	(15.68)
Long Radial	1.8	3.14	0.73	49.98	(19.68)
Offset Long Radial	1.8	3.14	0.76	49.98	(19.68)
Modified Long Radial	3.5	3.52	0.77	49.98	(19.68)

Where   TR = Taper Ratio

           AR = Aspect Ratio

     PEN = Penetration Ratio

       L = Length from Turbine Rotor Exit to
            Mixing Plane

FAN SHROUD

– – PARALLEL
– · – RADIAL
——— MODIFIED RADIAL

PLUG CENTERBODY
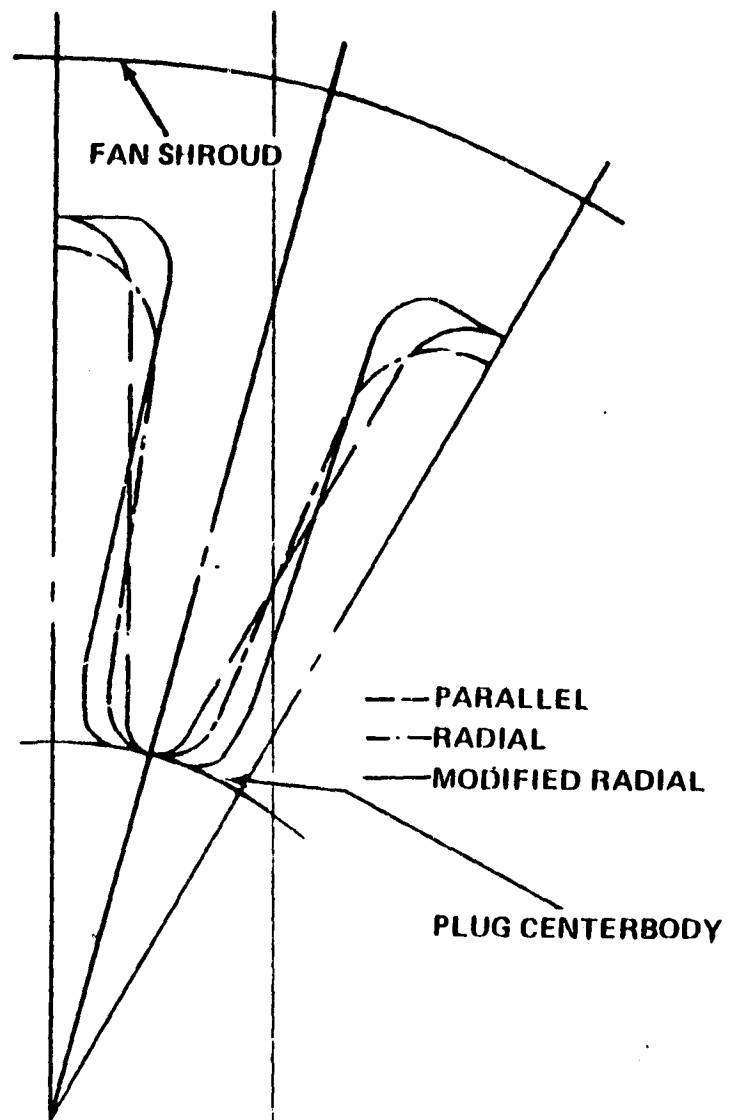
Figure 3-45. Basic Mixer-Lobe Geometries.

the bypass lobe is symmetric about the 0.26-radian (15°) line. The offset-design was moved outward in the radial direction to a new radius ratio so that the tip radius was identical to the tip radius of the parallel wall lobe.

3.4.3 Mixer-Lobe Analytical Results

The core flow was analyzed for all six lobe configurations. The bypass lobe was analyzed for the short- and long-parallel and radial designs only, since the bypass flow appeared to be relatively insensitive to the lobe geometry changes and was much less distorted than the core stream. Emphasis, therefore, was placed on analyzing the core streams.

3.4.3.1 Total-Pressure-Loss Contour Maps

A comparison of the total-pressure-loss contour plots indicates the parallel and radial designs have similar loss contours (Figure 3-46). The stretched versions of both the parallel and radial designs show improvement over their shorter counterparts while retaining contours similar to these counterparts. The offset-long radial contours (see Figure 3-47) are also similar to the long-radial. The modified long radial (also Figure 3-47) exhibits higher losses in the tip region than the other radials. The modified-radial contours also indicate a probable increased loss relative to the other designs.

Bypass-lobe loss contours for the four configurations analyzed were essentially the same. A typical loss contour is shown in Figure 3-48.

3.4.3.2 Velocity-Ratio Contour Maps

The velocity ratios of the short parallel and radial lobes are similar except for the area of higher velocity in the parallel design (see Figure 3-49). The stretched parallel and radial designs are also similar and show the higher velocities being pushed radially outward compared to the shorter versions (also Figure 3-49). The offset stretched-radial velocity contours are essentially the same as the stretched-radial contours (see Figure 3-50). The modified stretched radial (Figure 3-50) exhibits higher tip diffusion than the other designs. A typical bypass-velocity contour is shown in Figure 3-51.

3.4.3.3 Radial Total-Pressure Loss Profiles

Core-integrated radial total-pressure-loss profiles are shown in Figures 3-52 and 3-53. The profiles are determined by integrating in the circumferential direction at given radial locations. Figure 3-52 is a comparison of the short and long versions of the parallel and radial designs. Stretched designs show less

70
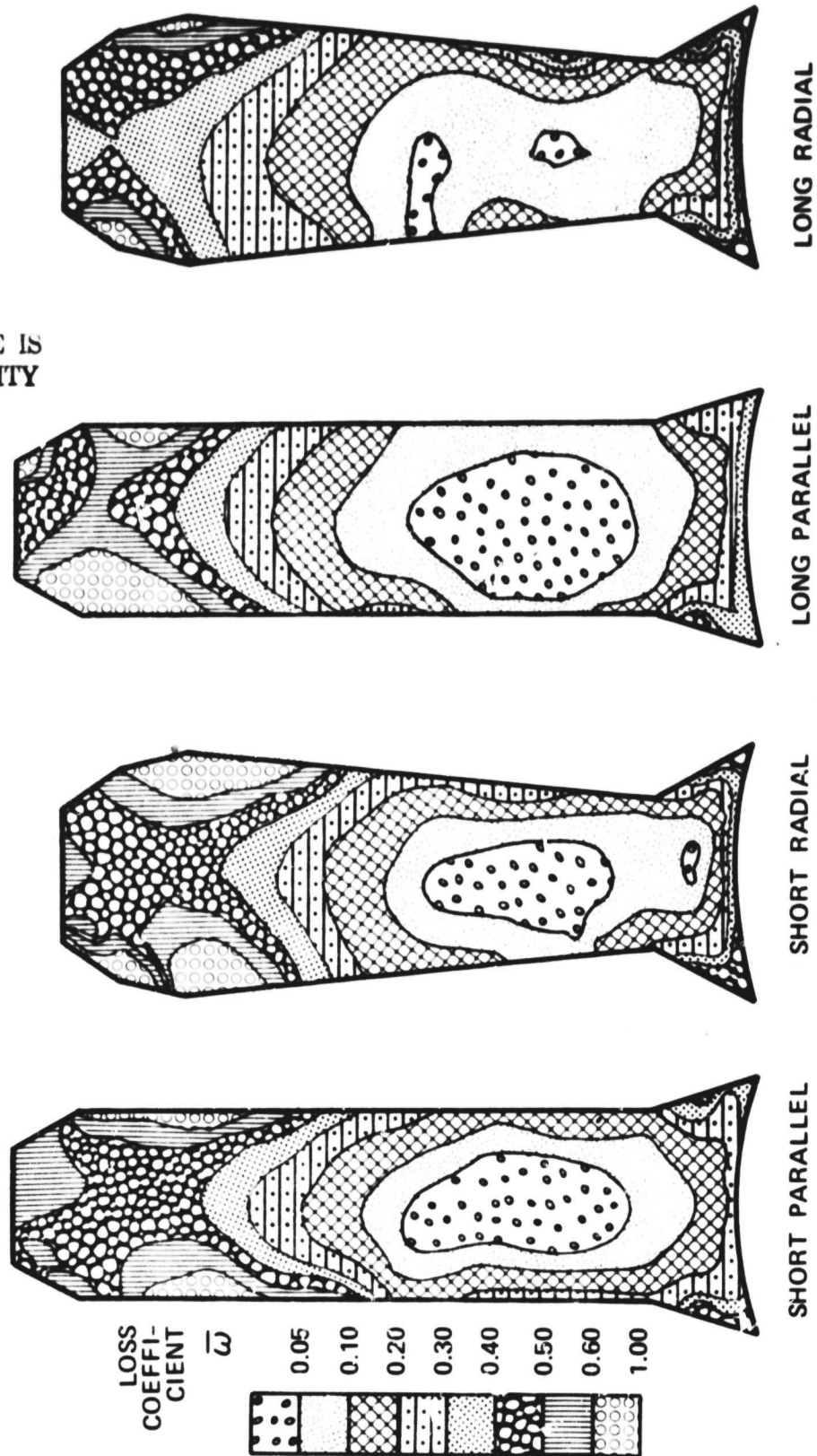
Figure 3-46. Parallel and Radial Mixer Lobe Predicted Pressure Loss Coefficient Contours.

71

3-D VISCOUS ANALYSIS

MODIFIED
LONG RADIAL

OFFSET
LONG RADIAL

LOSS
COEFFICIENT
$\bar{\omega}$

0.05
0.10
0.20
0.30
0.40
0.50
0.60
1.00

$$\bar{\omega} = 1 - \left(\frac{V_{ACT}}{V_{ID}}\right)^2$$
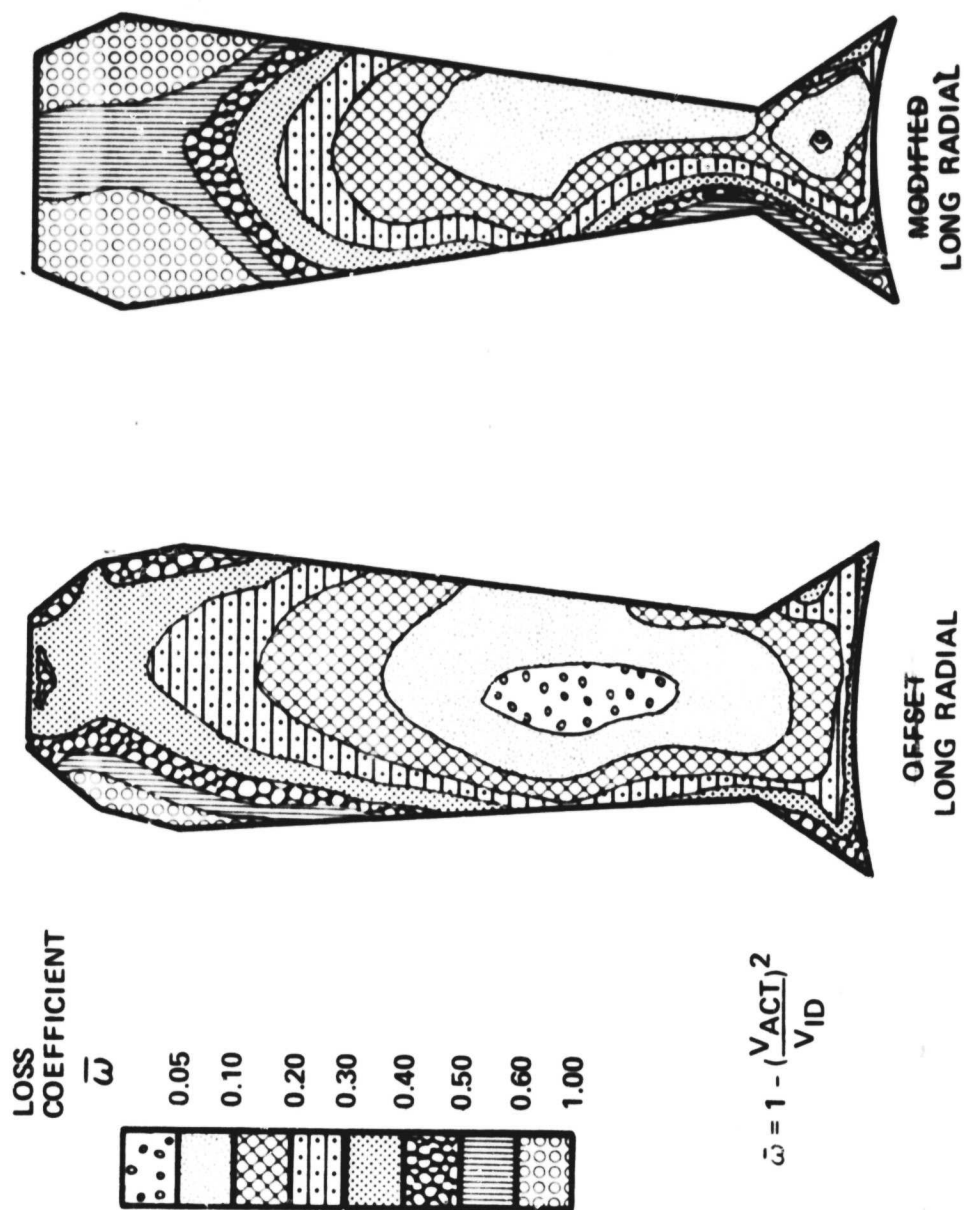
Figure 3-47. Mixer Modified Radial Lobe Predicted Pressure
Loss Coeficient Contours.

72

LOSS
COEFFICIENT
$\bar{\omega}$

0.8
0.6
0.5
0.4
0.3
0.2
0.1
0.05

$$\bar{\omega} = 1 - \left(\frac{V_{ACT}}{V_{ID}}\right)^2$$
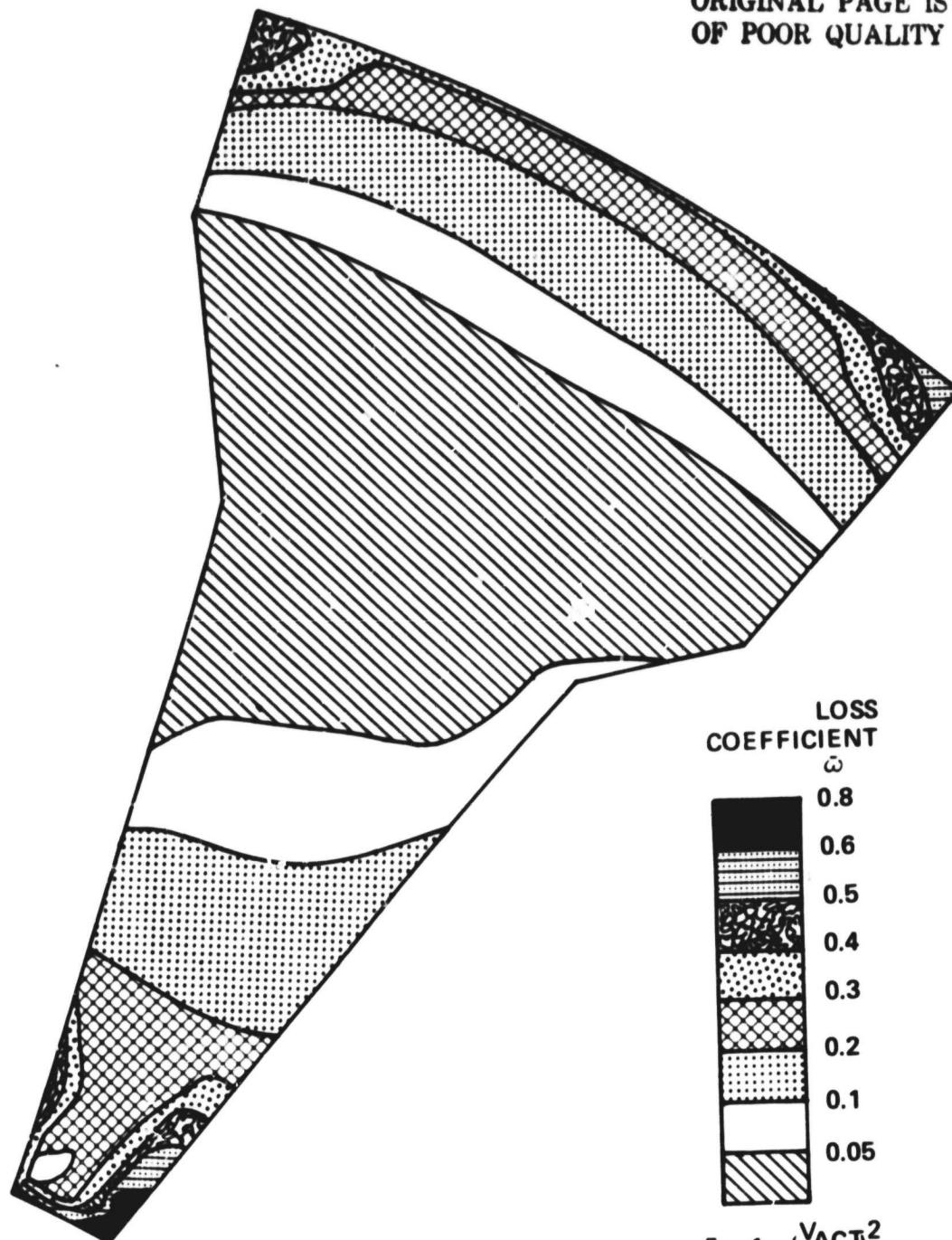
Figure 3-48.   Short Parallel Mixer, Bypass Lobe Total
Pressure Loss Contours.
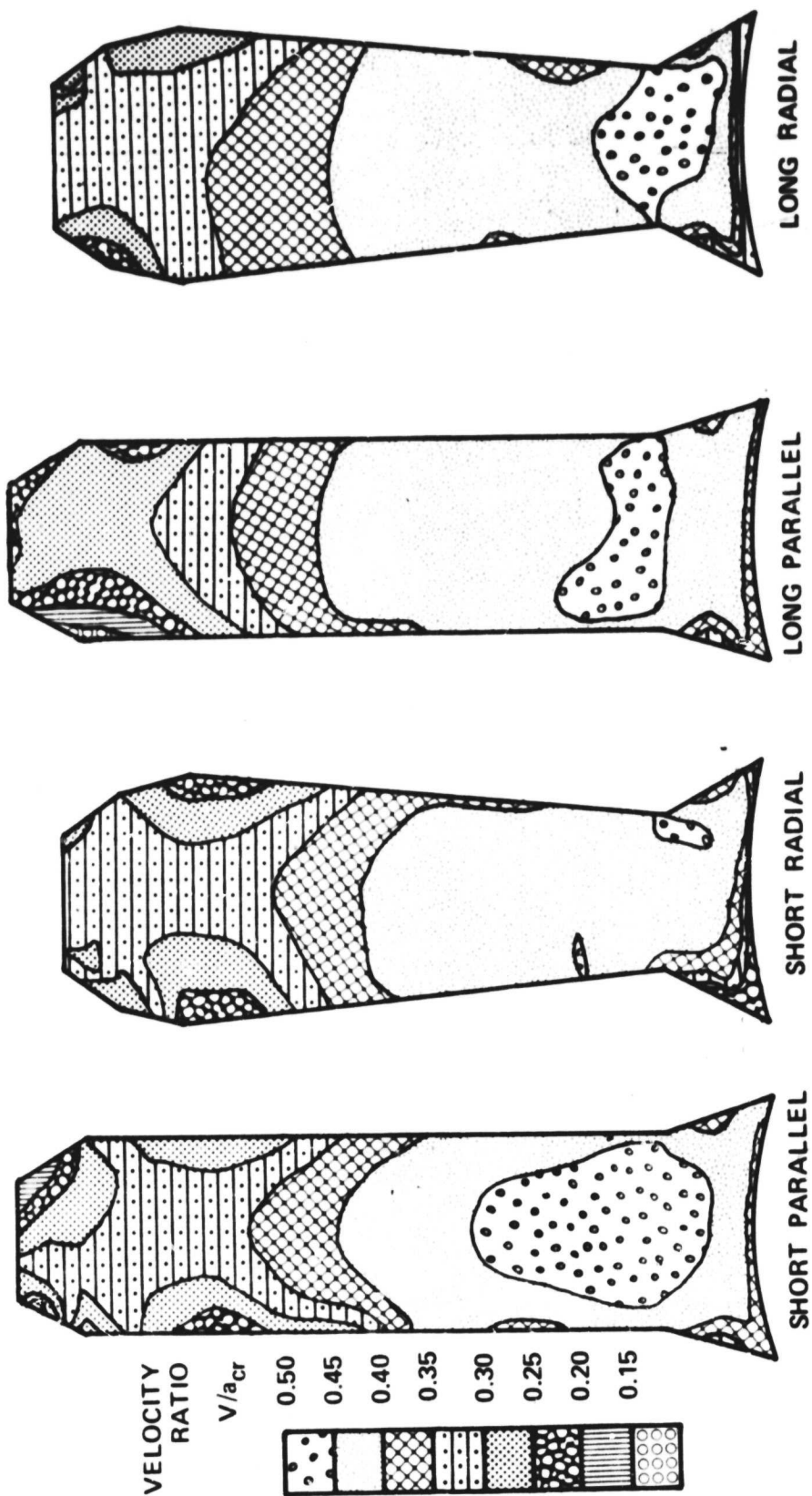
Figure 3-49. Parallel and Radial Mixer Lobe Predicted Velocity Ratio Contours.
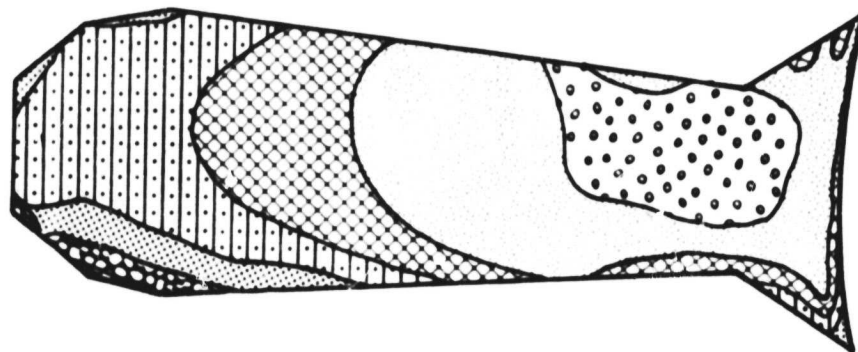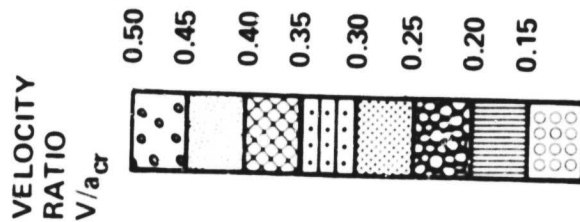
74

3-D VISCOUS ANALYSIS

MODIFIED
LONG RADIAL

OFFSET LONG
RADIAL

VELOCITY
RATIO
V/a_cr

0.50
0.45
0.40
0.35
0.30
0.25
0.20
0.15
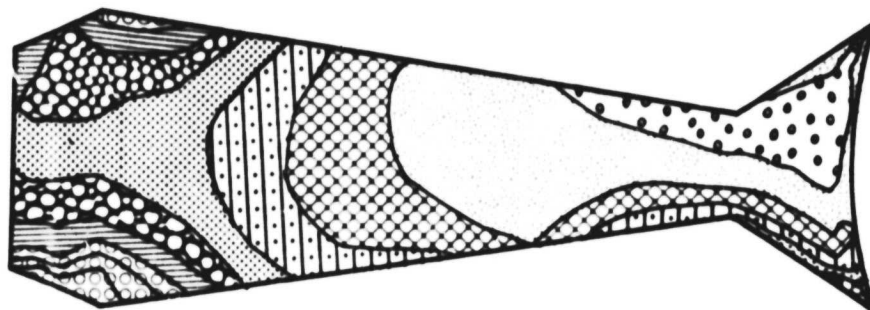
Figure 3-50. Modified Radial Mixer Lobe Predicted
Velocity Ratio Contours
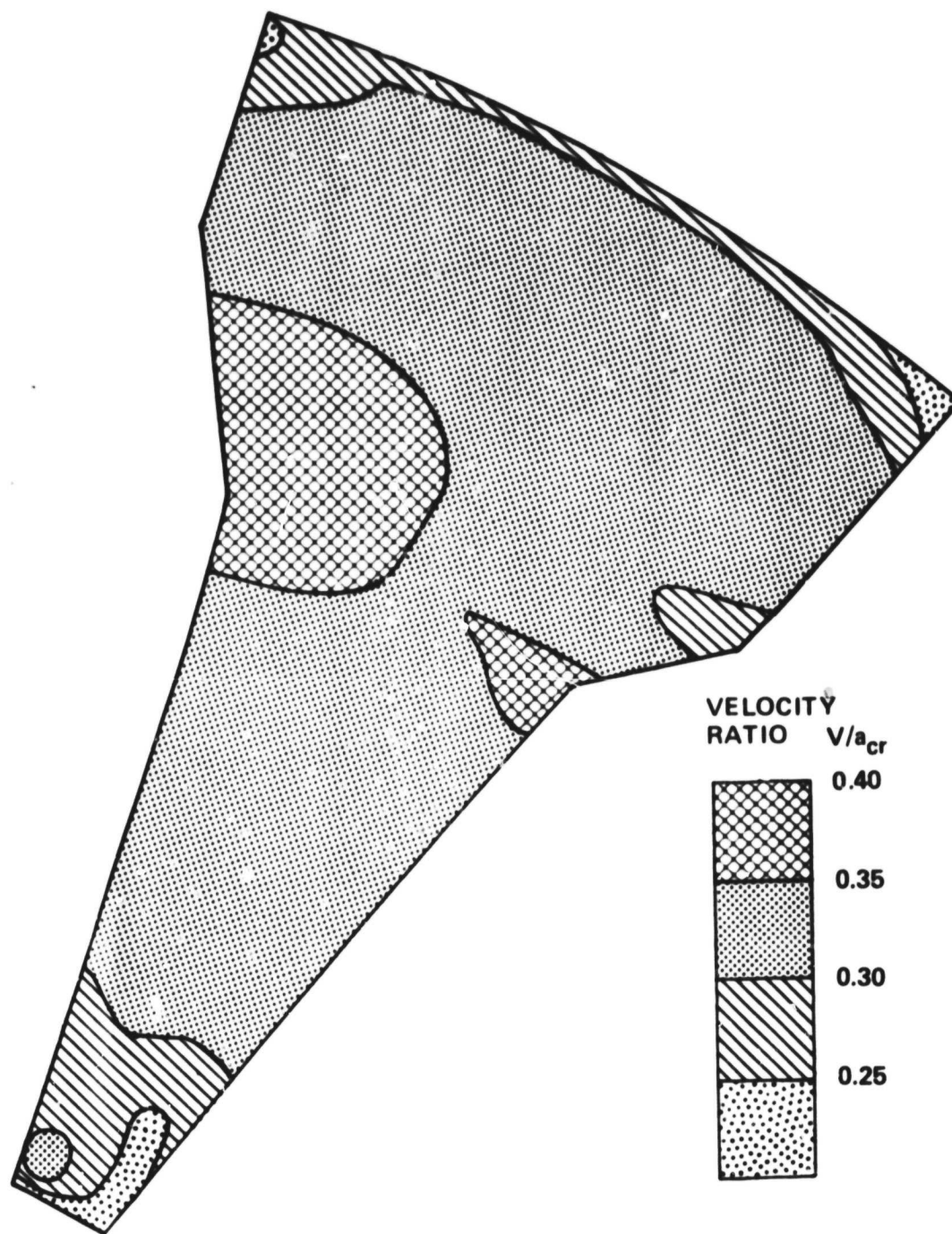
Figure 3-51. Short Parallel Mixer, Bypass Lobe Predicted Velocity Ratio Contours.
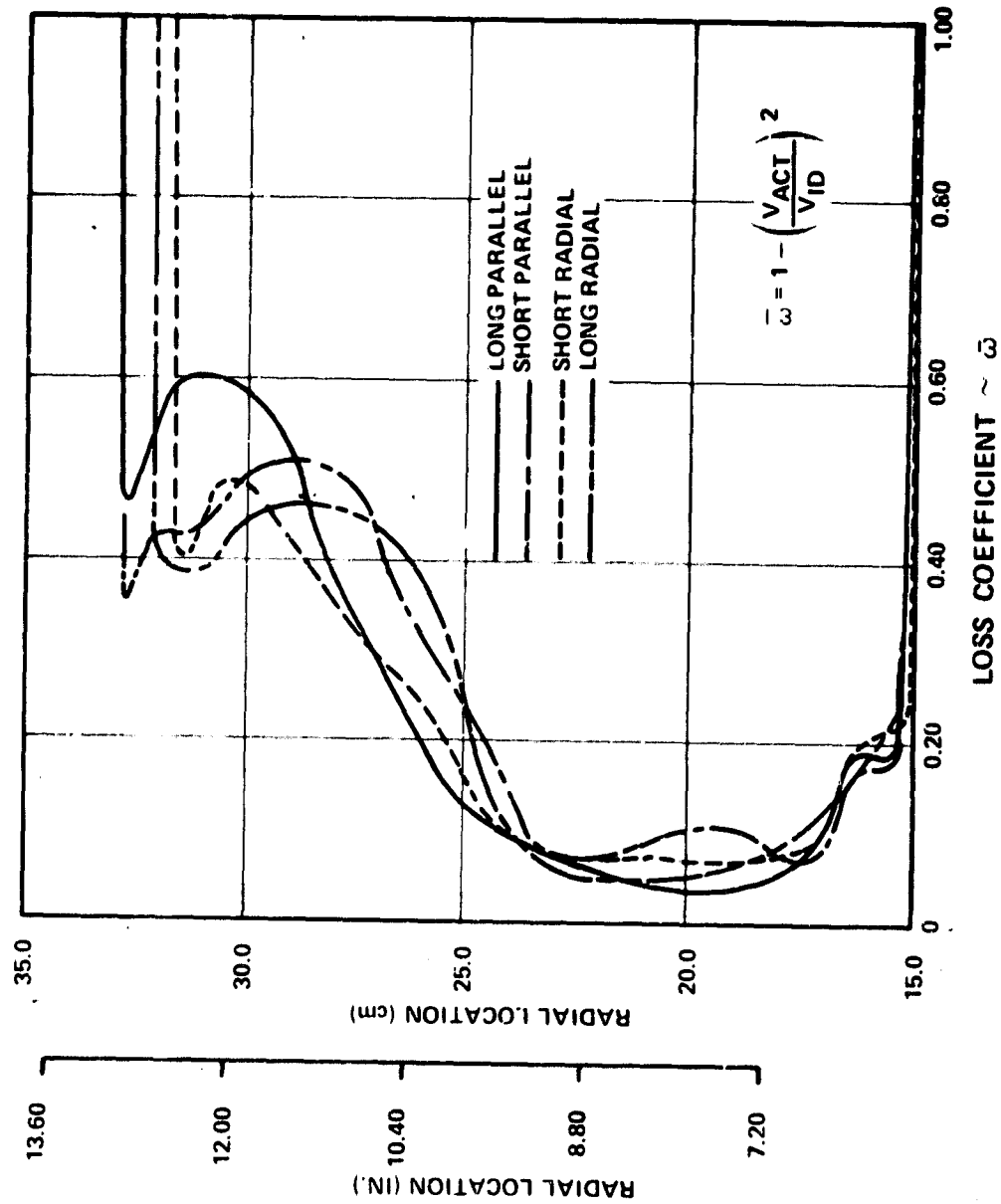
Figure 3-52. Comparison of Parallel and Radial QCGAT
Mixer Core Predicted Radial Loss Profiles.

loss in the mid-region than the shorter designs. The long radial design improved the tip loss over the short radial, but the long-parallel design increased the tip loss over the short-parallel. Modified and offset-long radial profiles are compared to the long-radial in Figure 3-53. The modified-radial shows losses much higher at the hub and tip sections than the long-radial. Profiles of the offset- and long-radial are the same except for a slightly lower tip loss for the offset design. In general, the stretched-core designs have better radial-loss profiles. The stretched-radial has the lowest tip-region loss, and the stretched-parallel has the lowest mid- and hub-region loss.

Bypass-radial total-pressure-loss profiles for the four configurations analyzed are shown in Figure 3-54. Basically, the profiles are the same, except for the short-parallel design which exhibits higher hub losses due to the narrow channels with high curvature in the hub region.

3.4.3.4 Integrated Total-Pressure Losses

A loss coefficient, $(\bar{\omega})$, and total-pressure losses are presented in Table 3-8 for the core and bypass lobe sections. Pressure-loss design goals of 2.5 percent for the core lobe and 0.8 percent for the bypass lobe are included for comparison. The modified-radial high-taper-ratio was the only design that exceeded the core-design-goal pressure loss. The initial purpose of the 3-D viscous lobe analysis was to rank the mixer-lobe designs in order of loss rather than expect actual absolute loss levels. Therefore, the core-lobe designs were ranked into three loss categories as shown in Table 3-9.

As shown in Table 3-9, core loss was reduced by lengthening the lobes, thus reducing core-shroud curvature and the tip diffusion rate. The modified radial design, which was an attempt to obtain a more uniform radial flow ratio between the core and bypass, resulted in an increased loss of about 1 percent over the other stretched designs.

3.4.4 Mixing Duct Three-Dimensional Viscous-Incompressible-Flow Analysis

The 3-D elliptic-mixing program is a general prediction procedure for three-dimensional flows. The program uses an implicit finite-difference method, in which the difference equations are formed by integration over a small control volume surrounding a grid point. A hybrid formula, which is a combination of the central and upwind difference schemes, is used to represent the convection and diffusion terms. The flow field is characterized by the three velocity components, temperature, and pressure. The calculation initially uses an estimated pressure field in the momentum equations to obtain a preliminary velocity field; then corrections to the pressure field are calculated so that the

78
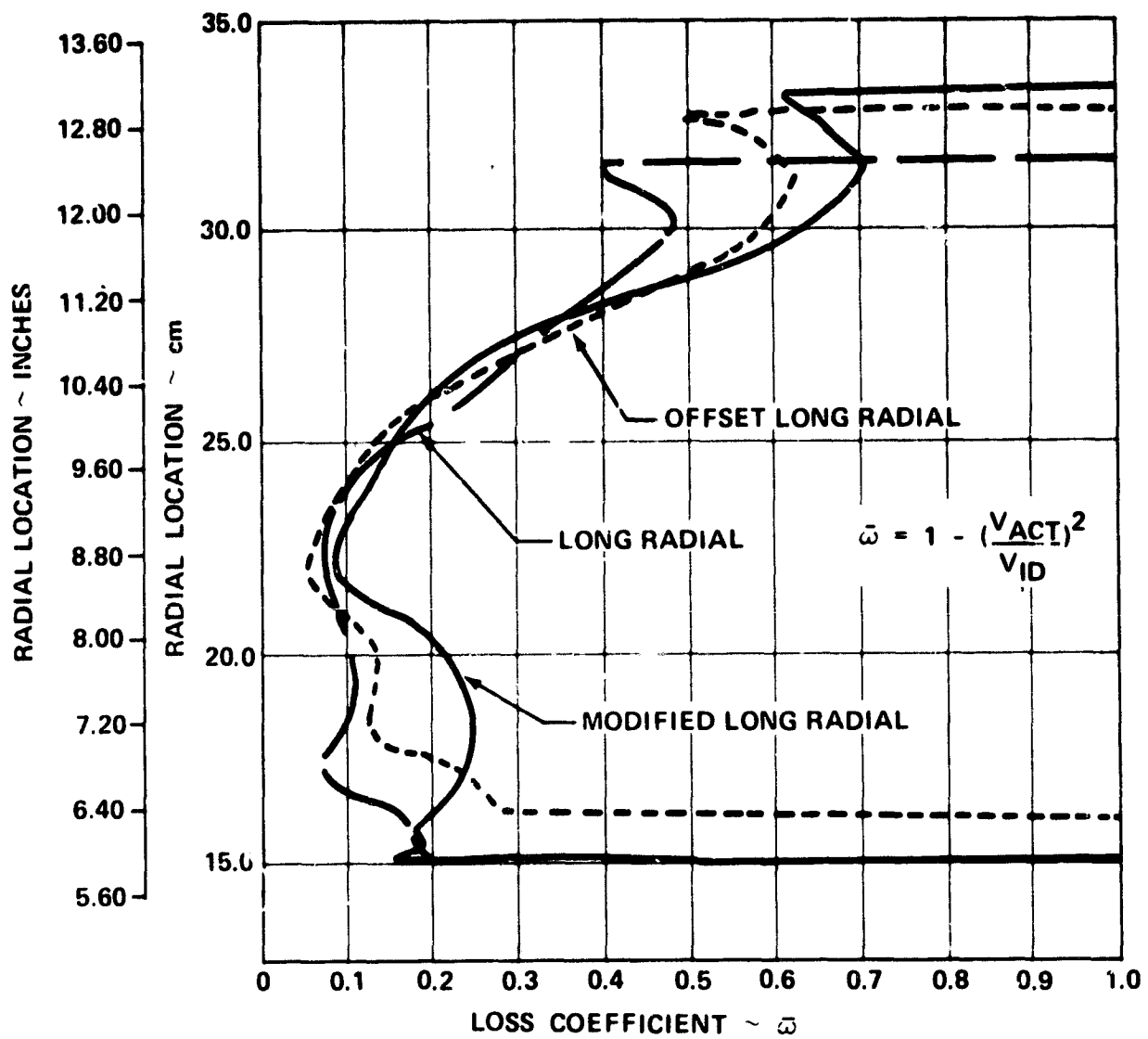
Figure 3-53. Comparison of Long Radial QCGAT Mixer Core Predicted Radial Loss Profiles.
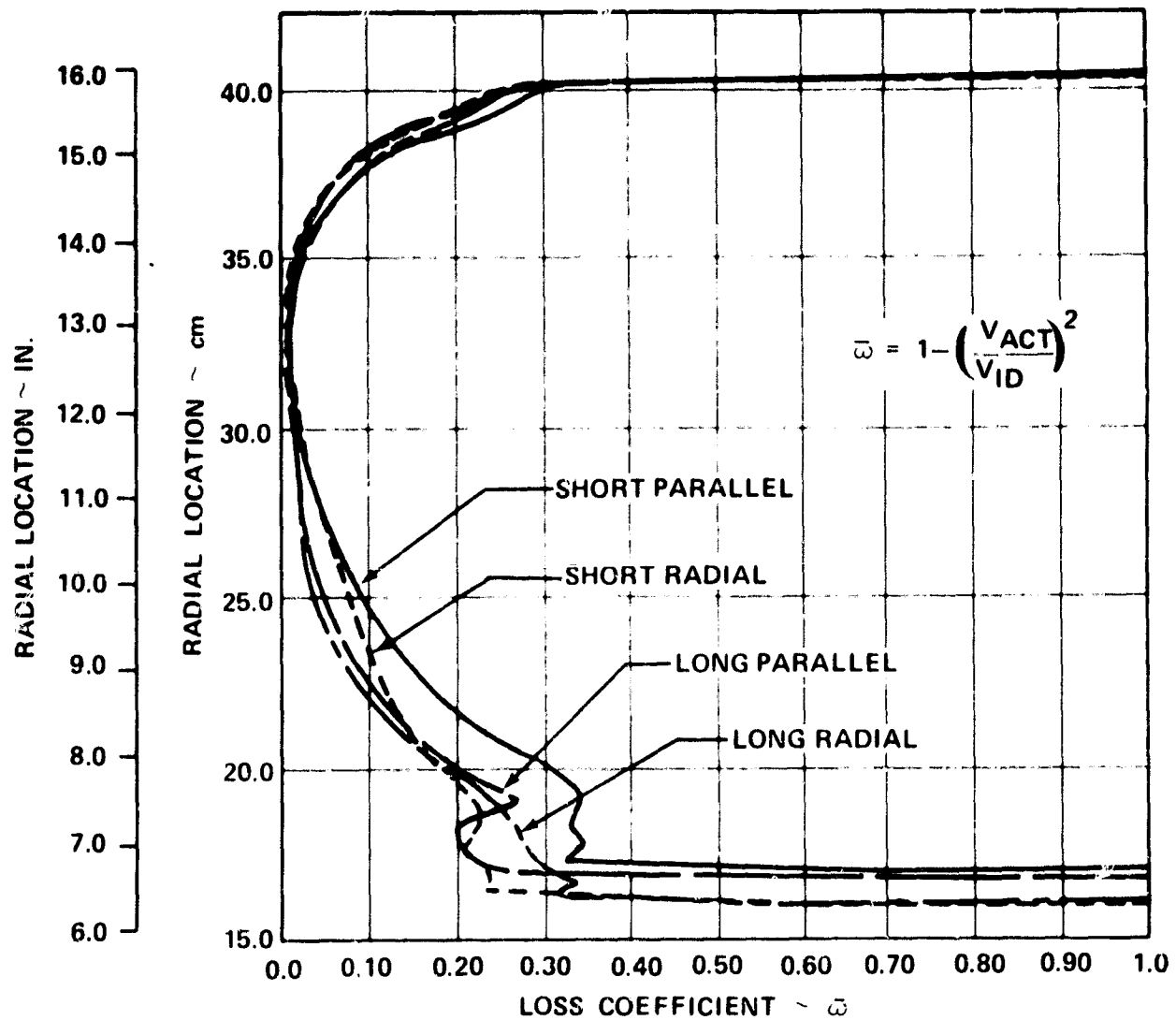
Figure 3-54. QCGAT Mixer Bypass Predicted Radial Loss Profiles.

80

TABLE 3-8. MIXER LOBE INTEGRATED DESIGN POINT LOSSES.

Configuration	$\bar{\omega} = 1 - \dfrac{V_{ACT}^2}{V_{ID}^2}$	$\Delta P_T / P_T$
Core Lobe		
Design Goal	0.230	0.0248
Short Parallel	0.255	0.0266
Short Radial	0.251	0.0252
Long Parallel	0.226	0.0196
Long Radial	0.212	0.0190
Offset Radial	0.215	0.0193
High Taper Ratio	0.292	0.0302
Bypass Lobe		
Design Goal	0.079	0.0078
Short Parallel	0.113	0.0112
Short Radial	0.087	0.0078
Long Parallel	0.080	0.0071
Long Radial	0.081	0.0071

TABLE 3-9. CORE $\Delta P_T / P_T \sim$ %.

2.0	2.5	3.0
Long Parallel Long Radial Offset Long Radial	Short Parallel Short Radial	Modified Long Radial

resulting velocity field will satisfy the continuity equation.
A 2-dimensional two-equation turbulence model is also included.
References 17, 18, and 19 describe the program equations in
detail.

3.4.5 Design Procedure and Geometric Definition

The initial flow conditions required for the analysis are
the velocity, static pressure, static temperature, and turbulence
level. Previous studies (ref. 19) comparing predicted and
experimental results for this type of flow analysis indicated that
the results are sensitive to initial conditions. Preliminary
analytical results were obtained using uniform initial conditions.
A further analytical refinement was made using the output profiles
from the 3-D viscous lobe analysis for the velocity, pressure,
and temperature initial conditions at the mixing plane. The
static pressures for both gas streams were assumed to be constant
at the mixing plane.

A single value of the turbulent kinetic energy factor is
required as an initial condition. Separate values were calculated
for each stream based on the turbulence levels presented in
Reference 19. A single turbulent kinetic energy factor of 0.003
was used in the calculations. This level is close to the core
stream value since only a fraction of the bypass stream is
involved in the initial mixing. Since the turbulence model is a
two-equation model, a dissipation length factor is required. A
length factor of 0.02 was used.

The grid setup had 11 nodes in the radial direction, 11 in
the circumferential direction, and 20 nodes in the axial direc-
tion. These values are the maximum allowed in the nozzle program
version at this time due to array size limitations. The wall
contours and lobe shape were approximated with a symmetric grid
system as shown in Figure 3-55. The grid spacing was altered
circumferentially and radially for each particular lobe shape to
account for the geometry changes.

3.4.6 Comparison of Mixing Duct Analytical Results with Uniform
Inlet Flow

Initially, the mixing duct with the reference compound split-
ter and three basic mixer-lobe geometries (parallel, radial, and
modified radial), were evaluated with the 3-D Elliptic Mixing
Program in parallel with the lobe analysis. Uniform initial inlet
conditions from the cruise design point were input and the veloci-
ties were compared at the end of the mixing duct. Peak velocity
levels were determined from the velocity profiles circumferentially
in line with the centerline of the core lobe. The analytical
results were reviewed at the end of the mixing duct.

82
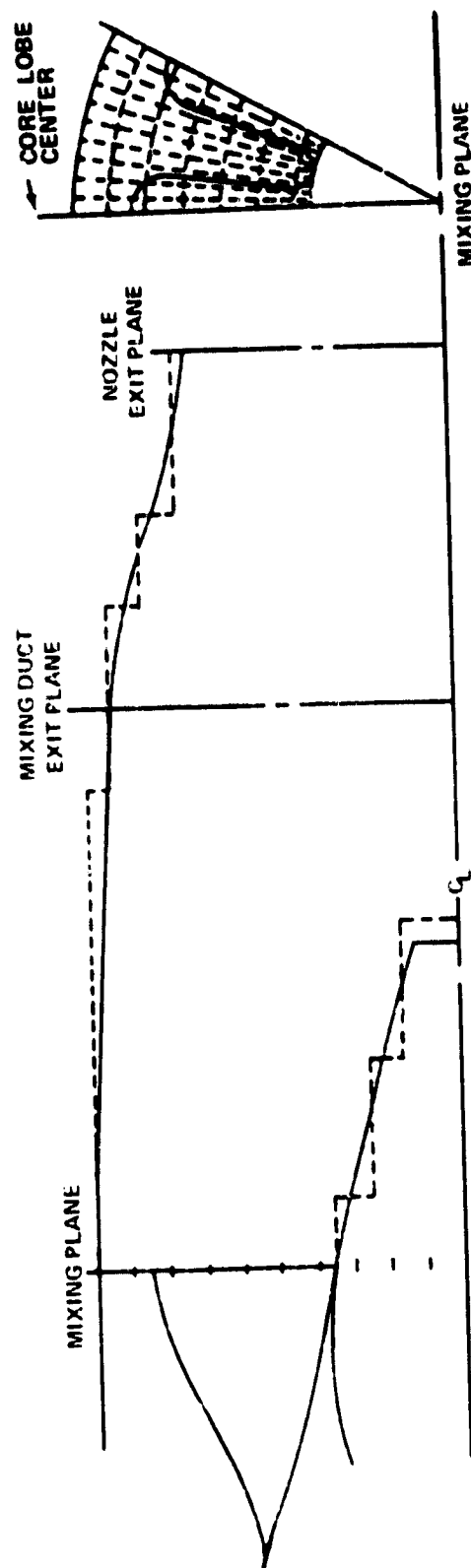
Figure 3-55. QCGAT 3-D Mixing Analysis Station Definitions.

The cruise design point condition was used for most of the mixing duct analysis due to its higher velocity split as shown in Table 3-10.

Figure 3-56 shows the mixing-duct exit-velocity profiles in line with the center of a core lobe based on uniform inlet conditions. The initial velocity profiles are also presented for comparison. All three lobe configurations decrease the peak velocity relative to the compound nozzle. The modified-radial has the lowest peak velocity and there is little or no difference in the peak velocities for the parallel- and radial-lobe designs. It should be noted that the compound-splitter circumferential velocity is constant whereas the velocity decreases circumferentially for the mixer lobes.

3.4.7 Comparison of Mixing Duct Results with Predicted Inlet Profiles

The effect of initial conditions on the mixing-duct exit-velocity profile was investigated. The lobe-exit profiles (computed from the 3-D viscous analysis) were used as initial conditions for the 3-D elliptic mixing-duct analysis. These profiles had typically lower velocities at the lobe tip, higher velocities at the lobe center, and lower velocity near the hub. As one would expect, similar profile changes are calculated at the mixing-duct exit as shown in Figure 3-57.

TABLE 3-10. AVERAGE MIXING PLANE VELOCITIES.*

Parameters	SLS T/O		Cruise D.P.	
	m/sec	(ft/sec)	m/sec	(ft/sec)
V_{Core}	165.6	543.5	197.2	647
V_{Bypass}	124.4	408	127.1	417
V_{Core}/V_{Bypass}**	1.33	1.33	1.55	1.55

*298°K (77°F) Day, M = 0.8, Alt = 12,192m (40K ft)
**Dimensionless

84
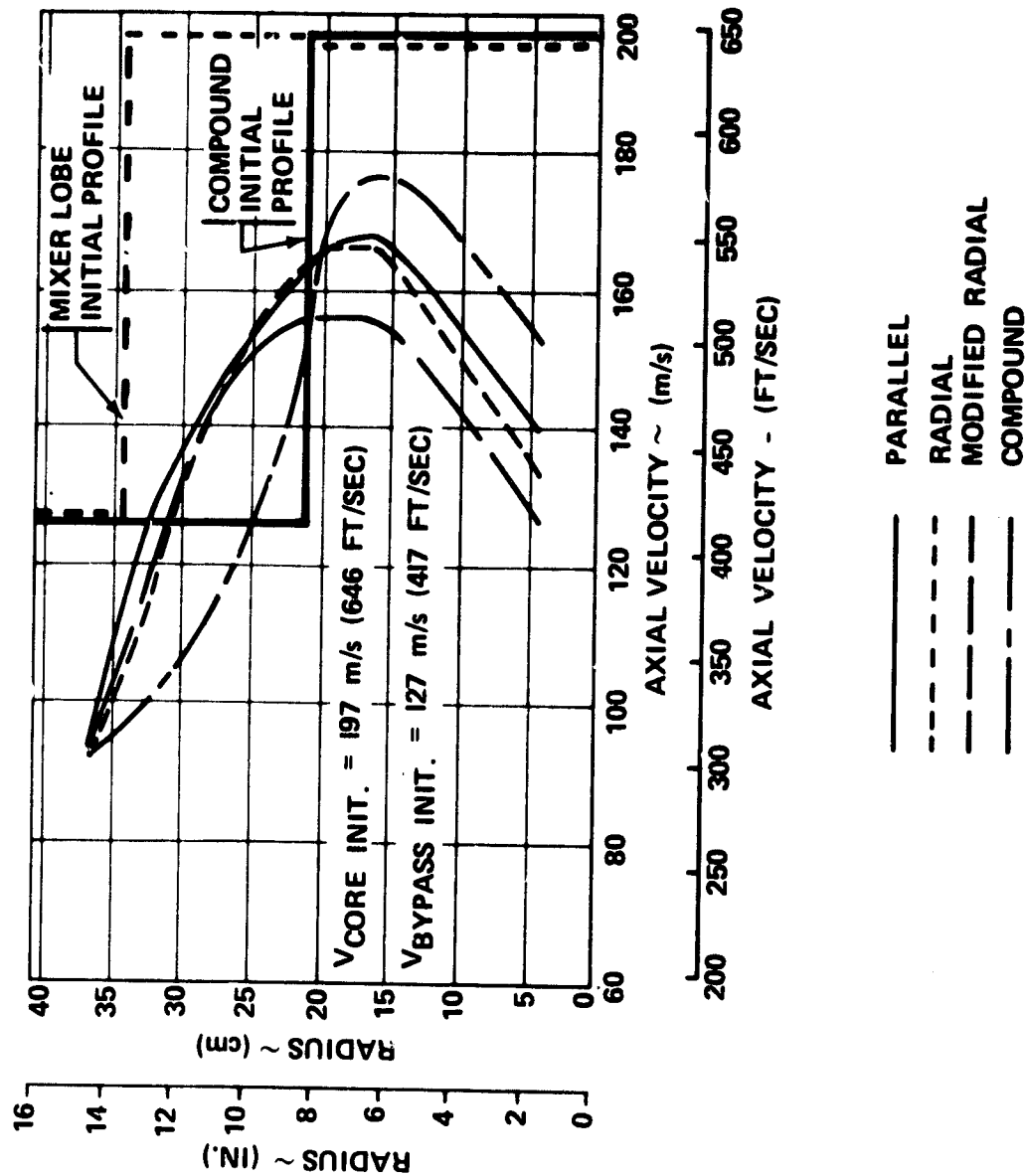
Figure 3-56. Core Centerline Predicted Velocity
Profiles at Mixing Duct Exit Plane.
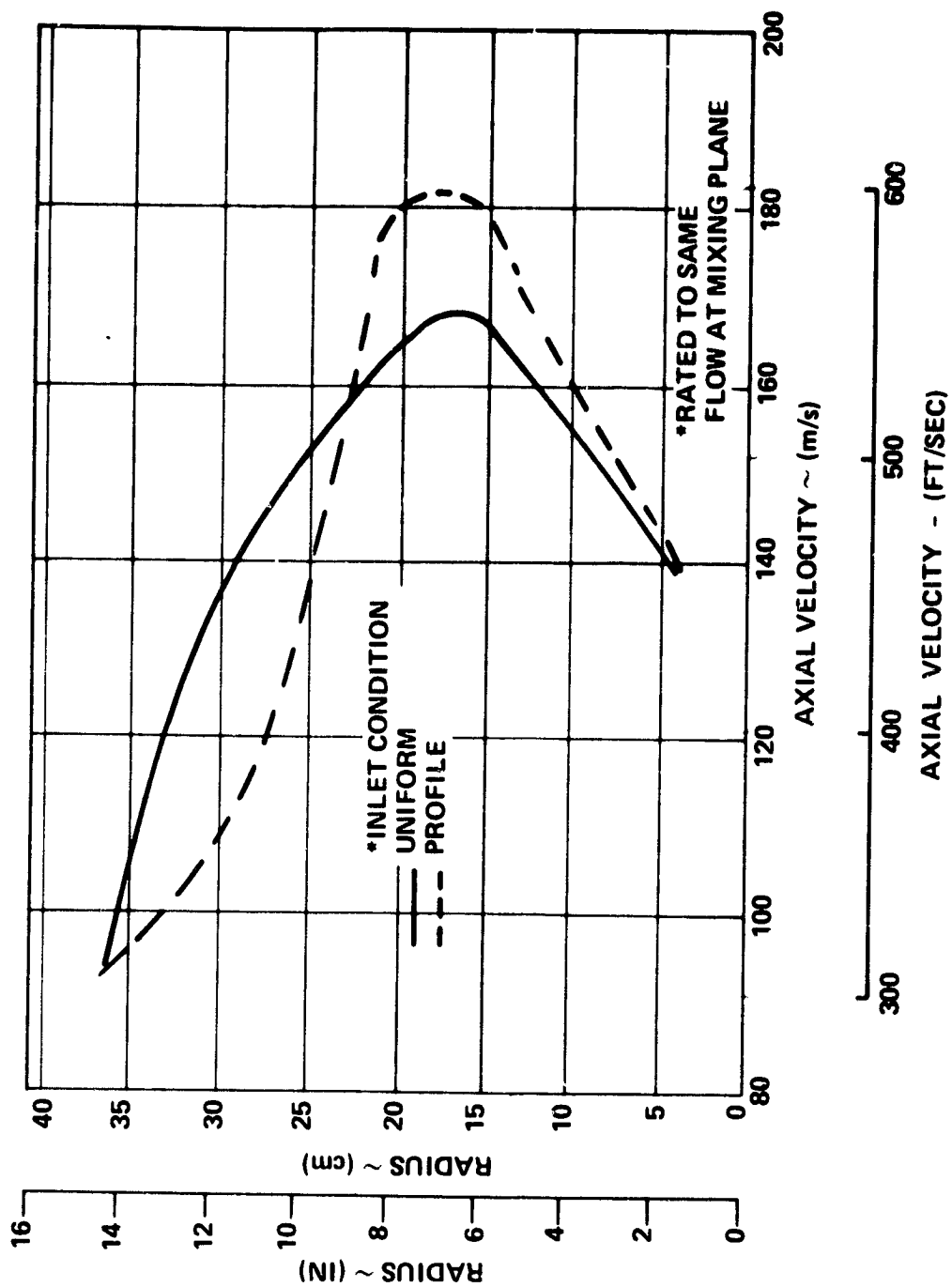
Figure 3-57. Parallel Mixer Core Centerline Predicted Velocity Profiles at Mixing Duct Exit Plane.

The calculated inlet profiles from the 3-D viscous analysis were scaled to maintain the same average velocity ratio for all configurations. The velocities were scaled until the averaged velocity and total pressure were equal to the compound splitter values. With the same average inlet conditions the mixer configurations have a higher initial core-peak velocity than the compound-splitter configuration as shown in Figure 3-58.

The effects of lobe shape on the mixing process were assessed by studying the calculated total temperature, total pressure, and velocity profiles at the mixing-duct exit plane as noted in Figure 3-55. The predicted total-temperature profiles (Figures 3-59 and 3-60) indicate that the lobe length had little or no effect on the total temperature decay rate, i.e., there is very little difference between the long and short parallel mixers, or the long and short radial mixers. The increased radius ratio or offset ratio had very little effect on the calculated total-temperature profiles. However, there is some indication that increasing the offset ratio produces slightly larger peak temperature zones. Parallel lobe temperature profiles compared to radial lobe temperature profiles show the peak temperatures are about the same but the radial lobes reduce the centerline zone temperature by 75°K (135°R). Use of the high-taper-ratio modified-radial rather than radial lobes reduces the peak total temperature by 75°K (135°R) and reduces the center zone temperature by 75°F (135°R) over the radial lobes and 150°K (270°R) over the parallel lobes. The compound nozzle has a peak temperature which is 94.4°K (170°R) hotter than the parallel or radial-lobe peak temperatures. The compound center zone temperature exceeds that of the parallel lobe value by 169.4°K (305°R) and it exceeds the radial lobe temperature by 244.4°K (440°R).

The predicted mixing-duct-exit total pressures are compared in Figures 3-61 and 3-62. The long- and short-parallel mixer total-pressure profiles are very nearly the same. The bypass total pressure loss is approximately 1 percent and the peak core-lobe total-pressure loss is about 2 percent. The long-radial mixer has the best total-pressure profile of the radial mixers. The peak lobe loss is about equal to the parallel lobes (2 percent), but the core mid-passage losses are higher (1 percent). In addition, a substantial portion of the bypass flow indicates a 2-percent total pressure loss as opposed to the 1-percent parallel lobe loss. The short-radial mixer and the offset-radial mixer show peak core-lobe losses of 3 percent. The high-taper-ratio lobe (modified radial) shows the highest peak-core lobe loss (4 percent), while the entire core midpassage zone indicates a 1-percent loss, and the entire bypass flow zone indicates a 2-percent total pressure loss. Centerline zone losses generated by the core centerbody are virtually the same for all of the mixers analyzed.

VELOCITY

$V_{MA} \neq V_C$

VELOCITY

$V_{MA} = V_C$

(SCALED TO SAME INLET CONDITIONS)

V_M = MIXER CORE PROFILE VELOCITY
V_{M_A} = MIXER CORE AVERAGED VELOCITY
V_C = COMPOUND CORE VELOCITY
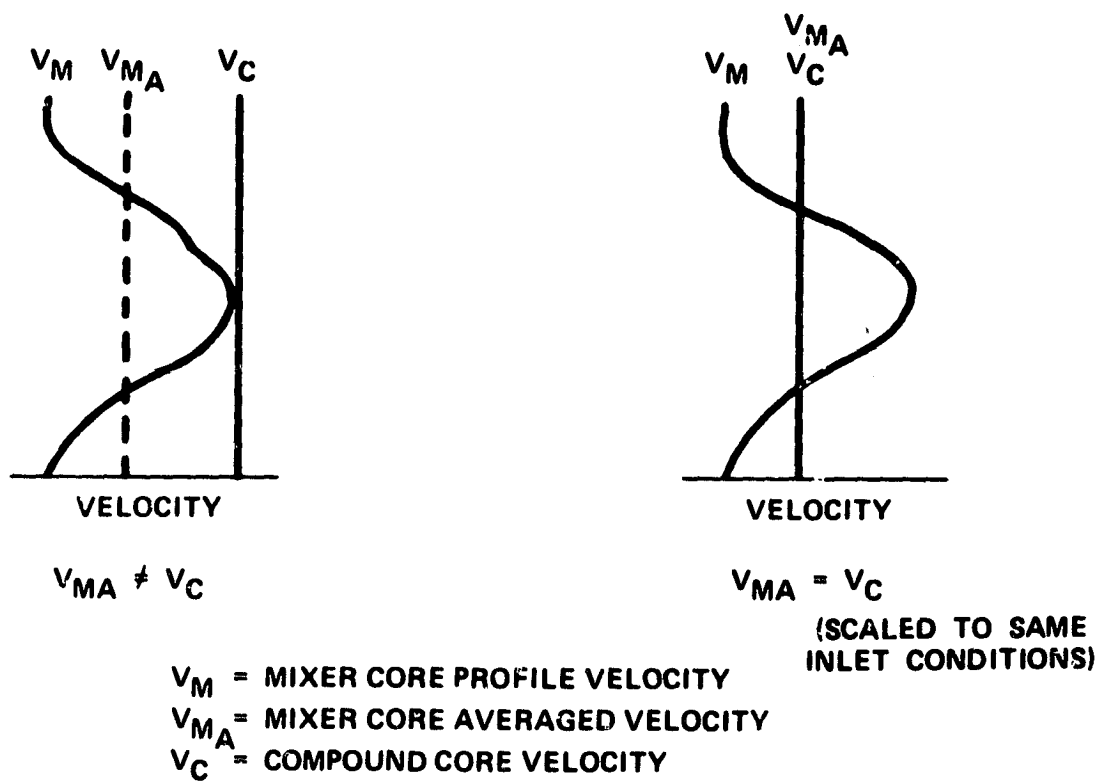
Figure 3-58. Core Peak Velocities.

12 LOBE MIXER TOTAL TEMPERATURE CONTOURS AT MIXING DUCT EXIT PLANE

COMPOUND
NOZZLE

LONG
PARALLEL
MIXER

SHORT
PARALLEL
MIXER

TOTAL TEMP °K	°R
753.9	1357
638.9	1150
566.7	1020
488.9	880
416.7	750
338.9	610
287.8	518
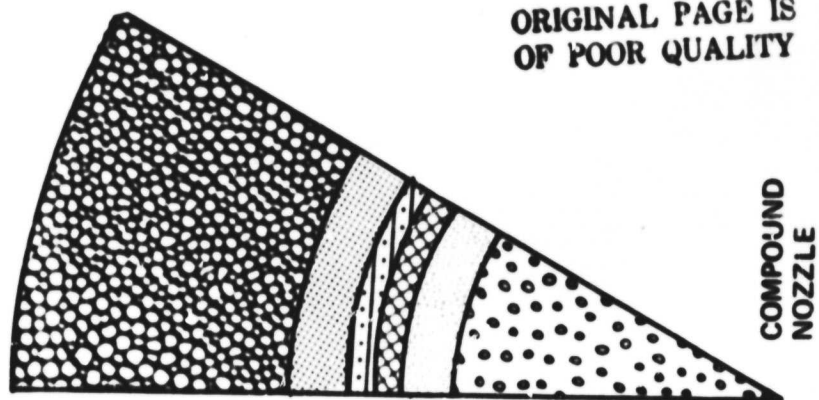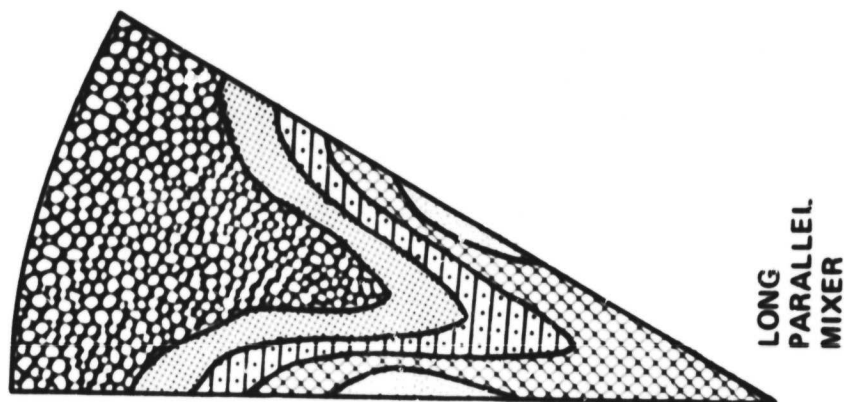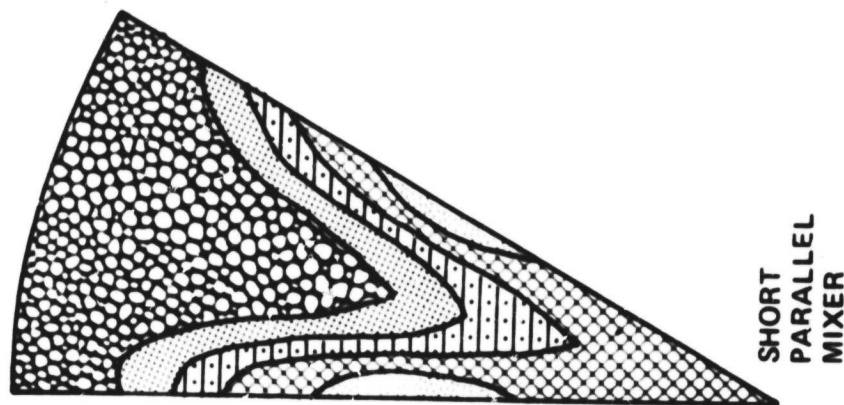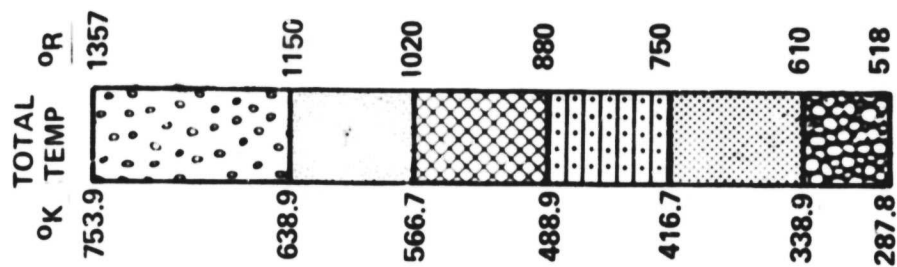
Figure 3-59. Parallel Mixers and Compound Predicted
Temperature Contours.

89

12 LOBE MIXER TOTAL TEMPERATURE CONTOURS AT MIXING DUCT EXIT PLANE

TOTAL TEMP	°R	°K
	1357	753.9
	1150	638.9
	1020	566.7
	880	488.9
	750	416.7
	610	338.9
	518	287.8

SHORT RADIAL MIXER

LONG RADIAL MIXER

LONG OFFSET RADIAL MIXER

LONG MODIFIED RADIAL MIXER
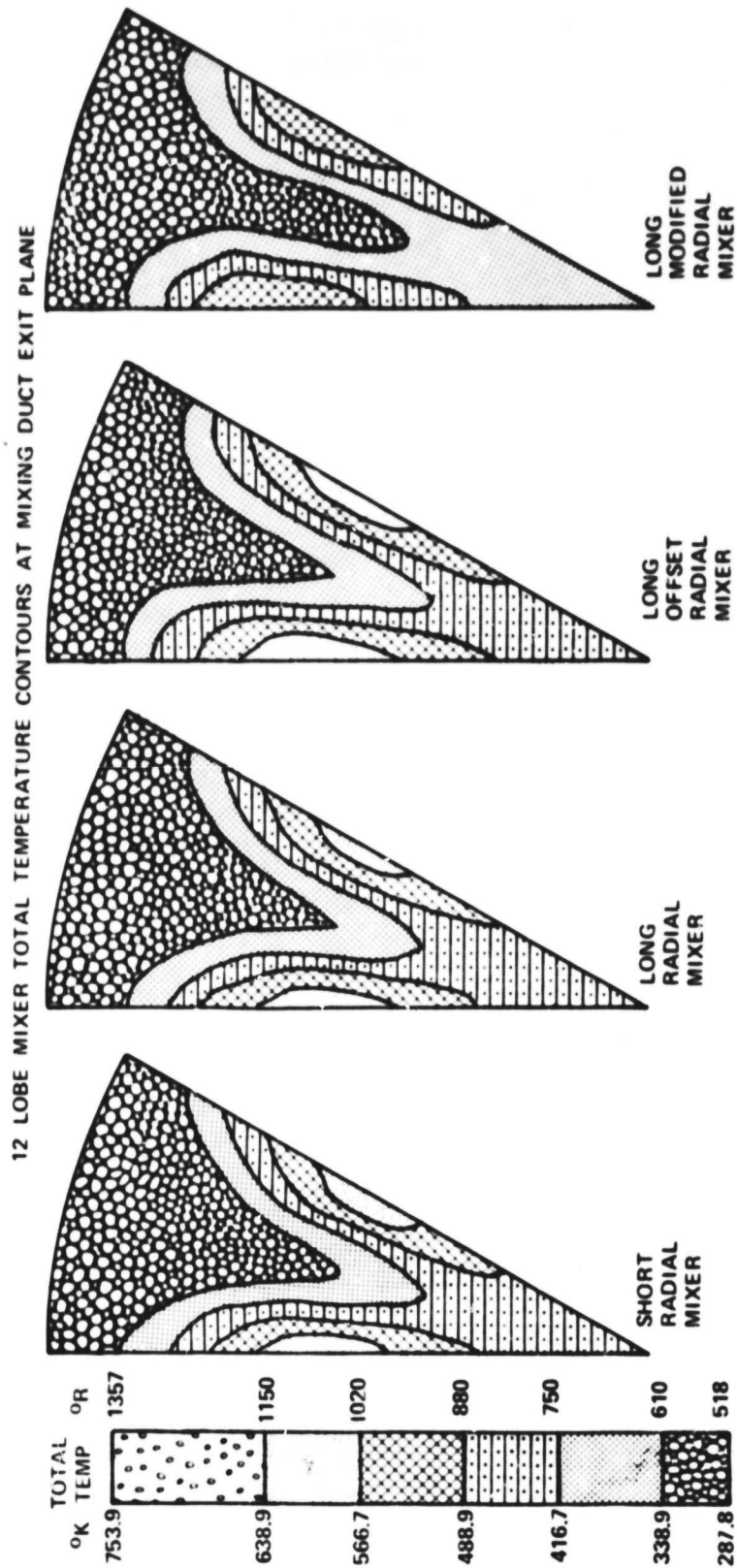
Figure 3-60. 3-D Mixing Analysis, Temperature Contours.

12 LOBE MIXER TOTAL PRESSURE CONTOURS AT MIXING DUCT EXIT PLANE

COMPOUND
NOZZLE

LONG
PARALLEL
MIXER

SHORT
PARALLEL
MIXER

TOTAL
PRESSURE
RATIO
P_T/P_{TCORE}

1.01

1.00

0.99

0.98

0.97

0.96
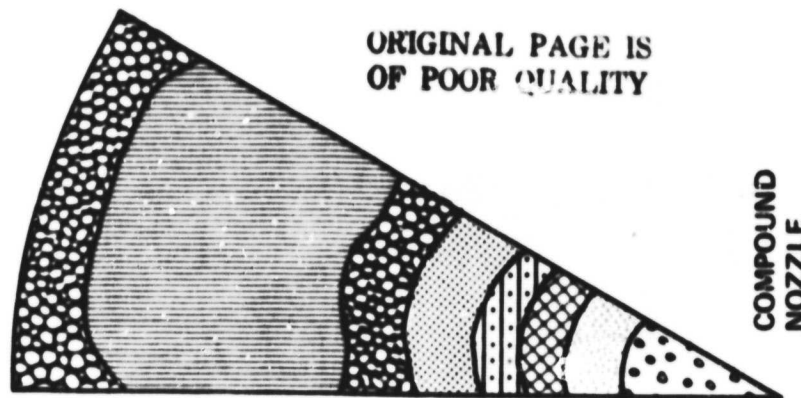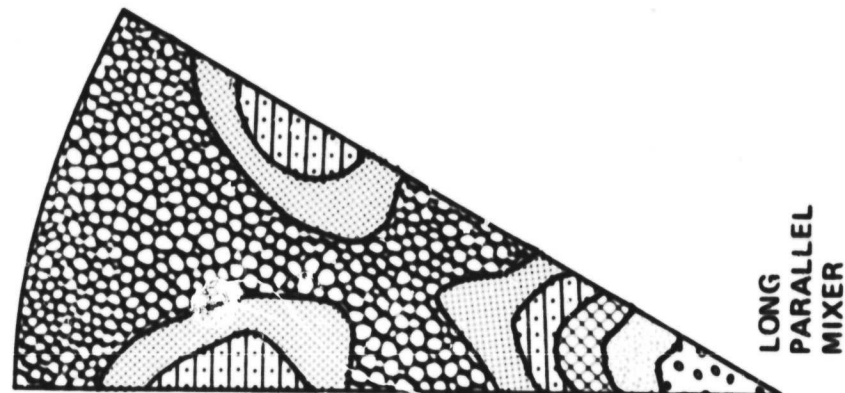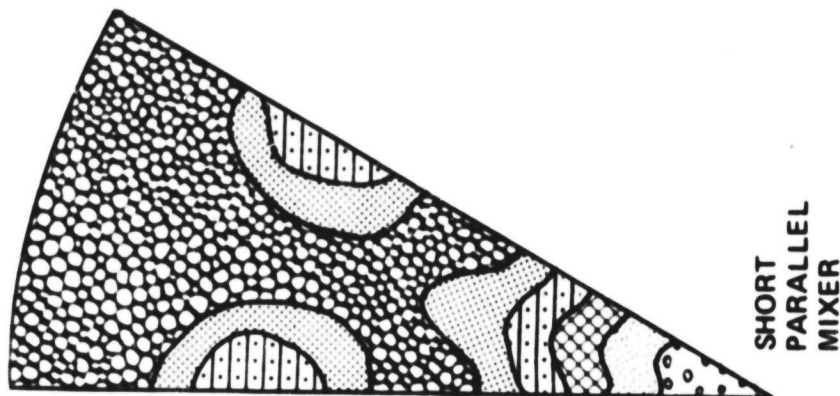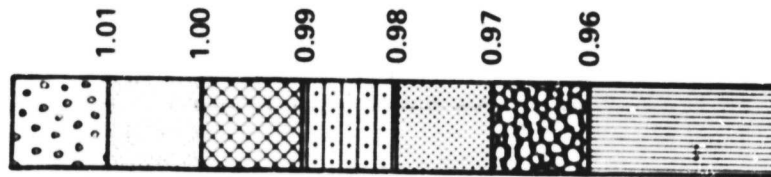
Figure 3-61.   Parallel Mixers and Compound   Predicted Pressure Contours.

12 LOBE MIXER TOTAL PRESSURE CONTOURS AT MIXING DUCT EXIT PLANE

LONG MODIFIED RADIAL MIXER

LONG OFFSET RADIAL MIXER

LONG RADIAL MIXER

SHORT RADIAL MIXER

TOTAL PRESSURE RATIO P_T/P_{TCORE}

1.01
1.00
0.99
0.98
0.97
0.96

Figure 3-62. 3-D Mixing Analysis Pressure Contours.

The velocity contours at the mixing-duct exit plane, Figures 3-63 and 3-64 show less variation since they are a composite result of the total-pressure losses and thermal-energy exchange. However, the high-taper-ratio (modified-radial) design shows substantially lower velocities. The relative peak velocities can be seen more clearly by plotting the radial-velocity profile at the circumferential centerline of a core lobe, as shown in Figure 3-65, and the circumferential velocity profile at the peak-velocity radial location, as shown in Figure 3-66. The peak velocities of the radial- and offset-radial are lower than the parallel, and the modified-radial has the lowest peak velocity. The modified, offset, and standard radial have lower bypass centerline velocities than the parallel because of a wider bypass lobe shape at this radial location.

The peak velocity decay profiles can be determined from an axial cut through the middle of a core lobe and perpendicular to the engine centerline as shown in Figures 3-67 and 3-68. The large number of decay zones for the mixers compared to the compound indicate a higher velocity decay rate for the mixers. Since the initial peak velocities varied for each configuration as shown in Table 3-11, it was more meaningful to non-dimensionalize the local peak velocity by the initial peak velocity in order to make a clearer comparison. Non-dimensionalizing the local delta velocity ($V_{peak} - V_{bypass}$) by the initial delta velocity (V_{core}) - V_{bypass}) gives a peak velocity decay rate curve as shown in Figure 3-69. The higher taper ratio (modified-radial) has the best velocity decay rate while the long-parallel has the lowest mixer decay rate. The compound nozzle has the lowest overall decay rate. In all cases it appears that the mixing-duct length is sufficient to maximize the velocity decay. In some cases it appears that the mixing duct could be substantially shorter without significantly increasing the mixing-duct-exit peak velocity.

Some average properties were calculated at the nozzle exit, even though the mixing analysis program is not set up for highly accelerating, high Mach-number regions. Average temperature and peak-velocity ratios were calculated for the configurations that were chosen for model scale testing (see Table 3-12). Calculated properties were averaged at the nozzle exit, since nozzle-exit properties would be obtained from the model testing. Integrated nozzle-exit temperatures indicate the short-parallel mixer has the highest calculated mixing while the compound nozzle has the lowest. Mixing efficiencies could not be calculated because the integrated total temperatures exceeded the 100 percent mixed value. A peak velocity-ratio term was calculated where V_1 and V_2 are the calculated unmixed velocities at the nozzle-exit. Peak velocity ratios appear to contradict the average temperatures, since the short-parallel having the highest mixing also has the highest peak velocity. This may be a result of the inadequacy of the mixing analysis program in regions of highly accelerating flow.

Figure 3-63. Parallel Mixers and Compound Predicted Velocity Contours.

94

ORIGINAL PAGE IS
OF POOR QUALITY

12 LOBE MIXER VELOCITY CONTOURS AT MIXING DUCT EXIT PLANE
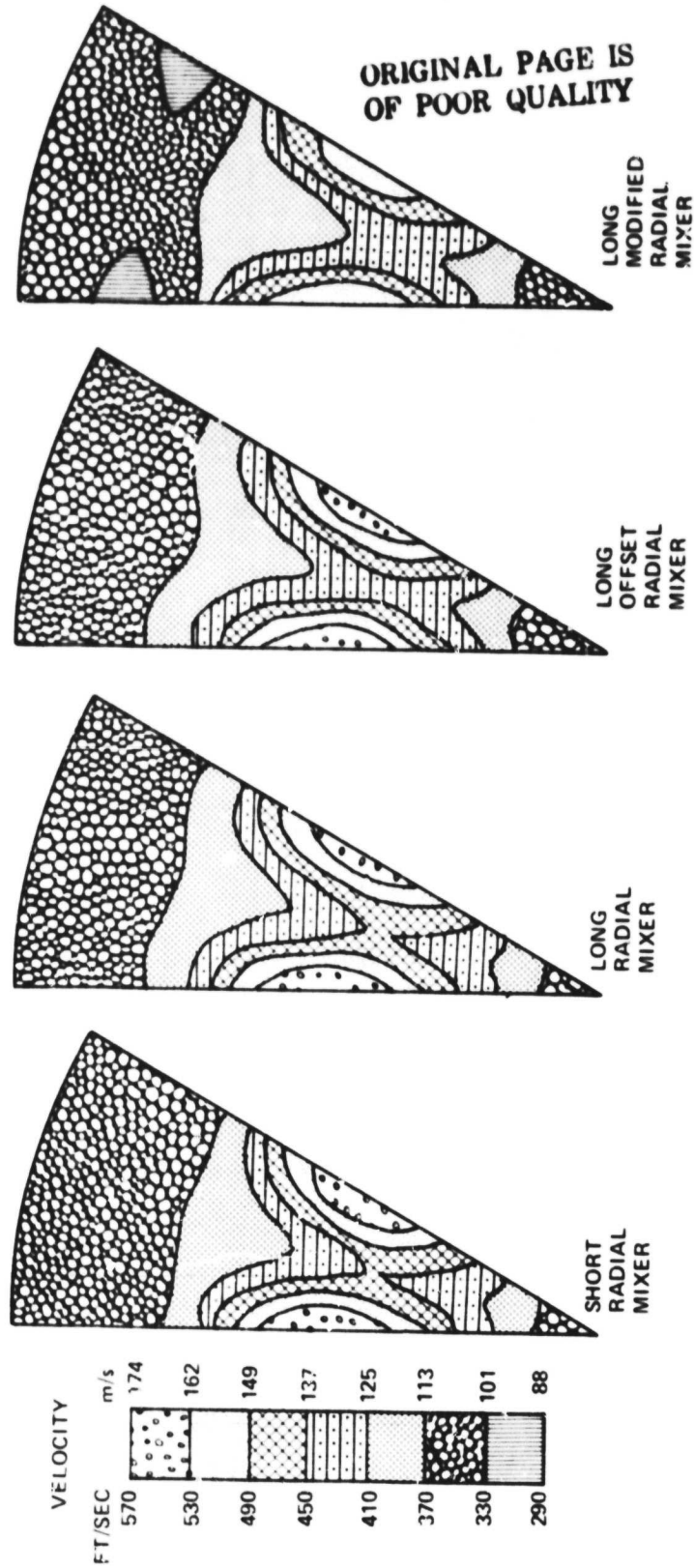
Figure 3-64. Radial and Modified Radial Mixer Lobe Predicted Velocity Contours.

95
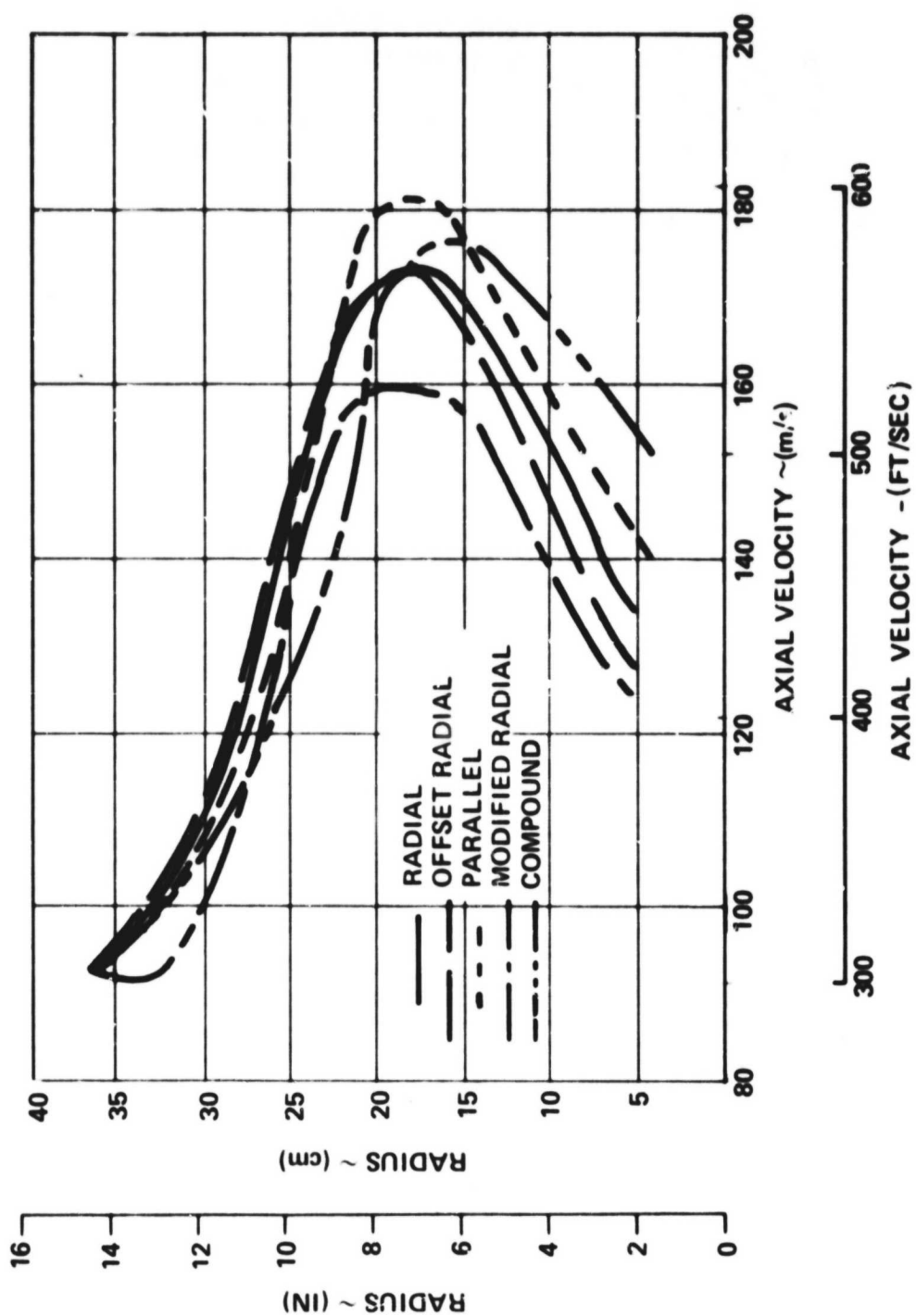
Figure 3-65. Core Centerline Predicted Velocity Profiles at Mixing Duct Exit Plane.
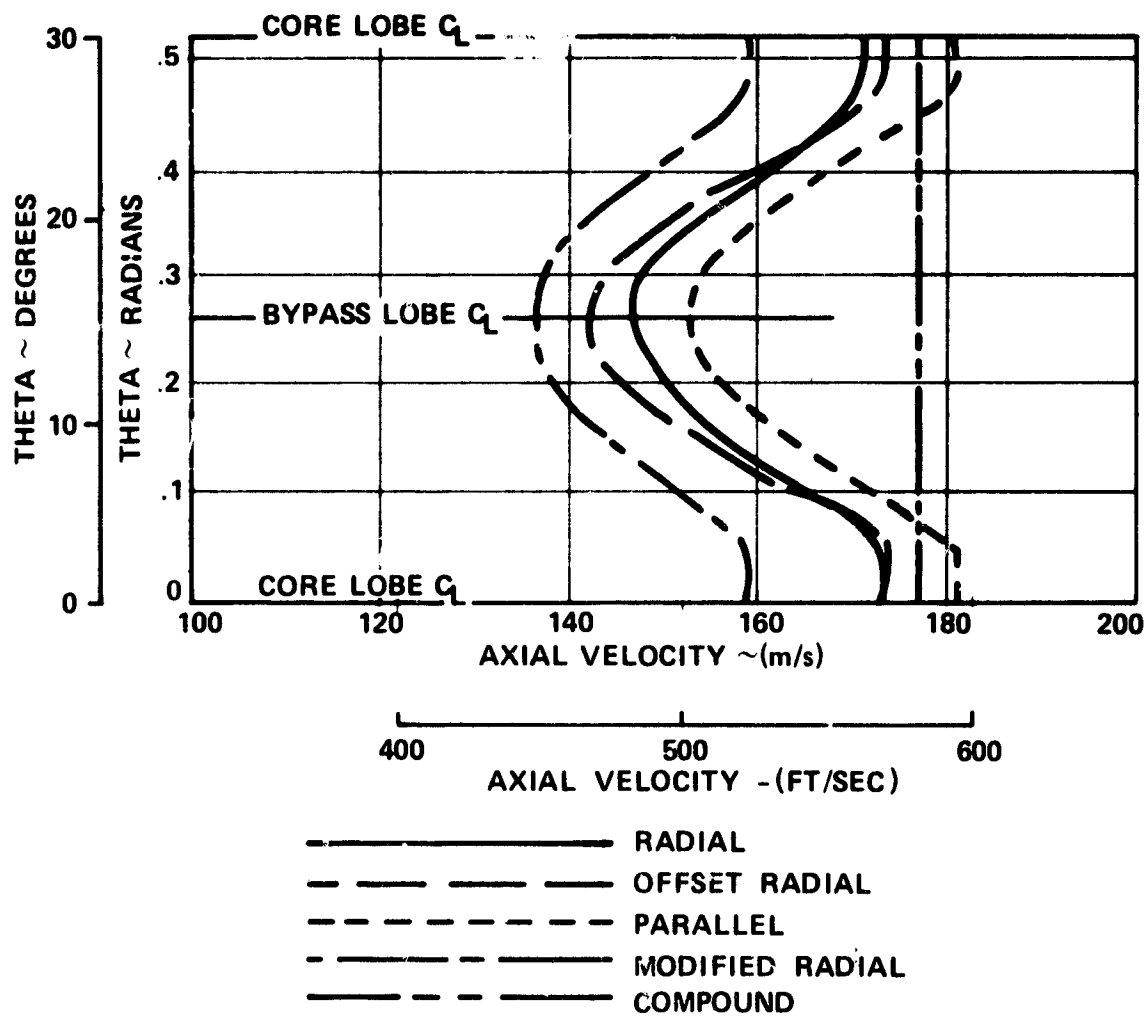
Figure 3-66.   Predicted Circumferential Velocity
Profiles at Mixing Duct Exit Plane.

12 LOBE MIXER VELOCITY PROFILE ALONG CORE LOBE CENTERLINE

LONG PARALLEL MIXER

SHORT PARALLEL MIXER

COMPOUND NOZZLE

VELOCITY

m/s	FT/SEC
233	730
210	690
198	650
186	610
174	570
162	530
149	490
125	410
101	330
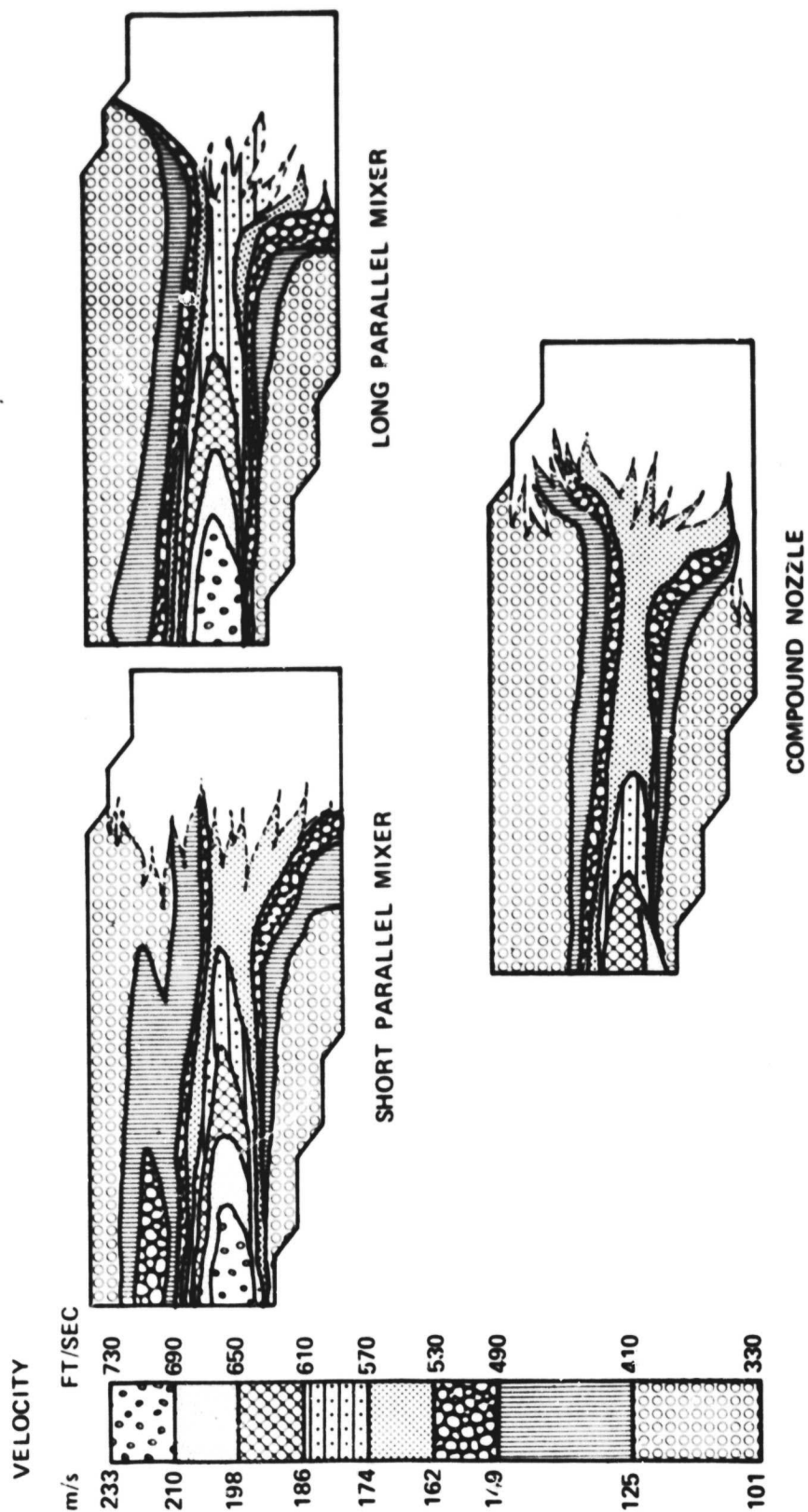
Figure 3-67.   Parallel Mixers and Compound Predicted
Axial Velocity Profiles.

98
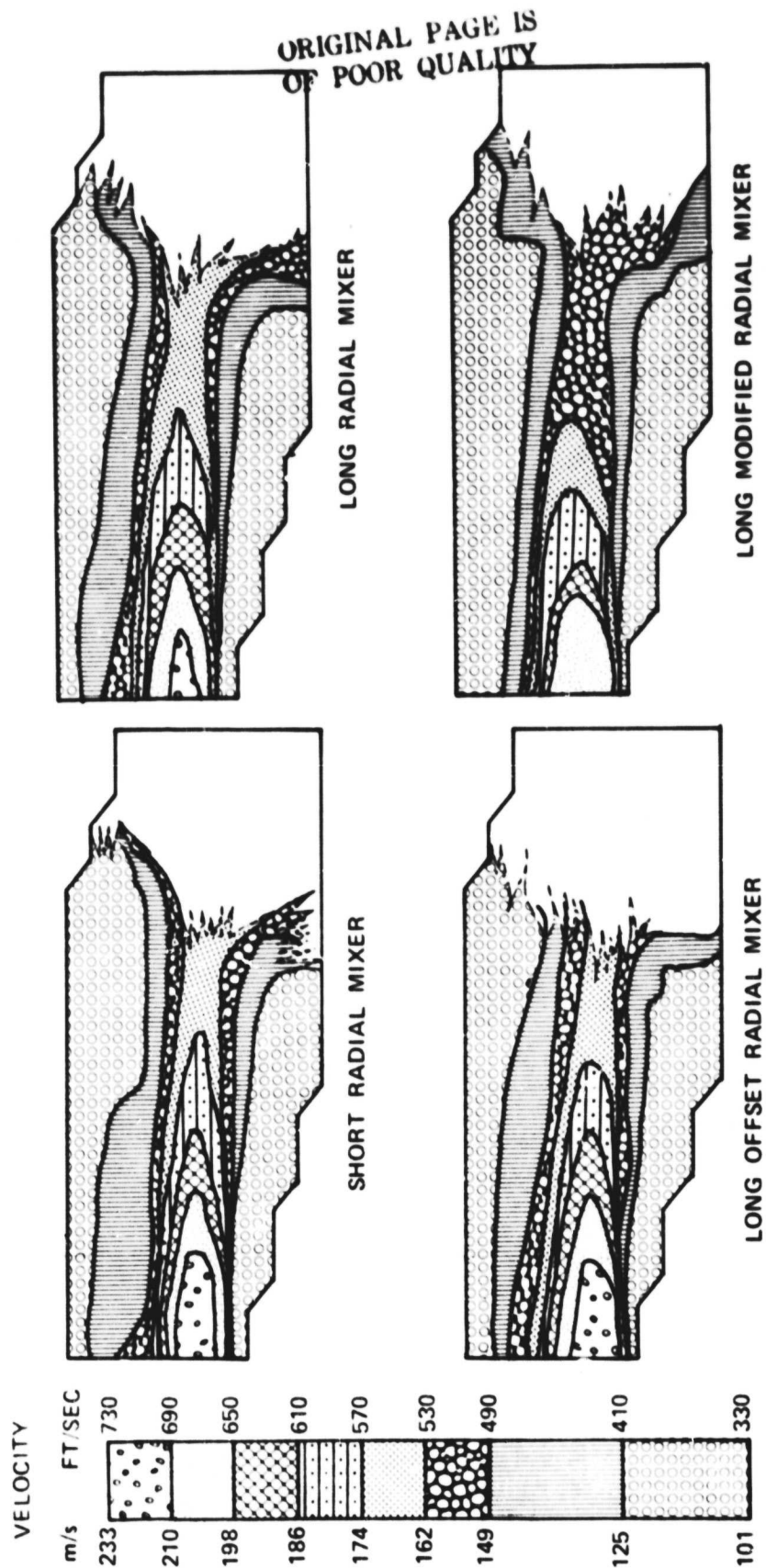
Figure 3-68. Radial and Modified Radial Mixers Predicted Axial Velocity Profiles.
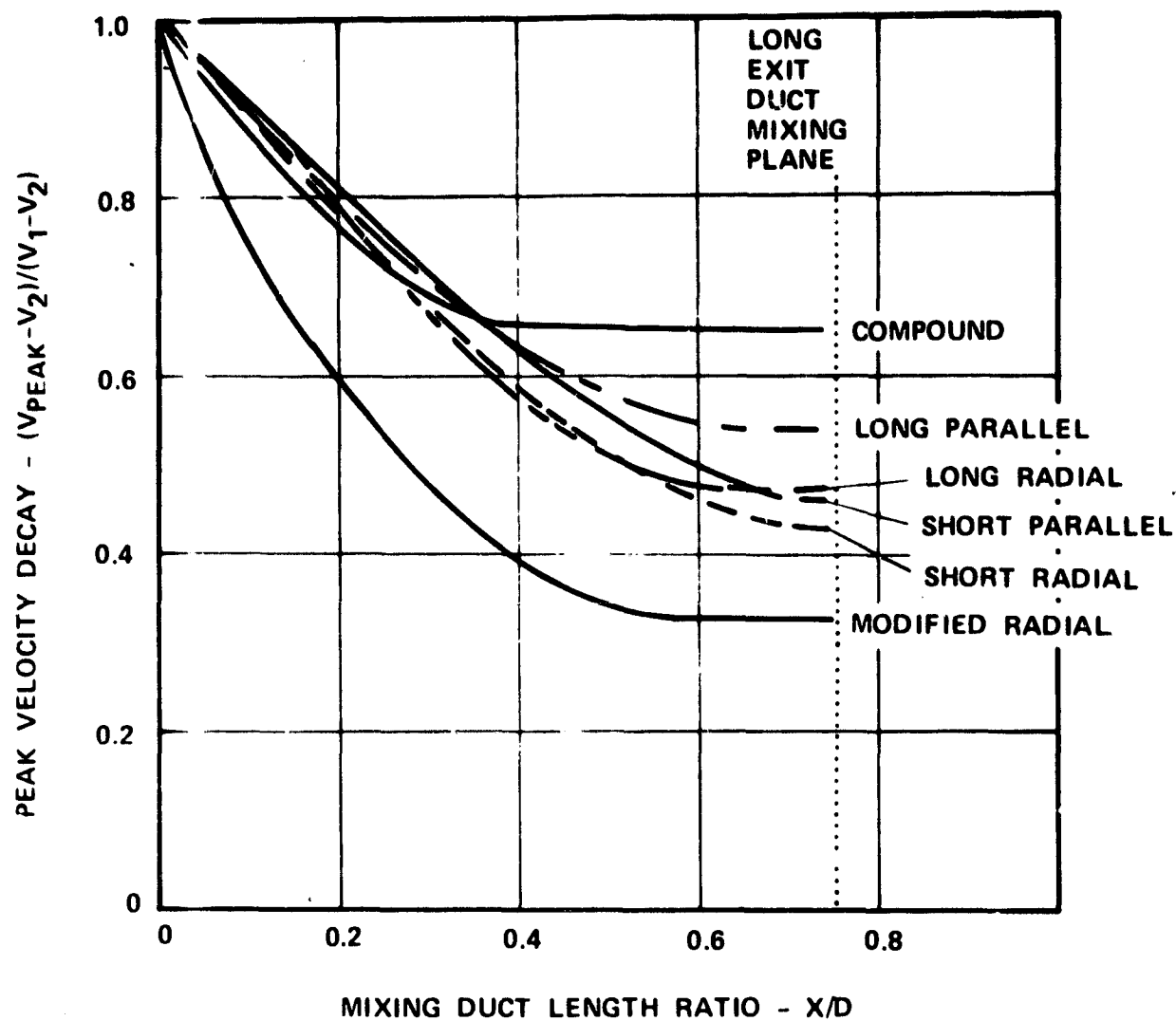
Figure 3-69. Predicted Velocity Decay Rate
Versus Mixing Duct Length Ratio.

TABLE 3-11. VARIATION IN CORE PEAK VELOCITY
AT THE MIXING PLANE.

Configuration	V_{peak}	
	m/s	FT/SEC
Compound	197.1	646.8
Short parallel	225.7	740.6
Short radial	229.0	751.2
Long parallel	230.9	757.4
Long radial	219.9	721.5
Offset radial	226.9	744.5
High taper ratio	229.6	753.3

TABLE 3-12. CALCULATED AVERAGE PROPERTIES
AT NOZZLE EXIT.

Configuration	$T_T/T_{5.2}$	$\dfrac{V_p - V_2}{\bar{V}_1 - V_2}$
Compound	0.5600	1.000
Short Parallel	0.5685	0.570
Long Parallel	0.5660	0.552
Long Radial	0.5643	0.525

SECTION IV
MODEL RIG TESTS

4.0 0.35 SCALE MODEL RIG TESTS

4.1 Test Procedures

4.1.1 Model Description and Instrumentation

Based on the empirical and theoretical analysis, four core-nozzle configurations and three mixing-duct lengths were selected for testing (see Attachment 1, Figures 6a-6c). Geometric parameters of the configurations are presented in Table 4-1 and the hardware required to build up each configuration is specified in Table 4-2. Configurations II, III and IV are illustrated in Figures 4-1 and 4-2. The model assembly drawing and individual hardware drawings are included in Fluidyne Test Report (Attachment 1, Figures 2 and 5a through 5k, respectively). One standard-compound splitter, one radial-wall mixer, and two parallel-wall mixers of differing lengths were tested with a long mixing duct. The best performing core mixer was then tested with two shorter mixing-duct lengths.

Detailed rig and model instrumentation locations are presented in Table 4-3. The bypass instrumentation consisted of four total-pressure rakes of twelve probes each, eight hub- and shroud-wall statics, and two total-temperature rakes of 4 probes each at the rig bypass charging station. This station coincided with the AiResearch bypass-rating station (STA 14). Core instrumentation at the rig core charging station (STA 5.0) consisted of four total-pressure rakes of five probes each, eight hub- and shroud-wall statics, and four total-temperature rakes of two probes each. The AiResearch core rating station (STA 5.2) was a considerable distance downstream of the rig core charging station (STA 5.0), therefore two temporary total pressure rakes of six probes each (see Attachment 1, Figure 5a) and three hub- and shroud-wall statics were located at the AiResearch core rating station (STA 5.2). Wall statics were also located axially along the plug and mixing duct. Base statics were located at the exit of the core nozzles (STA 16), while base and wall statics were located at the exit plane of the exit nozzle (STA 8). Instrumentation specifications and station locations are illustrated in Figure 4-3. Specific instrumentation details may be obtained from the model prints included in the Fluidyne Test Report (Attachment 1, Figures 5a-5k).

4.1.2 Test Matrix and Run Schedule

The run schedule for each configuration is detailed in Table 4-4. Each core nozzle (Configurations I through IV) was run with the fan shroud removed (core only at ambient temperature).

TABLE 4-1. QCGAT 0.35 SCALE MODEL EXHAUST
SYSTEM TESTS TEST CONFIGURATIONS.

No. Mixer Configuration	X/D	PEN	AR	TR	SR	L cm	L (In.)
I Standard Compound	0.752	-	-	-	-	39.83	15.68
II Short Parallel	0.752	0.77	3.5	1.0	1.24	39.83	15.68
III Long Parallel	0.752	0.77	3.5	1.0	1.24	49.99	19.68
IV Long Radial	0.752	0.73	3.14	1.8	1.00	49.99	19.68
V Short Parallel	0.501	0.77	3.5	1.0	1.24	39.83	15.68
VI Short Parallel	0.626	0.77	3.5	1.0	1.24	39.83	15.68

$N = 12$

$\phi = 0.26$ rad (15°)

$R_1 = 14.35$ cm (5.65 In.)

TABLE 4-2. CONFIGURATION DEFINITION.

Config.	Core Nozzle	Centerbody	Duct Spacer	Exit Nozzle
I	Splitter (SKP17162)	Short (SKP17160)	-	Long (SKP17167)
II	Short Parallel (SKP17163)	Short (SKP17160)	-	Long (SKP17167)
III	Long Parallel (SKP17168)	Long (SKP17169)	X (SKP17172)	Long (SKP17167)
IV	Long Radial (SKP17170)	Long (SKP17169)	X (SKP17172)	Long (SKP17167)
V	Short Parallel (SKP17163)	Short (SKP17160)	-	Short (SKP17166)
VI	Short Parallel (SKP17163)	Short (SKP17160)	X (SKP17172)	Short (SKP17166)
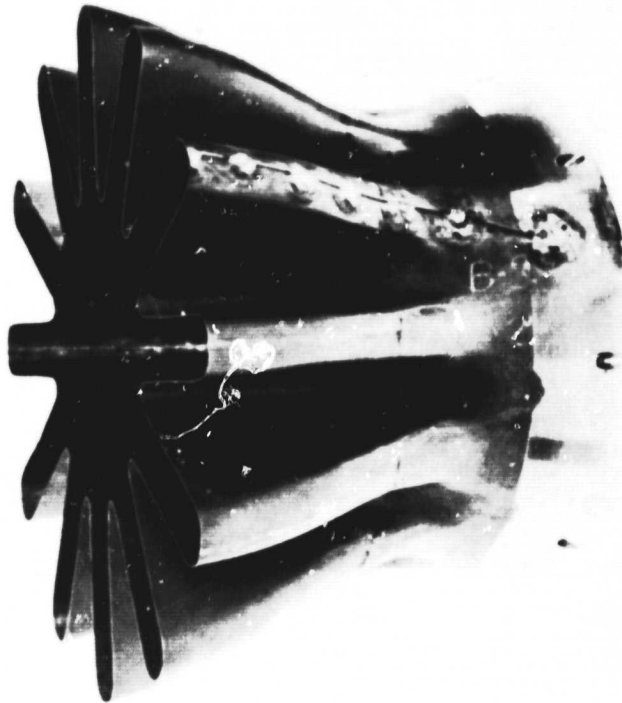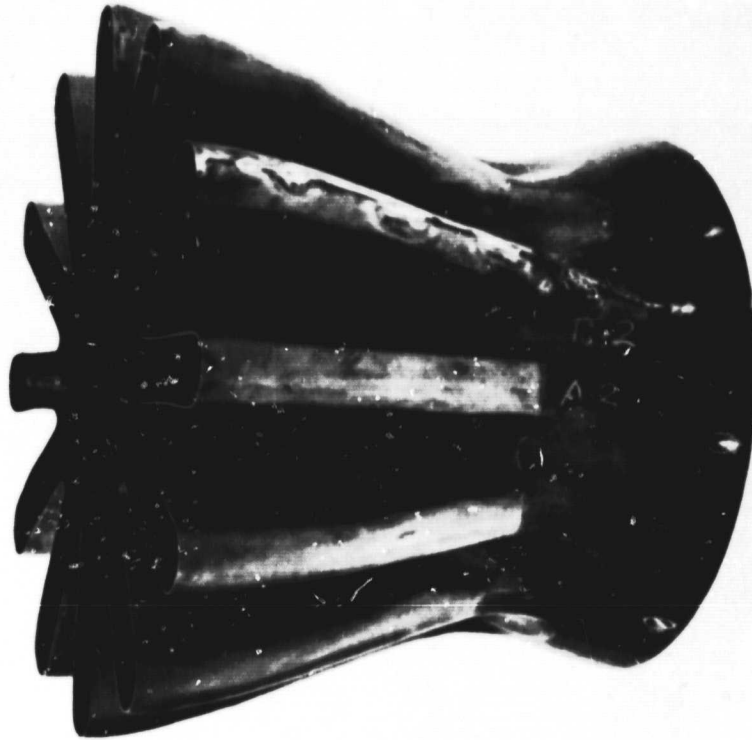
Figure 4-1. Parallel Mixer Models Configurations II, III, V, and VI.

105

MP-63963

Figure 4-2.   Radial Mixer Model Configuration IV.

106

TABLE 4-3. DETAILED INSTRUMENTATION LOCATION.

Axial Station cm	Axial Station (In.)	Cycle Station	Radial Location Rad	Radial Location Deg.	Radius R cm	Radius R (In.)	Description	No. Probes
105.16	41.4	5.2	0.52, 1.66	10, 210	12.67, 14.85, 16.75, 18.46, 20.02, 21.46	(4.990), (5.848), (6.595), (7.266), (7.880), (8.449)	Two removable core total pressure rakes of six probes each	12
40.89	16.1)	5.0	1.05, 2.62, 4.19, 5.76	60, 150, 240, 330			Four existing core total pressure rakes of five probes each	20
35.05	(13.8)	14.0	0, 1.57, 3.14, 4.71	0, 90, 180, 270			Four existing bypass total pressure rakes of twelve probes each	48
3.15	1.24)	5.0	0, 1.57, 3.14, 4.71	0, 90, 180, 270			Four core total temperature rakes of two probes each	8
35.05	(13.8)	14.0	2.62, 5.76	150, 330			Two bypass total temperature rakes of four probes each	8
105.16	41.4	5.2	0.87, 4.01	50, 210			Core shroud wall statics	7

Plug 1		Plug 2			Cycle Station	Rad	Deg.	cm	(In.)	Description	No. Probes
105.16	(41.4)	105.16	(41.4)		—		0, 0			Core centerbody wall statics	12
116.84	(46.0)	116.84	(46.0)				0, 0				
127.00	(50.0)	127.00	(50.0)				0, 0				
142.24	(56.0)	142.24	(56.0)			0, 0.26	0, 15				
147.32	(58.0)	152.40	(60.0)			0, 0.26	0, 15				
154.94	(61.0)	162.56	(64.0)			0, 0.26	0, 15				
162.56	(64.0)	172.72	(68.0)			0, 0.26	0, 15				
177.80	(70.0)	187.96	(74.0)				0, 0			Core centerbody base	
142.24	56.0)				6.0	0.70, 3.14	4, ?	21.72, 21.72	(8.553), (8.553)	Compound nozzle base statics	2

Mixer 'A'		Mixer 'C' and 'D'									
142.24	(56.0)	152.40	(60.0)		6.0	0.70, 3.95	40, 220.6	34.72, 24.81	(13.670), (9.766)	Mixer nozzle base statics	2
35.05	13.8)				14.0	0.52, 2.09, 3.66, 5.24	30, 120, 210, 300			Existing bypass adapter hub and shroud statics, four on each wall	8
40.89	16.1)				5.0	0, 1.57, 3.14, 4.71	0, 90, 180, 270			Four existing core hub wall statics, manifolded together	4
40.89	(16.1)				5.0	0.52, 2.09, 3.66, 5.24	10, 120, 210, 300			Four existing core shroud wall statics	4

Mixer 'A'		Mixer 'C' and 'D'				Rad	Deg.				
142.24	(56.0)	152.40	(60.0)		—	0, 0.26	0, 15			Mixing duct wall statics	10
147.32	(58.0)	157.48	(62.0)			0, 0.26	0, 15				
154.94	(61.0)	165.10	(65.0)			0, 0.26	0, 15				
162.56	(64.0)	175.26	(69.0)			0, 0.26	0, 15				
177.80	(70.0)	187.96	(74.0)			0, 0.26	0, 15				

Duct Exit 1		Duct Exit 2									
223.52	(88.0)	243.84	(96.0)		8.0	0, 3.14	0, 180			Exit nozzle base statics	2
223.52	(88.0)	243.84	(96.0)		8.0	1.57, 4.71	90, 270			Exit nozzle wall statics	2

107
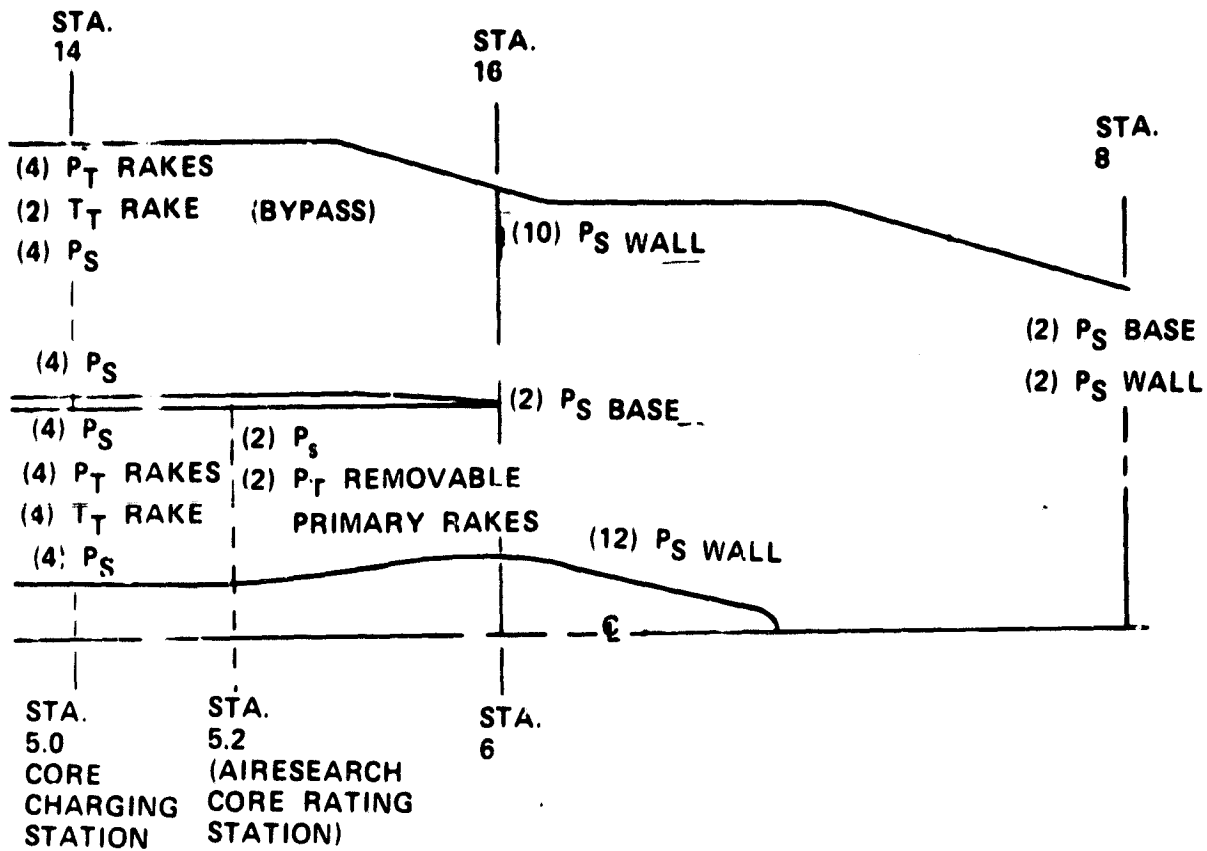
Figure 4-3. Instrumentation Locations.

TABLE 4-4.   TEST RUN SCHEDULE.

Configuration	Core Only	Dual Flow	Pressure Ratio(1) Schedule	Exit Survey	No. Data Points	Acoustic Survey
I	X		1		6	
		X	3		2	
		X	4		2	X
		X	4	X	2	
II	X		2		3	
		X	3		2	
.		X	4		2	X
		X	4	X	2	
III	X		2		3	
		X	3		2	
		X	4		2	X
		X	4	X	2	
IV	X		2		3	
		X	3		2	
		X	4		2	X
		X	4	X	2	
V		X	3		2	
		X	4		2	X
		X	4	X	2	
VI		X	3		2	
		X	4		2	X
		X	4	X	2	
I		X	5		14	
II		X	6		14	
II		X	7		1	
		X	8	X	3	
				TOTAL	83	

(1) See Table 4-5

109

Each configuration was then run with both streams at ambient temperature for the sea-level-static and cruise-design-point pressure ratios. Following this, the core stream was heated and each configuration was rerun with dual flow. The total temperature split for the dual flow was set to match the desired full-scale engine value. During one dual-flow hot run, the performance data were recorded at the beginning of the run, and acoustic data were recorded during the remainder of the run. This dual-flow hot run was designated the primary performance run. Another separate dual-flow hot run was made with the exit-nozzle survey rake. Installed rake interference effects were anticipated, thus leaving some question about the absolute level of the performance. Both the acoustic and survey runs lasted for approximately one to one and one-half minute.

The tested pressure-ratio schedules differed slightly from the test plan. The tested schedule is shown in Table 4-5. The desired pressure-split range could not be obtained with the compound splitter due to unchoking of the flowmeter at the low-pressure ratios and choking of the core stream in the rig adapter at the highest pressure ratios. The desired range was obtained with the compound mixer in the high-pressure-ratio end due to its lower core flow requirements.

4.1.3 Acoustic Test Setup

Acoustic testing of the QCGAT scale model nozzle configurations was conducted at the Fluidyne Engineering Corporation Medicine Lake hot flow test facility. Acoustic testing was conducted to provide a comparison of the relative noise levels and directivities of the nozzle configurations under consideration. This information was used, along with the aerodynamic performance information gained during the testing, in the selection of the final nozzle configuration for the QCGAT engine.

The acoustic test area was located in the area outside of, and adjacent to the mixed-flow test facility. The test area was bounded on three sides by concrete block walls and, as a result, the absolute sound pressure levels measured in this area were questionable. The test was valid however, in providing comparison of the noise levels on a relative basis. Six microphone locations were utilized for measurement of the noise directivity levels. The microphones were located at azimuth angles of 0.26, 0.35, 0.52, 0.70, 0.87 and 1.05 radians (15, 20, 30, 40, 50, and 60 degrees) from the nozzle exhaust centerline at a radius of 2.44 meters (eight feet) from the nozzle exit plane.

The microphones used were Bruel and Kjaer type 4133 (free field) with the microphone diaphragm oriented for normal incidence to the sound wave. The microphone height was located in the horizontal plane through the nozzle centerline.

110

TABLE 4-5. PRESSURE RATIO AND TEMPERATURE SPLIT SCHEDULE.

Schedule	Core PR	Bypass PR	T_T Split
1: 6 points	1.05	–	1.0
	1.10	–	1.0
	1.15	–	1.0
	1.20	–	1.0
	1.25	–	1.0
	1.30	–	1.0
2: 3 points	1.2	–	1.0
	1.35	–	1.0
	1.5	–	1.0
3: 2 points	1.392	1.426	1.0
	2.396	2.419	1.0
4: 2 points	1.392	1.426	2.49
	2.396	2.419	2.62
5: 14 points	1.2	1.2	2.49
	1.3	1.2	2.49
	1.4	1.2	2.49
	1.5	1.4	2.49
	1.6	1.4	2.49
	1.8	1.6	2.49
	1.8	1.6	2.49
	2.0	2.0	2.49
	2.2	2.0	2.49
	2.0	2.4	2.49
	2.2	2.4	2.49
	2.6	2.4	2.49
6: 14 points	1.2	1.2	2.49
	1.3	1.2	2.49
	1.5	1.4	2.49
	1.6	1.4	2.49
	1.4	1.6	2.49
	1.6	1.4	2.49
	1.8	1.6	2.49
	2.0	1.6	2.49
	1.8	2.0	2.49
	2.0	2.0	2.49
	2.5	2.0	2.49
	2.2	2.4	2.49
	2.6	2.4	2.49
	3.0	2.4	2.49
7: 1 point	2.5	2.0	1.0
8: 3 points	2.5	2.0	1.5
	2.5	2.0	2.0
	2.5	2.0	2.5

The microphones were located on the side of the nozzle centerline farthest away from the major reflecting wall such that the reflected signal would be subject to increased attenuation due to spherical divergence of the sound wave.

A schematic diagram of the acoustic test layout and the location of the microphones relative to the reflecting surfaces in the test area is shown in Figure 4-4.

Prior to actual acoustic testing, the test area required certain modifications in order to provide an area suitable for testing. Double stacked concrete culverts with an approximate 1.2 meters by 1.2 meters (4 feet by 4 feet) opening in the lower culvert are normally used as an exhaust deflector. A single culvert is located next to the double stacked culvert. These culverts are located immediately aft of the test cell.

For the acoustic testing, these culverts were removed from the immediate test area to accommodate the required microphone locations. The single culvert was completely removed from the test area. The double-stacked culvert was moved rearward as far as possible to the position shown in Figure 4-4. This culvert was used in this position to provide deflection of the exhaust stream.

A fiberglass lined plywood barrier was constructed across the test cell door opening. This door opening is 1.8 meters (6 feet) wide and under normal operation the nozzle exhaust exits through this opening. The intent of the barrier wall was to isolate the jet noise produced by the scale model nozzles from the test cell noise sources.

A photograph of the acoustic test setup with the acoustic isolation barrier across the door opening is also shown in Figure 4-4.

4.1.3.1 Acoustic Data Recording

Each scale-model nozzle-configuration was tested per the test run schedule of Table 4-4. Acoustic test surveys were conducted only at the pressure ratios of schedule No. 3. Each specified acoustic data point was operated continuously until the noise data for that condition was completed. The noise data of each microphone location was recorded on a Kudelski Nagra IV, dual channel tape recorder. Data was recorded for a minimum of 15 seconds at each microphone location using a tape speed of 38.1 cm/s (15 inches per second).

112

TWO STORY CONCRETE BLOCK BLDG.
(INTERIOR)

DOUBLE STACKED
CONCRETE CULVERT
FLOW DIVERSION

CONCRETE
SLAB

MICROPHONE
LOCATIONS

1.05 RAD
(60°)

0.26 RAD
(15°)

2.4 m
(8.0')

1 2 3 4 5 6

6.1 X 6.1 m
(20' X 20')
CORRUGATED
BLDG.

ACOUSTIC
ENCLOSURE
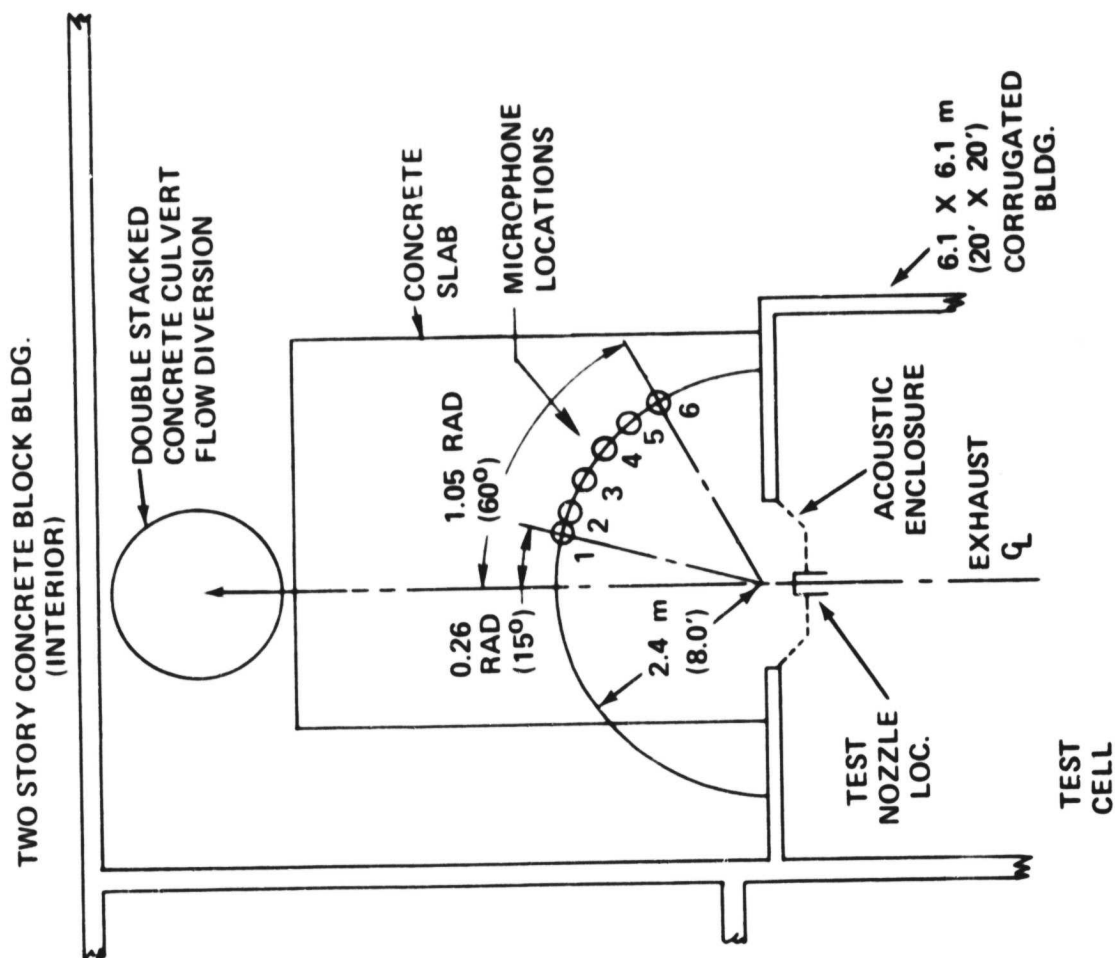
EXHAUST $\mathcal{C}_L$

TEST
NOZZLE
LOC.

TEST
CELL

Figure 4-4. QCGAT Scale Model Exhaust System Acoustic Setup.

113

MP-62956

Prior to each test sequence, the ambient noise of the test area was recorded at each microphone location. Individual measurements of ambient temperature, ambient pressure, relative humidity, wind velocity and wind direction were recorded immediately prior to and after each test sequence.

4.1.3.2 Acoustical Instrumentation

The acoustical instrumentation and equipment utilized during the acoustic testing are listed in Table 4-6.

4.1.3.3 Acoustic Test Schedule

As shown in Table 4-4, acoustic data was taken for each nozzle configuration at pressure ratio schedule No. 3. Table 4-5 shows the desired core and bypass pressure ratios and temperature split for this test schedule.

Prior to actual testing, it was determined that the air temperature in the reservoir tank used for supplying bypass air to the nozzle could vary from run to run due to pump work input and change in ambient air temperature. The resultant core and bypass flow velocities at the rating station, for a constant core and bypass pressure ratio, could vary significantly for each nozzle configuration tested.

As a result, it was decided that maintaining similar core and bypass velocities at the nozzle rating station was more important to the acoustic test results than maintaining a given pressure ratio schedule.

Consequently, the bypass rating station temperature was monitored at the beginning of an acoustic run. Since the core temperature was being set to a given temperature split between the two streams, both the core and bypass pressure ratios were adjusted to account for changes in tank temperature. This resulted in maintaining a relatively constant velocity at the nozzle rating station for each tested nozzle configuration.

4.1.3.4 Acoustic Data Reduction

Reduction and analysis of the acoustic data taken at the Fluidyne test facility was performed at the AiResearch acoustics laboratory. Data reduction was performed by 1/3 octave frequency analysis with an acoustic instrumentation package utilizing on-line computer capability. A schematic diagram of the acoustic data reduction and analysis system is shown in Figure 4-5.

The resultant acoustic data for each nozzle configuration at both the sea level static and cruise operating conditions are contained in Appendix D. The resultant acoustic data shows

114

TABLE 4-6. ACOUSTICAL INSTRUMENTATION.

- o Condenser Microphones, (6), B&K Type 4133

- o Microphone Preamplifiers, (6), B&K Type 2619

- o Portable Tape Recorder, (1), Kudelski Nagra IV-SJ

- o Sixteen Channel Microphone Power Supply (1), B&K Type 226

- o Condenser Microphone, (1), B&K Type 4145

- o Battery Cathode Follower, (1), B&K Type 2630

- o Pistonphone Calibrator, (1), B&K Type 4220

- o Microphone Cables, (6)

- o Microphone Windscreens, 1.27 cm (1/2 inch), (6), B&K Type UA0459

- o Psychrometer - Sling, (1) Taylor Model 1323

- o Wind meter, (1), Weather-Measure Corporation W121-SD

- o Microphone stands, (6)

```
┌─────────────────┐
│     ANALOG      │
│  TAPE RECORDER  │
└─────────────────┘
         │
         ▼
┌─────────────────┐
│    B&K 3347     │
│   THIRD-OCTAVE  │
│ REAL-TIME ANALYZER │
└─────────────────┘
         │
         ▼
┌─────────────────┐
│    B&K 183      │
│   INTERFACE     │
│   TO TEK 31     │
└─────────────────┘
         │
         ▼
┌─────────────────┐                              ┌──────────────────┐
│    TEK 31       │◄─────────────────────────────│   TEK 4921       │
│  CALCULATOR     │                              │   FLEXIBLE       │
└─────────────────┘                              │  DISK MEMORY     │
         │                                        └──────────────────┘
         ▼                                                ▲
┌─────────────────┐    ┌─────────────────┐
│   TEK 4014-1    │───►│    TEK 4923     │
│    GRAPHIC      │    │    DIGITAL      │
│   TERMINAL      │    │  TAPE RECORDER  │
└─────────────────┘    └─────────────────┘
         │
         │          ┌─────────────────────┐       ┌──────────────┐
         ├─────────►│  INTERTRAN 951A     │◄─────►│  CYBER 174   │
         │          │  MODEM 4300 BPS     │       │  COMPUTER    │
         │          └─────────────────────┘       └──────────────┘
         ▼
┌─────────────────┐
│   TEK 4631      │
│ HARD COPY UNIT  │
└─────────────────┘
```
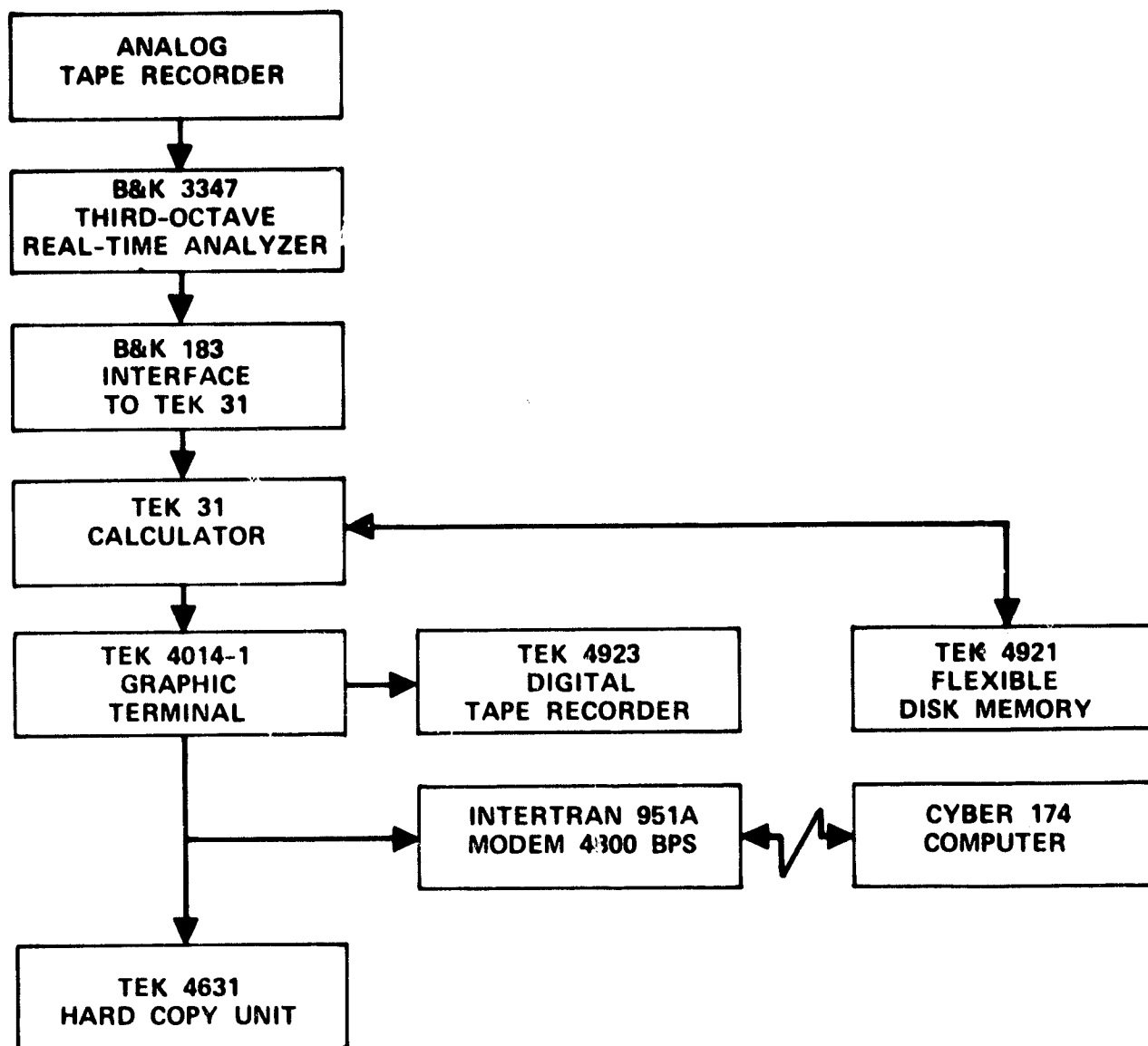
Figure 4-5.   Acoustic Data Analysis System.

conclusively that scale model configuration II provided the lowest relative noise levels of the six nozzle configurations tested.

4.1.4 Nozzle Exit Survey

The exit survey rake is shown in Figure 4-6 and the mounting structure is shown in Figure 4-7. The survey system was free-standing with no connection to the rig or model hardware. The rake was rotated about the nozzle centerline by an actuator and ring-gear system. The survey rake can be actuated through a 6.28 radian (360 degree) arc in increments of 0.017 to 0.279 radians (one to sixteen degrees). For this test it was set for 0.052 radian (three-degree) increments over a 0.523 radian (30-degree) segment. The control unit was activated by a manual stepping switch with tracking of the location provided by a digital readout. The survey rake sensors consisted of 15 thermocouples, 6 total-pressure probes, and 3 static-pressure taps (a pitot-static at the centerline of the survey rake and 2 wall statics on the nozzle-exit shroud).

The survey-rake system was mounted on an adjustable platform which allowed accurate locating of the rake relative to the nozzle. The survey-rake initial position was horizontal; therefore, the nozzle-exit-wall statics were at 1.57 and 4.71 radians (90 and 270 degrees). These were used as location points to aid in aligning the rake. The rake-centerline static-pressure tap was aligned in the same axial plane as the wall statics. The same alignment procedure was used for each configuration.

A survey run consisted of bringing the rig flow system up to the run condition and allowing the flow to stabilize. Perform-ance and survey data were recorded for the first rake location, the temperatures were recorded on a digital printer, and the pressures were recorded by photographing a manometer board. Once the photograph was taken, the controller manual stepping switch was activated. About three seconds were required for the rake to reach its new position as indicated by the controller digital readout. Approximately five seconds elapsed from the time the rake was in its new position until the new picture was taken. Visual observation of the mercury manometers indicated that pres-sure stabilization occurred within approximately one second after the rake reached each new position.

4.2 Data Reduction

4.2.1 Model Inspection

An enlarged end view tracing (10X scale) of each mixer core nozzle was made with a side view tracing machine. Each lobe area bounded at the hub by the plug radius was integrated with a digiti-zer machine, and lobe hub radii were inspected and averaged (see

117
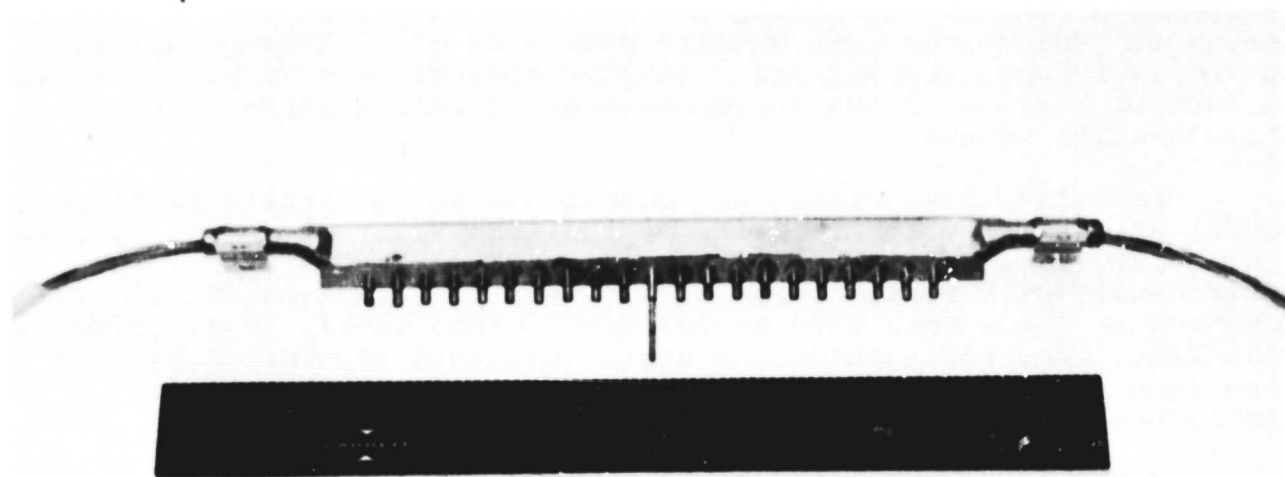
Figure 4-6. Exit Survey Rake.

118

Figure 4-7. Nozzle exit
Survey Rake Mounting
Structure.

119
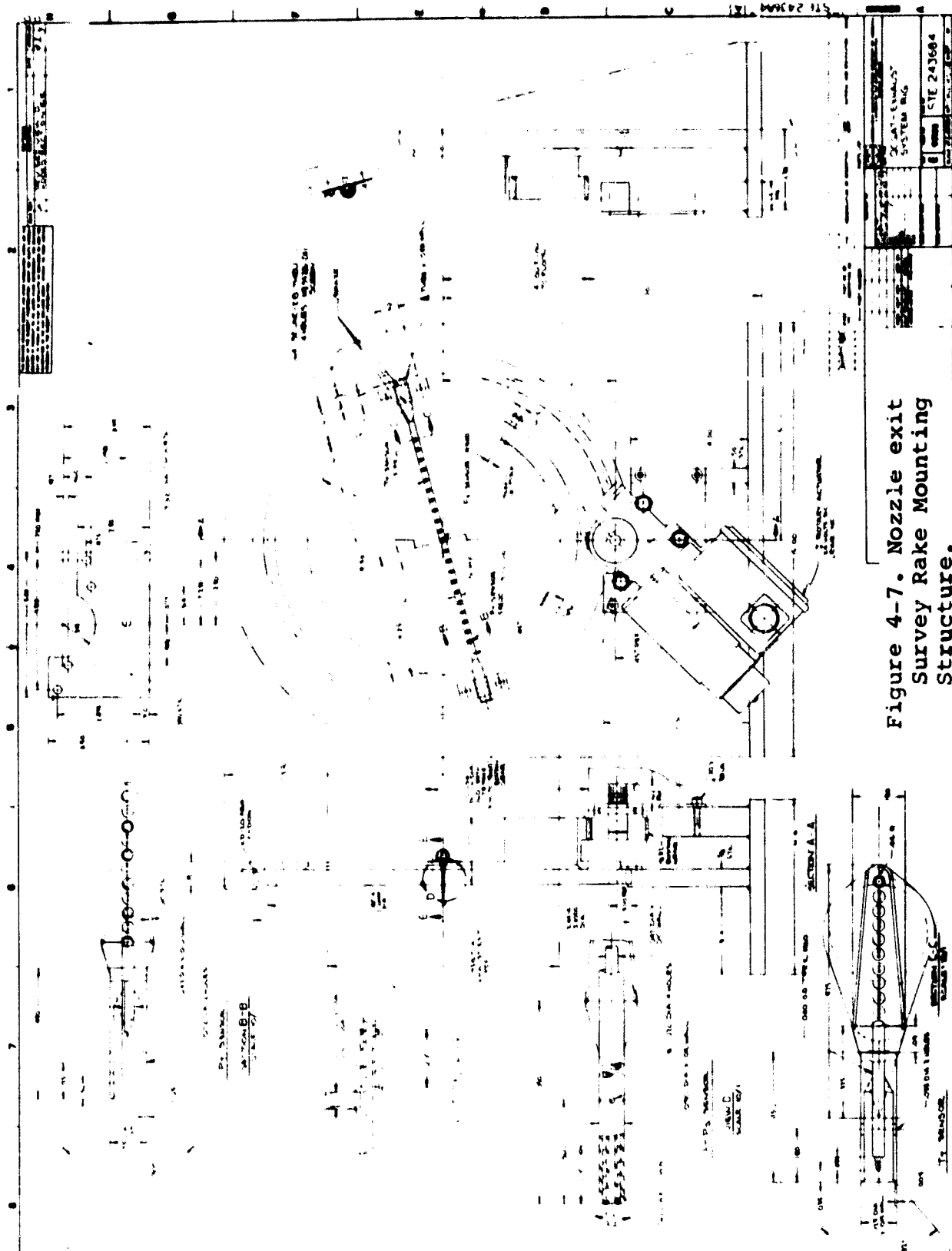
Table 4-7). If interference with the plug radius occurred, an incremental area was calculated based on the plug radius and average lobe-hub radius. This delta assembly area was added to the summation of the lobe integrated areas to obtain the assembled mixer core-nozzle exit areas.

Bypass-nozzle exit areas were obtained by subtracting the core-nozzle exit area and trailing-edge blockage area from the total mixing-plane area. The mixing-plane area dimensions conformed to blueprint specifications since the plug radius and fan-shroud radius conformed to specifications. The trailing-edge blockage was calculated from the print by the following:

$$A_{BLOCKAGE} = (PERIMETER)(THICKNESS)$$

The splitter core-nozzle area was initially inspected at four diameters; but, due to some asymmetry which occurred when the static pressure lines were soldered, it was reinspected at 18 diameters [every 0.1745 radians (10 degrees)] (Table 4-8).

The final inspected mixing plane areas used in the data reduction are presented in Table 4-9.

Nozzle-exit diameters were inspected at four locations. The inspected area for both exit shrouds (Drawings SKP17166 and SKP17167) was 320.947 cm^2 (49.747 in^2) for the model or 2619.99 cm^2 (406.10 in^2) full-size. This was essentially the same as the drawing specified area of 320.896 cm^2 (49.739 in^2) model scale or 2619.3 cm^2 (406.0 in^2) full scale.

Mixer-core lobe shroud-exit-diameter inspections were made at the rig site for two purposes. The first reason was to verify the core areas calculated with the effect of the plug interference when the mixers were installed. The second reason was to determine if any permanent area change occurred after having run several hot runs. Inspected diameters are shown in Table 4-10. Average delta diameters between installed and uninstalled mixers matched the estimated results within 0.254 cm (0.100 in). This is within 0.25 percent of the core area. Therefore, the core areas as calculated earlier were used as installed areas. After several hot runs, each mixer was removed and allowed to cool. Lobe shroud diameters were measured and compared to the initial uninstalled condition (see Table 4-10). All mixer lobe shroud diameters decreased slightly after having been run hot. The estimated area change was less than 0.36 percent. Geometric areas were not corrected to account for this small thermal shift.

120

TABLE 4-7.   INSPECTION DATA SCALE MIXER CORE NOZZLE.

Configura-tion	Lobe	Area Cm²	(In.²)	$R_{Lobe\ Hub}$ Cm	(In.)	Notes
Mixer C (SKP17160)	1	13.677	(2.130)	5.011	(1.973)	$\Delta R_{interference}$ 5.027 (1.979) -
	2	13.612	(2.110)	4.940	(1.945)	4.971 (1.957) = 0.056 Cm (0.022 in.)
	3	13.761	(2.133)	4.953	(1.950)	
	4	14.212	(2.203)	4.938	(1.944)	$A_{F.S.}$ = 1376.96 Cm² (213.43 In.²)
	5	13.948	(2.162)	4.935	(1.943)	
	6	14.187	(2.199)	4.925	(1.939)	$\Delta A = \pi\,(1.979^2 - 1.957^2)$
	7	14.045	(2.177)	5.014	(1.974)	
	8	13.909	(2.156)	5.044	(1.986)	$\Delta A = +0.272$
	9	13.916	(2.157)	4.890	(1.925)	
	10	13.787	(2.137)	4.890	(1.925)	
	11	13.999	(2.172)	5.052	(1.989)	A_{CORR} = 25.897 + 0.272 = 26.167
	12	14.006	(2.171)	5.060	(1.992)	
	Total	167.077	(25.897)	4.056	(1.957) Avg.	$A_{CORR.\ F.S.}$ = 1378.19 Cm² (213.62 In.²)
	Lobe Avg	13.922	(2.158)			
Mixer A (SKP17163)	1	13.670	(2.119)	5.194	(2.045)	$\Delta R_{interference}$ = 0.0
	2	13.768	(2.134)	5.202	(2.048)	
	3	13.316	(2.064)	5.123	(2.017)	$A_{F.S.}$ = 1338.90 Cm² (207.53 in²)
	4	13.703	(2.124)	5.118	(2.015)	
	5	14.258	(2.210)	5.232	(2.060)	$\Delta A_{Assembly}$ = 0 since all lobe radii
	6	13.477	(2.089)	5.149	(2.027)	are greater than the plug radius.
	7	13.581	(2.105)	5.144	(2.025)	
	8	13.606	(2.109)	5.232	(2.060)	
	9	13.806	(2.140)	5.271	(2.075)	
	10	13.903	(2.155)	5.220	(2.055)	
	11	13.568	(2.103)	5.215	(2.053)	
	12	13.361	(2.071)	5.194	(2.045)	
	Total	164.01	(25.423)	5.191	(2.0438) Avg.	
	Lobe Avg	13.671	(2.119)			
Mixer D (SKP17170)	1	13.471	(2.088)	4.800	(1.890)	$A_{F.S.}$ = 1348.13 Cm² (208.96 in²)
	2	13.464	(2.087)	4.795	(1.888)	
	3	13.968	(2.165)	5.026	(1.979)	R_{Avg} = 4.909 Cm (1.933 in)
	4	14.103	(2.186)	5.026	(1.979)	
	5	14.877	(2.306)	5.108	(2.011)	$\Delta R_{interference}$ = 0.117 Cm (0.046 in)
	6	13.897	(2.154)	5.080	(2.000)	
	7	14.383	(2.183)	4.920	(1.937)	ΔA = 3.645 Cm² (0.565 in²)
	8	13.948	(2.162)	4.997	(1.928)	
	9	13.342	(2.068)	4.811	(1.894)	A_{CORR} = 160.786 Cm² (26.162 in²)
	10	13.464	(2.087)	4.806	(1.892)	
	11	12.864	(1.994)	4.806	(1.892)	$A_{CORR\ F.S.}$ = 1377.86 Cm² (213.57 in²)
	12	13.658	(2.117)	4.841	(1.906)	
	Total	165.142	(25.597)	4.910	(1.933) Avg.	
	Lobe Avg	13.761	(2.133)			

NOTES:

$PLUG\ (PRINT)$ = 5.026 Cm (1.979 in)

$A_{PLUG\ (PRINT)}$ = 79.380 Cm² (12.304 in²)

121

TABLE 4-8. MODEL INSPECTIONS - SPLITTER (SKP17162).

Measure-ment No.	Angle		Diameter		Notes
	Radians	α (Degrees)	Cm	(In)	
1	0	(0)	17.539	(6.905)	Diameter measured
2	0.174	(10)	17.546	(6.908)	every 0.1745 rad,
3	0.349	(20)	17.655	(6.951)	(10°) same α orien-
4	0.523	(30)	17.848	(7.027)	tation as drawing.
5	0.698	(40)	17.810	(7.012)	
6	0.873	(50)	17.665	(6.955)	
7	1.047	(60)	17.564	(6.915)	$A_6 = 37.806 - \pi (1.979)^2$
8	1.222	(70)	17.564	(6.915)	$= 37.806 - 12.304$
9	1.396	(80)	17.604	(6.931)	$= 164.528 \text{ cm}^2$
10	1.571	(90)	17.645	(6.947)	(25.502 in.^2)
11	1.745	(100)	17.653	(6.950)	
12	1.919	(110)	17.638	(6.944)	
13	2.094	(120)	17.615	(6.935)	
14	2.268	(130)	17.610	(6.933)	
15	2.443	(140)	17.622	(6.938)	
16	2.617	(150)	17.645	(6.947)	
17	2.792	(160)	17.640	(6.945)	
18	2.966	(170)	17.597	(6.928)	

$$D_{AVE} = 17.622 \quad (6.938)$$

$$A_{AVE} = 243.909 \text{ cm}^2 \quad (37.806 \text{ in}^2)$$

TABLE 4-9. MIXING PLANE INSPECTED AREAS.

Core Nozzle Configuration	Core Area At Station 6.0		Scale Model Core Area At Station 6.0		Bypass Area At Station 16.0		Scale Model Bypass Area At Station 16.0	
	Cm^2	In^2	Cm^2	In^2	Cm^2	In^2	Cm^2	In^2
Splitter (I) (SKP17162)	1343.09	208.18	164.52	25.502	3149.34	488.15	385.79	59.798
Short parallel mixer (II) (SKP17163)	1338.90	207.53	164.01	25.422	3095.74	479.84	379.23	58.781
Long parallel mixer (III) (SKP17168)	1378.19	213.62	168.82	26.168	3056.44	473.75	374.42	58.035
Long radial mixer (IV)	1377.86	213.57	168.79	26.162	3056.57	473.77	374.43	58.037
Print areas	1354.84	210.0			3137.60	486.33 (splitter)		
					3079.80	477.37 (mixer)		

123

TABLE 4-10.   INSPECTED MIXER LOBE SHROUD DIAMETERS.*

Lobe	Uninstalled Mixer			Installed Mixer			Delta Diameter Installed-Uninstalled		
	II	III	IV	II	III	IV	II	III	IV
1	24.194 (9.525)	24.206 (9.530)	23.190 (9.130)	24.194 (9.525)	24.333 (9.580)	23.439 (9.228)	0.0 0.0	0.127 (0.050	0.249 (0.098)
2	24.257 (9.550)	24.359 (9.590)	23.241 (9.150)	24.257 (9.550)	24.420 (9.614)	23.442 (9.229)	0.0 0.0	0.061 (0.024)	0.246 (0.079)
3	24.097 (9.487)	24.264 (9.553)	23.241 (9.150)	24.097 (9.487)	24.417 (9.613)	23.352 (9.194)	0.0 0.0	0.152 (0.060)	0.112 (0.044)
4	24.244 (9.545)	24.234 (9.541)	23.139 (9.110)	24.244 (9.545)	24.374 (9.596)	23.467 (9.239)	0.0 0.0	0.140 (0.055)	0.328 (0.129)
5	24.130 (9.500)	24.219 (9.535)	23.139 (9.110)	24.130 (9.500)	24.369 (9.594)	23.437 (9.227)	0.0 0.0	0.150 (0.059)	0.297 (0.117)
6	24.168 (9.515)	24.359 (9.590)	23.114 (9.100)	24.168 (9.515)	24.407 (9.609)	23.444 (9.230)	0.0 0.0	0.048 (0.019)	0.330 (0.130)
						Avg.	0.0 0.0	0.254 (0.100)	0.114 (0.045)

Lobe	Uninstalled After Being Run Hot			Delta Diameter (Uninstalled) After Running Hot		
	II	III	IV	II	III	IV
1	24.130 (9.500)	24.204 (9.529)	23.192 (9.131)	-0.064 (-0.024)	-0.003 (-0.001)	0.003 (0.001)
2	24.229 (9.539)	24.359 (9.590)	23.228 (9.145)	-0.048 (-0.019)	0 (0.000)	-0.013 (-0.005)
3	24.081 (9.481)	24.226 (9.538)	23.045 (9.073)	-0.015 (-0.006)	-0.038 (-0.015)	-0.196 (-0.077)
4	24.229 (9.539)	24.201 (9.528)	23.233 (9.147)	-0.015 (-0.006)	-0.033 (-0.013)	0.094 (0.037)
5	24.084 (9.482)	24.204 (9.529)	23.144 (9.112)	-0.046 (-0.018)	-0.015 (-0.006)	0.005 (0.002)
6	24.160 (9.512)	24.257 (9.550)	23.114 (9.100)	-0.008 (-0.003)	-0.102 (-0.040)	0 (0.000)
			Avg.	-0.033 (-0.013)	-0.038 (-0.015)	-0.020 (-0.008)
			$\frac{\delta \Delta A}{A}$	-0.32	-0.35	-0.19

*Diameters given in cm and (in.)

124

4.2.2 Core-Only Data

The splitter-core-only configuration was initially run with two removable station 5.2 pressure rakes in place to obtain the pressure loss correlation from core station 5.0 to station 5.2. The core station 5.2 total-pressure rakes were then removed for the remainder of the testing. Thrust data was then obtained without the interference drag of the station 5.2 rakes.

For the initial series of core-only test runs, total pressures were measured at station 5.0 (rig core inlet charging station) and station 5.2 (AiResearch core rating station). Total pressure profiles for these two stations are presented in Figures 4-8 and 4-9. These total pressures were integrated by area averaging since the profiles are fairly uniform and the static pressure gradients are nearly uniform. The core-adapter-duct total-pressure loss is presented in Figure 4-10 as a function of the square of the inlet Mach number. The data falls close to the theoretical friction-loss calculation, which indicates the pressure loss is linearly proportional to the duct dynamic pressure over the range of test conditions. Therefore, the total pressure loss between station 5.0 and 5.2 could be entered into the test data reduction deck as $\Delta P/P_T = 0.01427 \, \gamma_{5.0} \, M_{5.0}^2$.

Core-only pressure ratios were kept below 1.3 since the core mixers are diffusers and, based on a 1-dimensional analysis, station 5.2 chokes when the pressure ratio across the nozzle reaches 1.3. The mixer-core nozzles typically have about a 10 percent lower flow coefficient than a splitter nozzle, hence the mixer-core nozzle could be run to a 1.5 nozzle pressure ratio.

The core-stream pressure losses from station 5.2 to station 6.0 were obtained from the core-only measured thrust coefficients. A throat efficiency term (C_S) of 1.0 was assumed for the standard compound core nozzle since the exit flow angle was estimated to be axial and there is no convergent section as in a typical convergent nozzle where $C_S = 0.997$. A throat efficiency of 1.0 was also used to calculate the mixer-nozzle pressure losses. Therefore, velocity profile and flow-angle effects are included in the pressure-loss term. The mixer-nozzle pressure losses were calculated in this manner in order to be consistent with the input for the compound flow analysis program. With a throat efficiency of 1.0 for the core nozzles, the delta thrust coefficient is:

$$\Delta C_F = 1.0 - C_F \text{ TESTED}$$
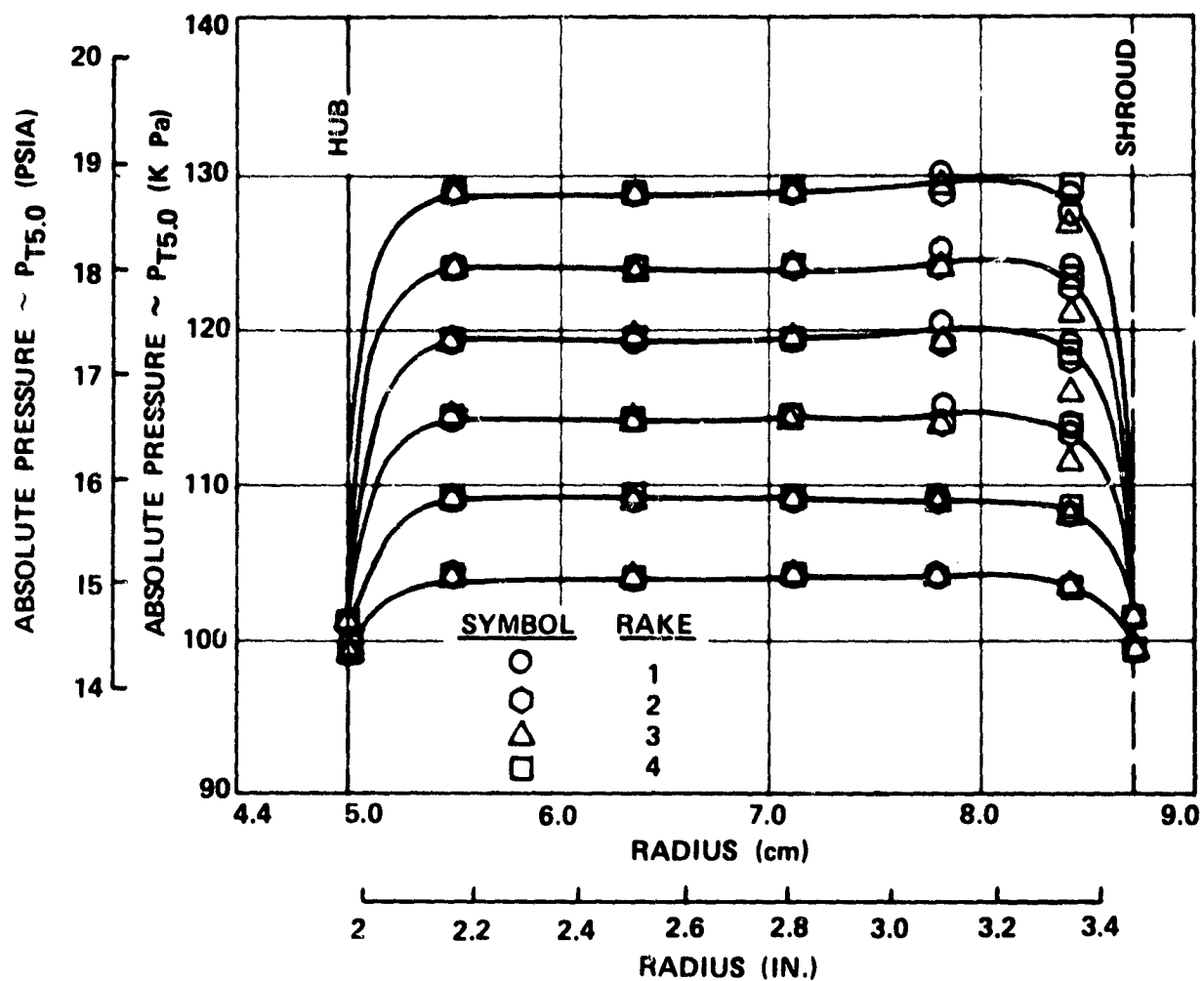
Figure 4-8. Station 5.0 - Total Pressure Profiles - Core Only Runs.
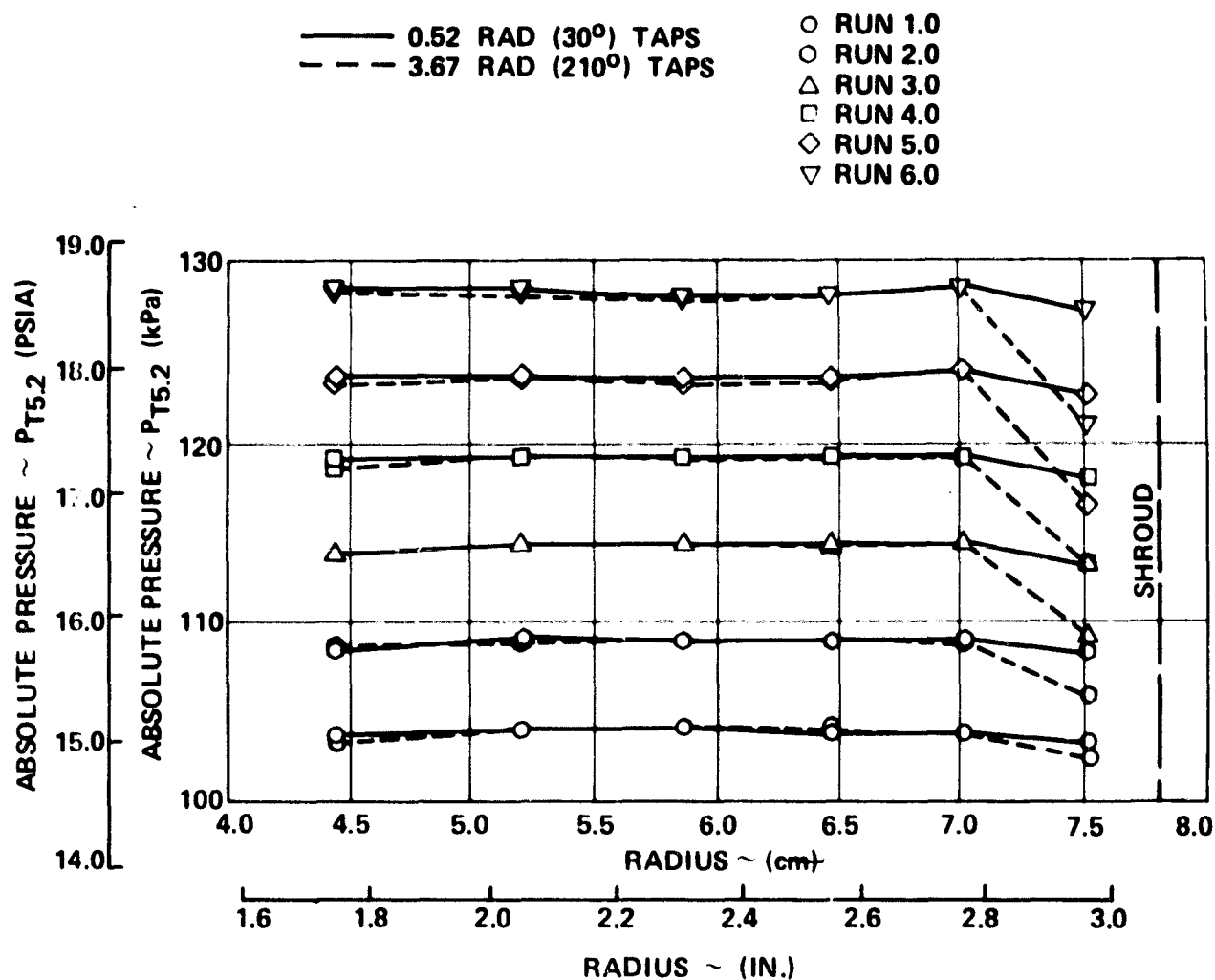
Figure 4-9. Station 5.2 - Total Pressure Profiles - Core Only Runs.

127
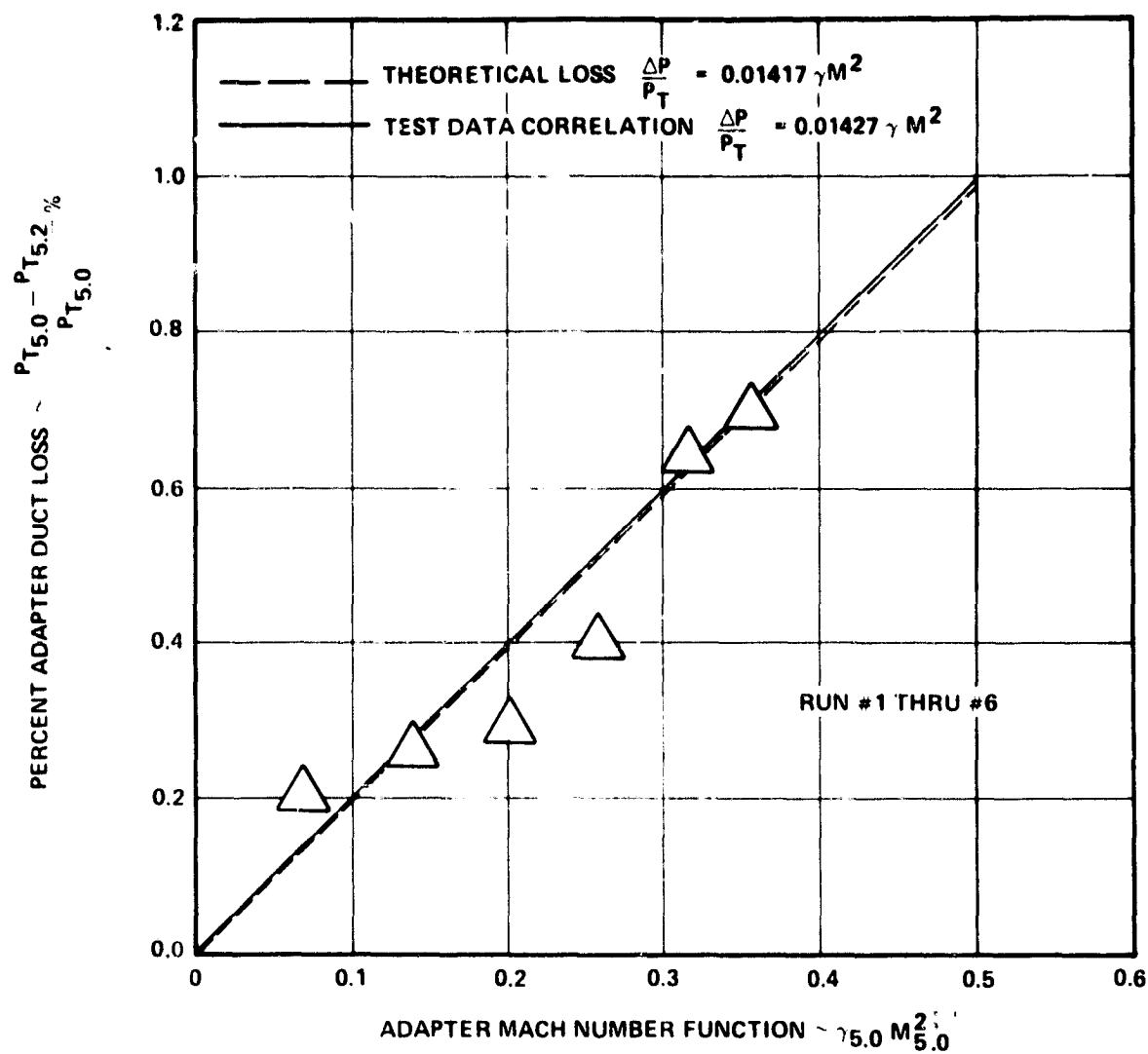
Figure 4-10.   Core Adapter Duct Total-Pressure Loss.

Sensitivity of ideal thrust to total-pressure loss as a function of nozzle-pressure ratio is obtained from the following equation:

$$\frac{F_{ID}}{P_T A^*} = \left[\frac{2\gamma^2}{\gamma-1} \left(\frac{2}{\gamma+1}\right)^{\frac{\gamma+1}{\gamma-1}} \left[1 - \left(\frac{P_\infty}{P_T}\right)^{\frac{\gamma-1}{\gamma}} \right] \right]^{1/2} \tag{13}$$

Pressure loss is thus determined as:

$$\Delta P_T / P_T = \Delta C_F \left(\frac{\Delta P_T / P_T}{\Delta F_{ID}/F_{ID}} \right) \tag{14}$$

Unfortunately, two out of the three core-only pressure-ratio points for the mixer configurations choked between station 5.2 and 6.0, evidently due to the 3-dimensional blockage effect of the lobes in conjunction with the local acceleration along the plug surface. Unrealistic high-pressure loss was obtained from the remaining 1.2 pressure-ratio point for each of the mixers. This is considered to be the result of the thrust accuracy at low-pressure ratios. The final mixer-core pressure losses were obtained from the procedure discussed in the following section.

4.2.3 Dual Flow Data

Typical core inlet total-pressure and total-temperature pro-files for a hot dual-flow run are shown in Figure 4-11. Core and bypass total-pressure probes were area weighted for simplicity since the error is negligible due to the uniform total-pressure profiles and static pressure data. Total temperature element locations were also area weighted. Typical fan inlet total-pressure and total-temperature profiles are shown in Figure 4-12.

The standard-compound exhaust nozzle cold-flow test data was used to establish the mixing duct total-pressure loss. The mixing-duct and bypass-duct losses were initially estimated by using the standard friction-loss analysis. The core total-pressure loss was obtained from the core-only test data. Minor adjustments were made to the mixing-duct and bypass-duct losses until the tested thrust coefficients and corrected airflows were matched. Both the sea-level static and cruise design point cold-flow test data was used in establishing the mixing-duct and bypass-duct total-pressure losses for the standard-compound exhaust system. The mixing-duct shroud friction loss was assumed to be the same for all configurations. After establishing the mixing-duct losses, the losses

129
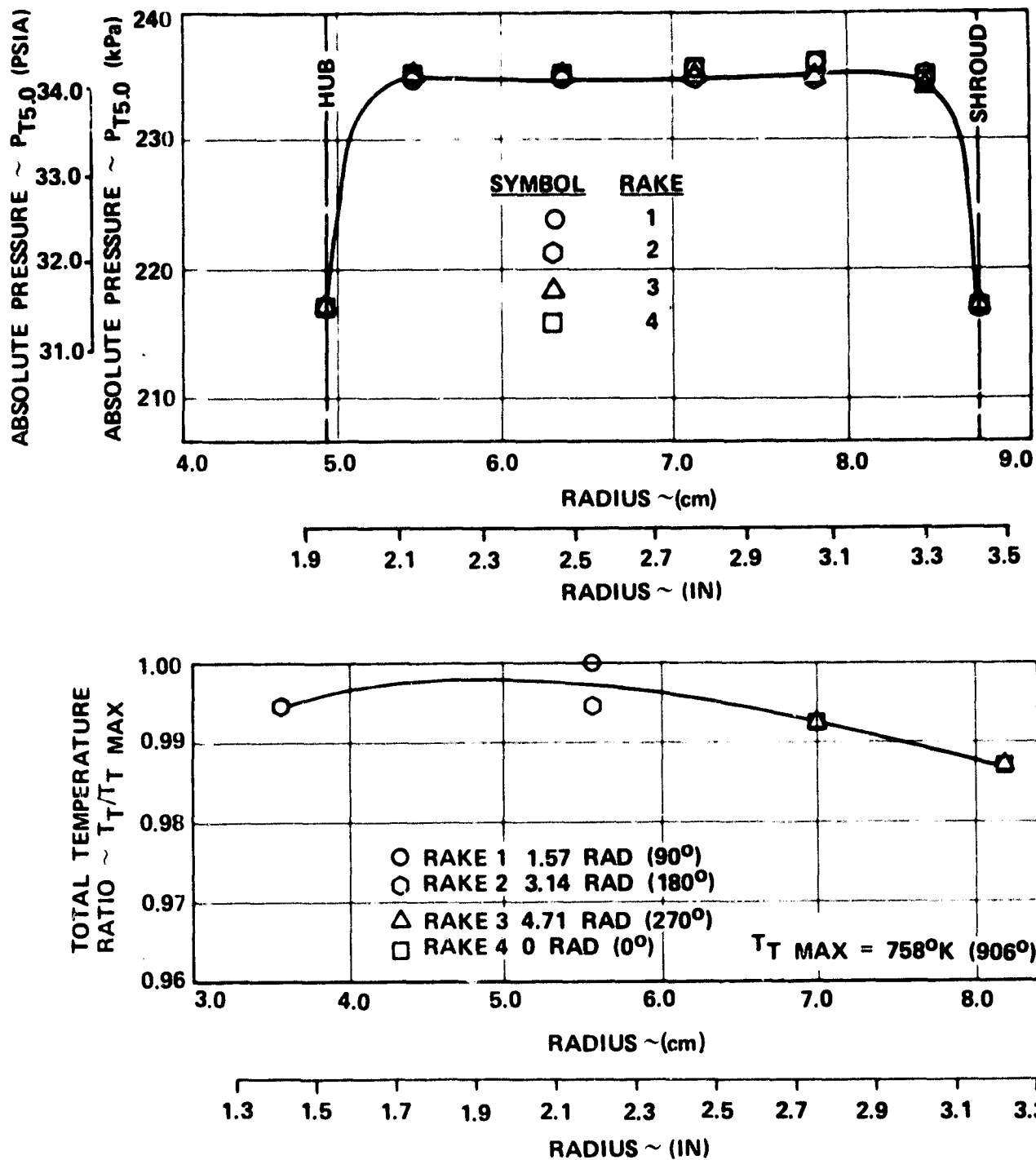
Figure 4-11.   Typical Core Inlet Total-Pressure and
                Total-Temperature Profiles.
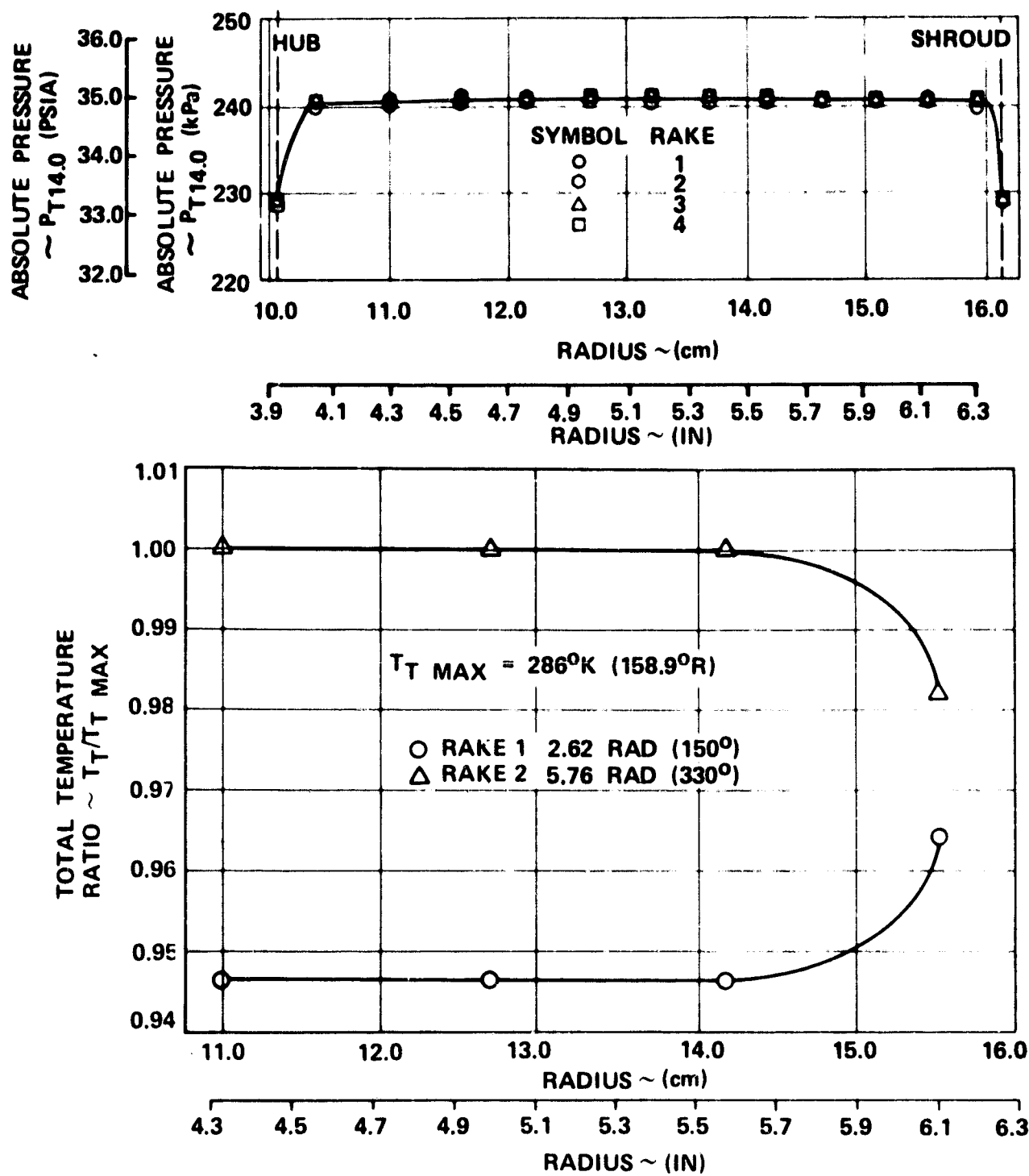
Figure 4-12.   Typical Fan Inlet Total-Pressure
and Total-Temperature Profiles.

131

through the mixer could be determined. The predicted core and by-pass losses were adjusted until the tested thrust coefficients and corrected flows were matched for each configuration. The cold flow sea-level static and cruise-design point data were again used to establish the losses for the respective configurations. The losses derived from the test data and the predicted losses were in good agreement. Details of the comparison are covered in Section 4.5.

The mixing efficiency can be determined by comparing the hot-flow and cold-flow test data. Before this is done, however, a heat transfer correction must be applied to the hot-flow data. During dual-flow hot runs, the core stream was heated to 921°K (1200°F) and controlled to a desired temperature to duplicate the predicted temperature split, T_T(core)/T_T(bypass), of the full scale engine. Each of the configurations were run with dual-flow, hot-core conditions at the SLS/TO and cruise design-point pressure-ratio settings. Since the core stream total temperature probes were located upstream of station 5.0 (inlet-charging station), the distance to the rating station 5.2 was approximately 40 inches. Therefore, heat transfer occurring between the rig charging and AiResearch rating station would lower the actual rating-station temperature from the measured inlet value. At the nominal design point, the delta temperature was calculated to be 4.4°K (8°F) or about 1 percent error in the core total temperature. Since total temperature affects not only ideal thrust but also the mixing-efficiency calculation, a temperature correction was included in the thrust data reduction program as shown below:

$$\Delta T = \frac{0.017 \left(T_{T5.0} - T_{T14.0} \right) \left(\dfrac{W_{5.0}}{7.3} \right)^{-0.2}}{1 + 2.5 \left(\dfrac{W_{5.0}}{W_{14.0}} \right)} \qquad (15)$$

The heat-transfer correlation included the effect of flow ratio between the cold and hot streams. For the range of flow ratios tested, the computed change in temperature ranged from 3.33°K (6°F) to 6.6°K (12°F).

With the corrected core total temperature, the derived thrust mixing efficiency can be determined. The difference between the thrust coefficients from the hot dual-flow runs and thrust coefficients from the cold dual-flow runs yields the thrust gain due to thermal mixing. Percent mixing is then obtained by dividing the tested thrust gain by the ideal thrust gain possible as shown below:

$$\eta_{MIX} = \frac{C_{F_{HOT}} - C_{F_{COLD}}}{C_{F_{100\%}} - C_{F_{0\%}}} = \frac{C_{F_{TEST}} - C_{F_{0\%}}}{C_F{}^{100\%} - C_F{}^{0\%}} \qquad (16)$$
$$\phantom{\eta_{MIX} = }{}_{\substack{IDEAL \\ MIXING}} \quad {}_{MIXING}$$

The ideal thrust gain is determined from the individual flow properties and continuity, momentum, and energy equations.

4.2.4 Exit Surveys

Exit-survey running time ranged from 1 to 1 1/2 minutes. During this period, adiabatic expansion of the flow from the pressure tank decreased the total temperature of the cold stream. Since the rig temperatures were set by holding a constant temperature ratio between the hot and cold streams, the core-flow total temperature also decreased throughout the survey run. The exit-survey data were recorded as the rake was moved to different theta locations therefore resulting in different inlet temperatures than the initial rake setting. A nondimensional correction was used to ratio the survey temperatures taken at each position as referenced to the initial inlet temperature. The correction is as follows:

$$\frac{T_T(N)}{T_{T5.2}} = \frac{T_T - \left(\dfrac{\Delta T_{5.2} - \Delta T_{T14.0}}{T_{T5.2} - T_{T14.0}}\right)\left(T_T - T_{T14.0}\right) - \Delta T_{T14.0}}{T_{T\,5.2}} \qquad (17)$$

where: T_T = Probe measured total temperature

$\Delta T_{5.2} = T_{T5.2} - T'_{T5.2}$

$\Delta T_{14.0} = T_{T14.0} - T'_{T14.0}$

primed (') denotes initial rake setting

not primed denotes subsequent rake settings

133

The equation is a linear interpolation as graphically shown in Figure 4-13. The correction was used at each rake setting. Inlet-station total-temperatures were recorded at each rake setting. Thus, all survey total-temperature data could be integrated, since each rake setting had been corrected to the same inlet reference conditions.

Survey-rake total- and static-pressure probes were calibrated at true Mach number levels of 0.5, 0.7, 0.9, and 1.2. The calibration curves for total and static pressure are shown in Figures 4-14 and 4-15, respectively. The calibration curves were fit with polynomial or linear fits where appropriate. The test range of the measured centerline pressure ratio (P_T/P_S) was 1.25 to 1.45. This fell between the Mach numbers 0.5 and 0.9 calibration points.

Initial exit-survey data reduction is explained in detail in Appendix A. The reduced data were area integrated and plotted.

4.3   Test Results and Data Analysis

An overall performance summary of the test configurations is presented in Table 4-11. Hot-flow thrust coefficients, mixing efficiencies, and jet noise reductions are shown. All mixer test configurations exceeded the thrust-coefficient design goals. Design goal mixing efficiency was met by Configurations II and VI (short parallel mixer) based on an average of both flight conditions. Configuration II also yielded the maximum jet noise reduction. The short-parallel-mixer lobe provided the better performance and lower jet noise relative to the long parallel or long radial lobes at sea level. The long mixing duct (X/D=0.752) provided better performance and lower jet noise at sea level relative to the shorter mixing ducts. The combination of the short parallel mixer and long mixing duct (test Configuration II) was chosen as the final full-scale exhaust-system design.

4.3.1   Mixing-Plane Flow Coefficients

Core and bypass mixing-plane flow coefficients for both the standard-compound and mixer-compound nozzles correlated well as a function of the total pressure ratio (see Figures 4-16 and 4-17). The standard splitter-compound core-flow coefficients matched the predicted level whereas the mixer-compound core-flow coefficient was lower in level and the characteristic shape was substantially different above a total pressure ratio of 1.0. The predicted mixer-core flow coefficients came from cold-flow testing of a mixer design with accelerating rather than diffusing flow through the lobes and much less core flow turning which tended to give a more uniform flow profile at the mixer exit. The bypass-flow coefficients were higher than predicted for both the standard- and mixer-compound nozzles. This was due to a smoother upstream duct with a more uniform area distribution and lower losses

134
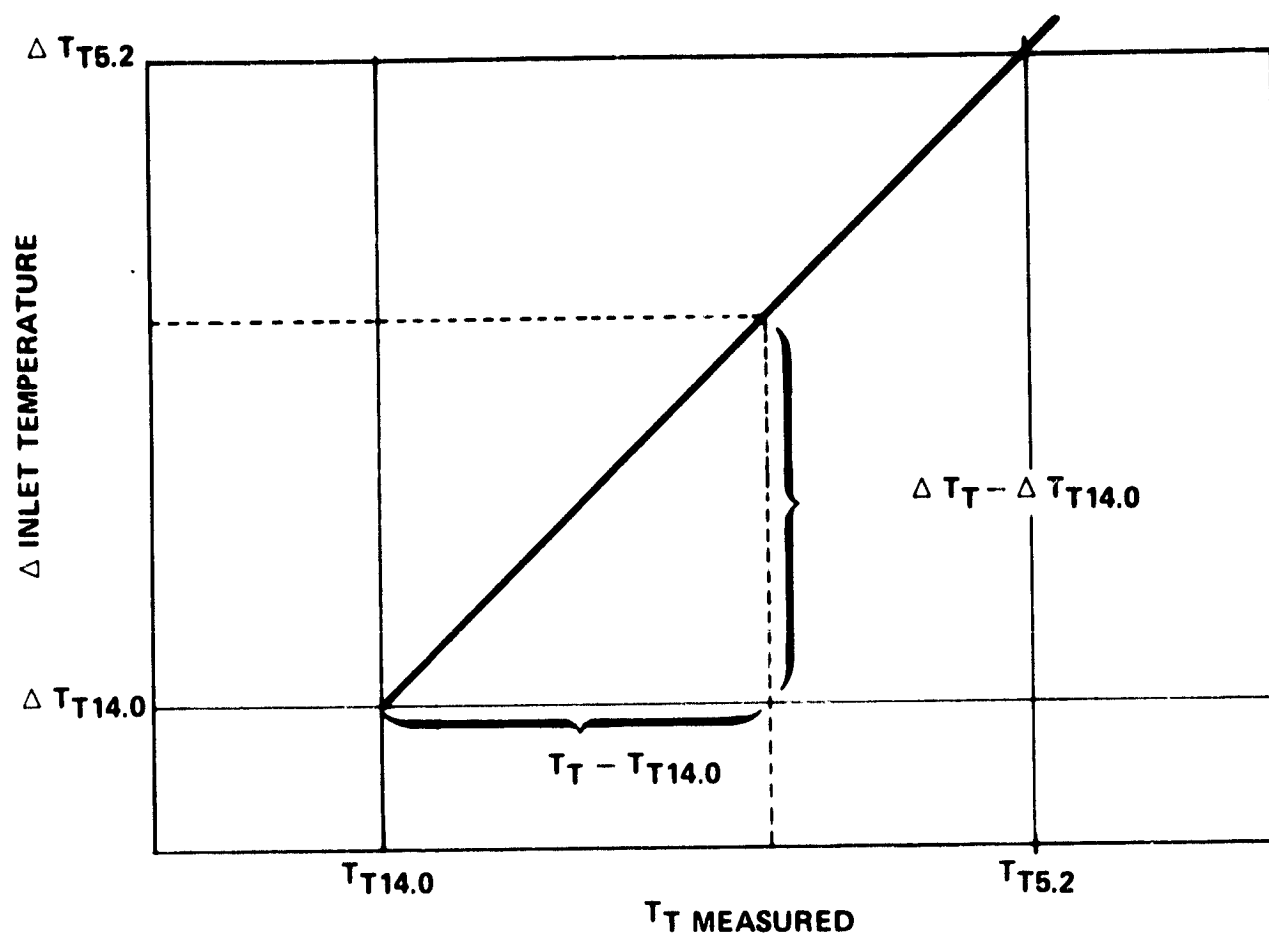
$$\text{IF } T_T = T_{T5.2} \Rightarrow T_{T(N)} = T_{T'5.2}$$

$$\text{IF } T_T = T_{T14.0} \Rightarrow T_{T(N)} = T_{T'14.0}$$

Figure 4-13. Inlet Total Temperature Correction.
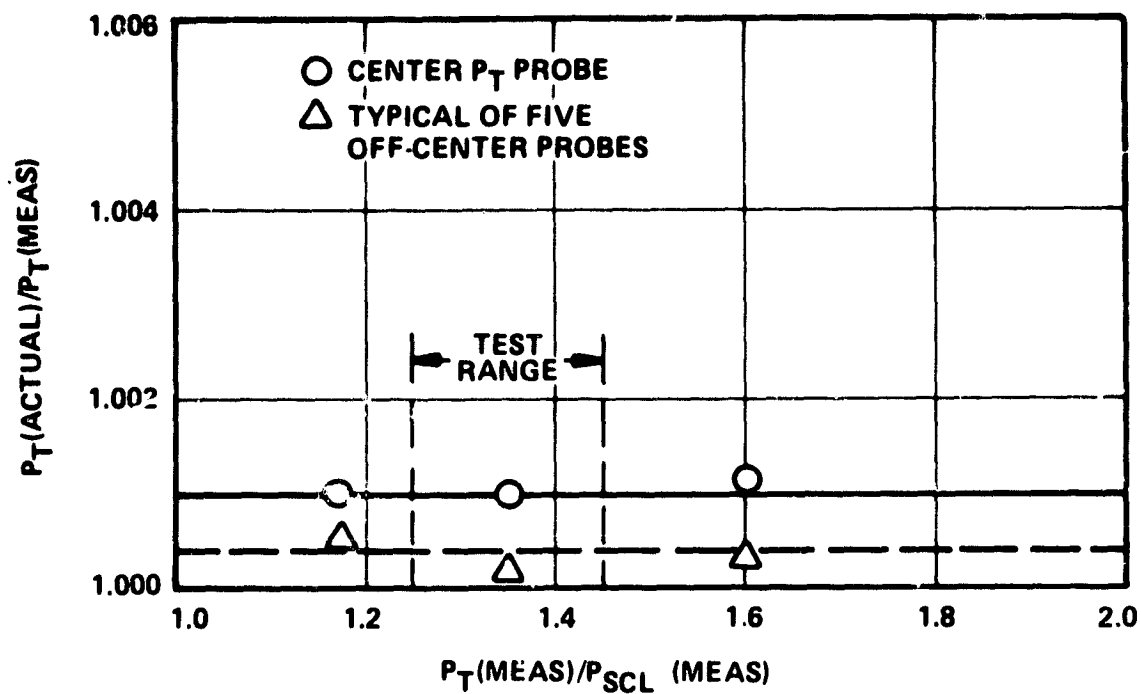
Figure 4-14. QCGAT Survey Rake P_T Probe Calibration.
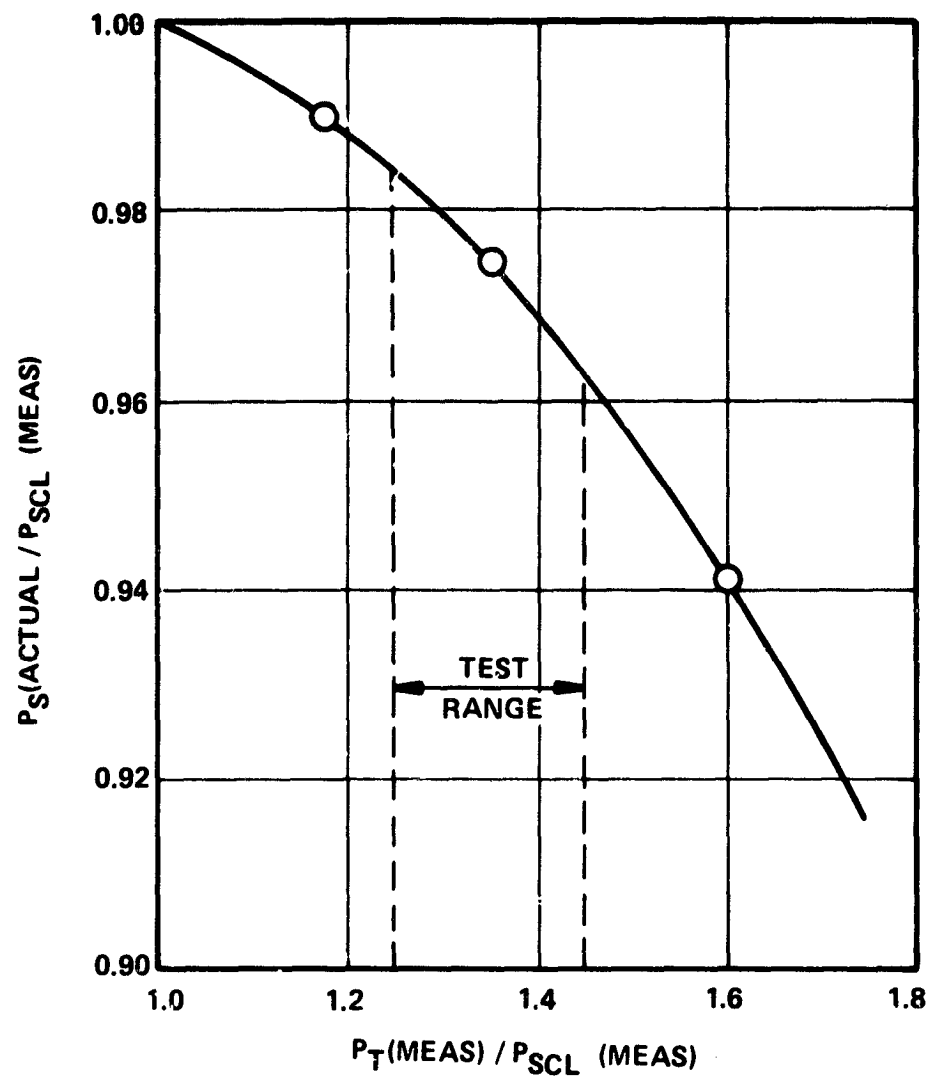
Figure 4-15. QCGAT Survey Rake P_S Probe Calibration.

TABLE 4-11. 2CGAT 0.35 SCALE MODEL EXHAUST SYSTEM TESTS
OVERALL PERFORMANCE AND ACOUSTIC SUMMARY.

Model No.	Mixer Compound Configuration	Sea Level Static		Cruise M = 0.8 Alt = 12,192 m (40K FT)		Takeoff Flyover ΔEPNdB
		C_{F_T}	r_{Mix}	C_{F_T}	r_{Mix}	
Goal	X/D = 0.750	0.9782	75.0	1.0005	75.0	--
I	Compound X/D = 0.752	0.9897	30.5	0.9940	--	0
II	Short parallel X/D = 0.752	0.9932	89.0	1.0050	72.1	-5.1
III	Long parallel X/D = 0.752	0.9902	37.1	1.0032	69.8	-2.9
IV	Long radial X/D = 0.752	0.9918	51.4	1.0075	65.5	-3.5
V	Short parallel X/D = 0.501	0.9902	62.6	1.0068	76.2	-4.0
VI	Short parallel X/D = 0.626	0.9908	75.6	1.0066	92.2	-4.5

*Takeoff noise level takeoff at 6.482 Km (3.5 NM) from brake release
ΔEPNdB jet noise reduction only

138
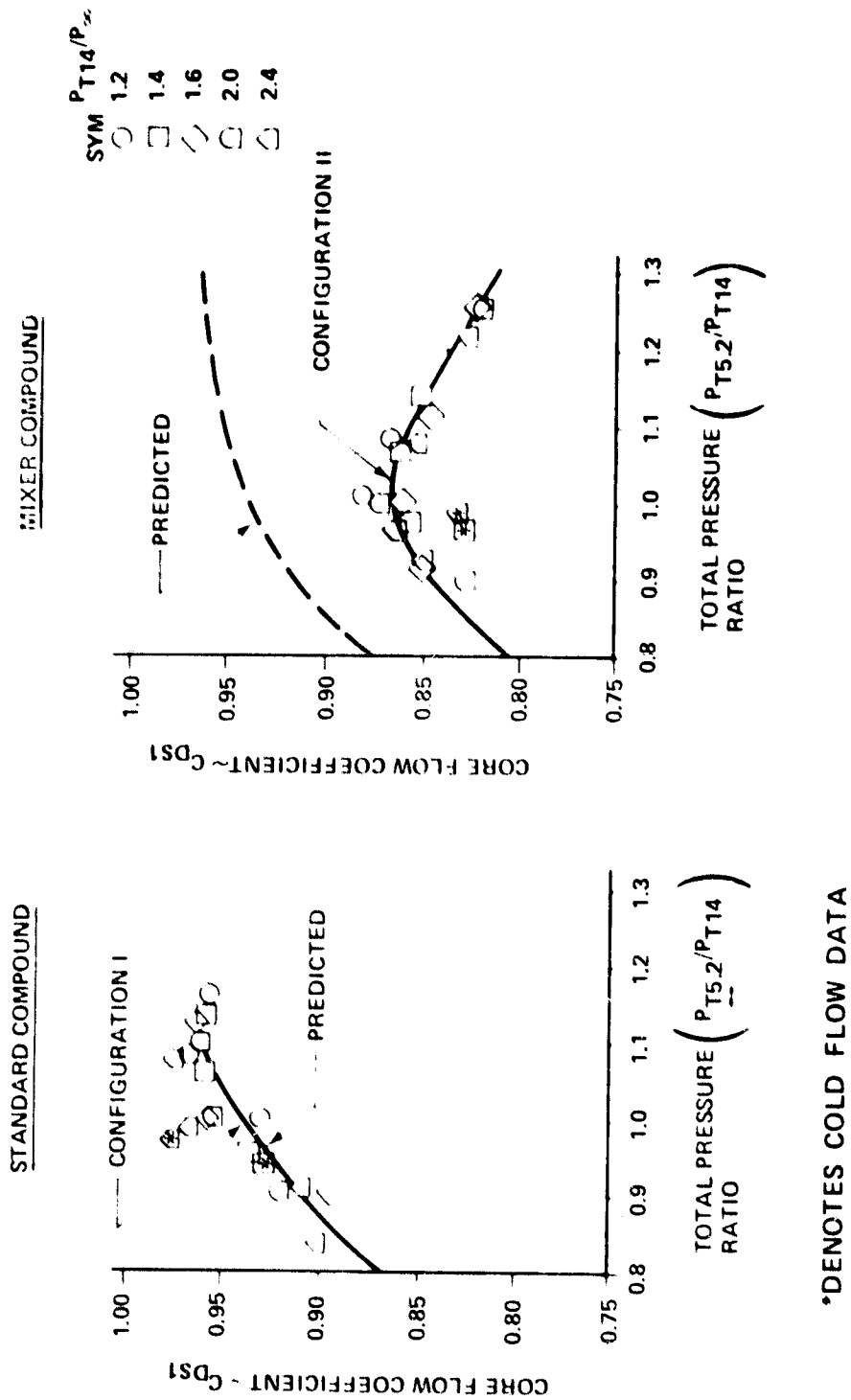
Figure 4-16. CCGAE Model Exhaust System Mixing Plane Core Flow Coefficients.
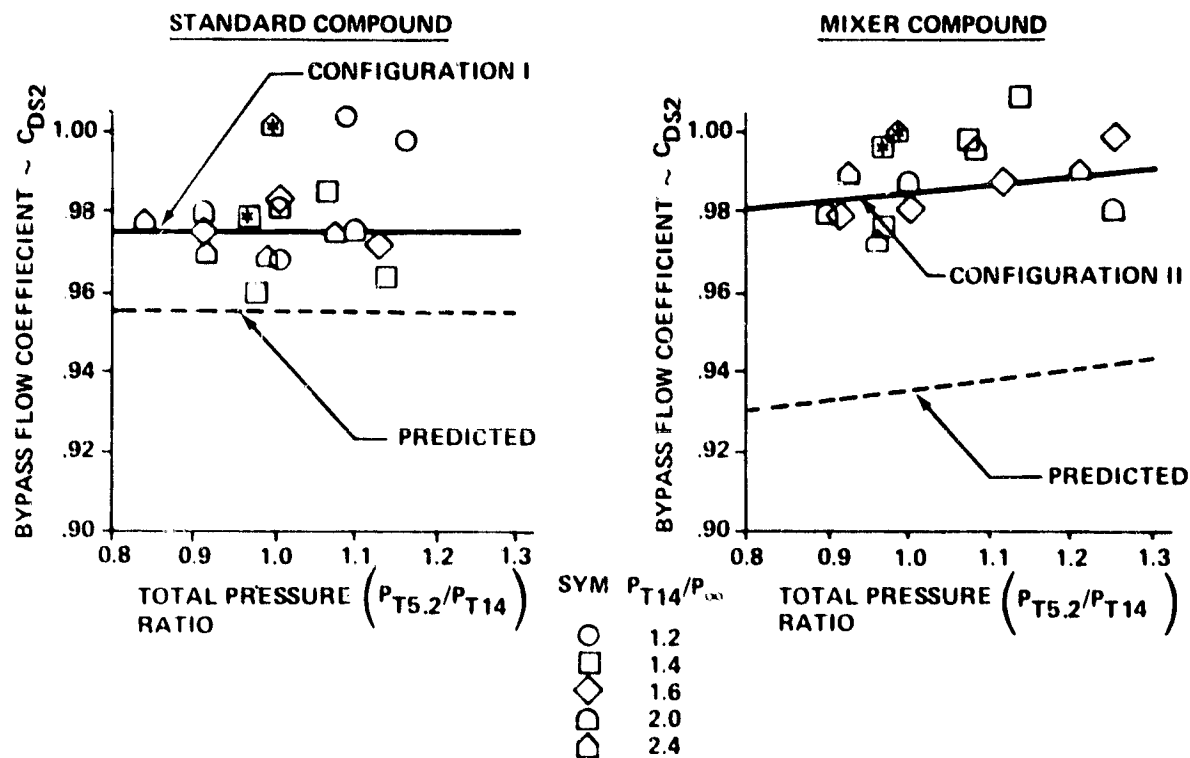
*DENOTES COLD FLOW DATA

Figure 4-17. QCGAT Model Exhaust System
Mixing Plane Bypass Flow
Coefficients.

compared to the IR and D mixer test data used for the prediction. Both the standard-compound and mixer-compound nozzles snow a shift in flow coefficients between cold and hot flow. Since cold inspected areas were used in both calculations, the effect of area change due to thermal growth and hot-flow temperature profile in the core stream are both affecting the flow coefficient shift. The standard-compound nozzles showed less than one-half percent difference in the core stream (see Figure 4-16) but 2- to 3-percent difference in the bypass stream (see Figure 4-17). The large difference in the bypass appears to be due to data scatter.

An increase of three-quarters of one percent was calculated for the mixer core area based on thermal growth. The data in Figure 4-16 indicates a total flow coefficient difference of three to three and one-half percent for the mixer core, which leaves about two percent to be attributed to temperature profile. Figure 4-17 shows a two- to three-percent difference in the mixer-bypass hot- and cold-flow coefficients. This is either attributable to data scatter or a much larger thermal growth effect than estimated.

Inlet flow consistency was checked by plotting core- and bypass-corrected flow versus the respective core and bypass inlet-pressure ratios (see Figures 4-18 and 4-19). Core-corrected flows fell within a total pressure error band of ± 0.5 percent and the bypass-corrected flows were within a total-pressure error band of ± 0.25 percent. The sensitivity of mixing-plane flow coefficients to inlet total pressure was based on an inlet total-pressure measurement error of ± 2 mm Hg or ± 0.25 percent. Flow-coefficient data fell within the inlet total-pressure error band as shown in Figure 4-20.

4.3.2 Exit-Plane Flow Coefficients

Cold- and hot-exit-flow coefficients for the standard- and mixer-compound-nozzle systems are presented in Figure 4-21. Cold-flow coefficients are higher than the predicted levels, primarily due to lower pressure losses in the bypass duct than were predicted. This was indicated by the mixing-plane bypass-flow coefficients in the mixing-plane flow coefficients. (See Section 4.3.1.)

Tested cold exit-flow coefficients between standard- and mixer-compound systems are nearly the same and appear to have characteristics similar to the predicted curves (see Figure 4-21). The decrease in exit-flow coefficient from cold to hot is about 0.5 percent for the standard-compound and about 2.5 percent for the mixer compound system (see Figure 4-21). The small decrease for the standard compound is due to the change in exit velocity gradient caused by the temperature profile. Since the mixer system

141
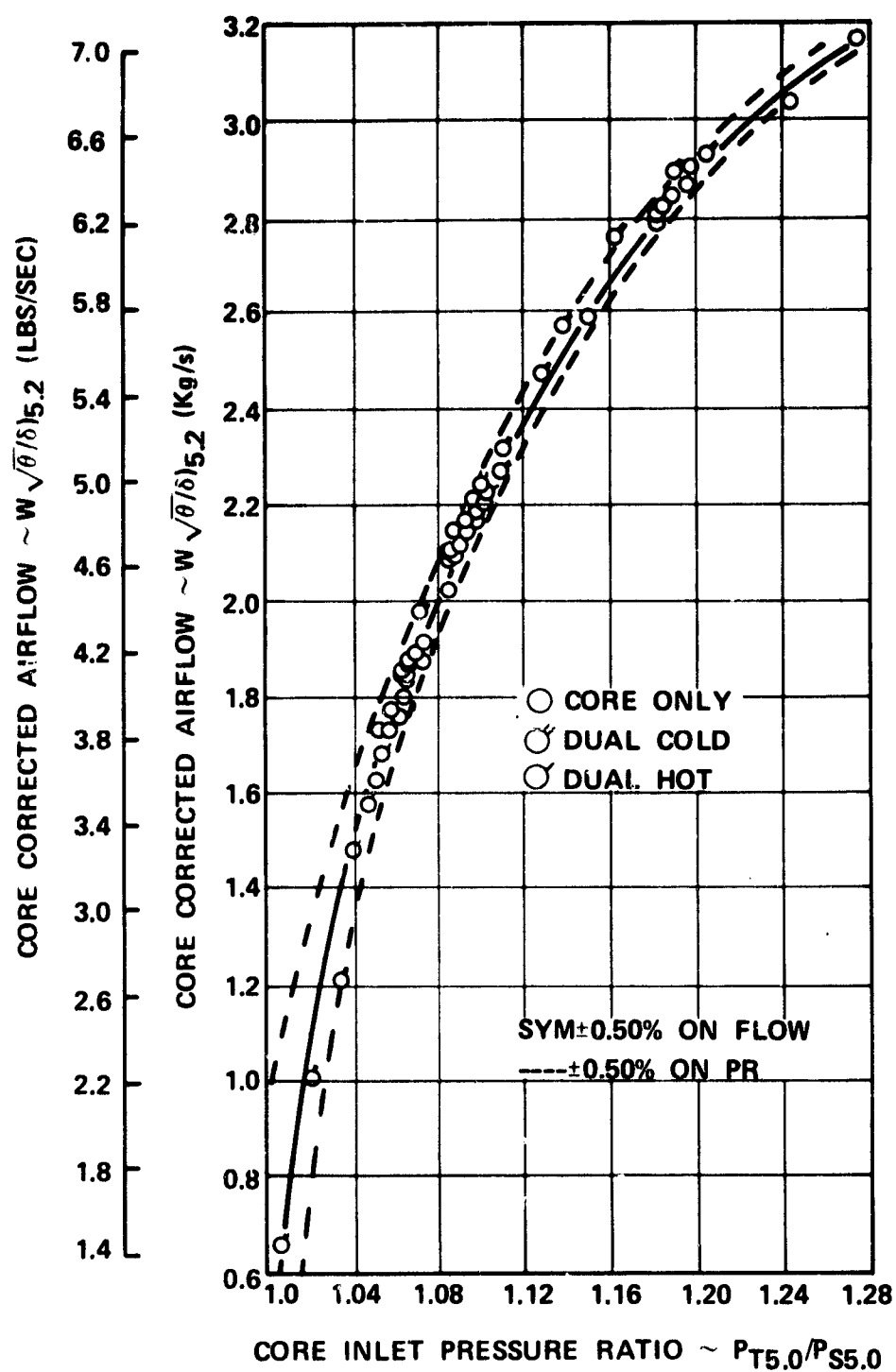
Figure 4-18. Corrected Core Airflow Versus Inlet
Pressure Ratios.

142
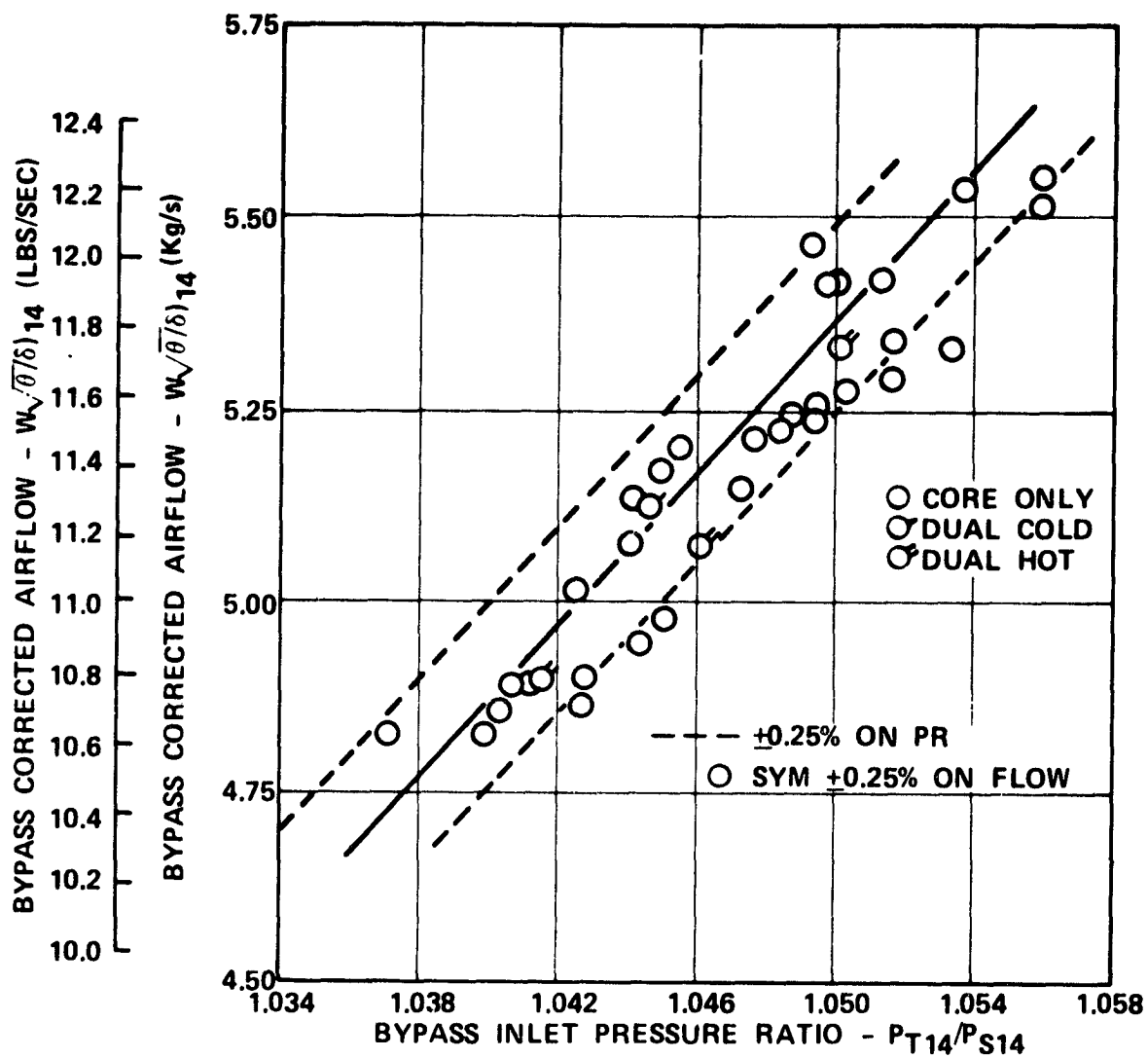
Figure 4-19. Corrected Bypass Airflow Versus Inlet
Pressure Ratios.
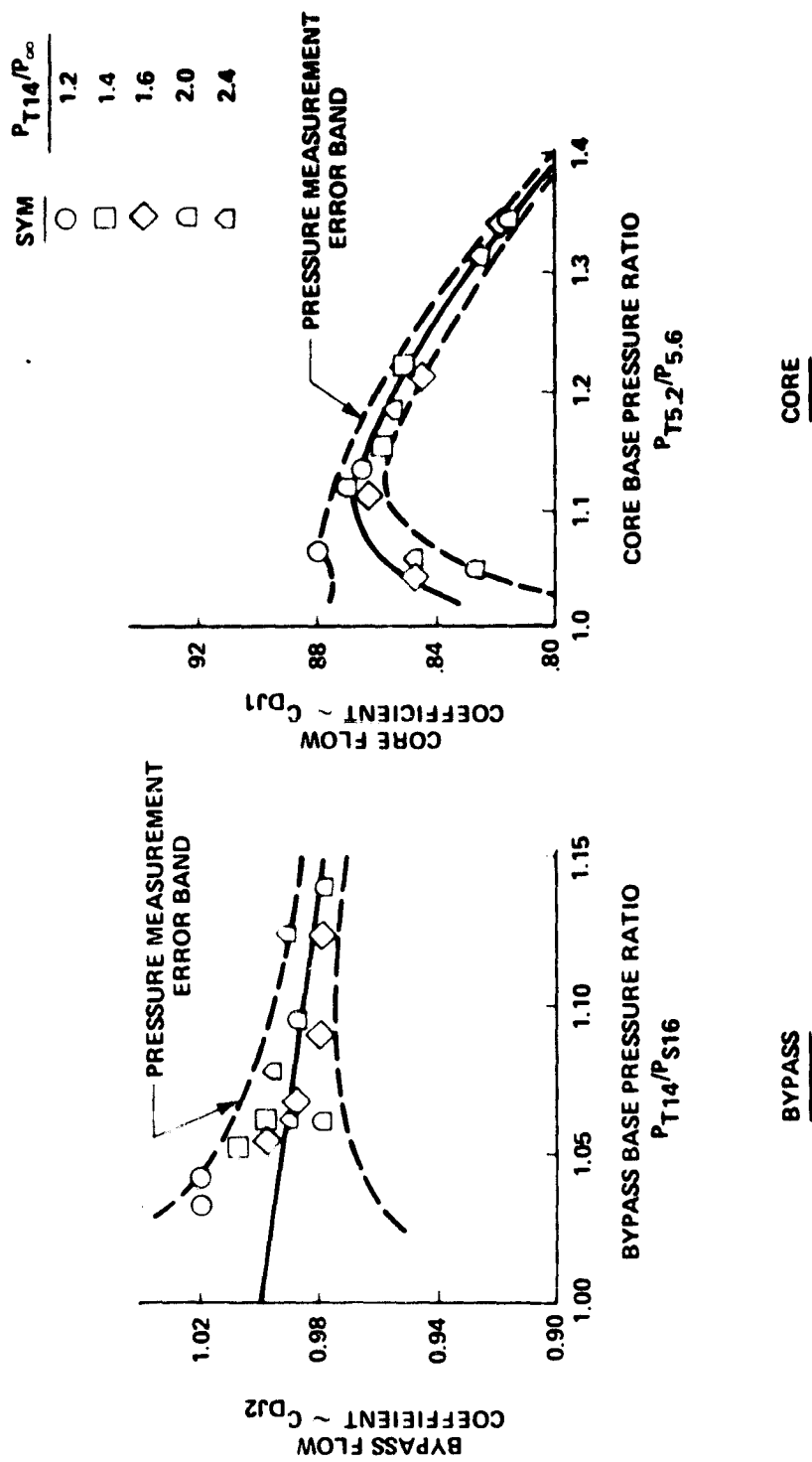
Figure 4-20. QCGAT Model Exhaust System Mixing Plane Flow Coefficient Sensitivity.

144

STANDARD COMPOUND (CONFIGURATION I)

PREDICTED COLD

O DUAL FLOW HOT DATA
C DUAL FLOW COLD DATA

NOTE BASED ON EQUAL PRESSURE
RATIO DATA POINTS

EXIT NOZZLE PRESSURE RATIO P_T/P_∞

SHORT PARALLEL MIXER COMPOUND (CONFIGURATION II)

PREDICTED COLD

DUAL FLOW HOT DATA
DUAL FLOW COLD DATA

EXIT NOZZLE PRESSURE RATIO P_T/P
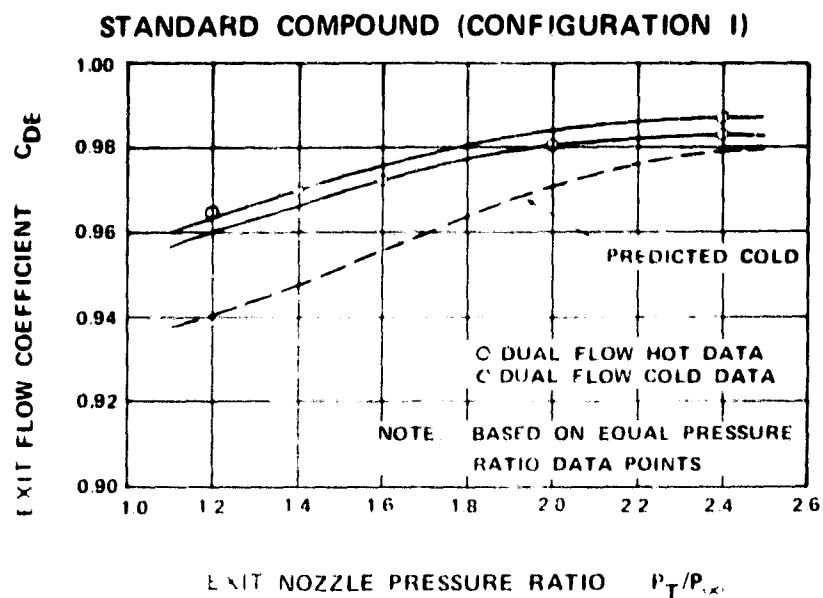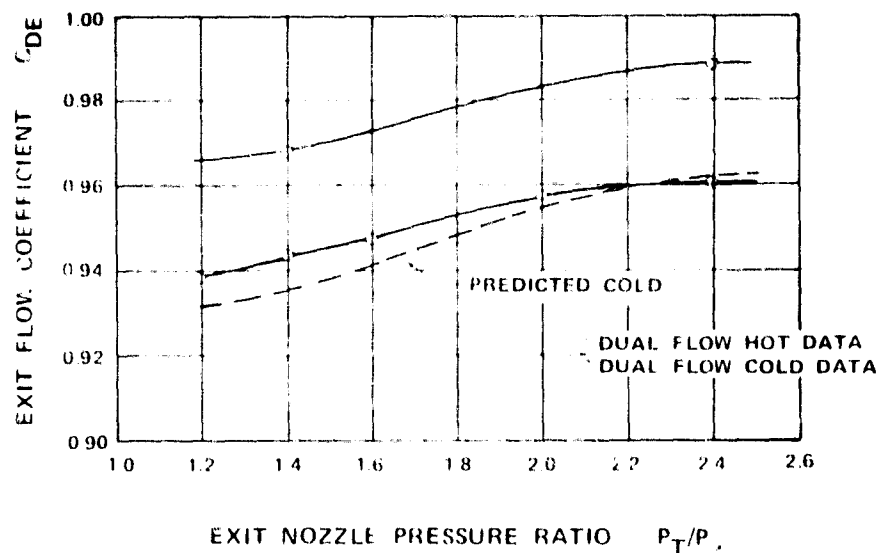
Figure 4-21. QCGAT Model Exhaust System Exit
Plane Flow Coefficients.

145

has less of a temperature profile, the large difference between cold and hot flow coefficients must be attributable to the pressure loss associated with a high degree of thermal mixing. Exit-flow coefficients presented in Figure 4-21 are based on equal-pressure-ratio data points. There is some indication from data matching that a family of curves may exist with peak values where the pressure ratios are equal.

4.3.3 Mixing-Duct Static Pressure Distributions

Static-pressure distribution along the mixing-duct shroud for configurations I through IV at the sea-level static and cruise-design point indicated constant static pressure through the constant area mixing duct (see Figure 4-22). Static pressures read the same at circumferential locations of 0° and 15°.

Plug-axial static-pressure distributions indicate that the flow field through the core was substantially different between standard- and mixer-compound nozzles. From the rating station 105.16 cm (41.4 in.) to station 116.84 cm (46 in.) (where the mixer lobes begin) the flow is diffusing with the standard-compound as designed, but is accelerating with the mixer-compound nozzles (see Figures 4-23 and 4-24). Because of the curvature effect of the plug, the flow accelerates locally along the plug surface from station 116.84 cm (46 in.) to station 127 cm (50 in.). However, the flow accelerates more rapidly with the mixer nozzles indicating an increased effective blockage due to the mixer lobes. The blockage effect of the lobes may have choked the core near station 127 cm (50 in.) as indicated by the local sonic velocity in Figure 4-23. It should be noted that at a core pressure ratio of 1.2, the acceleration affect of the lobe blockage is not as severe. Since the pressure ratio across the core nozzle at the design point is only about 1.1, this choking effect has no impact on the system operation. However, the local choking that occurred through the mixer lobes prevented the core-only pressure-ratio runs of 1.35 and 1.5 from being useful in obtaining a mixer-core total-pressure loss.

Plug static-pressure distributions from dual-flow runs at the sea-level static and cruise-design point are presented in Figures 4-25 and 4-26. The distributions indicate the same trends as the core-only distributions with slightly higher local acceleration with the mixer-core nozzles. The peak Mach number on the plug surface is 0.41 at sea-level static and 0.53 at the cruise-design point for the mixer-core nozzle. The standard-compound nozzle had lower plug peak Mach numbers of 0.36 at sea-level static and 0.45 at the cruise-design point.

146
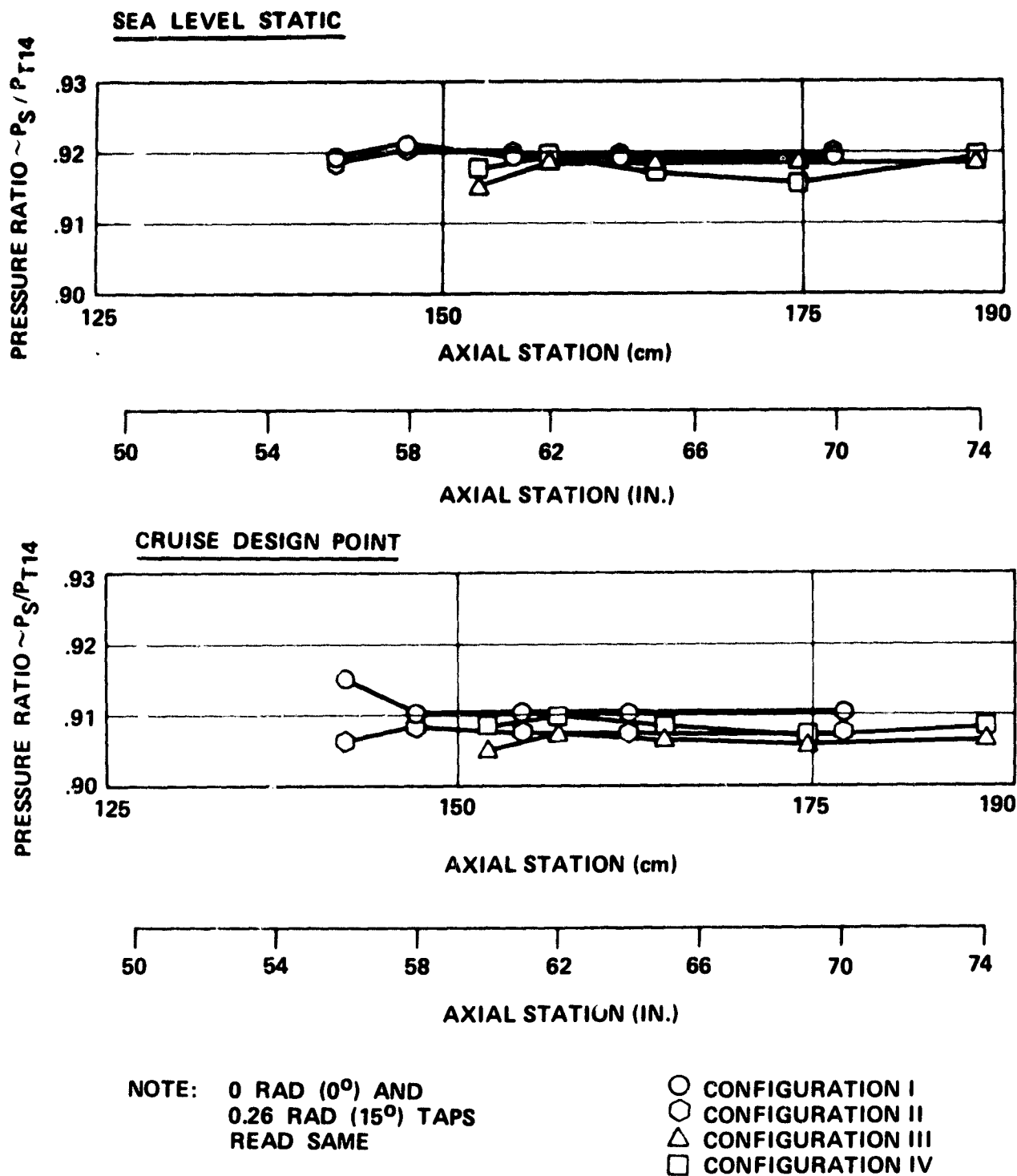
Figure 4-22. Mixing Duct Wall Static Pressure Distribution.
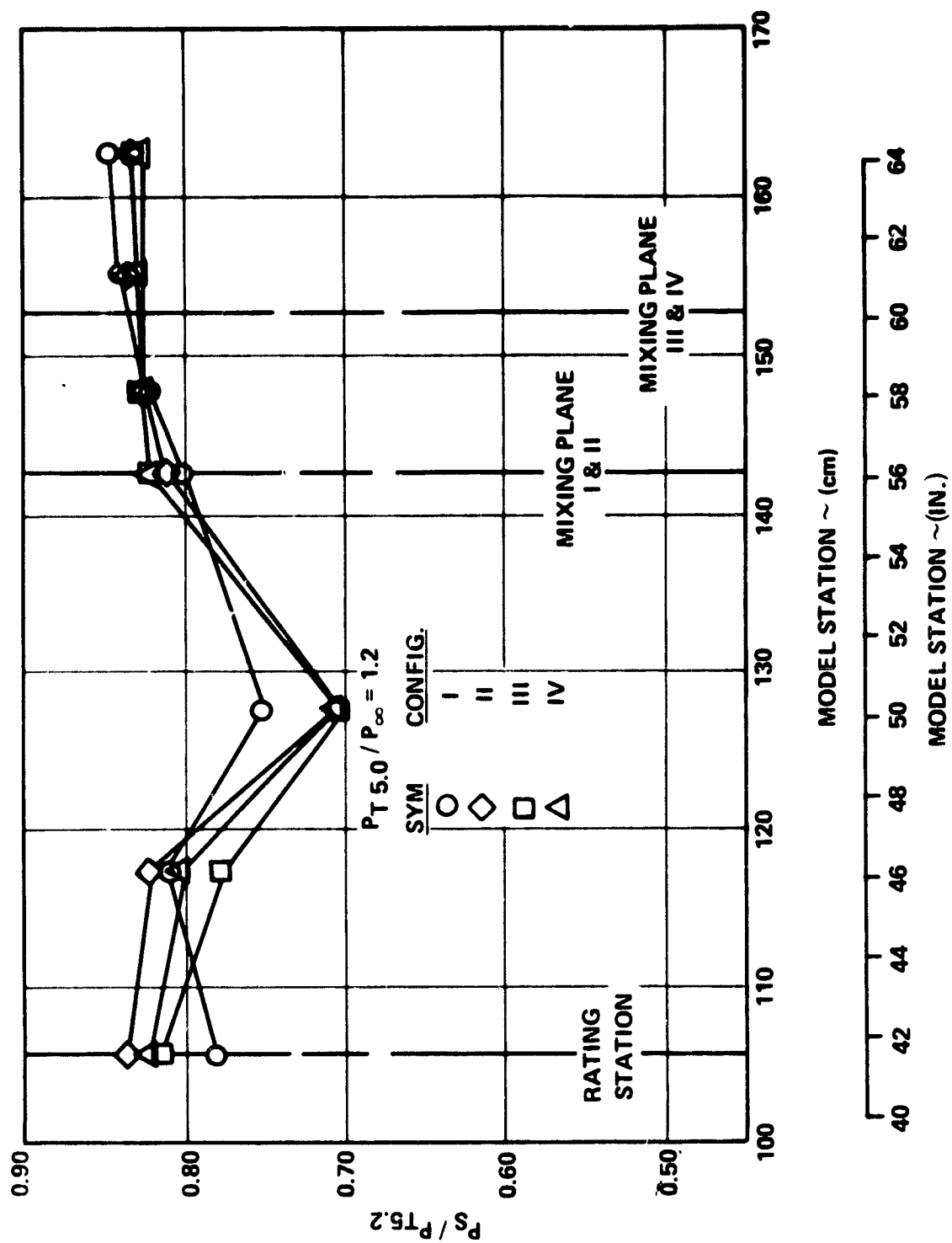
Figure 4-23. Plug Static Pressure Distribution Core-Only Flow Pressure Ratio = 1.2.

148
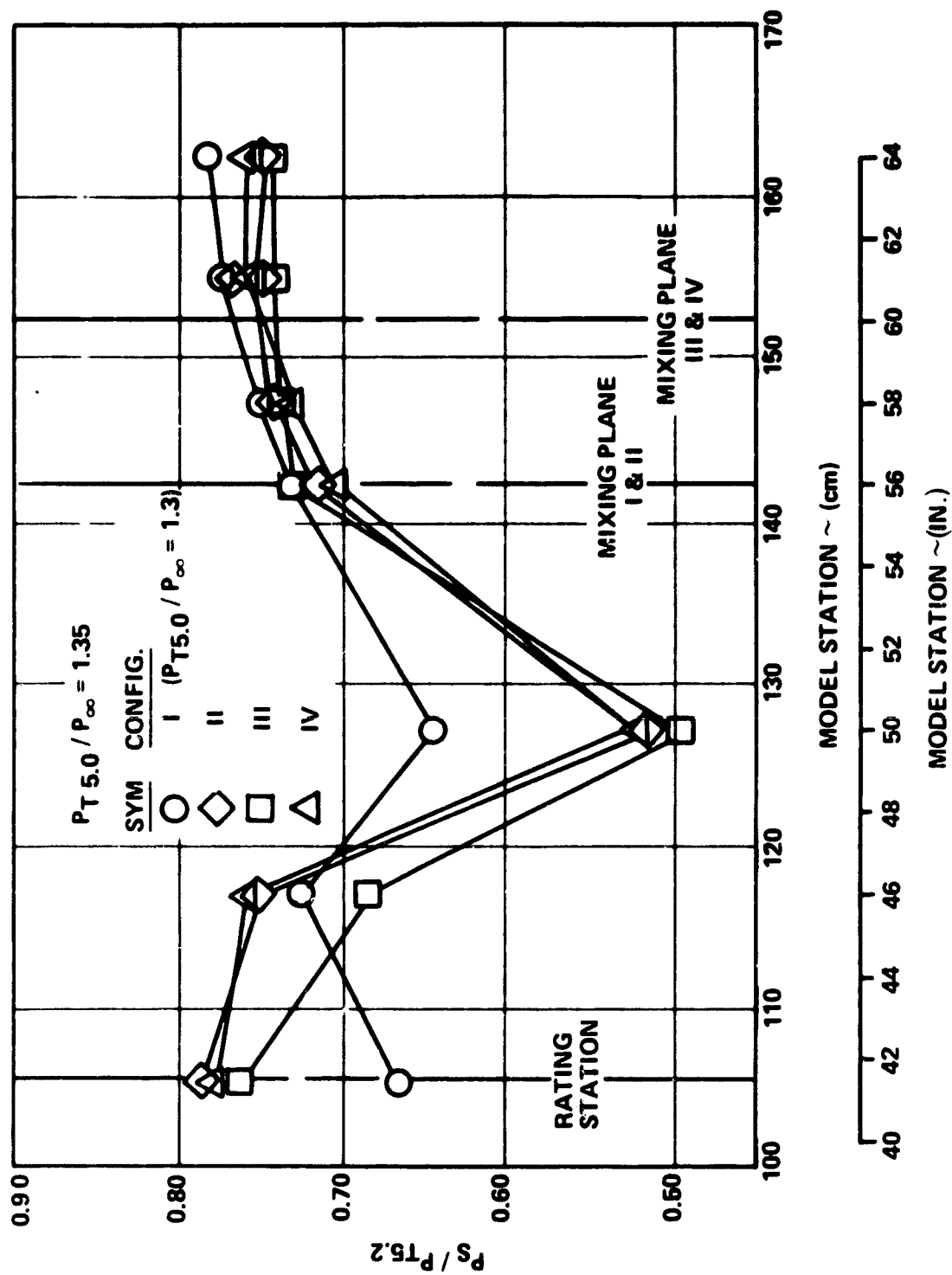
Figure 4-24. Plug Static Pressure Distribution Core-Only Flow Pressure Ratio = 1.35.

149
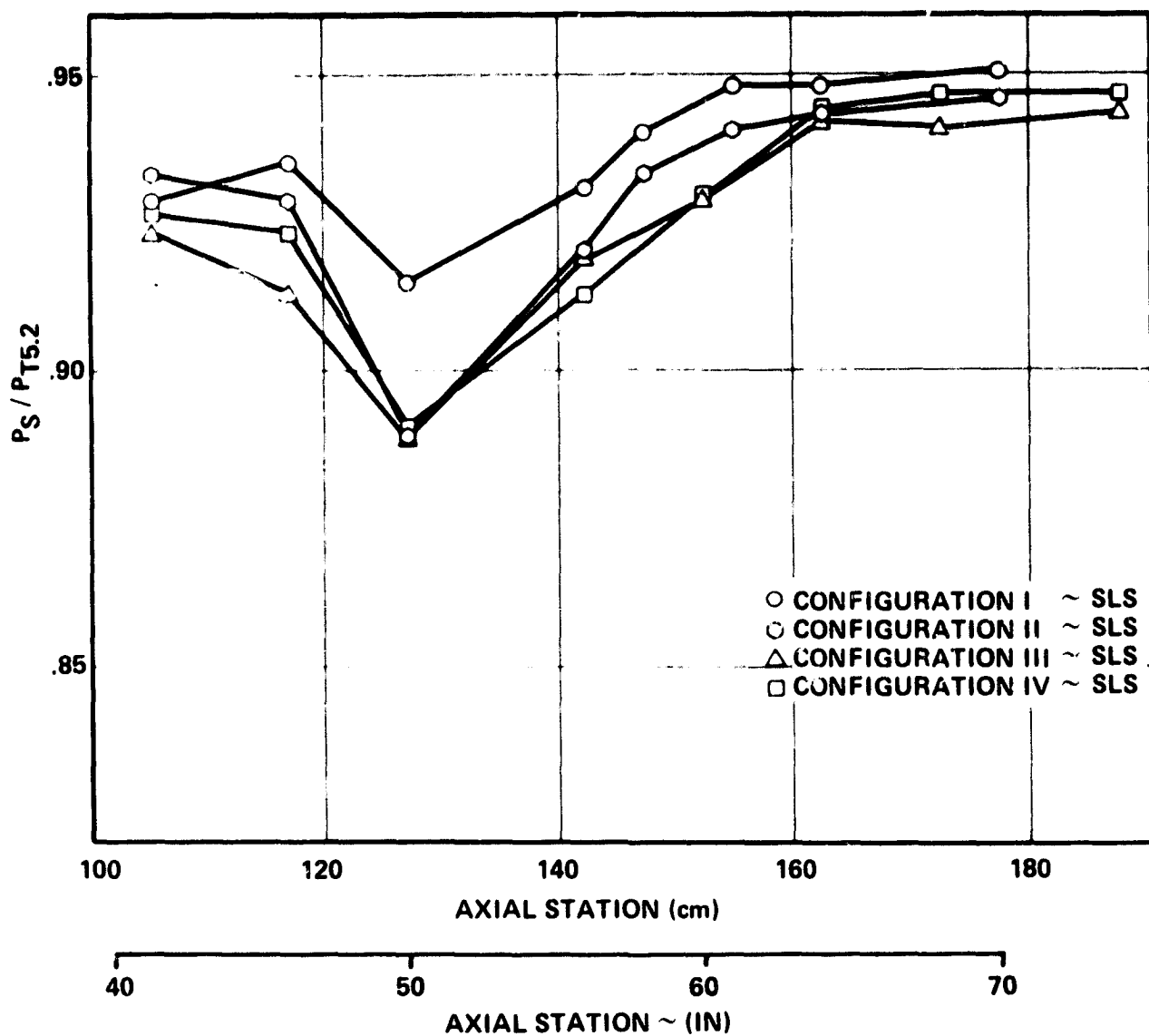
Figure 4-25. Plug Static Pressure Distribution Dual Flow, Sea Level Static Conditions.
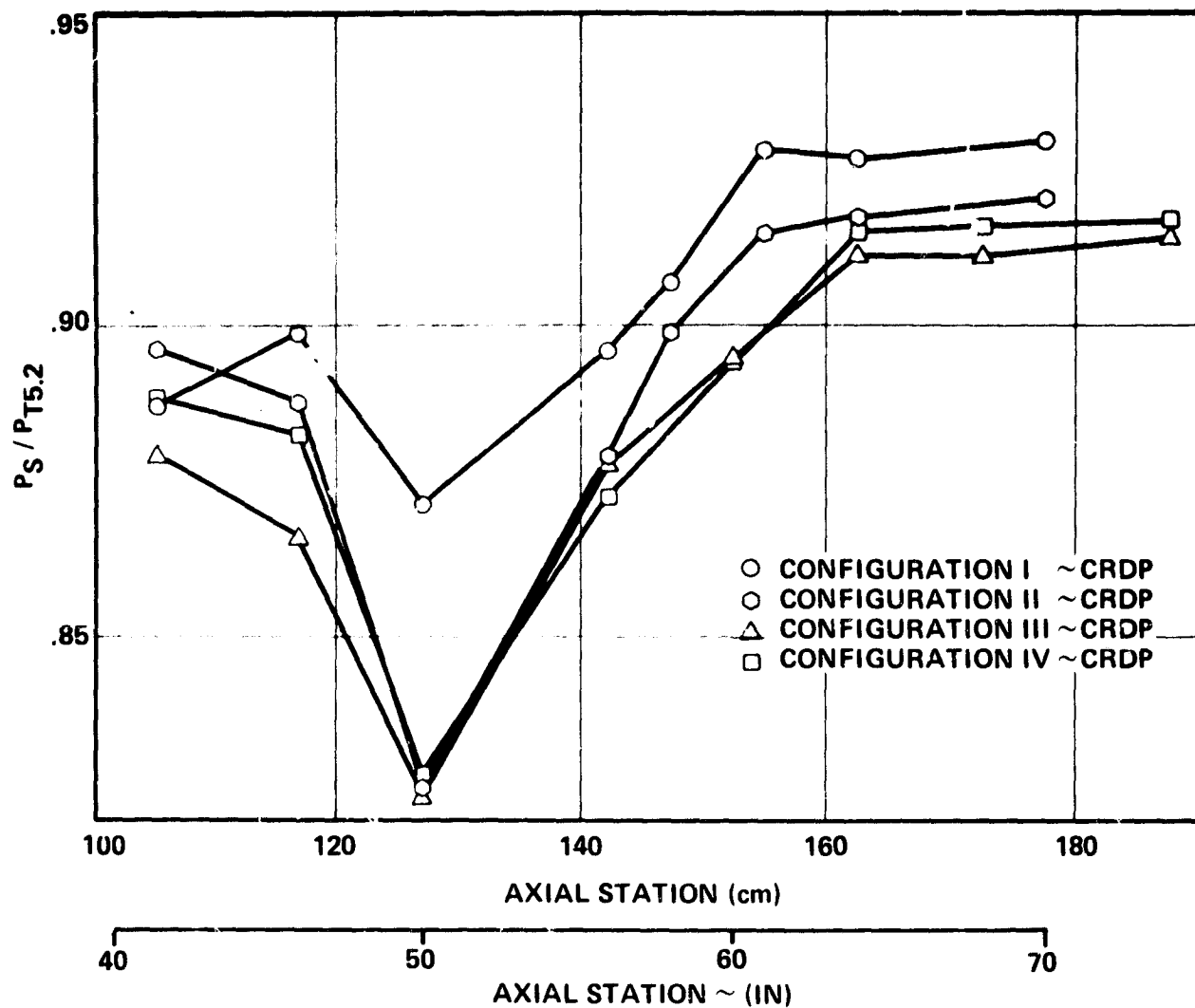
Figure 4-26. Plug Static Pressure Distribution Dual Flow, Cruise Design Point.

4.3.4 Mixing-Plane Radial Static-Pressure Gradients

A radial static-pressure gradient at the exit of the core nozzles (dual-flow mixing plane) existed for the core-only runs as shown in Figure 4-27. Configurations I and II had the same short plug while Configurations III and IV had the longer plug which also had less curvature. The splitter (Configuration I) has a pressure gradient of approximately 1 percent which is due to the curvature effect of the plug causing the flow to accelerate locally along the plug surface. Configuration II has a stronger gradient of approximately 2 percent from the plug to mid-lobe region but from the mid-lobe to the lobe-tip region the static pressure is constant. Configurations III and IV have a 1 percent pressure gradient from the plug to the mid-lobe region, which is the same as the splitter, but with a plug of less curvature. The gradient from mid-lobe to lobe-tip for the III and IV is roughly constant, this was also true for Configuration II.

The static-pressure gradient from the plug to mid-lobe region decreased from approximately 2 percent during core-only runs to approximately 1 percent in the dual-flow mode (see Figure 4-28). The gradient in the mid-lobe to the lobe-tip region changed from constant in the core-only to approximately 1 percent in dual-flow. A sharp gradient of 1-1/2 percent occurred from the lobe-tip to the fan-shroud region in dual flow. The overall static-pressure gradient is approximately 1 percent less for the sea-level-static runs than for the cruise-design-point runs. The pressure gradient is about 1/2 percent stronger from the cold to hot conditions at sea-level static but nearly the same at the cruise-design-point cold to hot conditions.

A comparison of the static-pressure gradients of each of the configurations at sea-level static and the cruise-design point is presented in Figures 4-29 and 4-30. Configuration III (long-parallel mixer) has a lower static-pressure gradient at both sea-level static and cruise-design point than the other mixer configurations. The mixer configuration gradients are slightly greater than the standard compound at sea-level static but are about the same at the cruise-design point.

Radial static-pressure gradients at off-design performance points are shown in Figures 4-31 and 4-32 for the standard compound (Configuration I) and the short parallel mixer (Configuration II) respectively. In both configurations, a larger static-pressure gradient occurs when the total-pressure ratio ($P_{T5.2}/P_{T14.0}$) is greater than 1.0. When the total-pressure ratio is less than 1.0, the gradient is a minimum. At a pressure ratio of 1.0, the core Mach number is slightly higher than that of the bypass, therefore, the core-static-pressure is slightly lower, causing some pressure gradient to occur as shown in Figures 4-31 and 4-32. As the pressure ratio increases to a value greater than 1.0, the core Mach

152
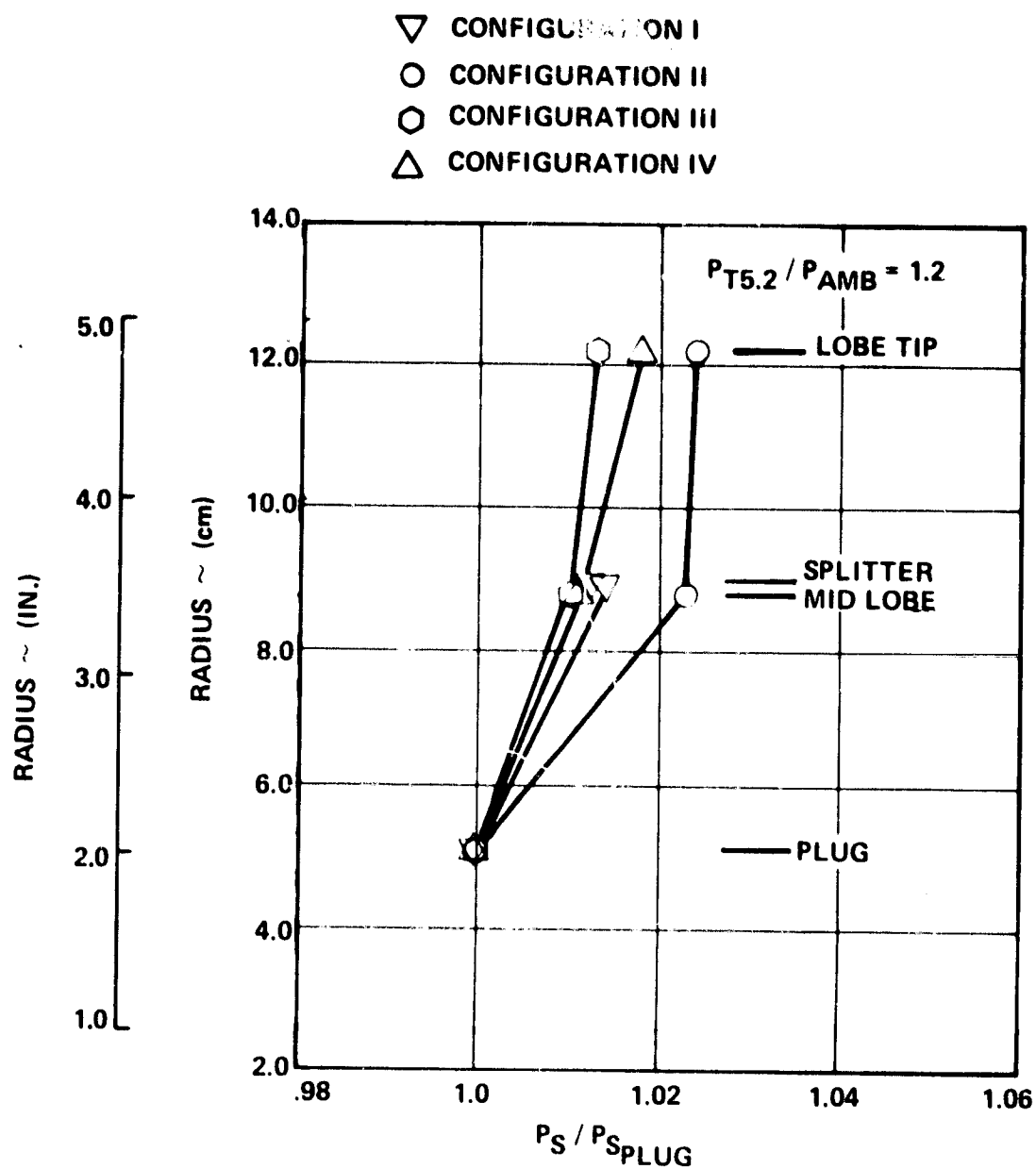
Figure 4-27.   Mixing Plane Radial Static Pressure Profiles, Core Only.
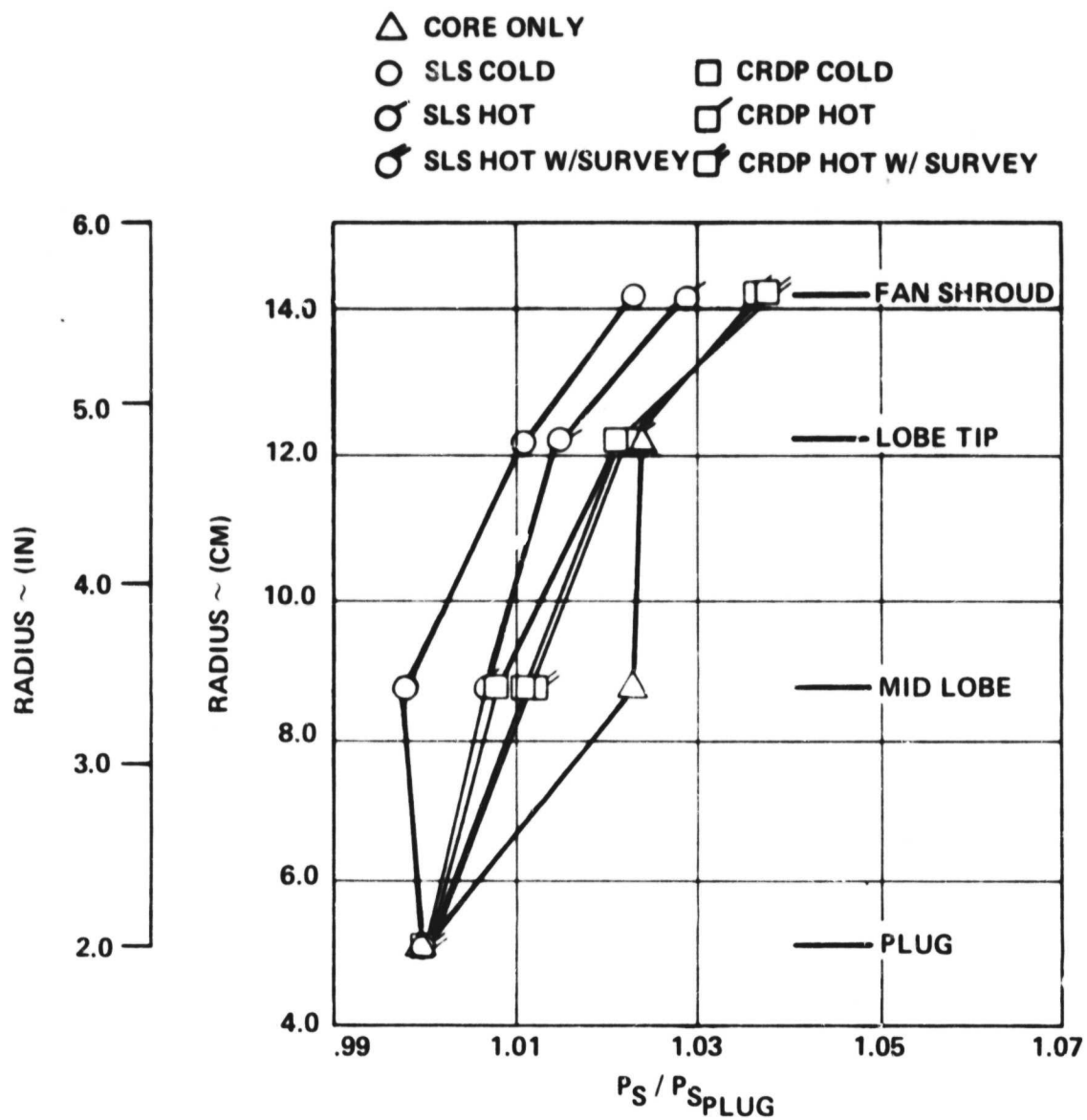
Figure 4-28. Mixing Plane Radial Static Pressure Profiles, Configuration II.
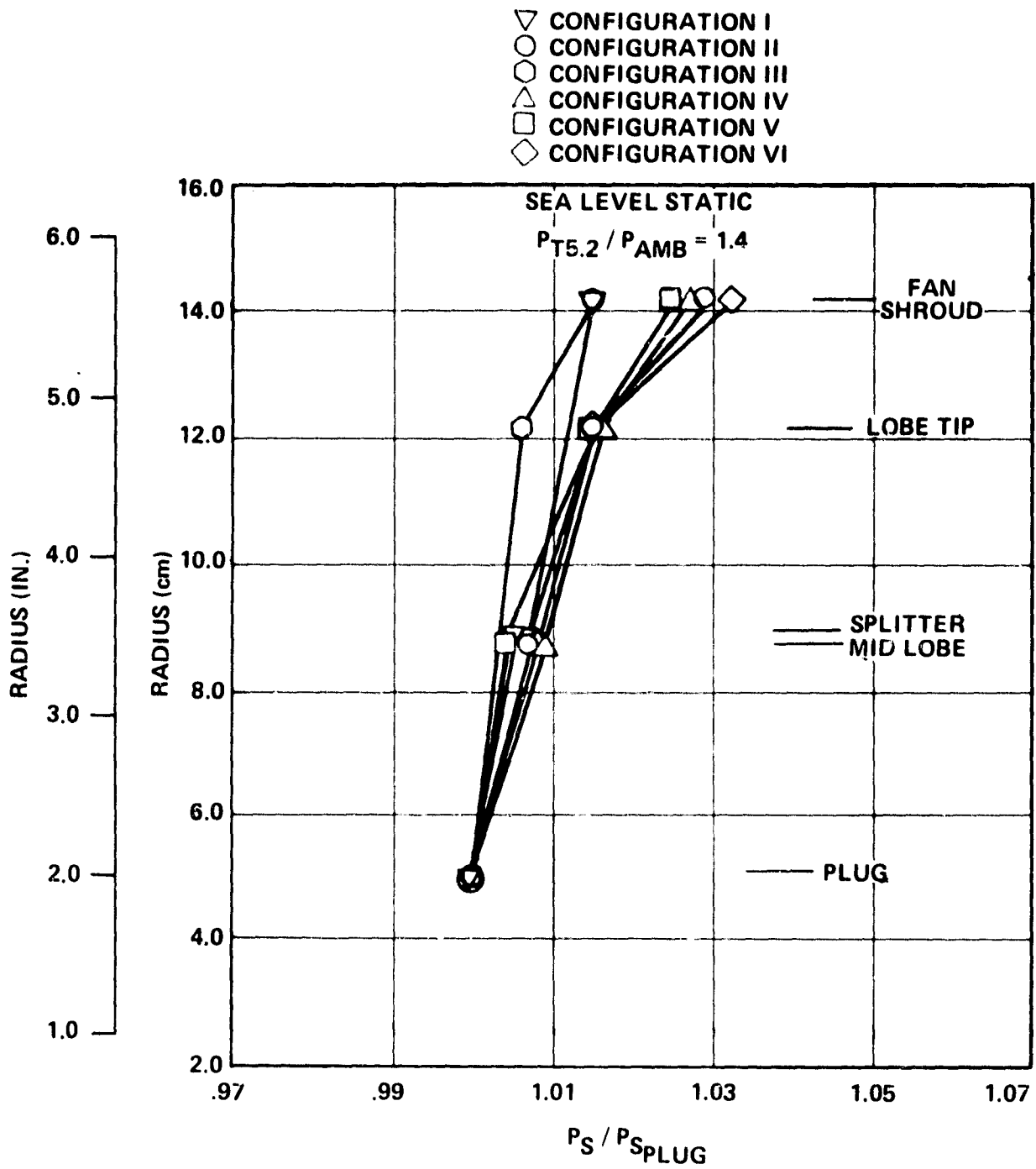
Figure 4-29. Mixing Plane Radial Static Pressure Profiles, Dual Flow Sea Level Static Conditions.

155
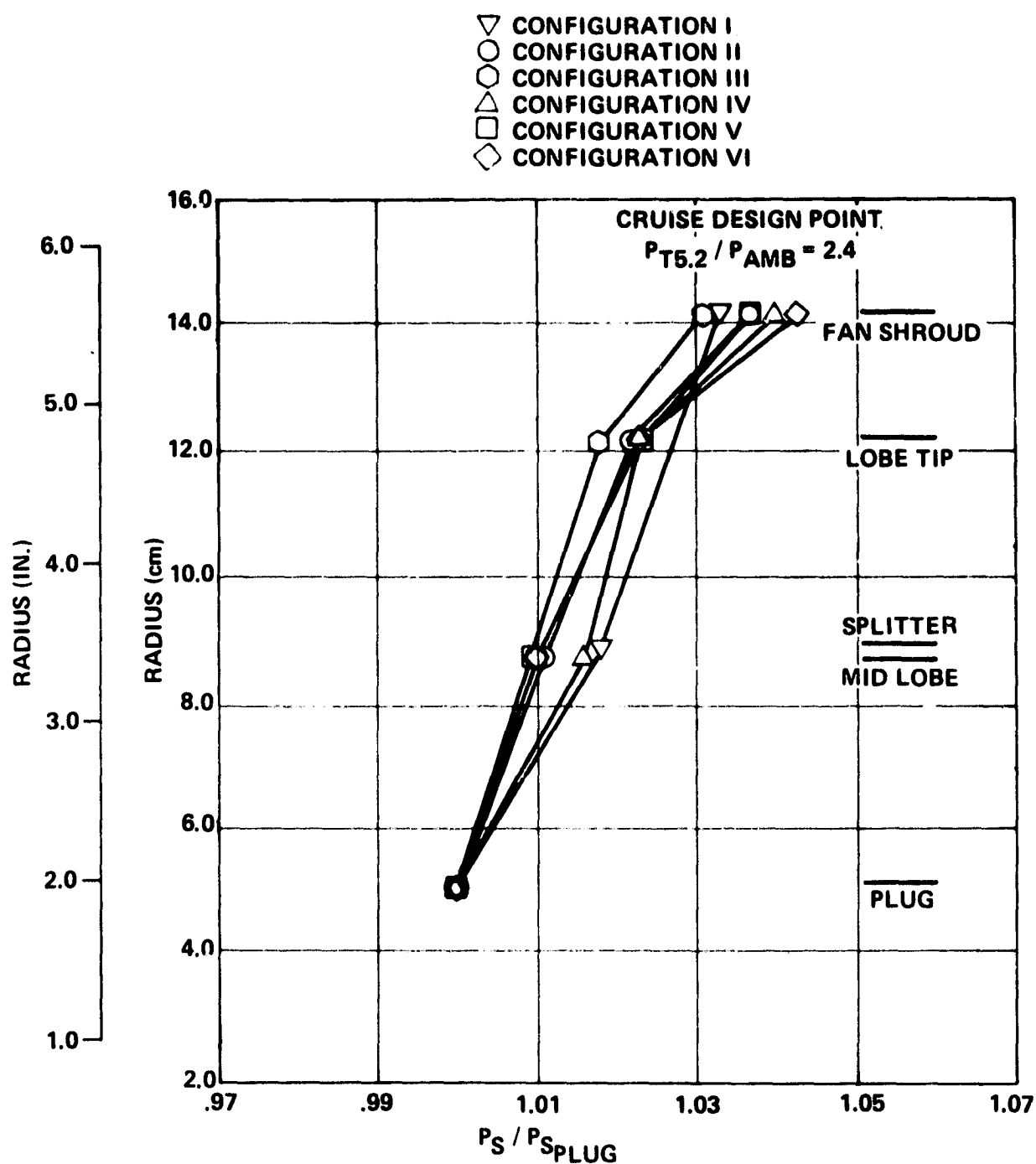
Figure 4-30. Mixing Plane Radial Static Pressure Profiles, Dual Flow Cruise Design Point Conditions.

156

CONFIGURATION I

○	$\lambda_{5.2}$ = 1.21	$\lambda_{14.0}$ = 1.20		+	$\lambda_{5.2}$ = 1.81	$\lambda_{14.0}$ = 1.60
⬡	$\lambda_{5.2}$ = 1.30	$\lambda_{14.0}$ = 1.20		⬠	$\lambda_{5.2}$ = 1.81	$\lambda_{14.0}$ = 2.00
△	$\lambda_{5.2}$ = 1.40	$\lambda_{14.0}$ = 1.20		□	$\lambda_{5.2}$ = 2.01	$\lambda_{14.0}$ = 2.00
□	$\lambda_{5.2}$ = 1.50	$\lambda_{14.0}$ = 1.40		△	$\lambda_{5.2}$ = 2.20	$\lambda_{14.0}$ = 2.00
◇	$\lambda_{5.2}$ = 1.59	$\lambda_{14.0}$ = 1.40		⬠	$\lambda_{5.2}$ = 2.01	$\lambda_{14.0}$ = 2.40
▽	$\lambda_{5.2}$ = 1.46	$\lambda_{14.0}$ = 1.60		⋈	$\lambda_{5.2}$ = 2.20	$\lambda_{14.0}$ = 2.40
✕	$\lambda_{5.2}$ = 1.60	$\lambda_{14.0}$ = 1.60		⋈	$\lambda_{5.2}$ = 2.59	$\lambda_{14.0}$ = 2.40
⬠	$\lambda_{5.2}$ = 1.40	$\lambda_{14.0}$ = 1.40		⬠	$\lambda_{5.2}$ = 2.40	$\lambda_{14.0}$ = 2.40
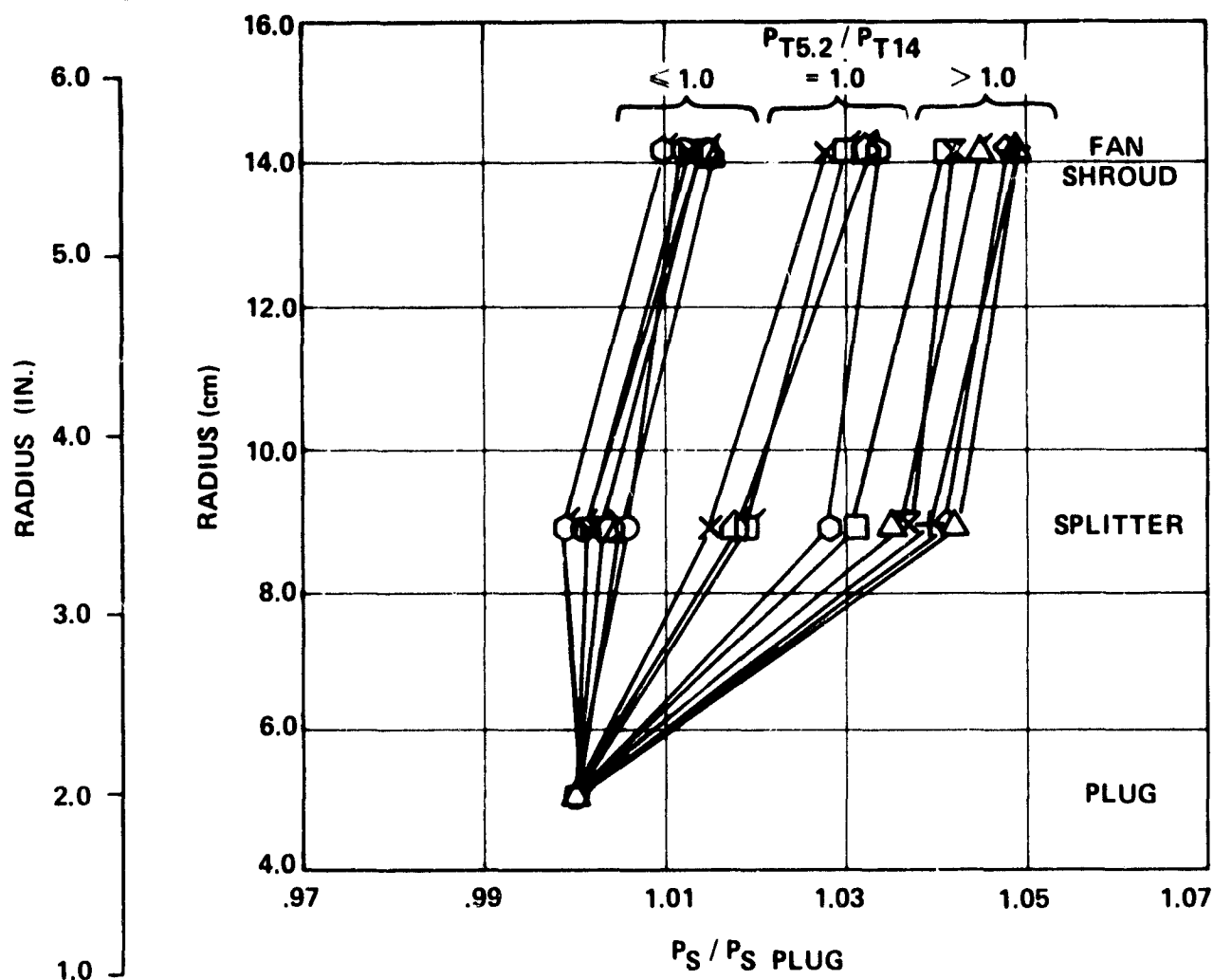
Figure 4-31. Mixing Plane Radial Static Pressure Profiles, Off-Design, Configuration I.

157

CONFIGURATION II

○	$\lambda_{5.2} = 1.21$	$\lambda_{14.0} = 1.20$	+	$\lambda_{5.2} = 2.01$	$\lambda_{14.0} = 1.60$
⬡	$\lambda_{5.2} = 1.30$	$\lambda_{14.0} = 1.19$	⟋	$\lambda_{5.2} = 1.80$	$\lambda_{14.0} = 2.01$
△	$\lambda_{5.2} = 1.51$	$\lambda_{14.0} = 1.41$	□	$\lambda_{5.2} = 2.00$	$\lambda_{14.0} = 2.00$
□	$\lambda_{5.2} = 1.60$	$\lambda_{14.0} = 1.40$	△	$\lambda_{5.2} = 2.51$	$\lambda_{14.0} = 2.00$
◇	$\lambda_{5.2} = 1.47$	$\lambda_{14.0} = 1.60$	⟋	$\lambda_{5.2} = 2.21$	$\lambda_{14.0} = 2.40$
▽	$\lambda_{5.2} = 1.60$	$\lambda_{14.0} = 1.60$	⋈	$\lambda_{5.2} = 2.59$	$\lambda_{14.0} = 2.40$
✕	$\lambda_{5.2} = 1.79$	$\lambda_{14.0} = 1.60$	✕	$\lambda_{5.2} = 2.93$	$\lambda_{14.0} = 2.40$
⬠	$\lambda_{5.2} = 1.40$	$\lambda_{14.0} = 1.40$	⬠	$\lambda_{5.2} = 2.40$	$\lambda_{14.0} = 2.40$
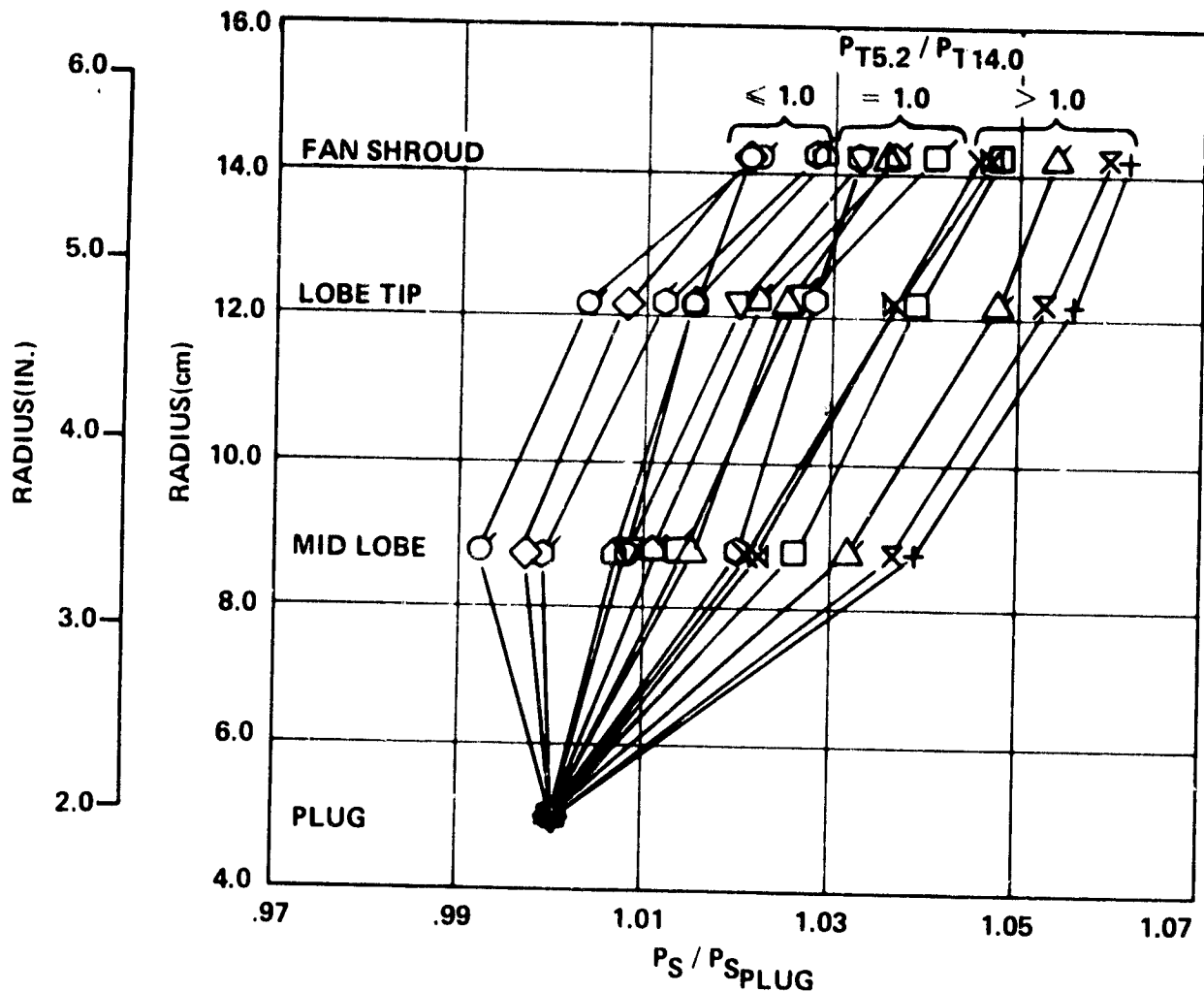
Figure 4-32. Mixing Plane Radial Static Pressure
Profiles, Off-Design, Configuration II.

158

number increases over the bypass Mach number and the static-pressure gradient increases. At total-pressure ratios less than 1.0, the bypass Mach number becomes greater than the core Mach number and the static pressure in each stream approaches the same value. This decreases the static pressure gradient as shown in Figures 4-31 and 4-32.

4.3.5 Acoustic Surveys Measured Noise Data Scaled to Full-Size Nozzle

The measured noise levels for each of the six scale model nozzle configurations are presented in Appendix D. The measured static noise data shows conclusively that Configuration II (short parallel mixer and long mixing duct) provided the lowest noise levels of the six configurations tested.

In order to provide additional information regarding the relative acoustic performance of the six nozzle configurations tested, the scale model noise data was scaled to a full size nozzle in flight and the resultant jet noise levels were "flown" simulating a FAR Part 36 takeoff noise certification procedure.

4.3.5.1 Scaling Procedure

The scaling procedure utilized the jet noise prediction methods of References 20 and 21. In this procedure, the scale model nozzle static jet noise levels were predicted based upon the known operating conditions for the nozzle. The predicted jet noise directivity levels were then compared to the measured noise directivity levels and a correlation, i.e., delta dB, between predicted and measured levels was established for each one-third octave frequency at each microphone location.

A jet noise prediction for the full-size nozzle configurations was then performed based upon the full-size nozzle geometry and operating conditions of each nozzle in flight. The necessary shift in frequency of the peak jet noise levels was also established. The resultant full-size nozzle jet noise levels were determined by algebraically adding the corrections established between the predicted versus measured scale model static noise levels to the predicted levels for the full-size nozzle, accounting for the necessary frequency shift. The scaling procedure is summarized in Figure 4-33.

Figure 4-34 presents a typical result of the scaling procedure in which the measured noise data for Configuration II has been scaled to a full-size nozzle configuration in flight. The data shown is based on the measured sea level static takeoff condition and is for microphone location 6 (1.04 Radians [60°] from the jet exhaust centerline). A similar scaling result was accomplished for each microphone location.

MEASURED SCALE
MODEL NOISE DATA

↓

CORRECT FOR
GROUND REFLECTION

↓

SPL_{FF}

↓

PREDICT JET [1]
NOISE FOR STATIC
SCALE MODEL
NOZZLE

SPL_M

→

DETERMINE
MEASURED VS PREDICTED
SPL CORRECTIONS

$\Delta SPL = SPL_{FF} - SPL_M$

↓

DETERMINE PEAK
FREQUENCY SHIFT
BETWEEN SCALE
AND FULL SIZE
NOZZLE

$\Delta FREQ$

←

PREDICT JET [1]
NOISE FOR FULL-
SIZE NOZZLE
IN FLIGHT

SPL_{FS}

↓

SCALE MEASURED
DATA TO FULL-
SIZE NOZZLE
IN FLIGHT

$SPL = SPL_{FS} + \Delta SPL + \Delta FREQ$

NOZZLE THRUST
COEFFICIENT

↓

↓

FLYOVER NOISE
PREDICTION

←

AIRCRAFT CLIMB
ANGLE WITH
NOZZLE CONFIG.

↓

SELECT BEST
NOZZLE CONFIG.

[1] BASED ON PREDICTION METHODS IN REFERENCES 20 AND 21.

Figure 4-33. QCGAT Model Nozzle Scaling Procedure.

160
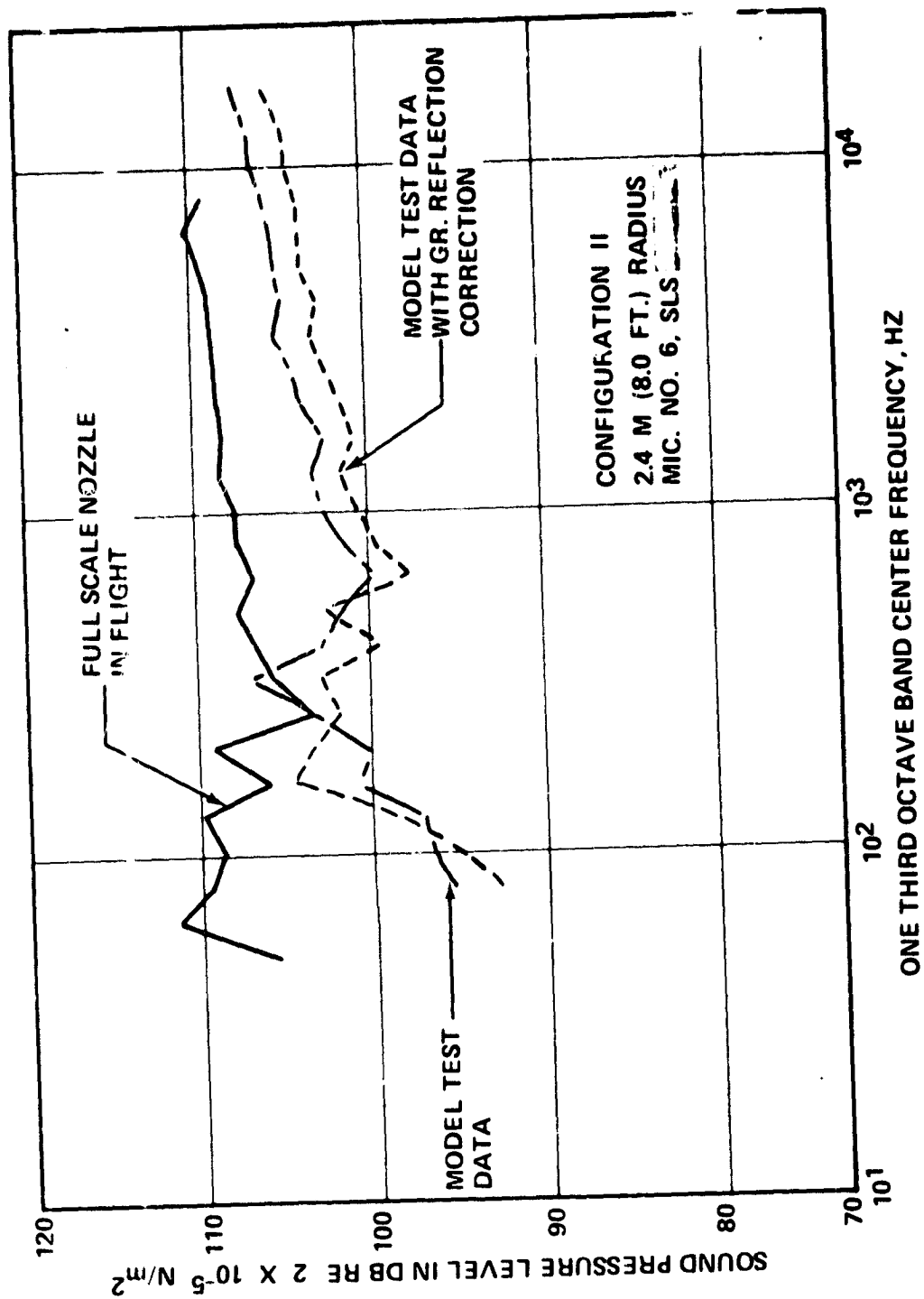
Figure 4-34. Scaling of Model Nozzle Data to a Full-Size Nozzle In Flight.

161

4.3.5.2 Flyover Procedure

The resultant full-size nozzle jet noise levels were "flown" by computer program to determine the relative jet noise levels corresponding to the FAR Part 36 takeoff certification condition in terms of effective perceived noise level (EPNdB) for each nozzle configuration, see Reference 22.

Figure 4-35 presents a summary of the flyover prediction procedure. The full-size nozzle jet noise directivity levels were "flown" along an assumed aircraft takeoff flight path. The aircraft flight profile used in the flyover prediction was the reference takeoff profile of the QCGAT conceptual aircraft. The aircraft flight profile, i.e. climb angle, was adjusted from the reference climb angle as a function of the measured nozzle thrust coefficient for each nozzle configuration by the following expression:

$$\text{Sin } \alpha = \frac{(F_{ID} \cdot C_F) - F_{ID}}{AGW} + \text{Sin } \alpha_R$$

where:

α	is the aircraft climb angle
F_{ID}	is the reference thrust
C_F	is the nozzle thrust coefficient
AGW	is the aircraft gross weight
α_R	is the reference climb angle

The results of the flyover noise analysis in the form of the relative jet noise level reductions in units of EPNdB for each mixer nozzle configuration is shown in Figure 4-36. The relative jet noise reductions are referenced to the compound nozzle with assumed zero percent mixing, i.e., evaluated acoustically as a co-annular system.

The results of the flyover analysis for the scaled up full-size nozzle configurations confirm the previous conclusions that nozzle configuration II will provide the lowest jet noise levels of the six nozzle configurations tested. This conclusion, combined with the superior sea level static aerodynamic performance for configuration II, resulted in this configuration being selected for use on the QCGAT engine.
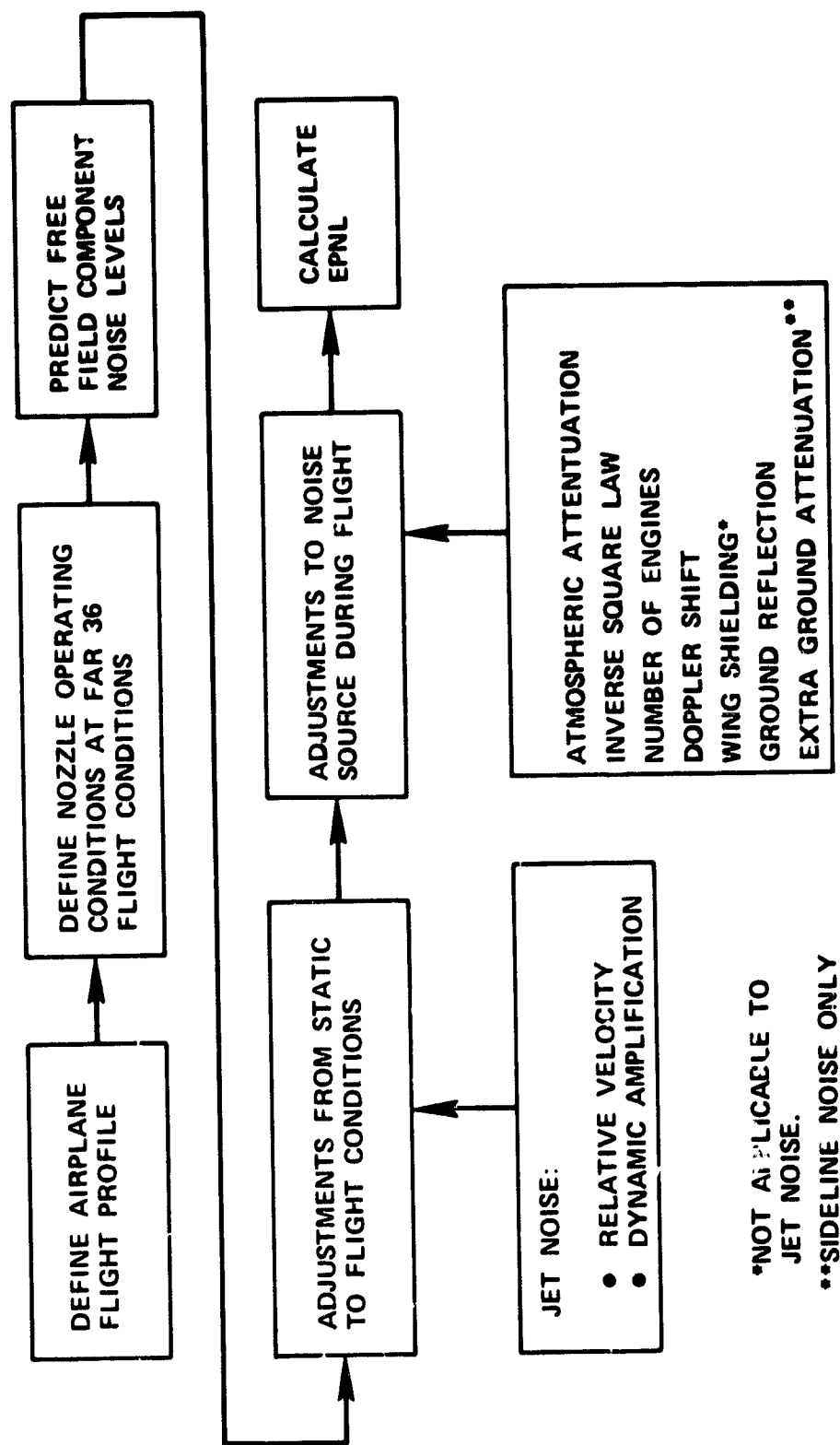
Figure 4-35. Flyover Noise Prediction Procedure.

163
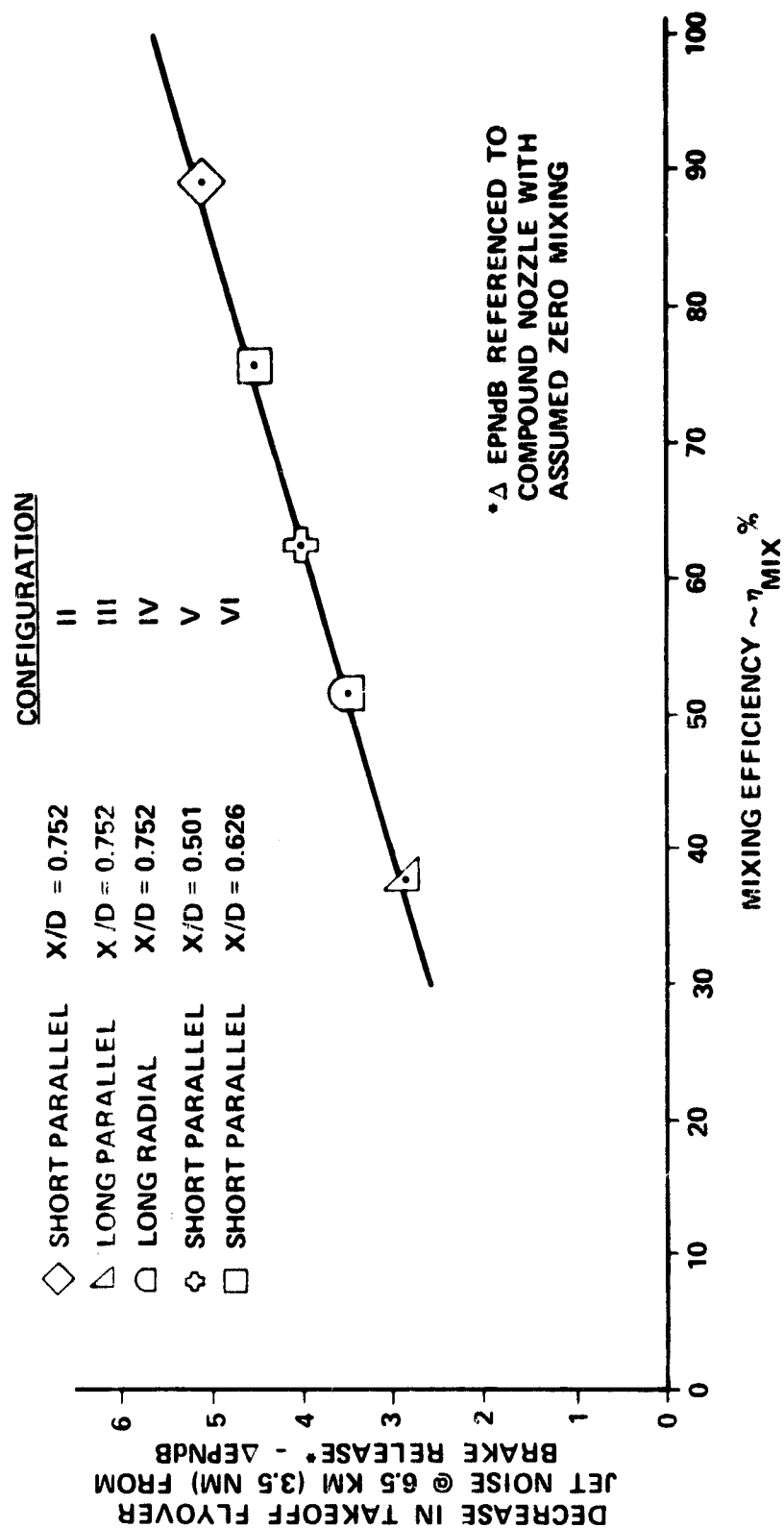
Figure 4-36. Flyover Jet Noise Reduction Versus Mixing Efficiency.

164

4.4 Exit Surveys

4.4.1 Contour Plots

A 0.52-Radian (thirty-degree) pie-shaped segment of the
exhaust duct at the exit plane was surveyed for the tested con-
figurations at the sea-level-static take-off and cruise-design
points. Since the sea-level-static take-off and cruise-design
point surveys were basically identical, only the sea-level-static
take-off contours will be discussed in detail in this section
with comparison of the surveys for both conditions covered in a
subsequent section.

Contour maps of total pressure ratio, total temperature ratio,
and velocity ratio for Configurations I through IV are presented
in Figures 4-37, 4-38 and 4-39, respectively. The survey plots of
the mixer configurations (II, III and IV) bound the region
between the centerlines of two core lobes.

A value for the total pressure split $(P_{T14.0}/P_{T5.2})$ at the
rating station is provided along with the total temperature split
$(T_{T14.0}/T_{T5.2})$ and the core critical velocity value $(a_{cr5.2})$ for
reference.

The standard-compound (Configuration I) exhibited large
isobar regions for the core and bypass flows at the nozzle exit.
This can be seen in Figure 4-37. From the contour values, the
bypass loss would be estimated at 0.7 percent and the core loss at
about 1.0 percent. This agrees well with the thrust data results
which will be covered in a later section. A small annular region
of apparent mixing occurred between the core and bypass regions.
In Configurations II and III (parallel mixers) core flow was
moved radially outward into the shroud region while bypass flow
was moved radially inward towards the hub region. Configuration
IV (radial mixer) shows the same trend as the parallel mixers but
to a larger degree. This would be expected from a geometry com-
parison as shown earlier in Figure 3-45.

Total temperature contours exhibit the same trends described
above for the total pressure contours but the trends are more
pronounced as shown in Figure 4-38. Again, a small thermal-mixing
region occurs for the standard compound with a large high tempera-
ture core center region present. The parallel mixers reduced the
peak temperature by approximately 25 percent compared to the
standard compound and the radial mixers which reduced the peak
temperature by approximately 47.5 percent. The peak temperatures
of the parallel mixers occurred in the hub region over a very
small area, whereas the radial mixer peak temperature occurred as
an annular mid-region of significant area. Hot-core flow regions
also occurred in the shroud regions of the parallel mixers
indicating core flow might have been exiting the mixer lobes with
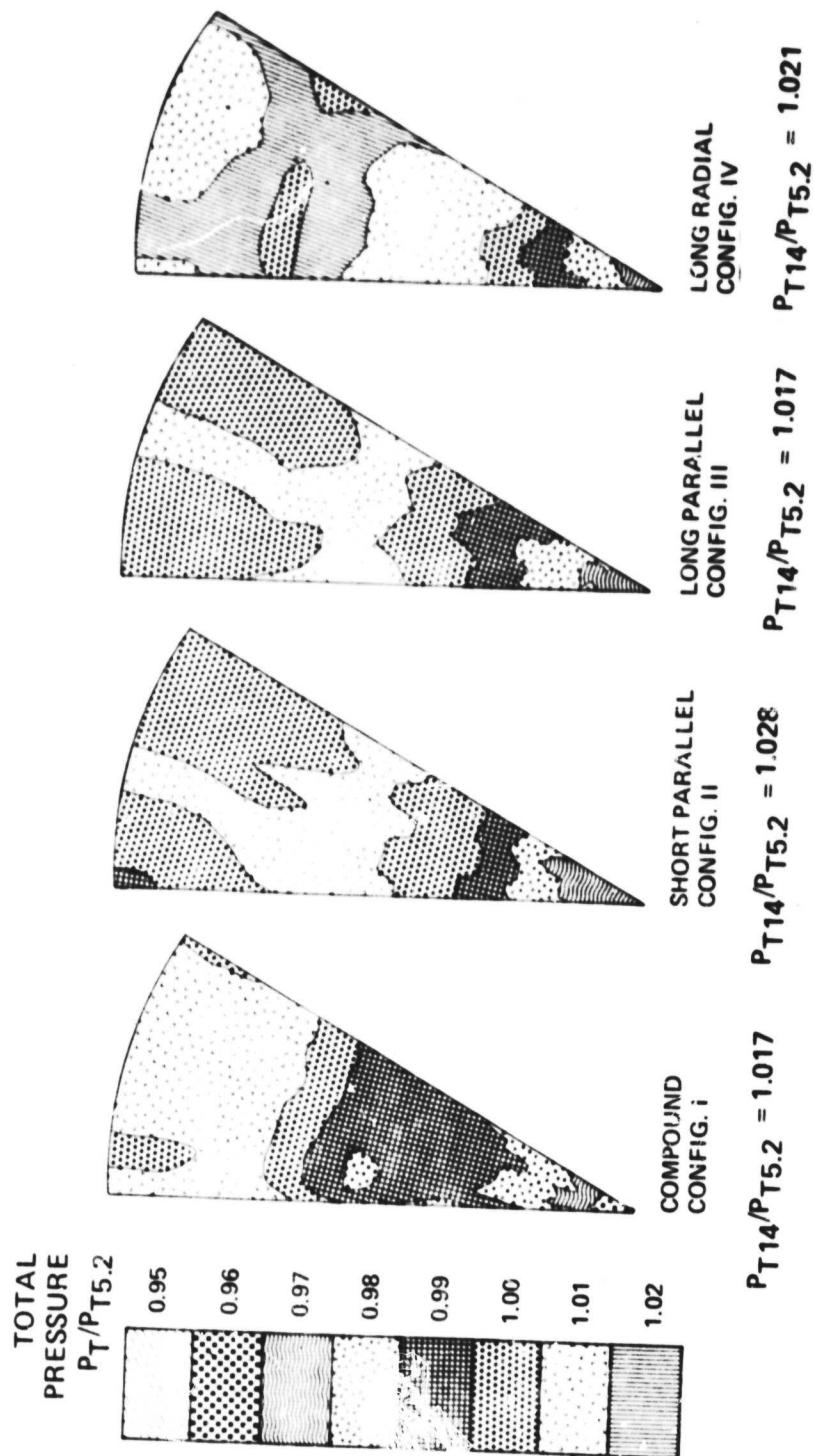
Figure 4-37. QCGAT Model Exhaust Exit Nozzle Pressure Surveys at Sea Level Static.
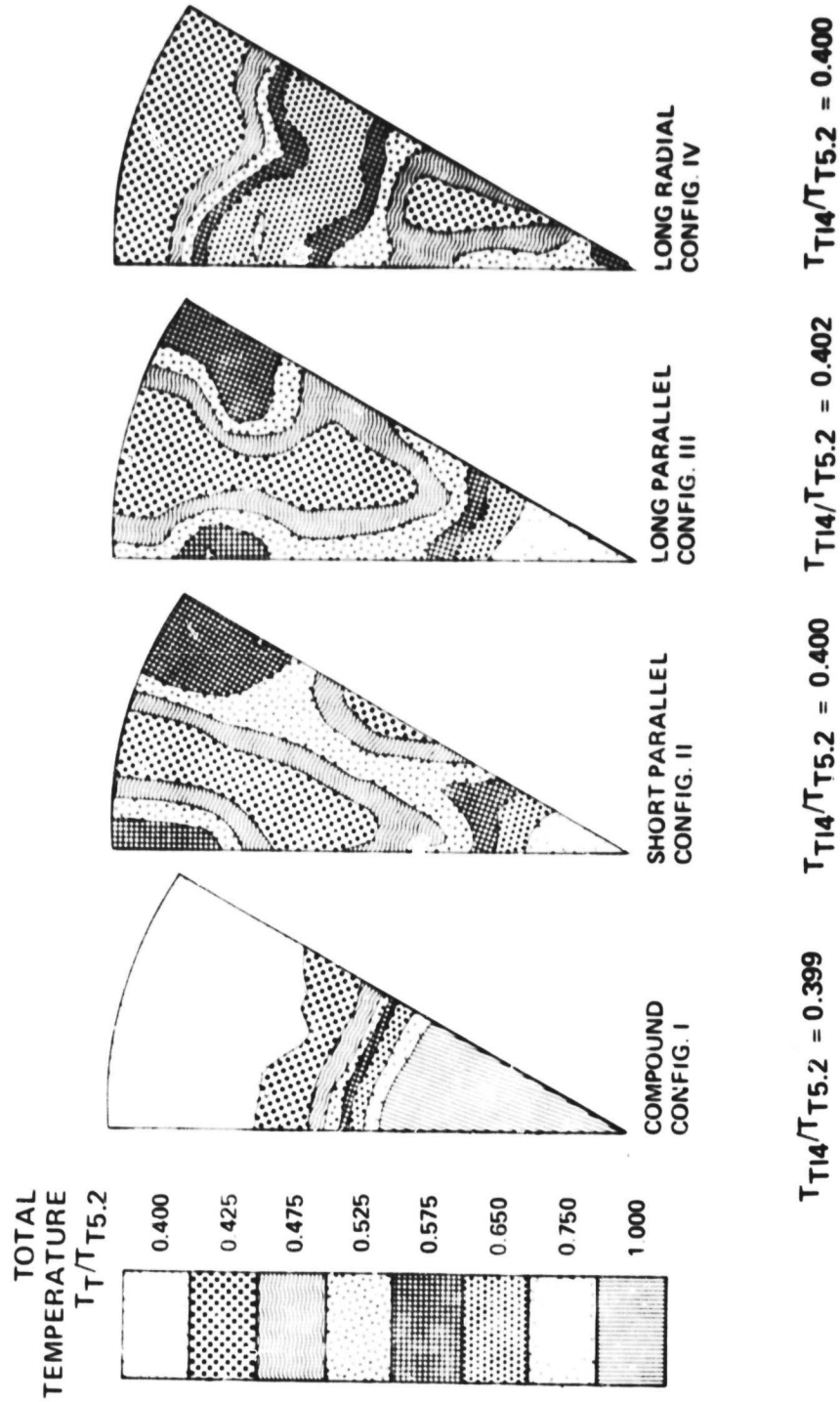
Figure 4-38. QCGAT Model Exhaust Exit Nozzle Temperature Surveys at Sea Level Static.

167
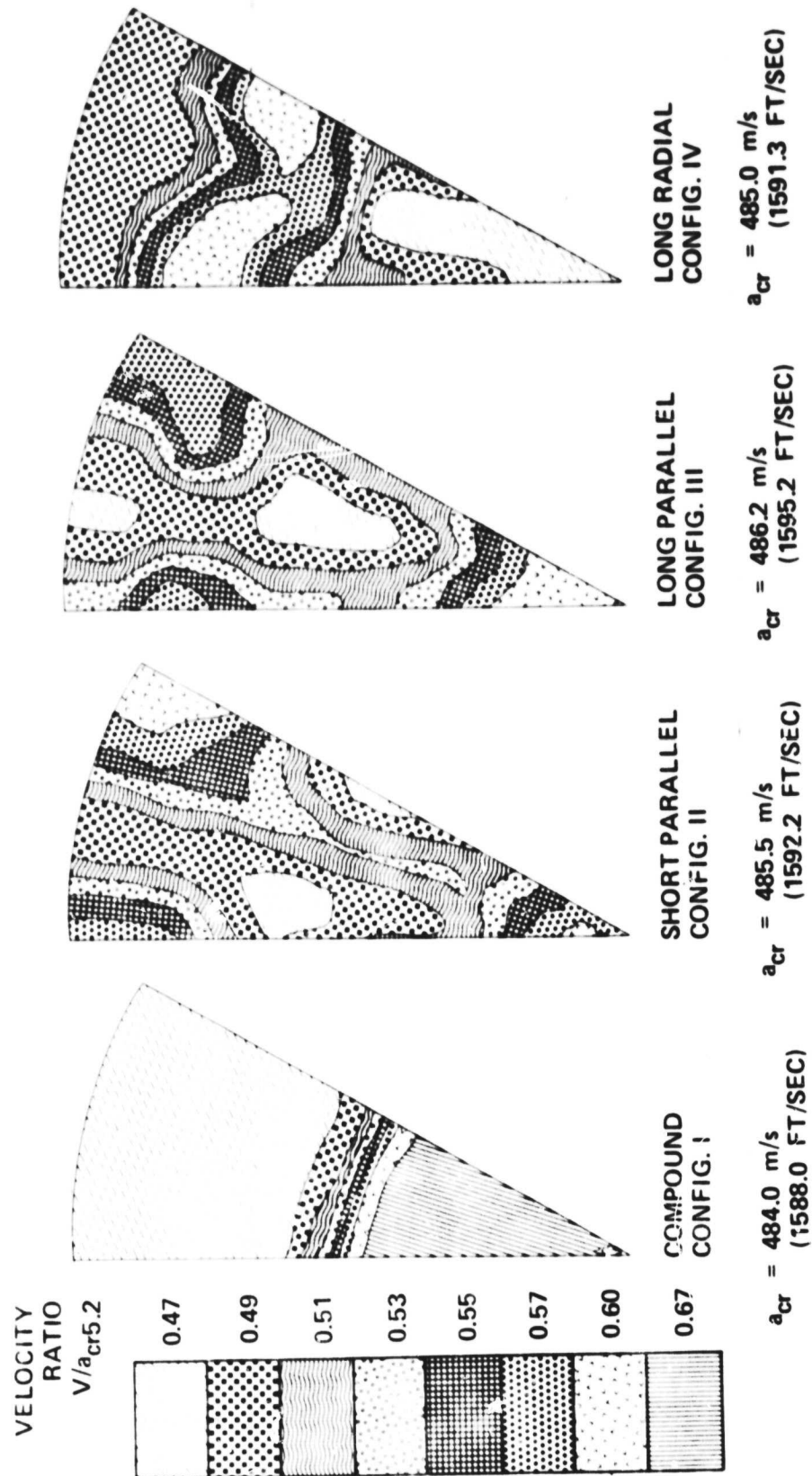
Figure 4-39. QCGAT Model Exhaust Exit Nozzle Velocity Surveys at Sea Level Static.

an outward radial velocity component. Configuration II appears
to have the smallest hot temperature zones and the smallest cold
temperature zones, indicating more thermal mixing than in the
other configurations.

The effects of thermal mixing and pressure loss determine
the velocity levels at the nozzle exit as shown in Figure 4-39.
As expected, the standard compound has two large velocity regions,
the high core velocity at the center and the lower bypass velocity
in the annular shroud region. All the mixer configurations
reduced the peak velocity region size and level relative to the
standard compound. The core critical velocity at rating station
5.2 at the sea-level-static setting is approximately 488 m/sec
(1600 ft/sec). Therefore, the mixer configuration peak velocities
were about 30.5 m/sec (100 ft/sec) lower than the standard com-
pound and were considerably reduced in size as shown in Figure
4-39.

Two additional mixing duct lengths with ratios of X/D = 0.50
and 0.63 were tested with the short parallel mixer to compare to
the long mixing duct (X/D = 0.75) results of Configuration II.
Comparisons of P_T, T_T, and velocity are shown in Figures 4-40,
4-41 and 4-42, respectively. The total pressure contours are
included for completeness (see Figure 4-40), but the comparison
is affected by the rating station total pressure split which var-
ied between the configurations by as much as one percent. No
immediate conclusion can be obtained based on the pressure con-
tours. However, in Figure 4-41, Configuration II has a smaller
high temperature region and smaller cold temperature region, indi-
cating a higher degree of thermal mixing than Configurations V or
VI. Velocity contours are similar for all three mixing duct lengths,
(see Figure 4-42). The shorter duct (Configuration V) has slightly
larger high velocity zones at the shroud and in the mid-region.
Configuration II has lower velocity zones at the hub and mid-
region than V and VI, thus Configuration II appears to have
slightly improved mixing due to the increased length over the
other mixing ducts.

4.4.2 Radial Profiles

Total temperature contour plots for the sea-level-static
take-off power setting were presented in the previous section.
The cruise design point contours were essentially the same, as can
be seen by comparing the radial temperature profiles at 0° (core
lobe centerline position), 6°, and 15° (bypass-lobe centerline
position) as shown in Figure 4-43. The radial profiles are
essentially the same at each of the three circumferential posi-
tions; thus the level of thermal mixing appears to have remained
the same between nozzle pressure ratio settings of 1.4 and 2.4.

MIXING DUCT LENGTH VARIATION

TOTAL PRESSURE RATIO $P_T/P_{T5.2}$

0.95
0.96
0.97
0.98
0.99
1.00
1.01
1.02

CONFIG. II
L/D = 0.75

$P_{T14}/P_{T5.2}$ = 1.028

CONFIG. V
L/D = 0.50

$P_{T14}/P_{T5.2}$ = 1.016

CONFIG. VI
L/D = 0.63

$P_{T14}/P_{T5.2}$ = 1.022
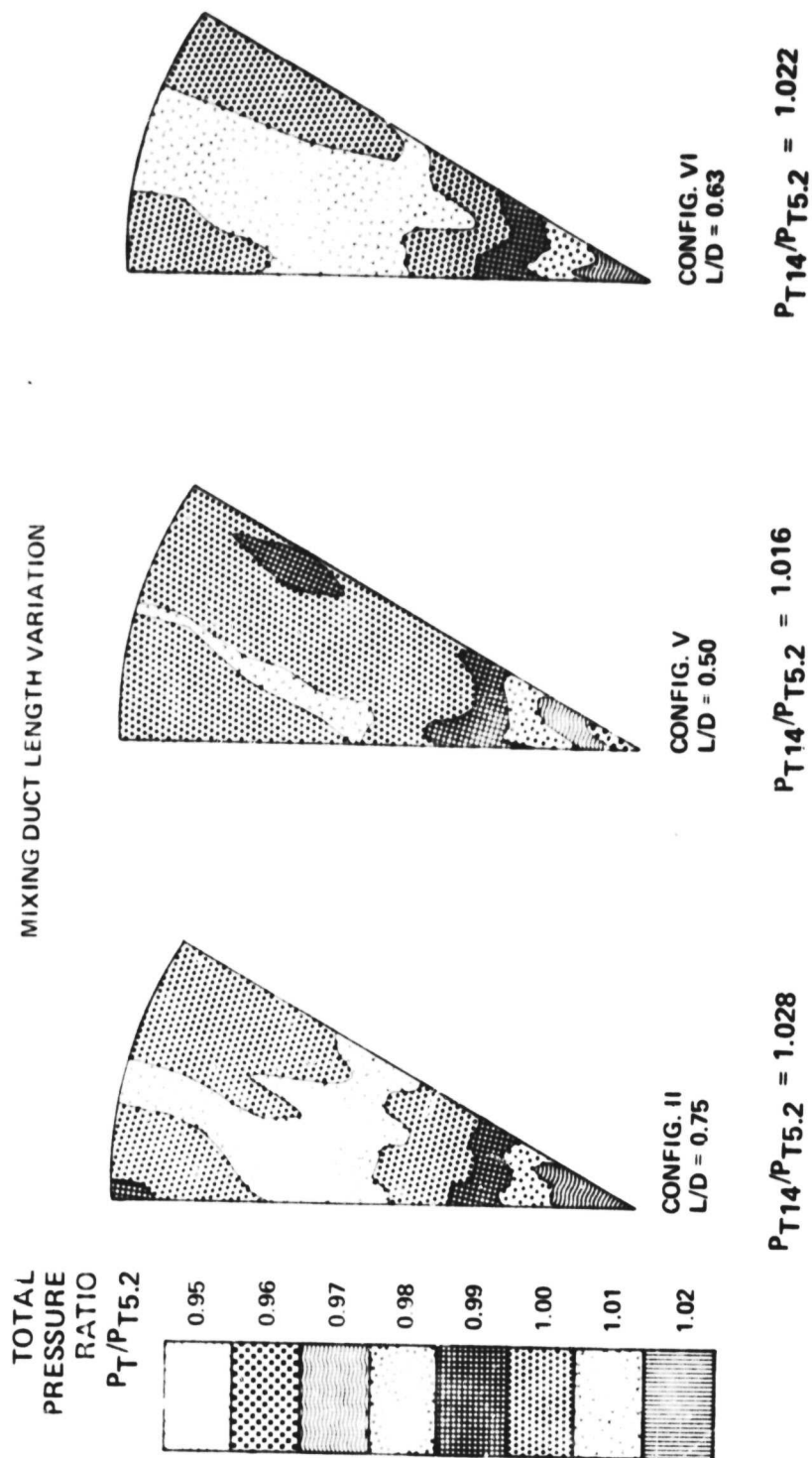
Figure 4-40. QCGAT Model Exhaust Exit Pressure Surveys at Sea Level Static With Duct Length Variations.
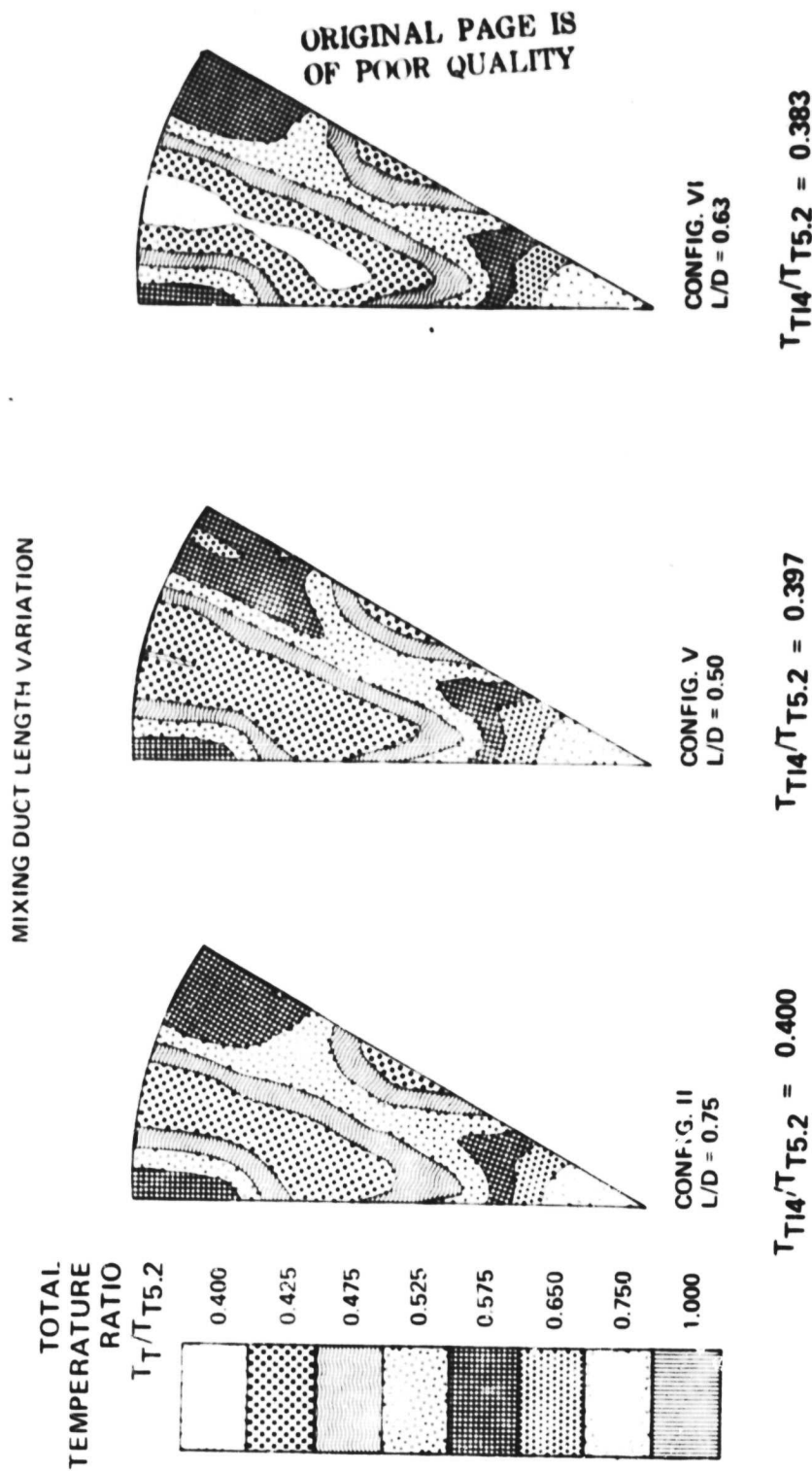
Figure 4-41. QCGAT Model Exhaust Exit Temperature Surveys at Sea
Level Static With Duct Length Variations.

171
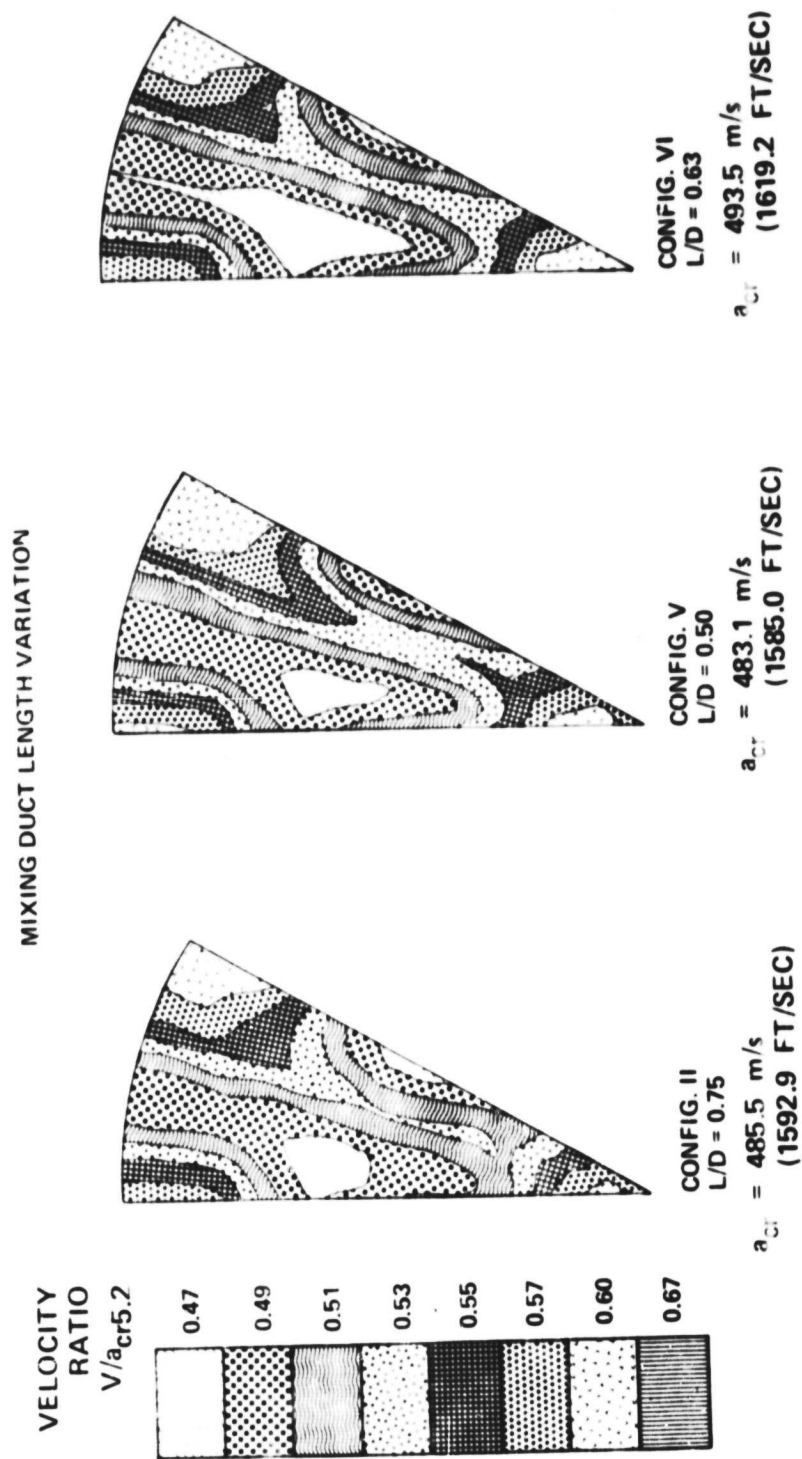
Figure 4-42. QCGAT Model Exhaust Exit Velocity Surveys at Sea Level Static With Duct Length Variations.
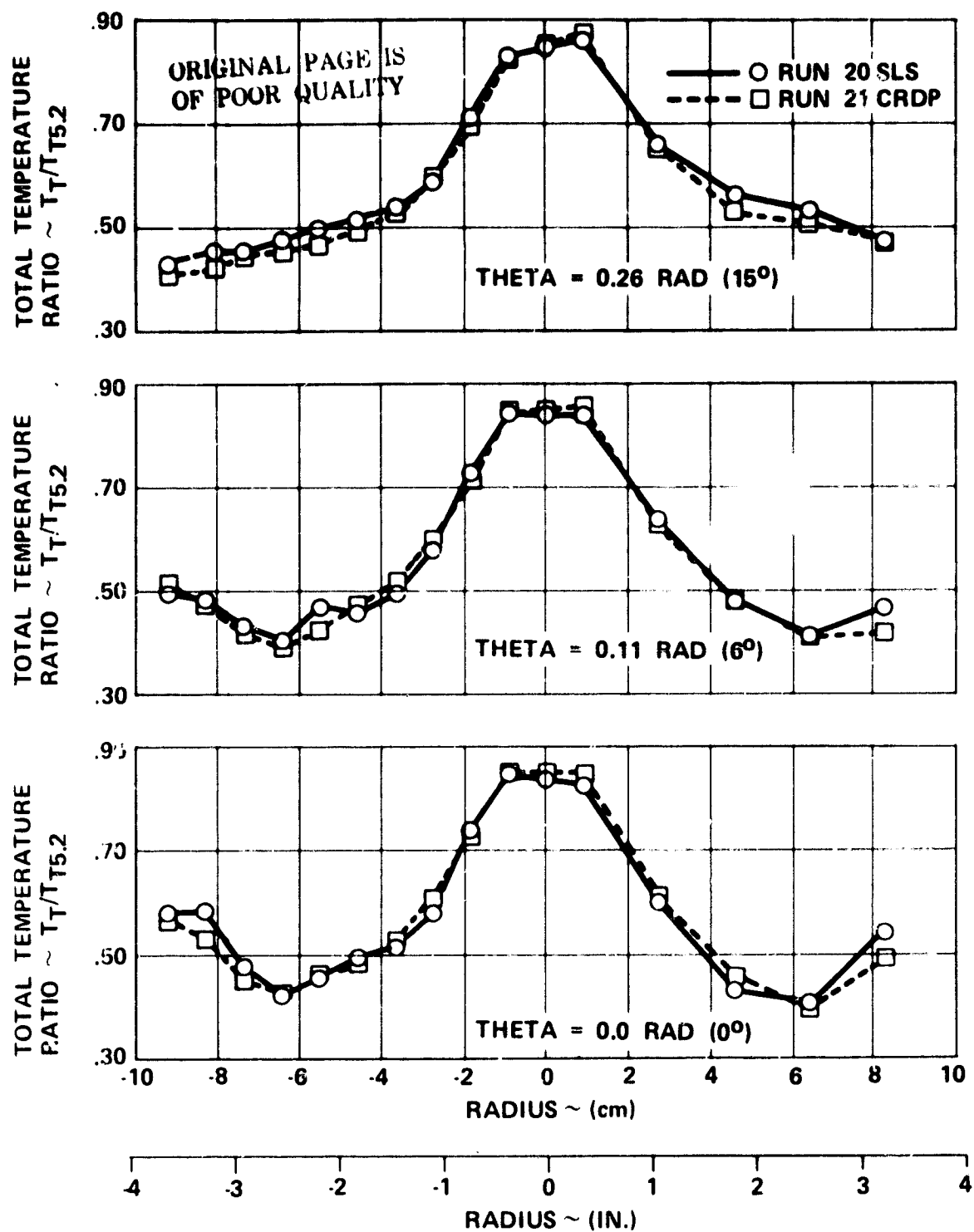
Figure 4-43.   Exit Survey Plane Radial Temperature Profiles.

173

The integrated exit total temperature was based on the ten
temperature elements recorded on the survey rake side without
pressure readings. The five thermocouples located on the same side
of the rake as the total pressures were used for backup thermo-
couples and a symmetry check. During the testing, all of the
thermocouples remained operational. The set of five backup
thermocouples was recorded but only used for a symmetry check.
A comparison of total-temperature radial profiles on both sides of
the rake indicated the exit nozzle temperature contours were
symmetric as shown in Figures 4-44, 4-45 and 4-46 for Configura-
tions II, I I, and IV, respectively. Configuration IV, the radial
mixer, had the largest deviations on the radial profiles. The
good degree of radial profile agreement on both sides of the
rake indicate that the integrated total temperatures are a good
representation of the entire nozzle exit.

4.4.3   Tested Versus Predicted Nozzle Exit Integrated Radial
Profiles

Tested and predicted total temperatures and velocities at the
nozzle exit were integrated circumferentially to obtain radial
profiles. The mixing-analysis prediction accuracy is questionable
in highly accelerating, high Mach number flow fields. (The
prediction procedure, however, appears to be valid with some
modifications.) Since the standard compound system produces a
symmetric flow field, the circumferentially-integrated radial
profile is the best representation of the radial profile. The
standard compound system, therefore, provides a comparison of the
basic mixing between predicted and tested data. The predicted
temperature profile at the nozzle exit indicates a larger degree
of mixing than the tested profile as shown in Figure 4-47. As
shown in Figure 4-48, the predicted velocity profile is essentially
linear from the peak core value to the shroud, whereas the test
data indicates that two separate velocity streams still exist
with a small mixing zone between them. At this point, it is uncer-
tain as to whether the static pressure gradient, the temperature
mixing or the high Mach number region is the cause of the poor vel-
ocity agreement at the nozzle exit. To remove the effect of the
temperature profile difference between test and predicted, the
predicted velocity profile was corrected by the square root of the
measured to predicted temperature ratio. The resulting velocity
profile as shown in Figure 4-48 is in fair agreement with the meas-
ured velocity profile. Therefore, it appears the predicted temper-
ature mixing at the nozzle exit is not valid due to a high amount
of mixing occurring in the accelerating region of the prediction
analysis. However, as shown earlier in Figure 4-47, the tempera-
ture profile at the end of the constant area mixing duct is in
good agreement with the measured profile characteristic. On
this basis, the mixing analysis appears to be valid in the region
of low Mach number up to the mixing duct exit, but predicts
excessive mixing through the highly accelerating region. A better

174
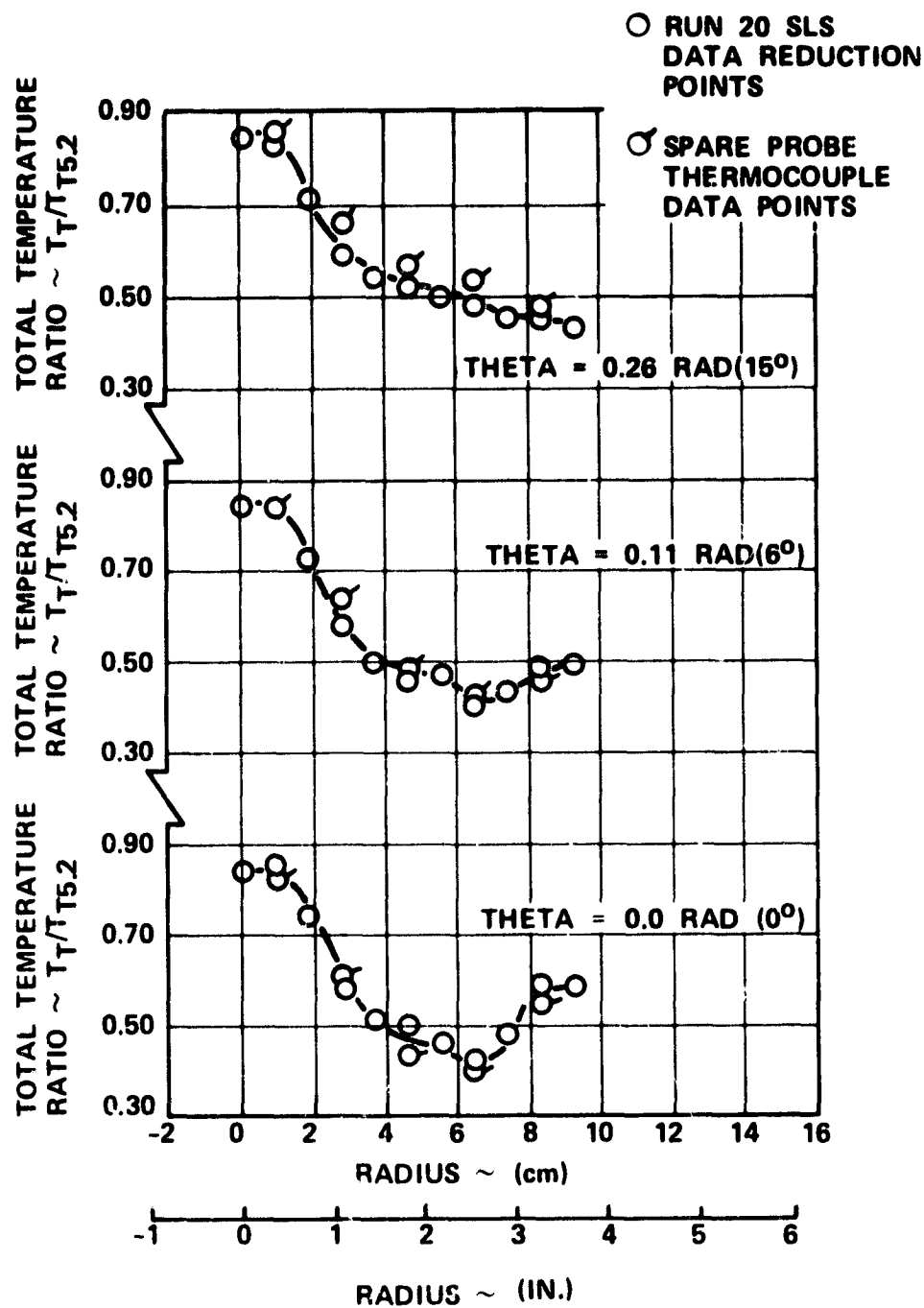
Figure 4-44. Configuration II Nozzle Exit Radial
Temperature Profile Comparison.
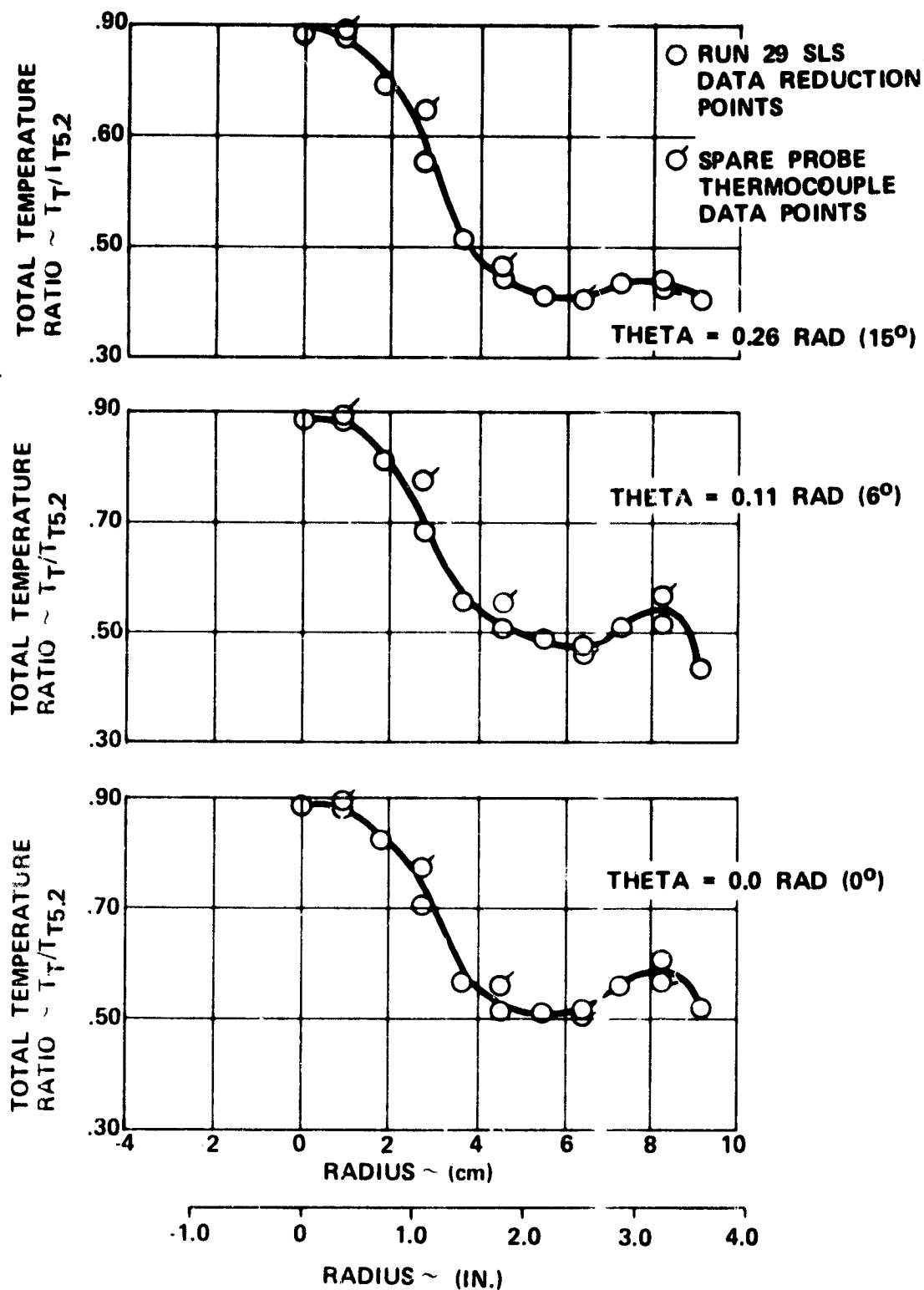
Figure 4-45. Configuration III Nozzle Exit Radial
Temperature Profile Comparison.
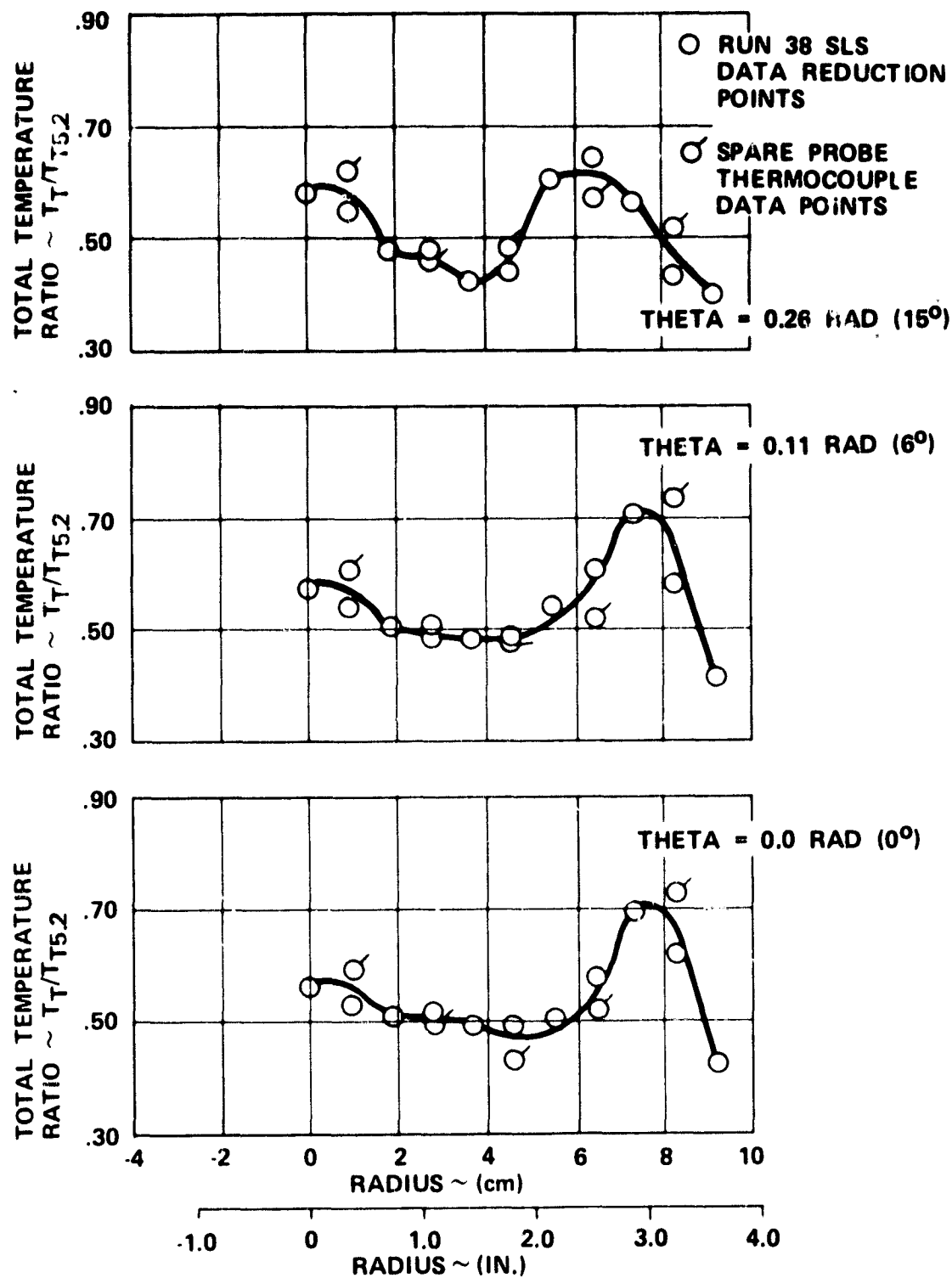
Figure 4-46. Configuration IV Nozzle Exit Radial Temperature Profile Comparison.

$\mathcal{C} - 3$

STANDARD COMPOUND (CONFIGURATION I)
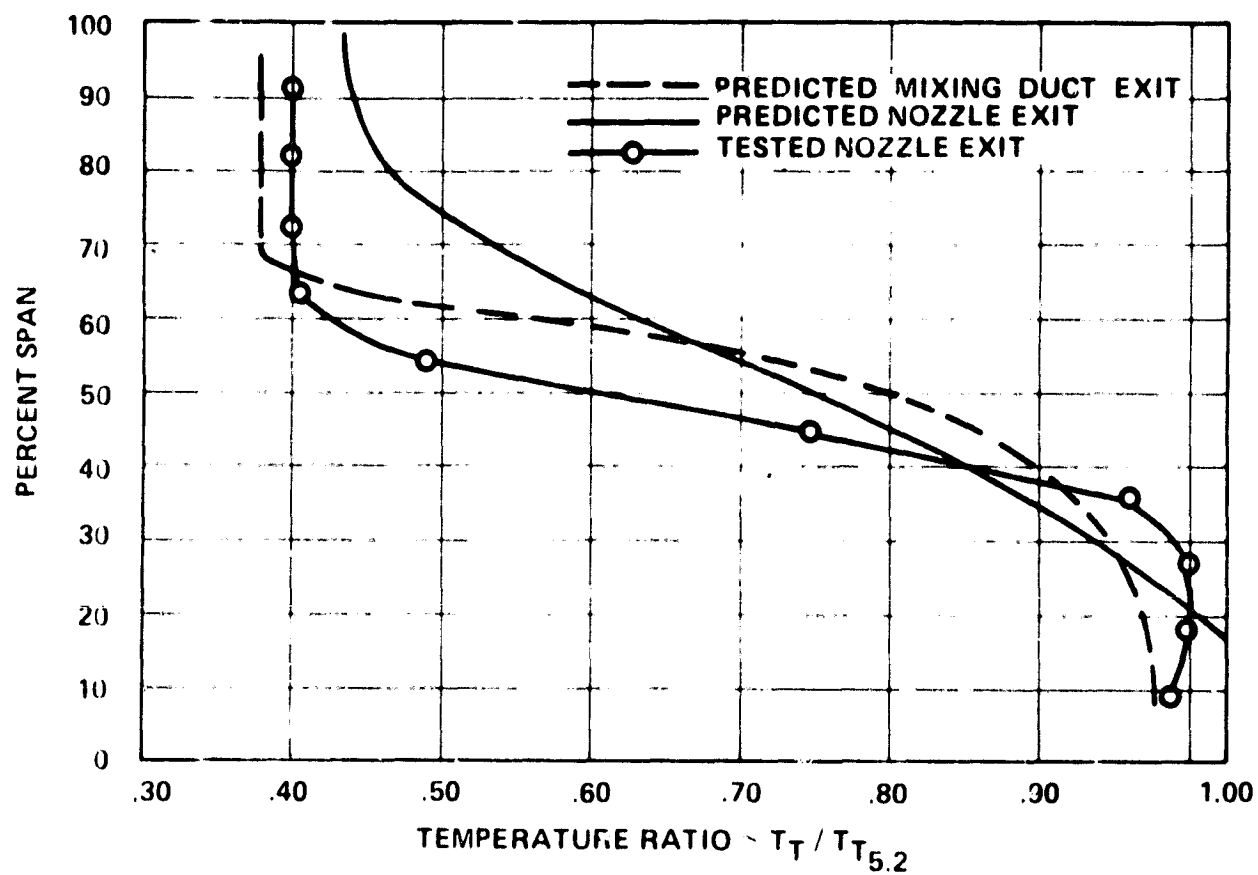
Figure 4-47. Nozzle Exit Versus Mixing
Duct Exit Temperature.

STANDARD COMPOUND (CONFIGURATION I)
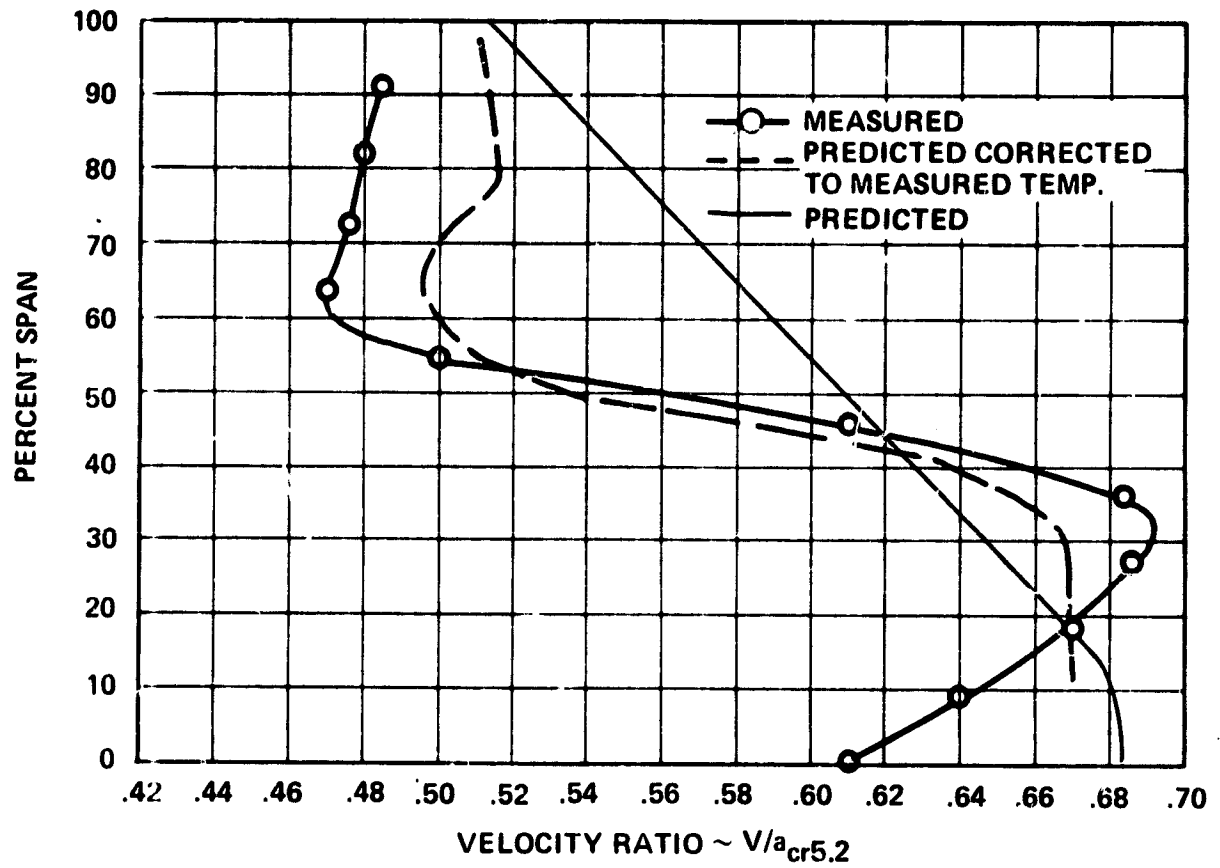
Figure 4-48. Nozzle Exit Velocity Profile.

match of the mixing-duct exit profile with the measured data might be obtained by adjusting the input turbulence level mixing length or initial static pressure gradients. Integrated radial temperature and velocity profiles for the mixer configurations (II, III, and IV) are presented in Figures 4-49, 4-50 and 4-51. In the parallel mixers, Figure 4-49 and 4-50, the test data indicates less hot flow occurred in the mid region than was predicted and more hot flow occurred at the hub and shroud than predicted.

The radial configuration (see Figure 4-51) produced a larger concentration of high temperature in the upper mid-region than was predicted and a lower amount of hot flow at the shroud and in the hub region. Some of the mixer temperature difference between tested and predicted data could be caused by flow angle at the mixing plane which was input axially into the mixing-analysis program. This may not have been the case as was discussed earlier in Section 4.4.1.

Tested versus predicted results indicate some additional work is required in the analysis section to obtain better agreement with test data.

4.5 Mixing Efficiency Determination

Mixing efficiency is the measure of the percentage of actual thermal mixing thrust gain to the ideal thermal mixing gain as defined below:

$$\eta_{mix} = \frac{F_{ACT} - F_{0\%}}{F_{100\%} - F_{0\%}} = \frac{(C_{T\ HOT} - C_{T\ COLD})\ meas.}{(C_{T\ 100\%} - C_{T\ COLD})\ meas.} \tag{18}$$
$$\text{IDEAL}$$

This reduces to:

$$\eta_{mix} = \frac{\sqrt{T_T} - \sqrt{T_{T\ AVE}}}{\sqrt{T_{T\ MIX}} - \sqrt{T_{T\ AVE}}} \tag{19}$$

where
T_T = measured exit temperature

$T_{T\ AVE}$ = momentum averaged inlet temperature

$T_{T\ MIX}$ = energy derived inlet temperature

180
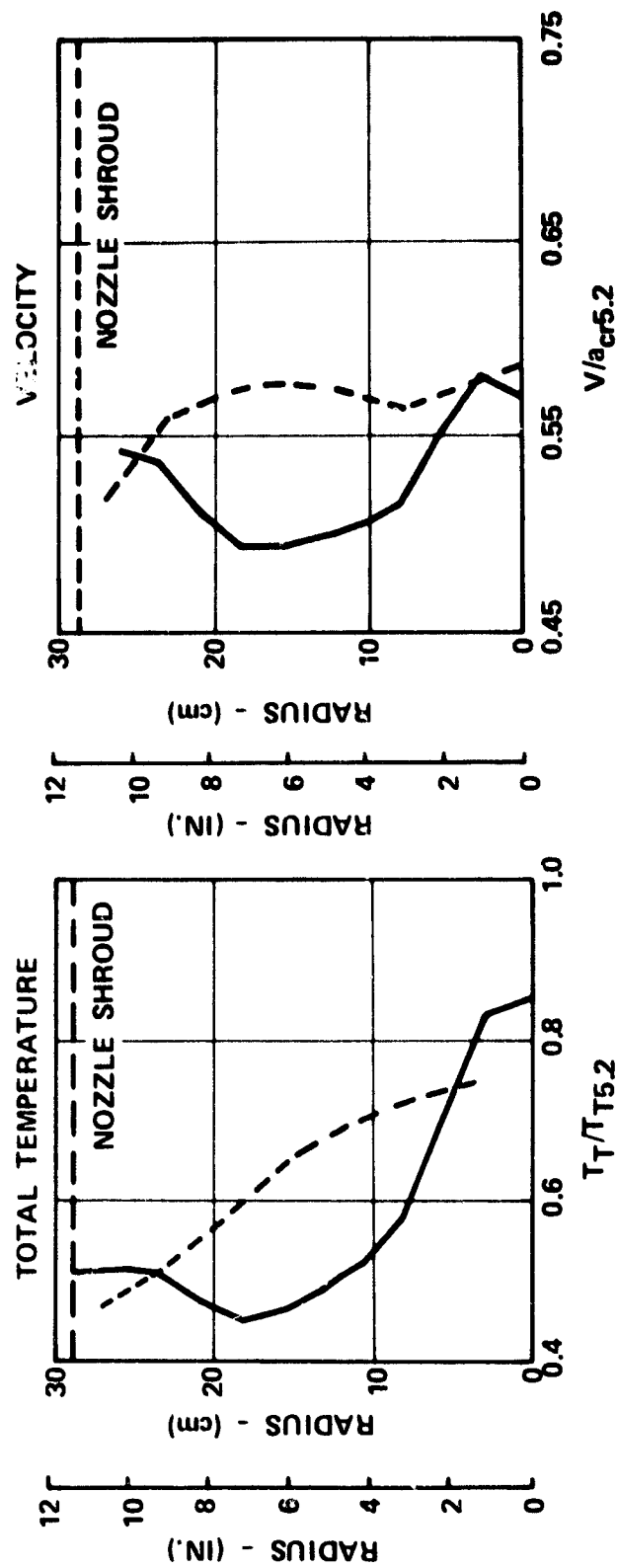
Figure 4-49. Short Parallel Nozzle Exit Radial Profiles.

181
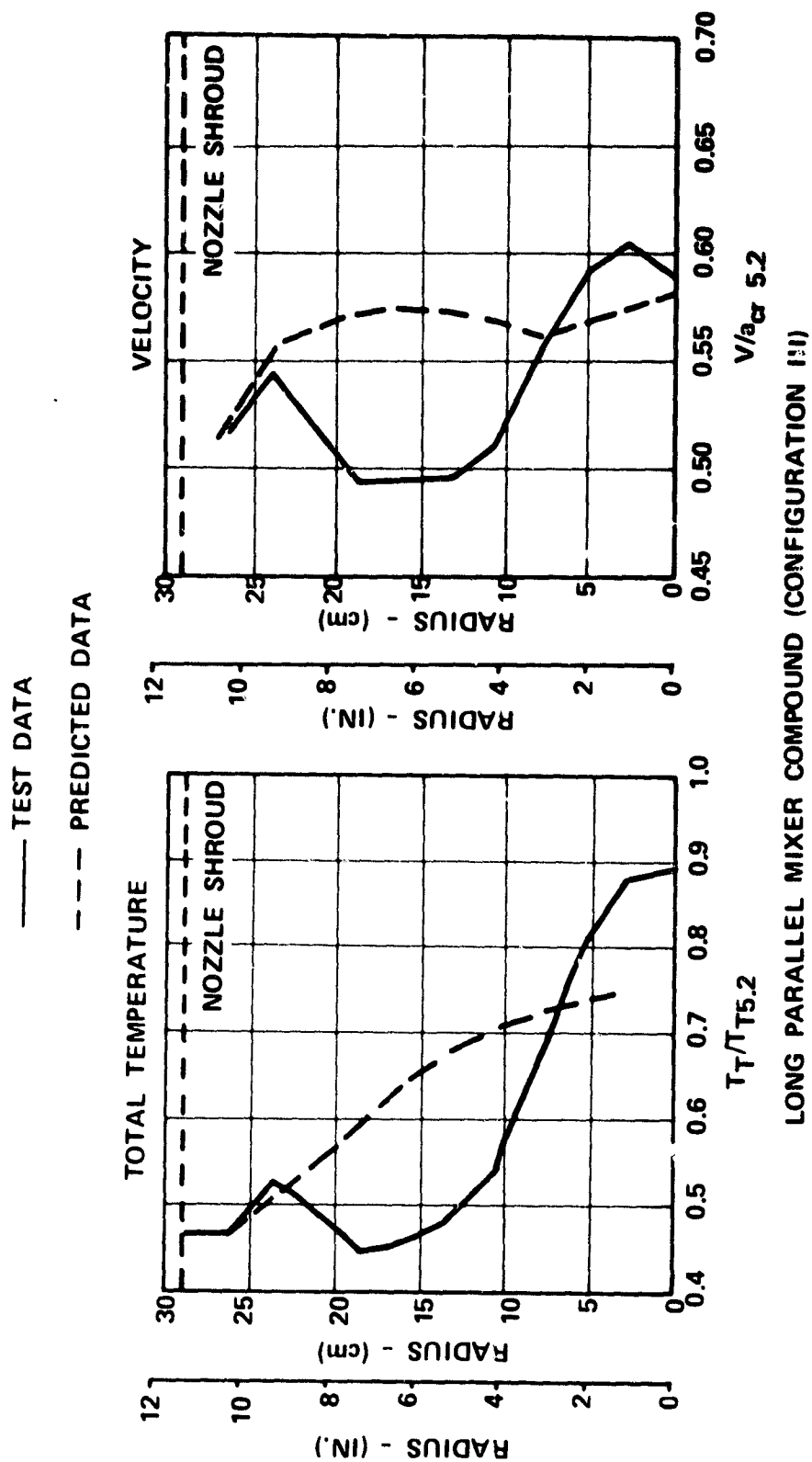
Figure 4-50. Long Parallel Nozzle Exit Radial Profiles.
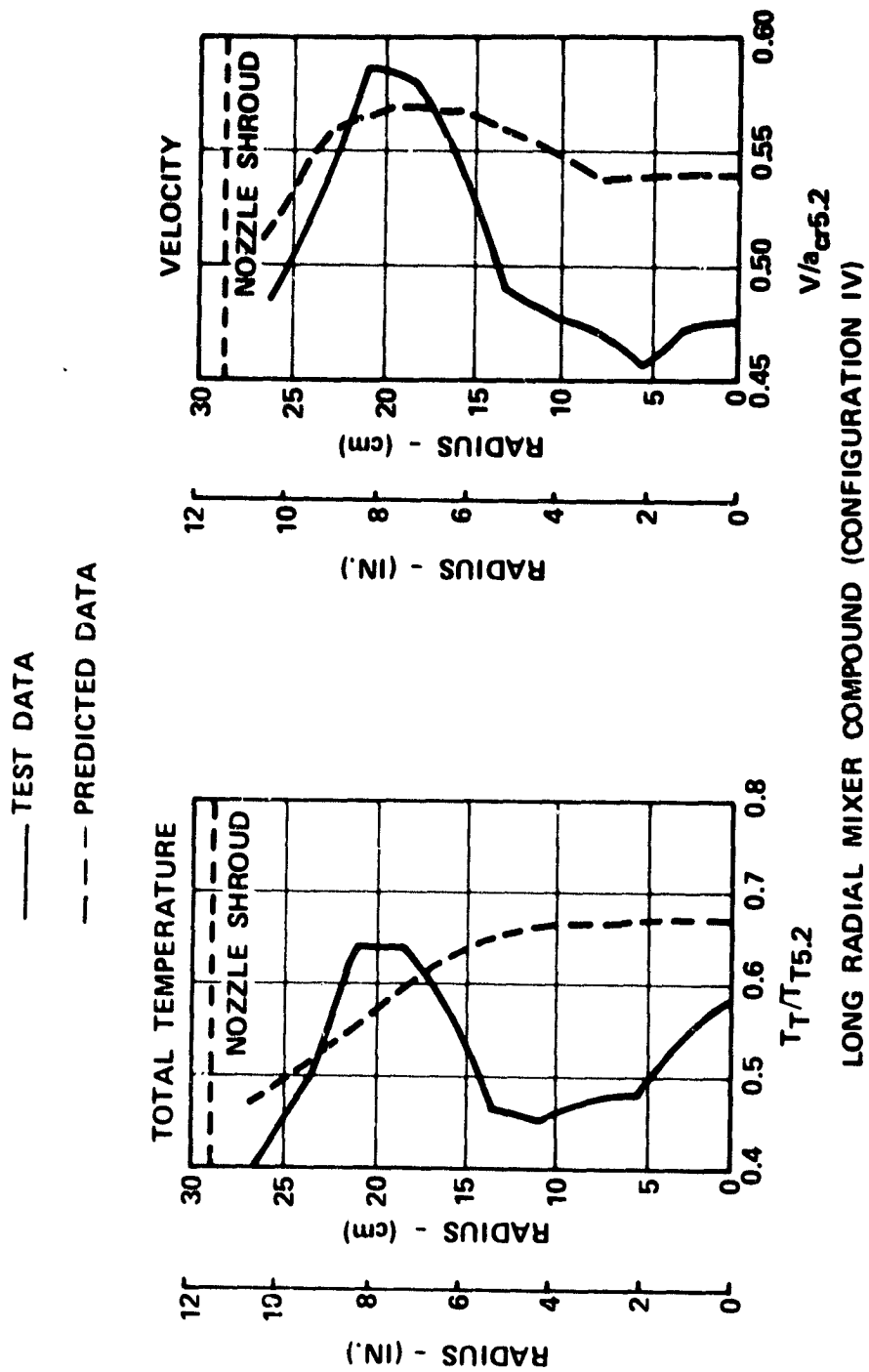
Figure 4-51. Long Radial Nozzle Exit Radial Profiles.

183

Therefore, mixing efficiency can be obtained from measured thrust data, or measured exit temperature. Mixing efficiencies calculated by both methods have been shown versus Frost's interface function in Section 3.3.3.

Frost's interface function was defined utilizing a configuration with no centerbody. The correlating diameter in the interface function, therefore, was the mixing duct inlet diameter. However, in this test a centerbody was used and several appropriate diameter definitions were possible, such as the equivalent area diameter, the hydraulic diameter, and the mixing-duct shroud diameter. The mixing efficiencies were plotted versus interface functions with each of the above diameter definitions and the result was that the data best correlated when plotted versus the hydraulic diameter as shown in Figure 4-52. Mixing efficiencies derived from measured exit temperatures agreed well with Frost's mixing curve for the configurations I, II, V, VI while mixing efficiencies derived from measured thrust were slightly below the curve but showed the same trends. Based on a thrust measurement accuracy of +0.25 percent each, for the hot and cold data points, the error on thrust-derived mixing-efficiency is +15 percent at the cruise design point and +24 percent at the SLS take-off condition. Based on a rating station temperature measurement error of +2 degrees and an exit plane temperature measurement and integration error of +5 degrees, the measured temperature derived mixing efficiency error would be about +10 percent at both SLS and the cruise design point. The majority of the data scatter falls within these limits.

The effect of temperature ratio between the hot and cold flow streams on the mixing efficiency was investigated during the testing. Configuration II was run at a selected pressure-ratio condition for a set of three different temperature ratios, i.e., 2.5, 2.0, and 1.5. Mixing efficiency remained relatively constant as temperature ratio varied (shown in Table 4-12). The low thrust-derived mixing efficiency at the 1.5 temperature ratio can be explained by the measurement error band. The C_{PT} measurement error of +0.0035 is essentially equal to the calculated ideal gain of $\Delta C_{PT\ IDEAL} = 0.0041$; therefore, the derived mixing efficiency for that point was ignored. Results are based on only three data points; thus, additional testing is recommended to verify that mixing efficiency and total temperature ratio are independent.
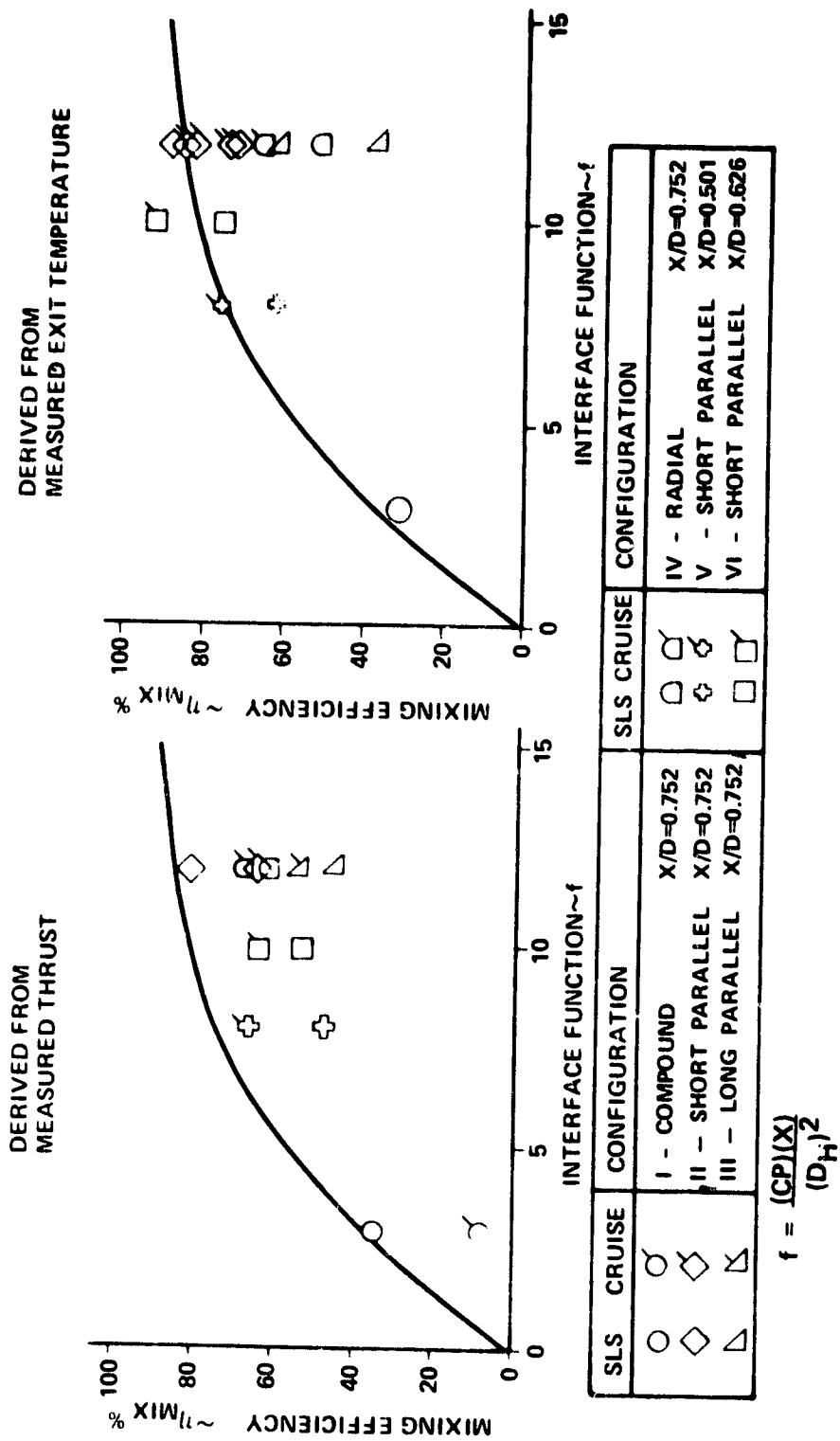
Figure 4-52. QCGAT Mixing Efficiencies.

185

TABLE 4-12.   TEMPERATURE RATIO EFFECT ON MIXING EFFICIENCY.

SHORT PARALLEL MIXER COMPOUND (CONFIGURATION II) $P_{T5.2}/P_\infty = 2.5$ $P_{T14}/P_\alpha = 2.0$		
$T_{T5.2}/T_{T14}$	$\eta_{MIX}(\%)$ (Measured Thrust)	$\eta_{MIX}(\%)$ (Measured Exit Temp.)
2.5	72	85
2.0	81	73
1.5	17	87

4.6   Thrust Coefficient Comparison

Tested cold-and hot-flow thrust coefficients for configurations (I through VI) at the sea-level-static take-off and cruise-design points are presented in Table 4-13. The hot-flow thrust-coefficient predictions based on predicted losses and 0.75-percent mixing were met by each of the mixer-compound exhaust systems at both flight conditions. At the sea-level-static point, Configuration II had the maximum performance with a $C_F = 0.9932$. Configuration II's poorer cold flow performance (indicative of higher pressure losses) was offset by the maximum gain cold to hot, indicative of producing the best thermal mixing. At the cruise design point, the radial mixer (Configuration IV) produced the best hot performance, $C_F = 1.0075$. However, among Configurations II, V, and VI, the short parallel mixer in each case was within 0.25 percent of the radial performance. The thrust-coefficient data indicated Configuration II would provide the best overall performance compromise for both sea-level static and cruise operation.

The compound-flow-analysis (CFA) program was used to match tested cold dual-flow-thrust coefficients at design and off-design points utilizing both the procedure discussed in Section 4.2.3 and the pressure loss results to be presented later. The CFA program matched the cold-thrust-coefficient data within 0.1 percent at design and off-design points for each of the mixer configurations as shown in Table 4-14.

The mixing efficiency was varied (while maintaining the loss models derived from cold data) in order to match the hot flow performance matrices of Configurations I and II. Both configurations, I and II, were matched to their performance test data within 0.5 percent with a single mixing efficiency value, except for two low pressure-ratio points where measurement error becomes

TABLE 4-13. THRUST COEFFICIENT COMPARISON.

Flight Condition	Configuration	C_F (Cold)	C_F (Hot)	ΔC_F (Hot-Cold)
SLS $PR_{5.2} = 1.4$ $PR_{14.0} = 1.4$	Predicted	0.9673	0.9782	0.0109
	I	0.9845	0.9897	0.0052
	II	0.9815	0.9932	0.0117
	III	0.9836	0.9902	0.0066
	IV	0.9829	0.9918	0.0089
	V	0.9834	0.9902	0.0068
	VI	0.9831	0.9908	0.0077
CRDP $PR_{5.2} = 2.4$ $PR_{14} = 2.4$	Predicted	0.9829	1.0005	0.0176
	I	0.9919	0.9940	0.0021
	II	0.9896	1.0050	0.0154
	III	0.9906	1.0032	0.0126
	IV	0.9908	1.0075	0.0167
	V	0.9906	1.0068	0.0162
	VI	0.9906	1.0066	0.0160

TABLE 4-14. DUAL-COLD-FLOW THRUST-COEFFICIENT-MATCHING
WITH COMPOUND-FLOW ANALYSIS.

Configuration	SLS 298°K (77°F) Day		CRDP M = 0.8 Alt=12,192m (40K ft)	
	C_{FT} Match	C_{FT} Test	C_{FT} Match	C_{FT} Test
I	0.9846	0.9845	0.9908	0.9919
II	0.9815	0.9815	0.9893	0.9896
III	0.9836	0.9836	0.9902	0.9906
IV	0.9833	0.9829	0.9902	0.9908

quite large (see Table 4-15). The standard-compound system was matched to the sixteen-point performance matrix with a mixing efficiency of 20 percent. A mixing efficiency of 65 percent was required to best match the Configuration II performance matrix. Thrust measurements used for performance evaluation were obtained with the survey rake removed. Thrust measurements were also taken with the survey rake in place during each exit survey run. An overall average increase in thrust coefficient of 0.4 percent was observed with the survey rake placed at the exit of the nozzle. Due to the apparent influence of the exit survey rake, this data was not used in establishing the absolute performance levels. However, it was used to substantiate tested performance differences.

The effect of temperature ratio on the thrust level was investigated during the testing. Configuration II was run at a single pressure-ratio setting and thrust was measured at temperature ratios of 2.5, 2.0, and 1.5. Absolute measured thrust levels decreased with decreasing temperature ratio as shown in Figure 4-53. Exit surveys were taken during these runs; therefore, the measured thrust levels included the effect of the survey rake. The increment of thrust gain (hot to cold) with the survey rake effect removed indicates that the thrust gain is reduced by one-half in going from a temperature ratio of 2.5 to 1.9.

Comparing measured to ideal thrust gain versus temperature ratio produces the result that mixing efficiency remains constant (see Figure 4-53, η_{mix} values). Mixing efficiencies derived from measured exit temperatures indicate the same trend.

4.7 Total Pressure Loss

4.7.1 Cold Flow Derived Pressure Losses

Initially, the core-only thrust data was used to obtain the core-pressure losses. Pressure losses derived in this manner for Configuration I (standard compound) correlated linearly with corrected flow squared as would be expected. Some deviation from a linear relationship occurred at the two higher flow points where the Mach number at the rating station was greater than 0.7, and the rig adapter was close to choking (see Figure 4-54). Since two of the three core-only pressure-ratios for the mixer configurations choked locally through the mixer lobes, the unchoked pressure-ratio point was the only point reduced to obtain a pressure-loss value. For these mixer runs, the rating station Mach number was about 0.5, but the Mach number somewhere through the lobes was much higher. For one of the mixer-core choked runs, the rating-station Mach number was about 0.6. Based on these single core-only pressure-ratio runs, the mixer-core losses were approximately 3.5 percent at the cruise-design-point corrected flow. However, when this value of core loss is used

TABLE 4-15. DUAL-HOT-FLOW THRUST-COEFFICIENT-MATCHING
WITH COMPOUND-FLOW ANALYSIS

STANDARD COMPOUND (CONFIGURATION I)				
$P_{T5.2}/P_\infty$	$P_{T14.0}/P_\infty$	C_F Test	C_F/CFA ($\eta_{mix} = 20\%$)	$\dfrac{CFA-Test}{Test}$
1.2	1.2	0.9832	0.9811	-0.0021
1.4	1.4	0.9897	0.9893	-0.0004
1.6	1.6	0.9904	0.9920	0.0016
2.0	2.0	0.9916	0.9959	0.0043
2.4	2.4	0.9940	0.9968	0.0028
1.3	1.2	0.9843	0.9692	-0.0153
1.4	1.2	0.9855	0.9542	-0.0318
1.5	1.4	0.9850	0.9848	-0.0002
1.6	1.4	0.9837	0.9782	-0.0056
1.4	1.6	0.9924	0.9872	-0.0052
1.8	1.6	0.9864	0.9858	-0.0006
1.8	2.0	0.9946	0.9921	-0.0025
2.2	2.0	0.9925	0.9930	0.0005
2.0	2.4	0.9954	--	--
2.2	2.4	0.9939	0.9939	0.0000
2.6	2.4	0.9943	0.9953	0.0010

TABLE 4-15.   DUAL-HOT-FLOW THRUST-COEFFICIENT-MATCHING
WITH COMPOUND-FLOW ANALYSIS.   (CONTD)

	SHORT PARALLEL MIXER COMPOUND (CONFIGURATION II)			
$P_{T5.2}/P_\infty$	$P_{T14.0}/P_\infty$	C_F Test	C_F/CFA ($\eta_{mix} = 65\%$)	$\dfrac{CFA-Test}{Test}$
1.2	1.2	0.9922	0.9814	-0.0109
1.4	1.4	0.9932	0.9927	-0.0005
1.6	1.6	0.9956	0.9969	0.0013
2.0	2.0	1.0016	1.0032	0.0016
2.4	2.4	1.0049	1.0059	0.0010
1.3	1.2	0.9832	0.9668	-0.0167
1.5	1.4	0.9914	0.9876	-0.0038
1.6	1.4	0.9796	0.9801	0.0005
1.4	1.6	0.9931	0.9937	0.0006
1.8	1.6	0.9950	0.9903	-0.0047
2.0	1.6	0.9786	0.9812	0.0026
1.8	2.0	0.9964	0.9993	0.0029
2.5	2.0	0.9911	0.9927	0.0016
2.2	2.4	1.0020	1.00205	0.0005
2.6	2.4	1.0076	1.0036	-0.0040
2.9	2.4	0.9992	0.-980	-0.0012
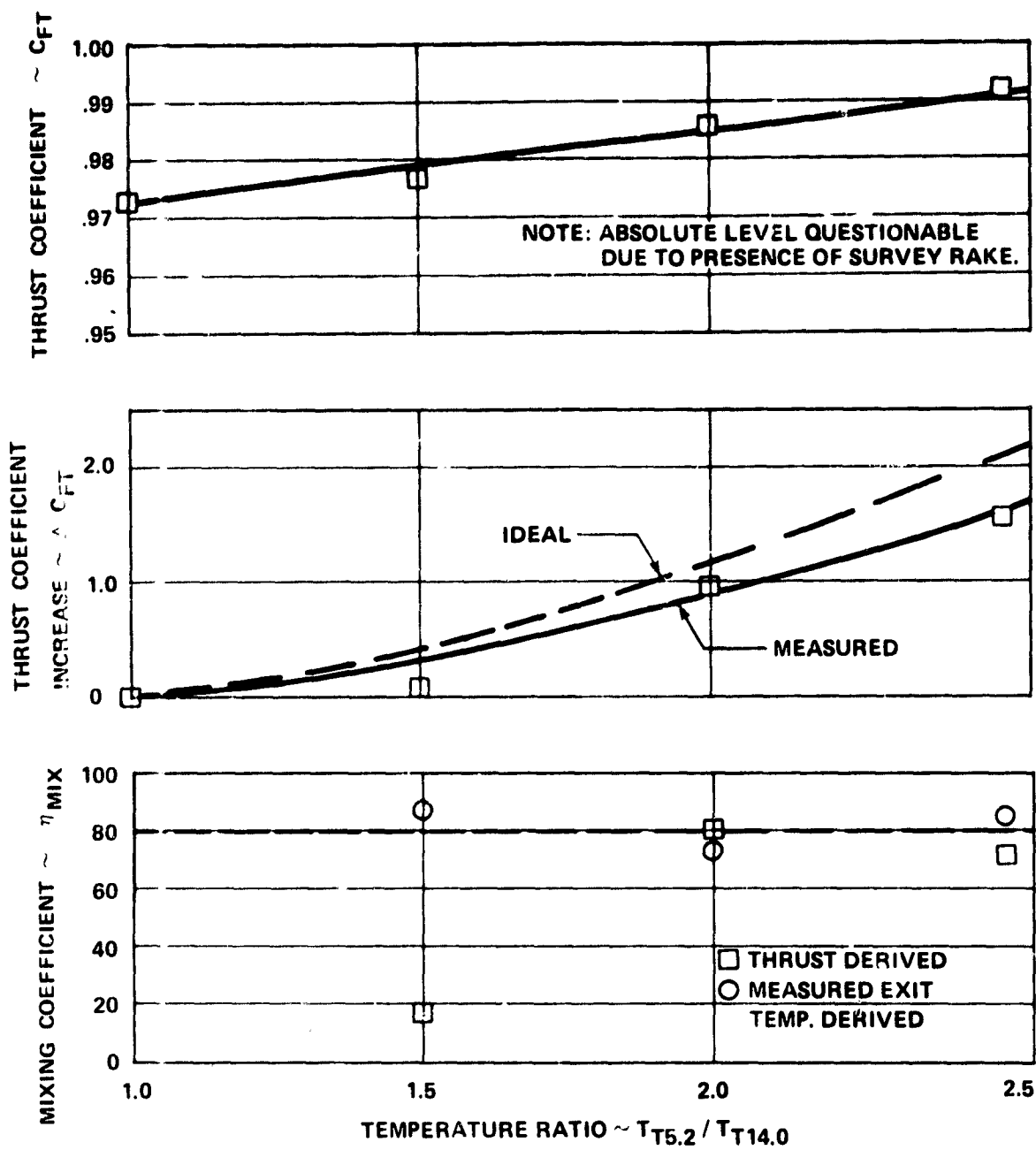
Figure 4-53. Temperature Ratio Effect.
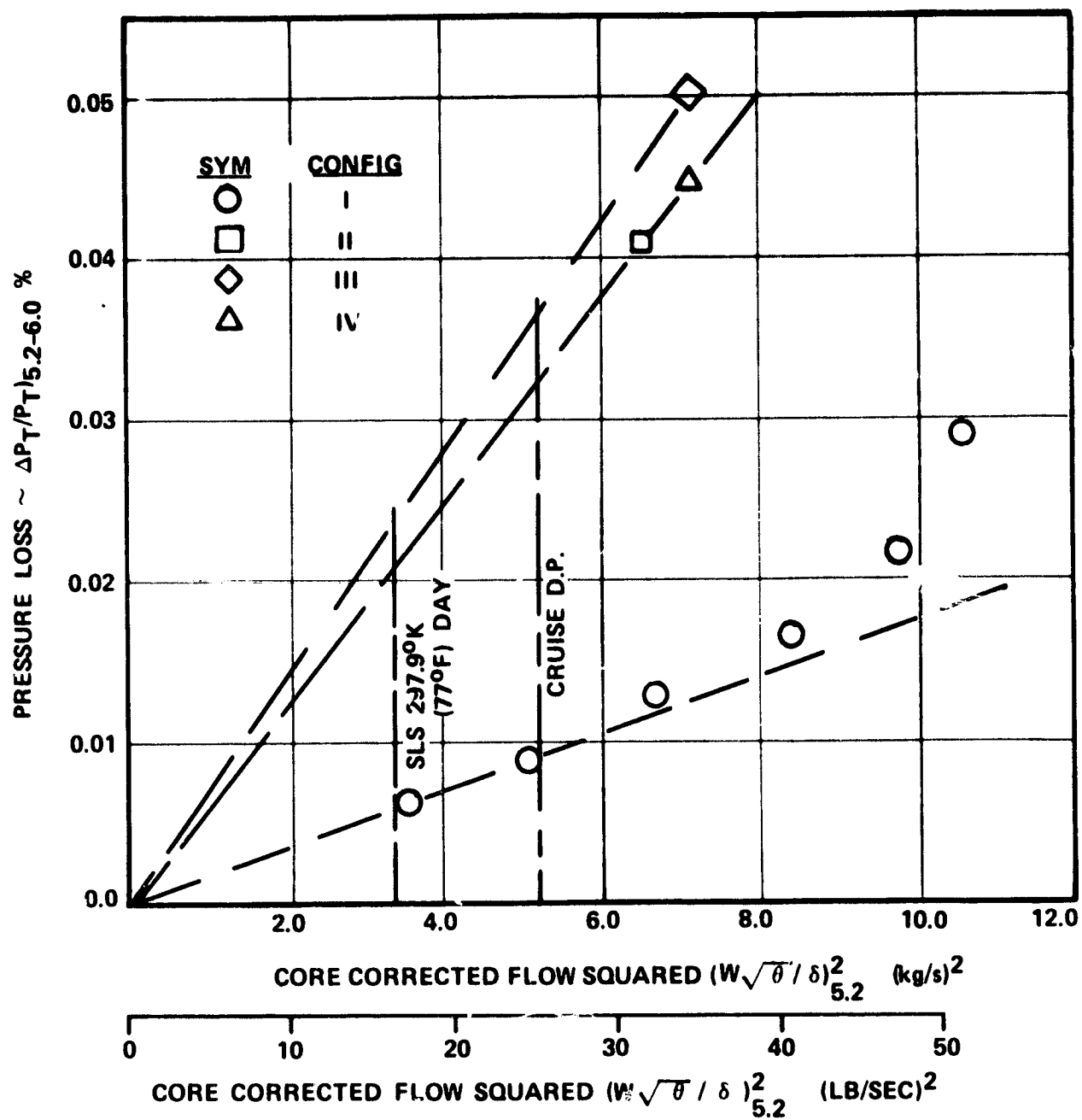
Figure 4-54. Total-Pressure Loss, Core Only Flow.

193

for the mixer configurations, the predicted dual cold-flow thrust-coefficient results were much lower than tested. Since the mixer-core-only runs were operated at a very high Mach number locally through the lobes, the mixer-core-only pressure loss is questionable when ratioed down to a lower corrected flow. Therefore, the mixer-core-only losses were derived from the dual cold-flow thrust coefficients as described earlier in Section 4.2.3. Cold-thrust-coefficient matching results were presented earlier in Section 4.6. Total-pressure losses based on matching cold-dual-flow-thrust coefficients are shown in Table 4-16.

TABLE 4-16. CRUISE DESIGN POINT PRESSURE LOSSES.

Configuration	$\Delta P/P_T$		
	Core	Bypass	Mixing Duct
I	0.0090	0.0048	0.0023
II	0.0225	0.0048	0.0023
III	0.0135	0.0048	0.0023
IV	0.0135	0.0048	0.0023

4.7.2 Tested Versus Predicted Losses

Tested and predicted losses for the core nozzles are ratioed to a predicted convergent-nozzle loss and compared to a semi-empirical loss correlation previously discussed in Section 3.3.1 (see Figure 4-55). The convergent nozzle has an exit equivalent hydraulic diameter of 1.0 (therefore, no centerbody), and, in the case of a diffusing core, it includes the diffusion loss based on an area ratio of a conical diffuser. Tested Configurations I, III, and IV fall very close to the semi-empirical curve while Configuration II has a somewhat higher loss. Tested losses are lower than the predicted values for all the mixer configurations; however, the 3-D viscous analysis predicted the same loss ranking as the test results.

Tested versus predicted losses for the final mixer configuration are presented in Table 4-17 for the cruise-design-point and sea-level-static-takeoff point.

4.8 Component Performance Maps

4.8.1 Test Maps

The sixteen-point data matrix tested for Configuration II was used to generate performance characteristic maps required for evaluating engine-cycle match. The initial predicted-flow and

194
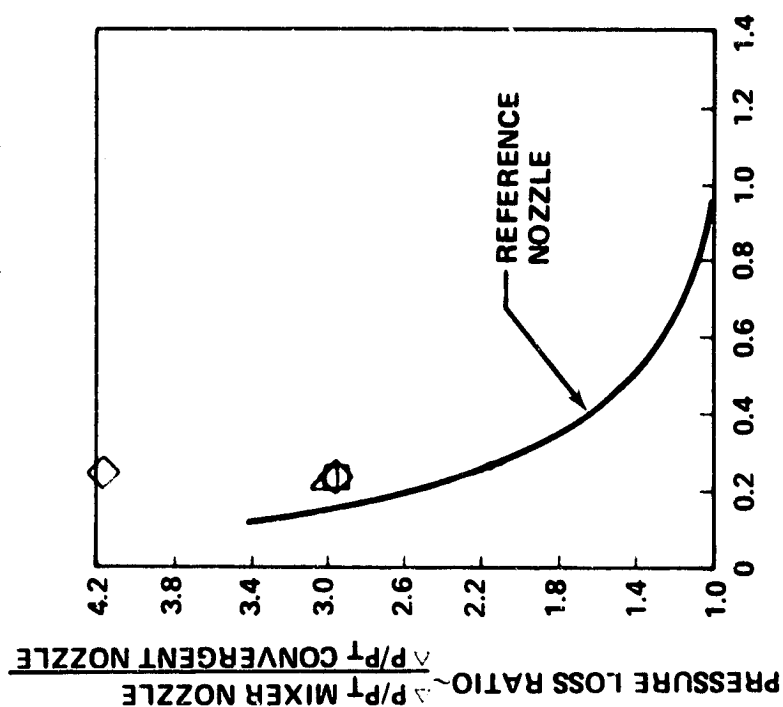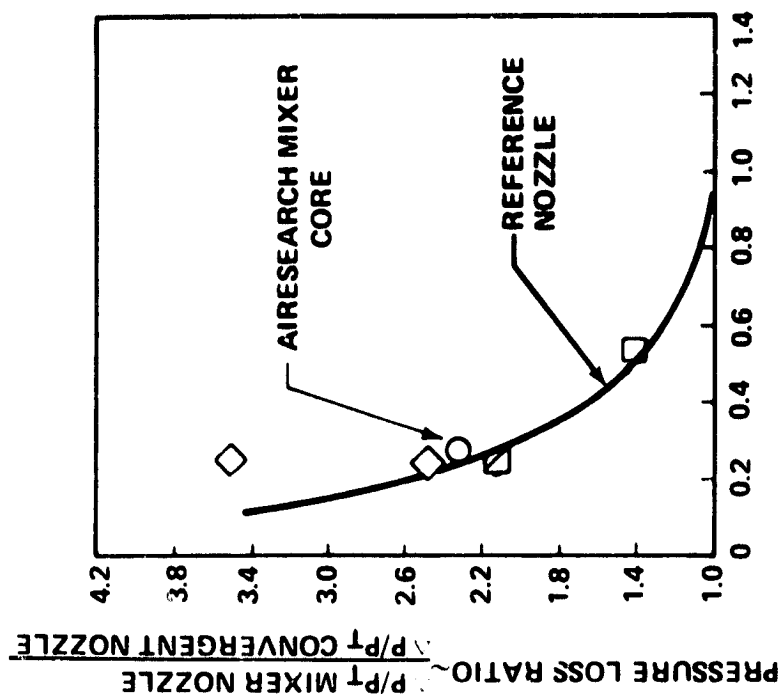
Figure 4-55. QCGAT Model Mixer Nozzle Total-Pressure Loss Ratio.

195

TABLE 4-17. QCGAT MODEL TOTAL-PRESSURE LOSS BREAKDOWN.

Flight Condition	Total-Pressure Loss $\Delta P/P_T$								
	Core			Bypass			Mixing		
	Prelim Des.	3-D Viscous	Test	Prelim Des.	3-D Viscous	Test	Prelim Des.	3-D Viscous	Test
Cruise Design Point M=0.8 Alt=12,192m (40K ft)	0.0248	0.0209	0.0225	0.0297	0.0118	0.0077	0.0044	0.0044	0.0042
S.L.S. Takeoff 298°K(77°F) Day	0.0161	-	0.0147	0.0241	-	0.0066	0.0031	-	0.0031

thrust-coefficient maps were used as a base reference from which tested flow and thrust deviation values were calculated. Corrected flow deviations were generated and lines of constant bypass-pressure ratio were plotted as a function of core-pressure ratio (see Figures 4-56 and 4-57 for the core and bypass, respectively). The flow-deviation lines were then crossplotted and interpolated to generate a uniform map. The thrust coefficient deviation values generated in the same manner as above relative to the predicted map along with calculated thrust-coefficient-deviation values from the compound-flow-analysis program updated with the loss and mixing models discussed in earlier sections, are shown in Figure 4-58.

The deviation values derived from test data are a constant 1.25 percent higher than the predicted levels except in the low-pressure-ratio range where the deviation is greater than 1.25 percent . Thrust coefficients calculated with the compound-flow-analysis program produced a constant 1.25 percent deviation level over the full range of pressure ratios tested. Because of the increased thrust-measurement error at lower pressure ratios, a thrust scalar of 1.25 percent was applied to the full predicted map. This allows for measured thrust error margin at the low-pressure-ratio range and provides a thrust map that is conservative in this range.

Corrected flow maps are presented in Figures 4-59 and 4-60 along with the actual test data points. Limit lines due to static pressure and splitter-area choking are included. The static-pressure-limit line corresponds to no flow for one-dimensional-inviscid analysis. Also, the approximate location where the rig-core-sonic nozzle unchokes is shown to indicate the pressure ratio boundaries of the test. The thrust-coefficient map is presented in Figure 4-61. As discussed above, the map is lower than the test data at the low-pressure-ratio end, but agrees well everywhere else.

4.8.2 Tested Versus Predicted Maps

The predicted core- and bypass-corrected-flow characteristics matched the tested characteristics exceptionally well (see Figure 4-62). Throughout the performance matrix, the measured core flow was lower than predicted and the bypass measured flow was higher than predicted. At both the cruise design point and the off-design sea-level-static takeoff point the predicted corrected-flow levels were within 5 percent of measured levels as shown in Table 4-18.

Tested thrust coefficient-levels were higher than predicted due to lower-than-predicted pressure losses (see Figure 4-63). The characteristic shapes of the predicted thrust-coefficient curves matched very close to the tested characteristics as indicated earlier by the constant-thrust scalar required to match the predicted levels to the test data.
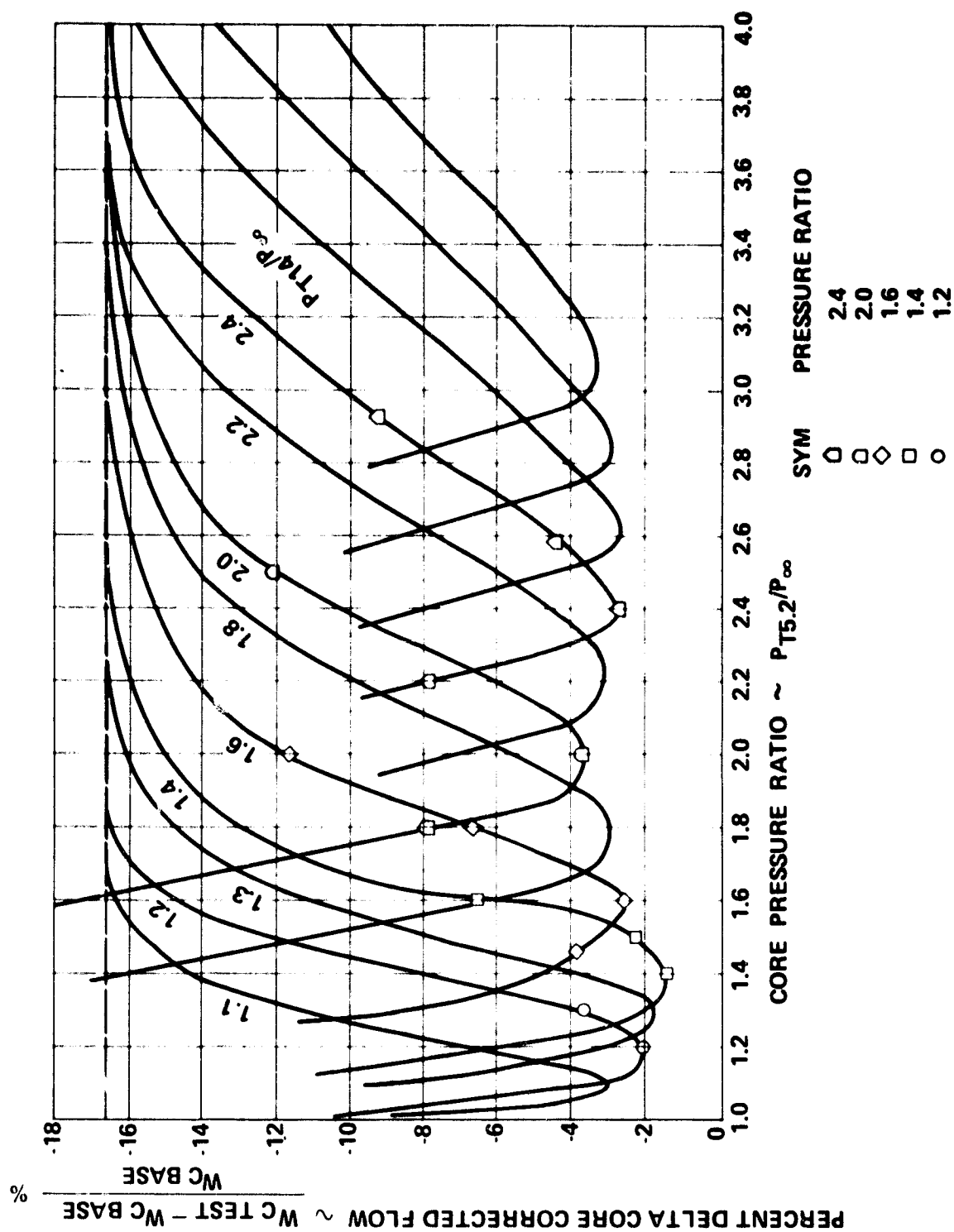
Figure 4-56. Test Versus Predicted Core Corrected-Flow Deviation.
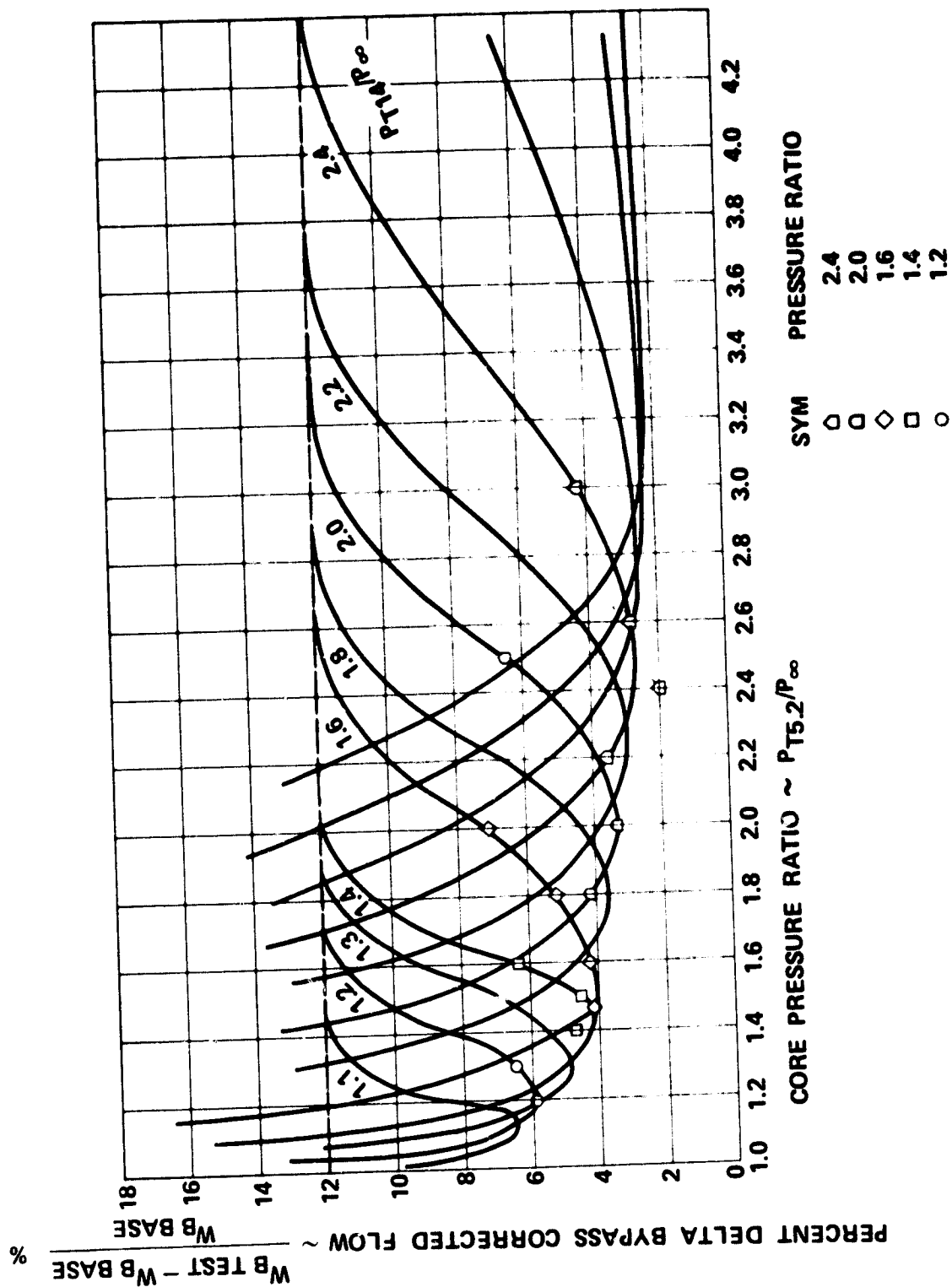
Figure 4-57. Test Versus Predicted Bypass Corrected Flow Deviation.
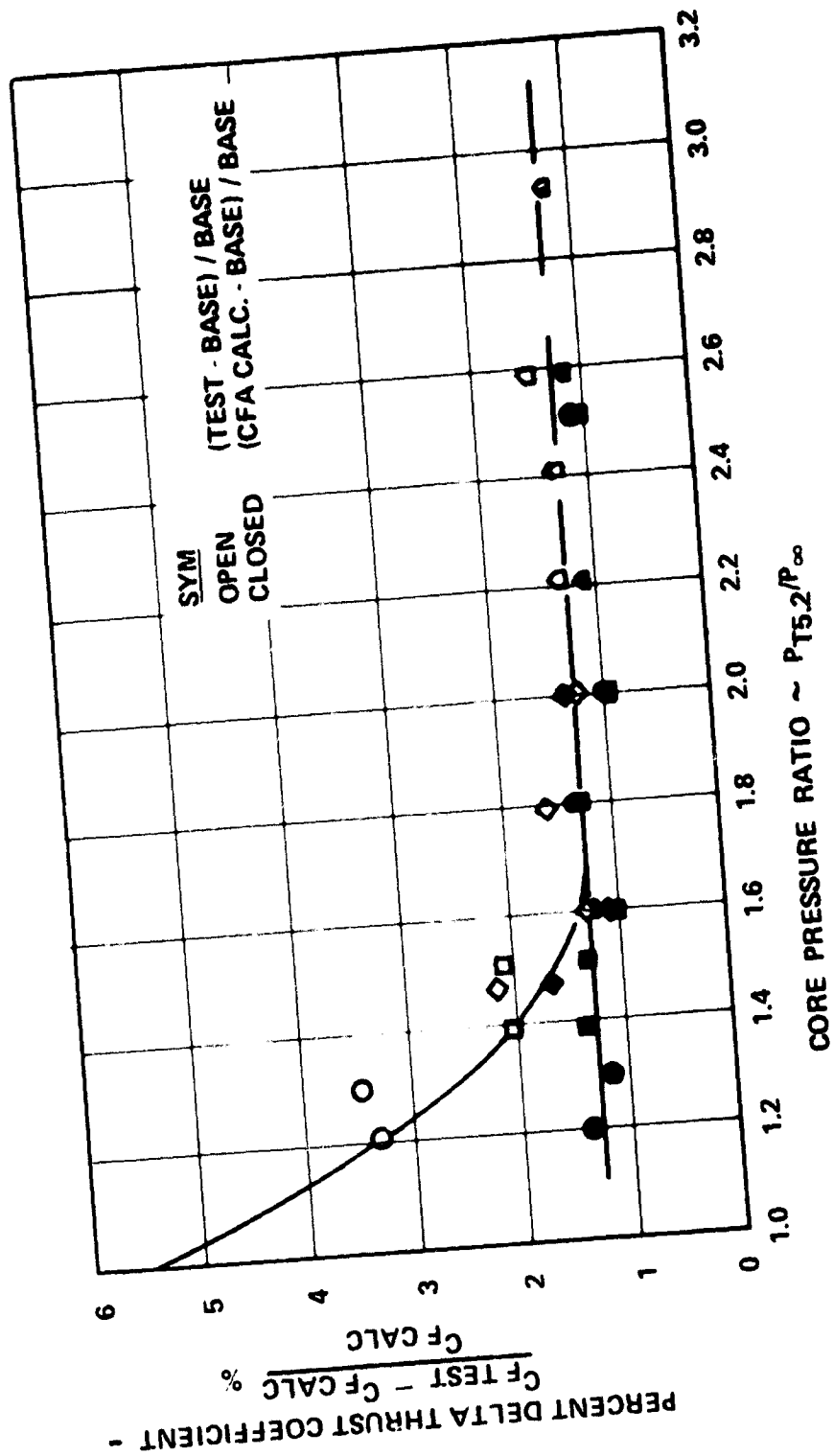
Figure 4-53. Test Versus Predicted Thrust Coefficient Deviation.

200
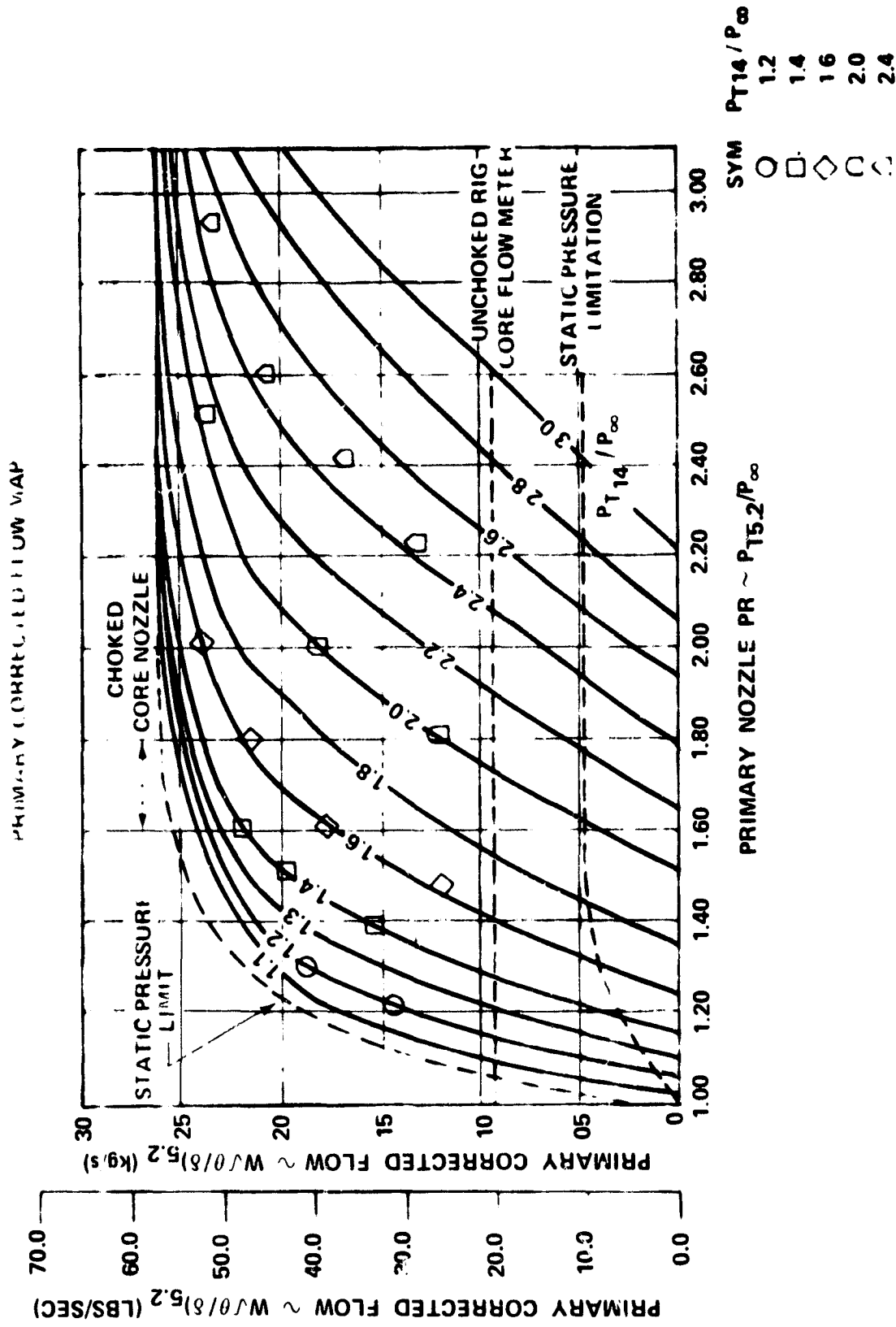
Figure 4-59. QCGAT Primary Corrected Flow Matched to Test Data.
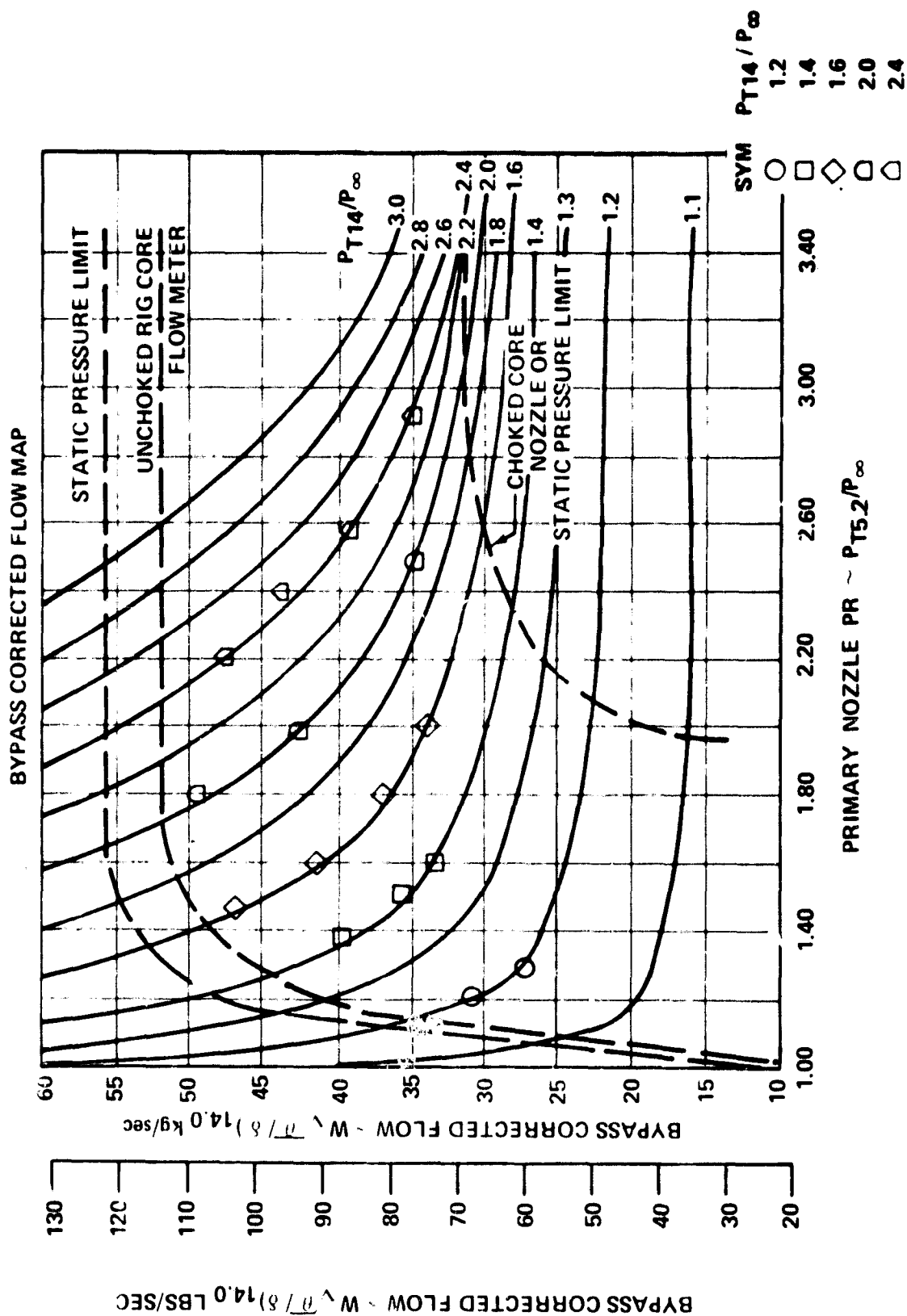
Figure 4-60. QCGAT Bypass Corrected Flow Matched to Test Data.
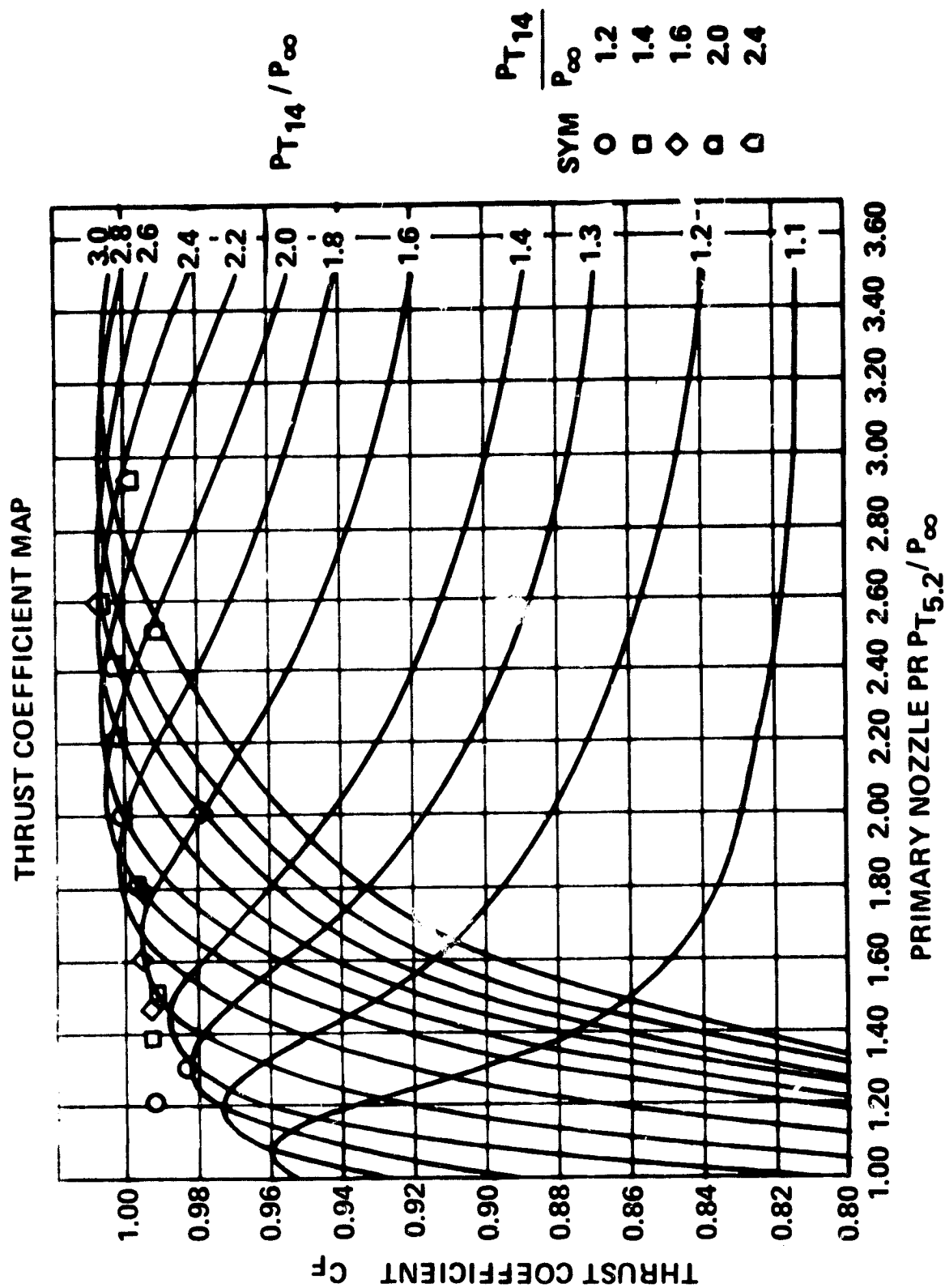
Figure 4-61. QCGAT Thrust Coefficient Matched to Test Data.
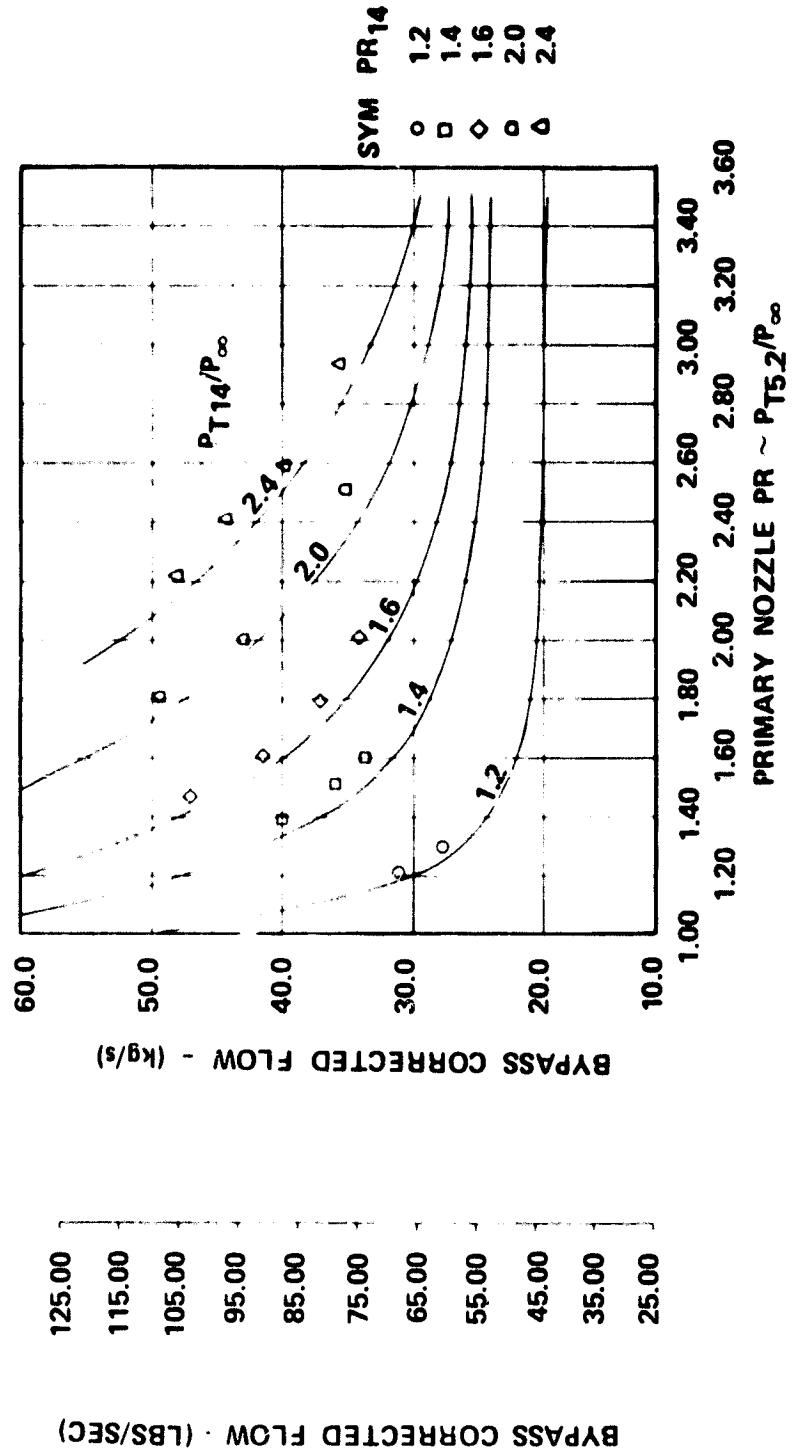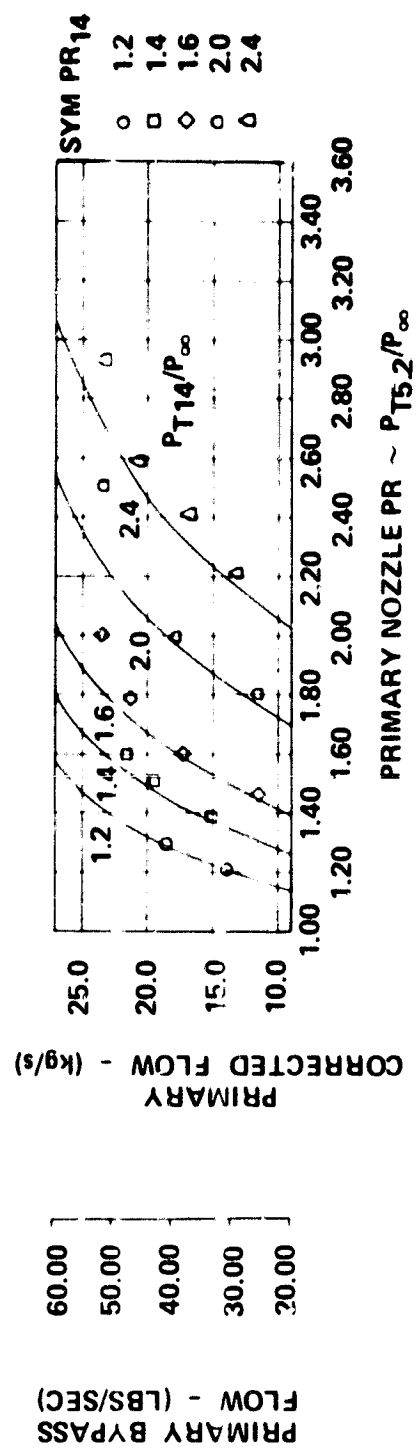
Figure 4-62. QCGAT Corrected Flow Test Data Versus Prediction.
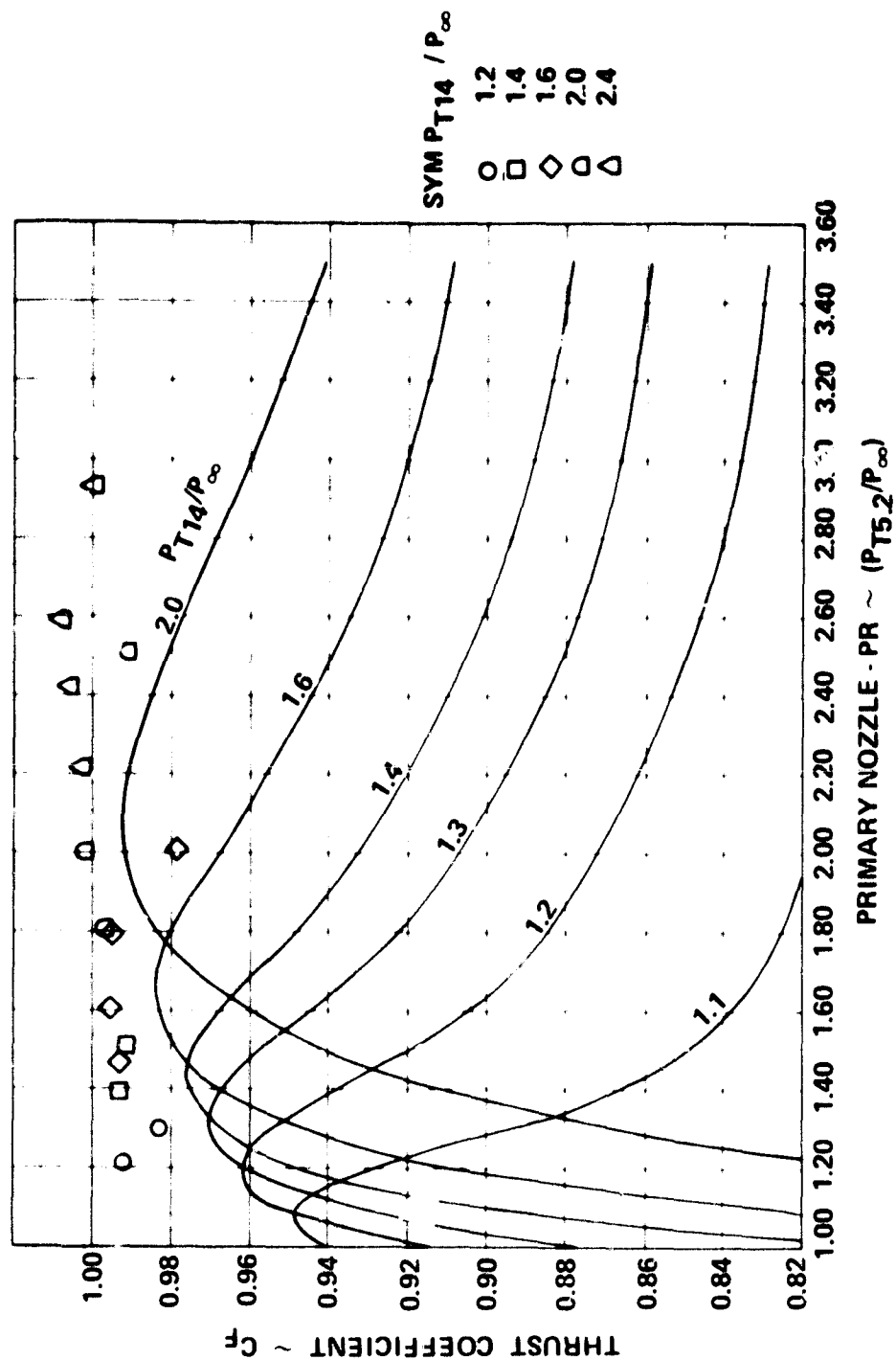
Figure 4-63. QCGAT Thrust Coefficient Test Data Versus Prediction.

TABLE 4-18. PERCENT DIFFERENCES OF MEASURED TO PREDICTED CORRECTED FLOW LEVELS.

Flight Condition	[(W_{Corr})Predicted $-$ (W_{Corr})Test]$/(W_{Corr})$Test	
	Core	Bypass
Sea-Level-Static Takeoff	+1.5%	-4.1%
Cruise Design Point	+3.6%	-2.6%

Overall, the predicted compound-flow-analysis results had the following characteristics:

(a) matched tested flow map characteristic shapes,

(b) predicted the inlet-plane flow match within 5 percent at cruise and sea level,

(c) matched tested thrust-coefficient characteristics.

The predicted flow maps were scaled using the inspected test areas and tested flow coefficients. Agreement with the tested core-corrected flows is excellent (see Figure 4-64). Scaled bypass corrected flow matches the test data well for total pressure split ($P_{T5.2}/P_{T14} \leq 1.0$) but deviates as the pressure split becomes >1.0 as is also shown in Figure 4-64. The bypass-flow error may be due to differences between the predicted loss model and the actual test losses or the exit-flow coefficient definition which is based on equal-pressure-ratio ($P_{T\ Core}/P_{T\ Bypass} = 1.0$) data points.

The effect of pressure loss differences between predicted and tested data was removed by running the performance map data points through the compound-flow-analysis program with the tested areas, flow coefficients, and pressure loss model as discussed in previous sections. Updating the predicted pressure-loss model did not produce the required match with test data as shown in Figures 4-65 and 4-66. However, the pressure loss update did result in good agreement with the tested thrust coefficients (see Figure 4-67.) These results indicate an exit flow coefficient map with lines of constant bypass pressure ratio may be required in the prediction analysis to improve off-design matching, but design-point flow matching and performance level capability produce good agreement with test results.

206
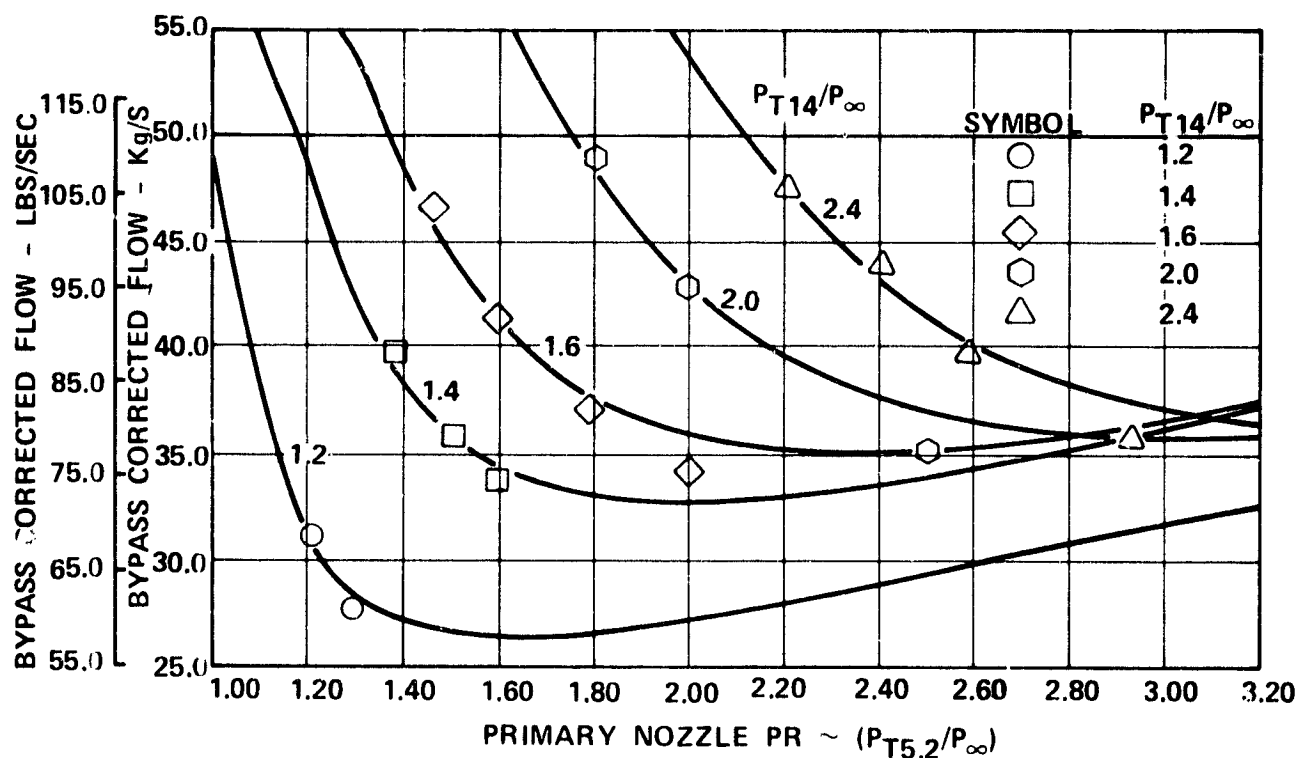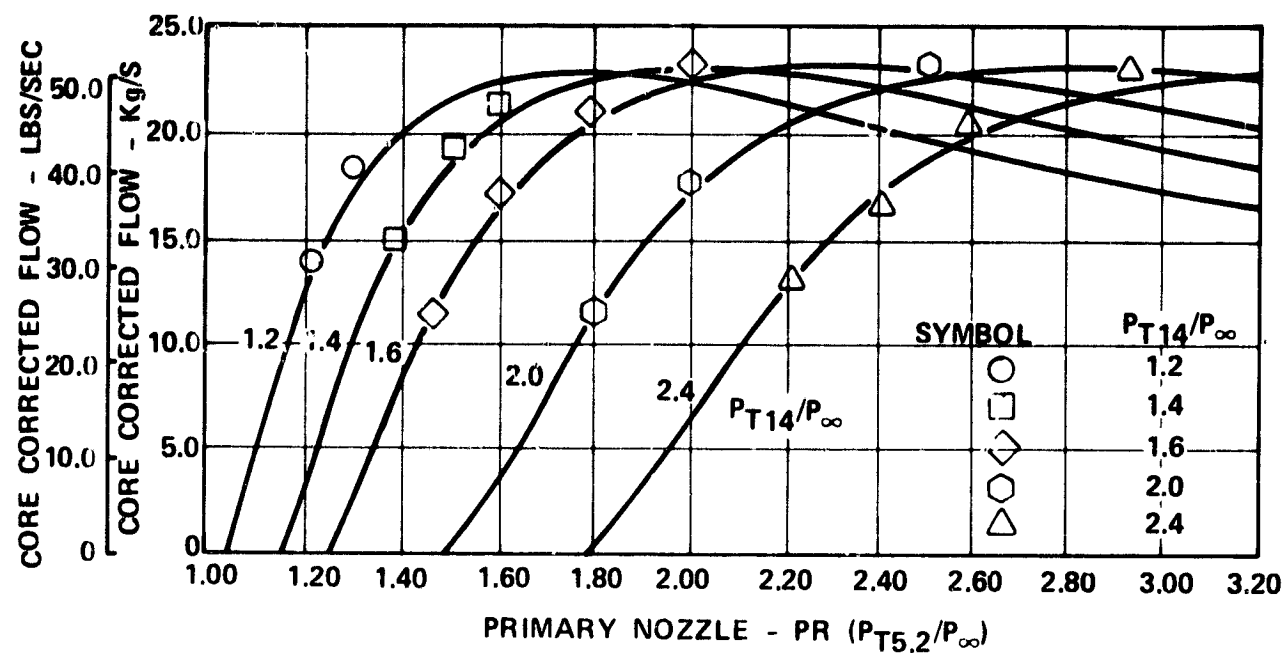
Figure 4-64. QCGAT Predicted Flow Maps Scaled to Test Areas and Flow Coefficients.
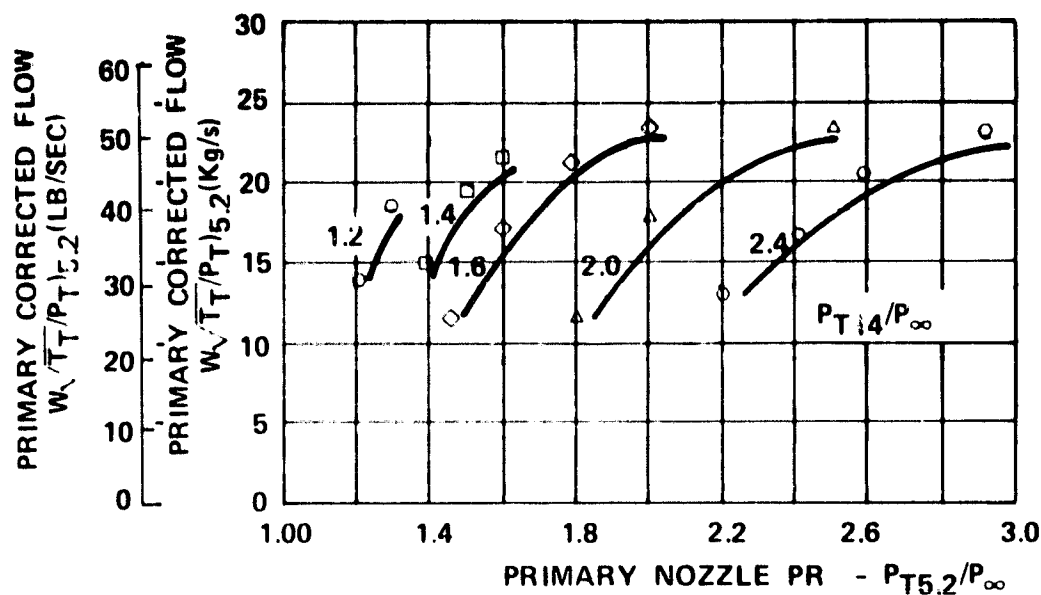
Figure 4-65. QCGAT Primary Corrected Flow Test Data Versus Predicted With Test Areas, Flow Coefficients, and Pressure Losses.
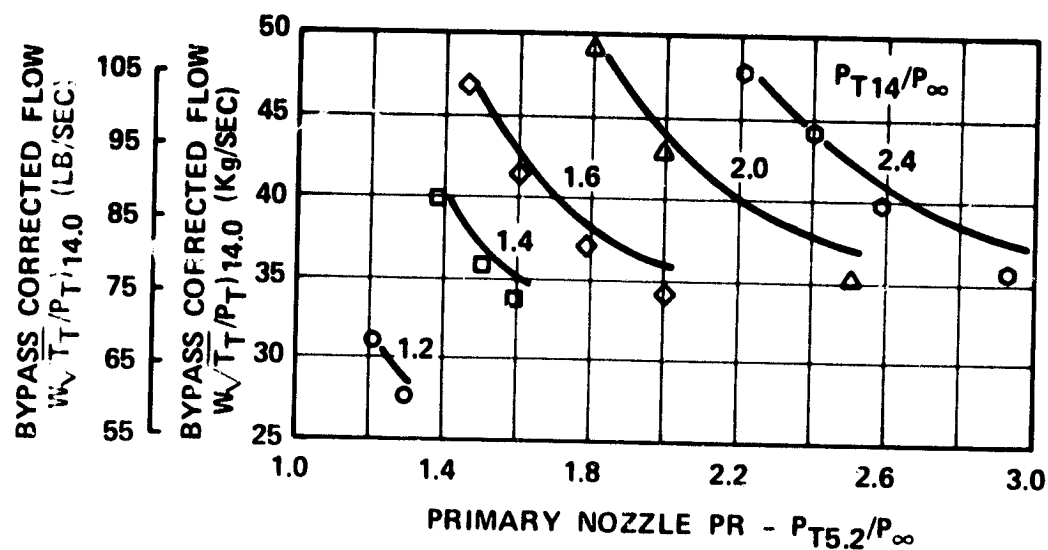
Figure 4-66. QCGAT Bypass Corrected Flow Test Data
Versus Predicted With Test Areas, Flow
Coefficients, and Pressure Losses.
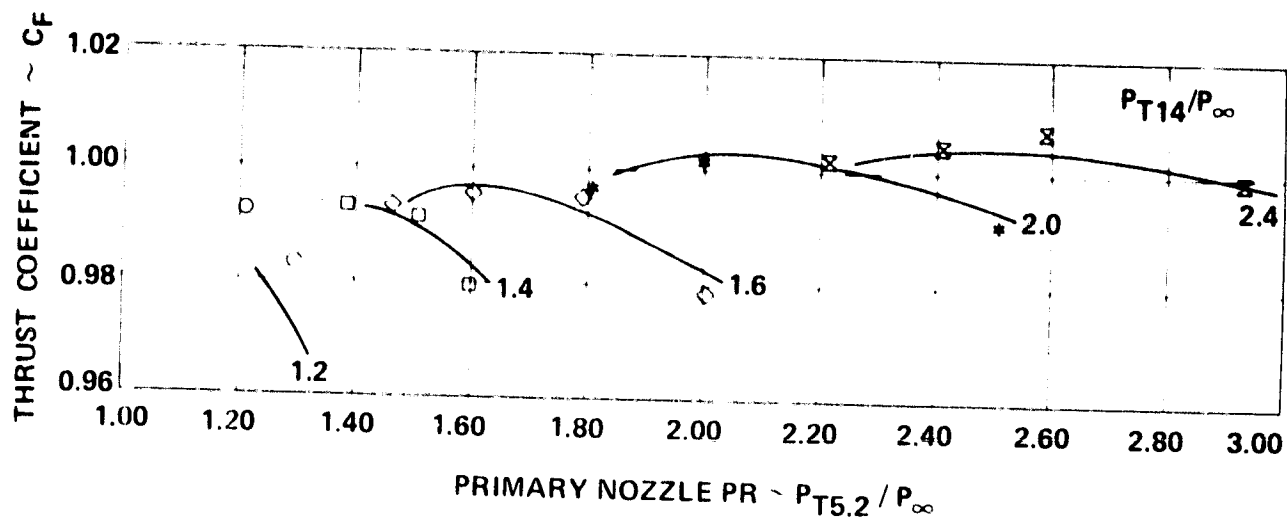
Figure 4-67. QC JAT Thrust Coefficient Test Data Versus Prediction With Tested Pressure Losses.

SECTION V

FULL-SCALE AREA SIZING

5.0 QCGAT CYCLE OPTIMIZATION WITH SHORT PARALLEL MIXER-COMPOUND EXHAUST SYSTEM

Since the tested flow maps presented earlier in Section 4.8.1 varied from the predicted maps, an area scaling analysis was required in order to match the exhaust system to the engine cycle at the dual-nozzle design point. The scaling procedure consisted of varying the core, bypass, and exit areas by +5 percent which produces core- and bypass-flow deviations from the desired engine cycle match point. Typical core- and bypass-flow-deviation lines for a given bypass-area scalar are presented in Figures 5-1 and 5-2. From these curves, intersection points of zero-flow deviation are determined which define zero-flow deviation lines for constant bypass-area scalars as a function of core- and exit-area scalars. (See Figure 5-3.) Intersection of the bypass- and core zero-flow deviation lines defines the exit-area scalar and a locus set of core- and bypass-area scalars that will match the desired engine cycle point (see Figure 5-3). The selected full-scale core-area scalar was chosen to match the test-model nominal core area, thus the full-scale mixer geometry could be scaled directly from the mixer-model scale coordinates and the full-scale core-stream aerodynamic contours would be identical to those tested. Selection of the core-area scalar defines the bypass-area scalar as shown in Figure 5-3.

The area scalars determined in the above manner were applied to the tested maps which were then run through the engine-cycle analysis program. Results of the engine cycle analysis on the dual-nozzle cruise-design point are shown in Table 5-1. Fan speed (N_1, high-pressure compressor speed (N_2) and the turbine inlet temperature ($T_{T4.1}$) matched the dual-nozzle design point as indicated by the comparison of column c with column a. Matching the mixer compound system (column c) results in a 5.4-percent increase in thrust over the reference-coannular nozzles (column a), and a 3.8-percent increase over the mixer-compound Preliminary Design Review predicted levels (Column b). Also, an improvement in TSFC of 5.4 percent over the reference coannular nozzles and 3.2 percent over the predicted levels was obtained. These improvements in thrust and TSFC are the result of optimizing to the cruise-design point.

At this optimized cruise-design-point match condition, the sea level static performance was evaluated with the same turbine inlet temperature ($T_{T4.1}$) as the reference coannular nozzle (see Column f, Table 5-1) and also with the same $T_{T4.1}$ as the predicted mixer compound nozzle (see Column g). The different turbine inlet temperatures ($T_{T4.1}$) resulted from the predicted mixer compound

CRUISE DESIGN POINT
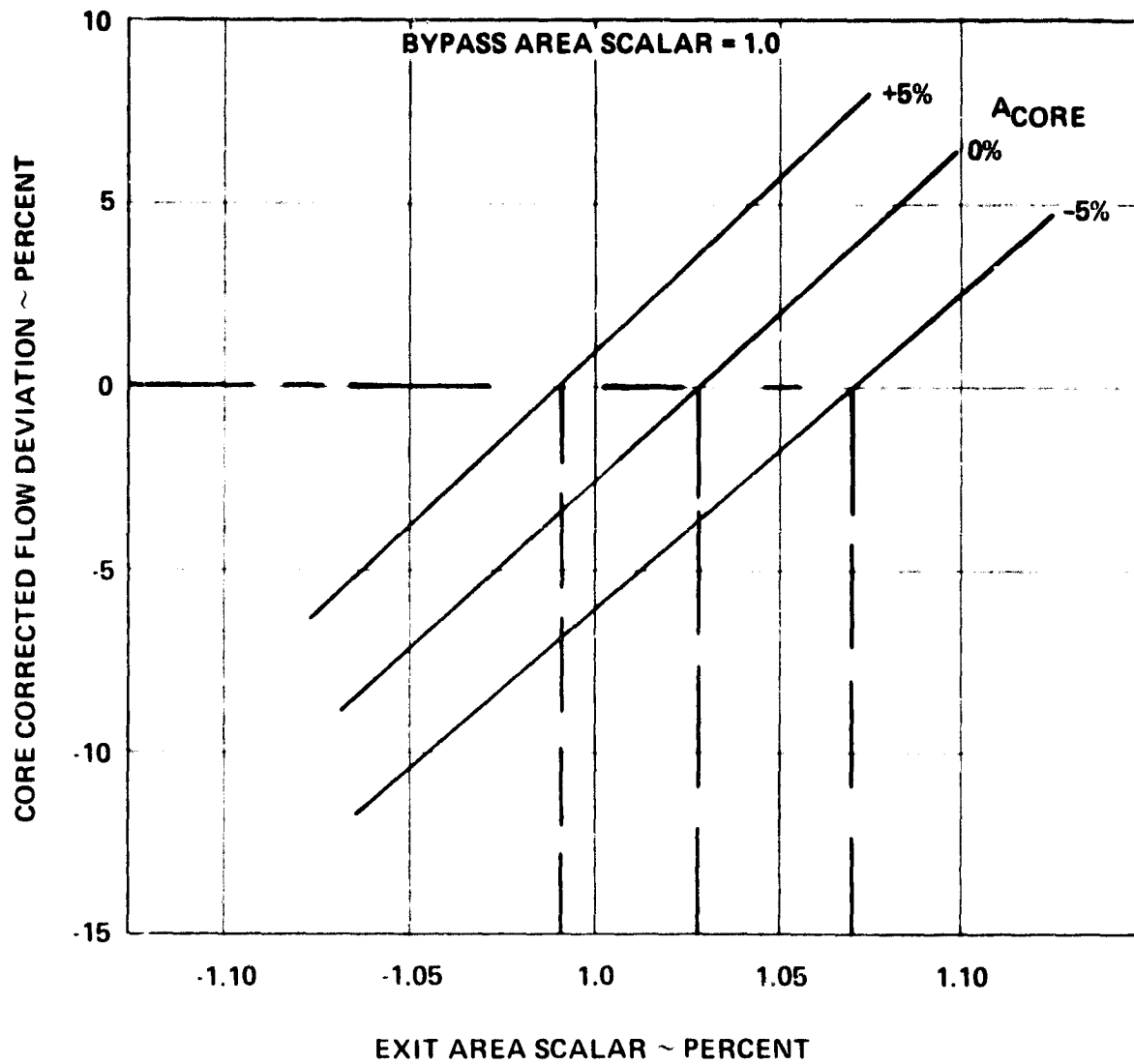
Figure 5-1. Core Flow Deviation Versus Area Scaling.

212
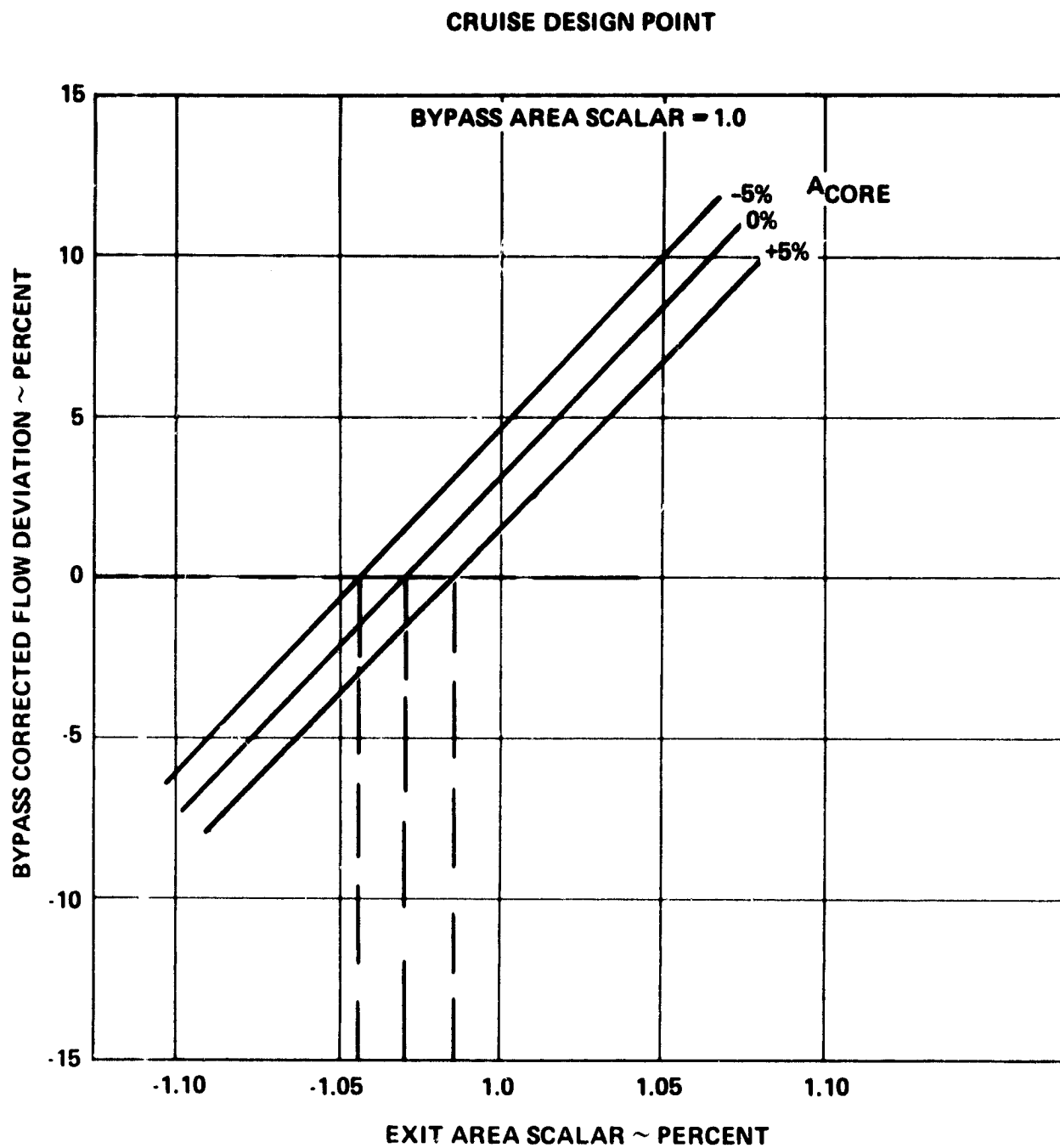
Figure 5-2. Bypass Flow Deviation Versus Area Scaling.
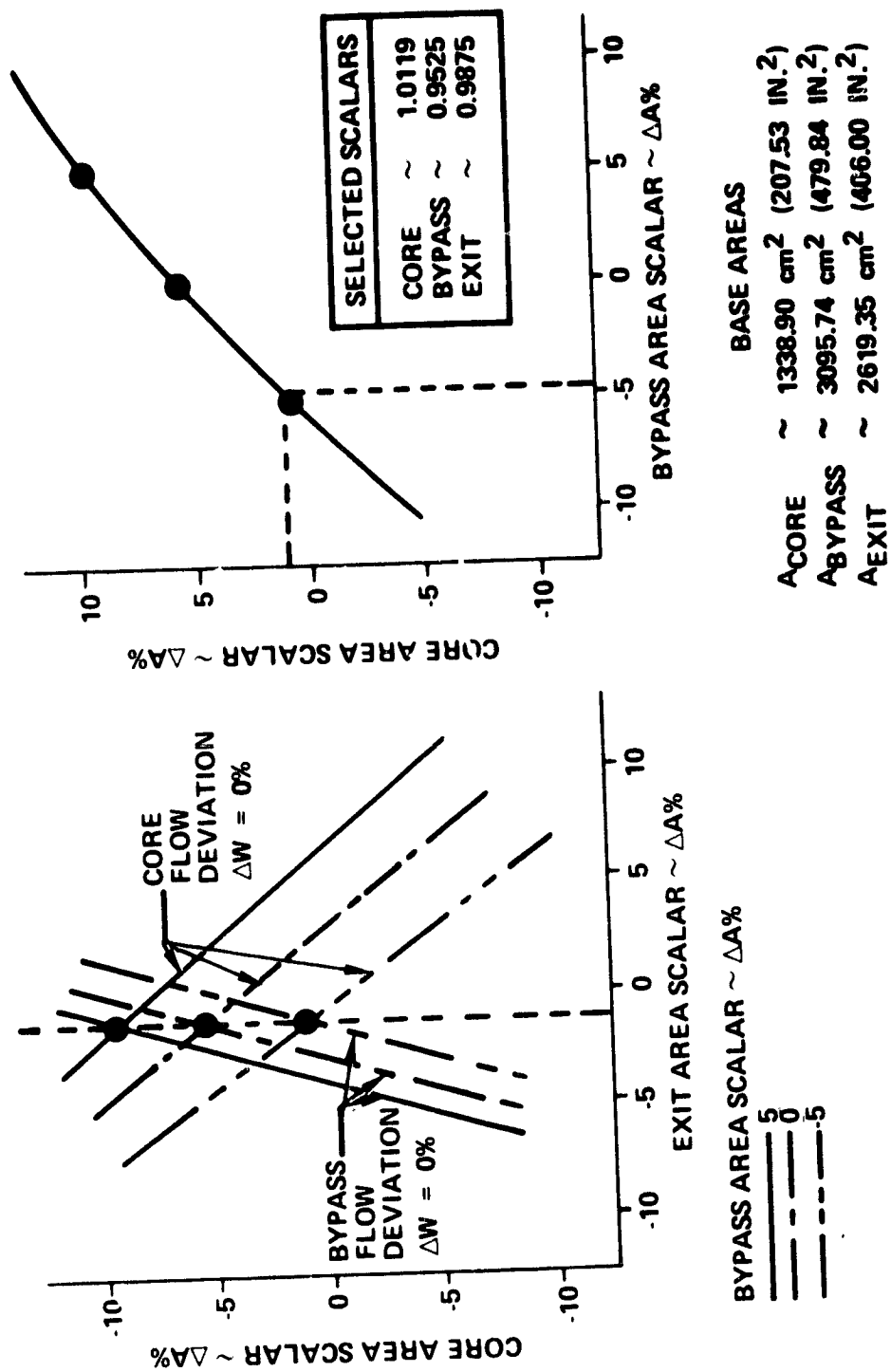
Figure 5-3. QCGAT Mixer Compound Area Sizing Aero Design Point Matching.

TABLE 5-1. QCGAT MIXER COMPOUND AREA SIZING AERO
DESIGN POINT MATCHED CYCLE PERFORMANCE.

Parameter	Cruise			Sea Level Static			
	(a) Reference Coannular Nozzles	(b) Nacelle PDR Compound Mixer Nozzles	(c) Configuration II Aero Design Point Matched	(d) Reference Coannular Nozzles	(e) Nacelle PDR Compound Mixer Nozzles	(f) Configuration II Aero Design Point Matched	(g) Configuration II Aero Design Point Matched
F_N N(lb)	3955.58 (889.25)	4018.48 (903.39) [+1.6%]	4167.45 (936.88) [+5.4%]	17,514.47 (3937.41)	17,312.92 (3892.1) [-1.2%]	17,040.29 (3830.81) [-2.7%]	17,800.76 (4001.77) [+1.6%]
TSFC Kg/hr/N (lb/hr/lb)	0.0775 (0.7599)	0.0757 (0.7433) [-2.2%]	0.0733 (0.7185) [-5.4%]	0.0430 (0.4218)	0.0437 (0.4289) [-1.7%]	0.0429 (0.4210) [-0.2%]	0.0429 (0.4209) [-0.2%]
N_1 rad/s (rpm)	2118.2 (20231)	2120.3 (20251)	2115.9 (20209)	1944.9 (18731)	1944.9 (18576)	1927.2 (18407)	1956.6 (18688)
N_2 rad/s (rpm)	2948.6 (28162)	2948.9 (28165)	2947.8 (28155)	3002.2 (28674)	3012.6 (28774)	2998.1 (28635)	3014.1 (28788)
$T_{4.1}$ °K (°F)	1266.5 (1820.3)	1266.5 (1820.3)	1266.5 (1820.3)	1316.2 (1837.75)	1327.9 (1858.85)	1316.2 (1837.75)	1327.9 (1858.85)

215

nozzles (Column e) requiring a higher $T_{T4.1}$ than the reference
nozzle (Column d) in order to meet sea level static thrust. At
the reference nozzle $T_{T4.1}$, the design-point match is 2.7 percent
low on sea-level thrust (see Column f). At the higher $T_{T4.1}$, the
design-point match is 1.6 percent in excess of the sea-level thrust.
However, the desire was to decrease the turbine-inlet temperature
at sea level static to the level of the reference nozzles and
still meet reference-nozzle thrust. This could be accomplished in
two ways. Since there is an excess level of thrust at the cruise
design point, the cycle areas could be rematched to trade excess
cruise thrust for additional sea level static thrust. The other
alternative was to increase the sea level static exit area with
a convergent-divergent nozzle, therefore maintaining the cruise-
design-point match. However, in this instance, the use of a
convergent-divergent nozzle would have required additional testing
to obtain the performance map characteristics. Since time pre-
vented this option, the area-trade study was performed by the
engine-cycle-analysis group. The exit area was increased 2.9 per-
cent over the cruise-design-point match in order to decrease the
cruise net thrust to the 409.6 kg (903 lb) predicted level as shown
in Figure 5-4 at an altitude condition of 12,192 m (40,000 ft).
The core-area scalar was maintained at 1.0 for the reasons dis-
cussed earlier. The bypass-area scalar was allowed to vary, but,
as shown in Figure 5-5 (sea-level conditions), decreasing the
bypass area does not produce a significant increase in thrust.
Also, in order to maintain sufficient fan-surge margin, the bypass
scalar was chosen as 1.0. A summary of the areas from the model
test to the final sizing are shown in Table 5-2. Percent changes
are relative to tested areas.

TABLE 5-2. MODEL TEST AREA SIZING.

| | Model Test Areas | Match to Dual Nozzle | | | |
		Critical Design Point	% Change	Final Sized Areas	% Change
Core	1338.90 cm^2 (207.53 in.^{2})	1354.84 cm^2 (210.0 in.^{2})	1.2	1354.84 cm^2 (210.0 in.^{2})	1.2
Bypass	3095.74 cm^2 (479.84 in.^{2})	2948.70 cm^2) (457.05 in.^{2})	-4.75	2948.70 cm^2 (457.05 in.^{2})	-4.75
Exit	2610.35 cm^2 (405.0 in.^{2})	2586.64 cm^2 (400.93 in.^{2})	-1.25	2661.87 cm^2 (412.59 in.^{2})	1.6
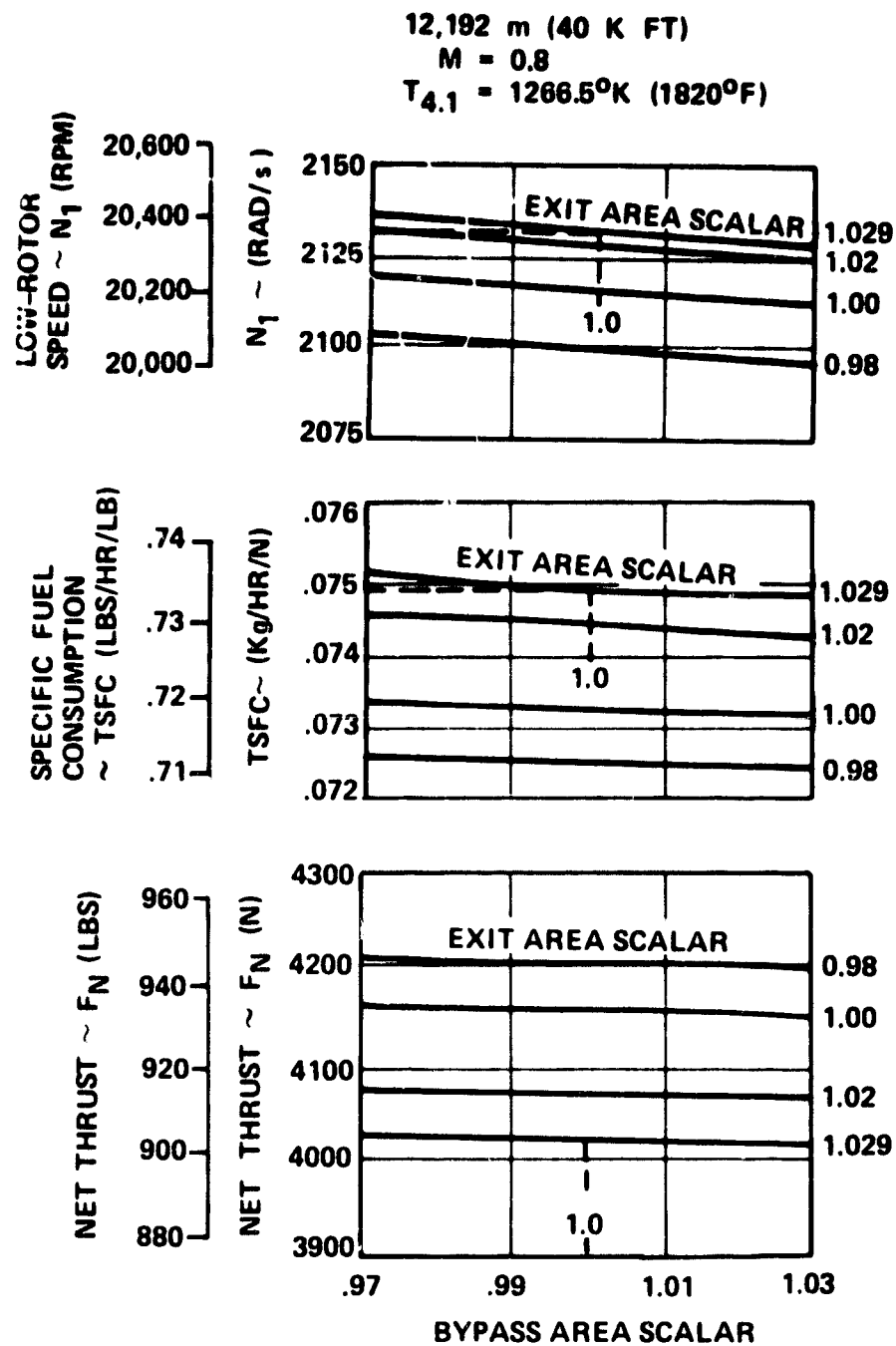
Figure 5-4. QCGAT Mixer Compound Area Sizing
Cycle Optimization at Altitude.
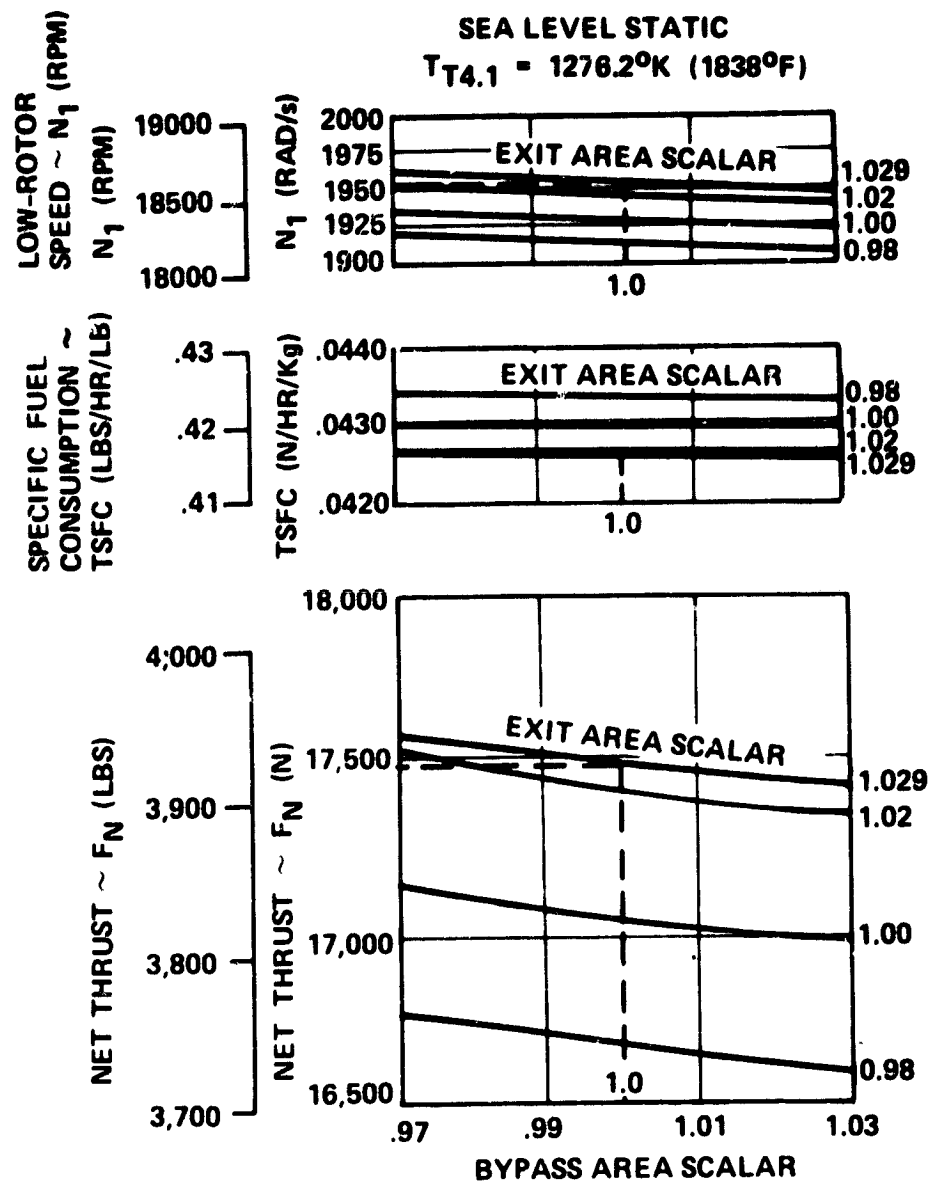
Figure 5-5.   QCGAT Mixer Compound Area Sizing
Cycle Optimization at Sea Level.

Table 5-3 presents the results from the engine-cycle analysis with the final-sized areas. Cruise net thrust (Column III) matches the Preliminary Design Review level (Column II) which is still a 1.6-percent increase over the reference coannular nozzles. A 1.0-percent improvement in TSFC is obtained relative to the Preliminary Design Review level and 3.2-percent relative to the coannular system. At sea level, the turbine inlet temperature ($T_{T4.1}$) was reduced to the coannular nozzle level, while thrust was increased to the reference nozzle level (see Columns IV and VI), resulting in a 1.0-percent improvement in TSFC relative to the reference coannular nozzle system.

The mixer-compound-exhaust-system-design geometry finally selected is presented in Table 5-4. Selection of the short parallel-mixer from the model test results shortened the mixer lobe length by 10.16 cm (4.0 in.) relative to the Nacelle PDR, thereby reducing the exhaust system overall length by 10.16 cm (4.0 in.).

TABLE 5-3. QCG T MIXER COMPOUND AREA SIZING OPTIMIZED CYCLE PERFORMANCE.

	Cruise			Sea Level Static		
	I Reference Coannular Nozzles	II Nacelle PDR Compound Mixer Nozzles	III Configuration II Cycle Optimization Matched	IV Reference Coannular Nozzles	V Nacelle PDR Compound Mixer Nozzles	VI Configuration II Cycle Optimization Matched
F_n -N (lbs)	3955.58 (889.25)	4018.43 (903.35) +1.6%	4019.41 (903.6) +1.6%	17,514.47 (3937.41)	17,312.92 (3892.1) -1.2%	17,491.74 (3932.3) -0.1%
TSFC-Kg/hr/N (lb/hr/lb)	0.0775 (0.7599)	0.0758 (0.7433) -2.2%	0.0750 (0.7355) -3.2%	0.0430 (0.4218)	0.0437 (0.4289) +1.7%	0.0426 (0.4176) -1.0%
N_1 rad/s (rpm)	2118.2 (20231)	2120.3 (20251)	2131.8 (20361)	1961.1 (18731)	1944.9 (18576)	1953.3 (18656)
N_2 rad/s (rpm)	2948.6 (28162)	2948.9 (28165)	2948.0 (28157)	3002.2 (28674)	3012.6 (28774)	3001.0 (28663)
$T_{T4.1}$ -°K (°F)	1266.5 (1820.3)	1266.5 (1820.3)	1266.5 (1820.3)	1276.2 (1837.75)	1287.9 (1858.85) +21.1	1276.2 (1837.7)

TABLE 5-4. QCGAT EXHAUST SYSTEM PERFORMANCE
DESIGN GEOMETRY.

Parameter	Proposal	Engine PDR	Nacelle PDR	Nacelle DDR
Exit area cm^2 (in.^{2})	2714.2 (420.7)	2619.3 (406.0)	2619.3 (406.0)	2661.9 (412.6)
Minimum area cm^2 (in.^{2})	2714.2 (420.7)	2619.3 (406.0)	2619.3 (406.0)	2661.9 (412.6)
Inlet area cm^2 (in.^{2})	3922.9 (615.8)	4516.1 (700.0)	4516.1 (700.0)	4387.0 (680.0)
Core splitter area cm^2 (in.^{2})	1324.5 (205.3)	1354.8 (210.0)	1354.8 (210.0)	1354.8 (210.0)
Bypass splitter area* cm^2 (in.^{2})	2648.4 (410.5)	3161.3 (490.0)	3161.3 (490.0)	3032.3 (470.0)
Mixing duct length cm (in.)	35.56 (14.0)	60.96 (24.0)	60.96 (24.0)	60.96 (24.0)
Nozzle length cm (in.)	30.48 (12.0)	40.64 (16.0)	40.64 (16.0)	40.64 (16.0)
Lobe length** cm (in.)	50.2 (20.0)	51.3 (20.2)	61.5 (24.2)	51.3 (20.2)
Total length** cm (in.)	116.8 (46.0)	152.9 (60.2)	163.1 (64.2)	152.9 (60.2)
Lobe number	9	12	12	12

*Includes splitter base area.
**Lobe and total length relative to turbine rotor exit.

t

SECTION VI

SUMMARY OF RESULTS

6.0 SUMMARY OF RESULTS

o   The short parallel mixer compound exhaust system
      (Configuration II) provides the best overall exhaust
      system performance for the QCGAT Engine. The cruise
      performance exceeds the design goal by 0.45 points
      (ΔC_{F_T} = 0.0045) and the sea level static performance
      is the best of all the tested systems exceeding the
      design goal by 1.5 points (ΔC_{F_T} = 0.0150).

o   The acoustic data shows conclusively that the short
      parallel mixer compound exhaust system (Configuration
      II) provided the lowest relative noise levels of the
      six nozzle configurations tested. This results in a
      maximum tone corrected perceived noise level reduc-
      tion of 4.1 PNdB$_t$ and a predicted flyover jet noise
      reduction of 5.1 EPNdB. The jet-noise reduction was
      found to be proportional to the achieved mixing
      efficiency.

o   Selection of the short parallel mixer compound exhaust
      system (Configuration II) for the QCGAT Engine yields
      a potential cruise-thrust increase of 5.4 percent and
      cruise TSFC reduction of 5.4 percent. However, the
      final exhaust system engine cycle area optimization
      resulted in a TSFC reduction 3.2 percent at cruise
      and a 1.0 percent at sea-level. The cruise thrust was
      increased by 1.6 percent while the takeoff temperature
      was reduced by 11.7°C (21.1°F) at nominally the same
      takeoff thrust as the reference nozzles.

o   The 3-D-viscous compressible flow analysis predicted
      the same total-pressure loss ranking of the mixer
      nozzles as derived from the test data. The turbulent
      mixing model analysis overpredicted the amount of
      thermal mixing.

SECTION VII

RECOMMENDATIONS

7.0 RECOMMENDATIONS

o   It is recommended that the short parallel mixer
     compound exhaust system (Configuration II) be used
     for the QCGAT nacelle. The recommended exhaust
     system areas are:

     Core Area   = 1354.84 cm^2 (210.00 in^2)
     Bypass Area = 2948.70 cm^2 (457.05 in^2)
     Exit Area   = 2661.87 cm^2 (412.59 in^2)

o   It is recommended that additional testing be conducted
     in which the mixing plane and constant-area mixing-
     duct-exit plane be surveyed for both mean flow and
     turbulence structure. This data would determine flow
     characteristics at each of these stations and would
     provide comparative data for improvement of the
     analytical design and optimization tools.

APPENDIX A

SURVEY RAKE DATA REDUCTION
AND
FORMATTED VARIABLES TO BE
PUNCHED ON PAPER TAPE

APPENDIX A

SURVEY RAKE DATA REDUCTION

STATIC PRESSURE INTERPOLATION

PSWAV = Average of Nozzle Exit-Wall Statics $\sim$

$$(\#161 + \#162)/2.0$$

PS(1) = Rake Centerline Static

$$PS(N) = PS(1) + (PSWAV - PS(1)) \frac{(0.3617)(N-1)}{3.9787}$$

where N = 1, 11

TOTAL PRESSURE INTERPOLATION

$$PT(2N) = (PT(2N+1) + PT(2N-1))/2.0$$

where N = 1, 5

This interpolates between the measured total pressures.

TOTAL TEMPERATURE CORRECTION

$$\Delta T_{5.2} = T_{T5.2} - T'_{T5.2}$$

$$\Delta T_{14} = T_{T14} - T'_{T14}$$

where: $T'_{T5.2}$ and T'_{T14} are the values at the 1st rake setting to $T_{T5.2}$ and T_{T14} are the values at the current rake setting.

$$T_T(N) = T_{TPROBE} - \left(\frac{\Delta T_{T5.2} - \Delta T_{T14}}{T_{T5.2} - T_{T14}}\right) (T_T - T_{T14}) - \Delta T_{14}$$

*REQUIRED <u>ONCE</u> FOR EACH SURVEY RUN

WRITE (100)   NS, NX, NY, ICNT, ABL, ITITL, GAM, DEGRAN, APRIME, PSTG, RGAS, TMIX, TREF

100 FORMAT   (3I3, I4, F5.1, I2, F6.3, F7.2, F8.1, F7.3, F8.0, 2F8.2)

Where: $NS = 1$

$NX = 12 \sim$ (No. Thetas +1)

$NY = 13 \sim$ (No. Radii +1)

$ICNT = 132 \sim$ (NX-1) (NY-1)

$ABL = 12.0 \sim$ (No. of Lobes)

$GAM = \gamma 5.2$

$$DEGRAN = \frac{\left[\dot{M}\sqrt{\frac{\gamma R T_T'}{\gamma-1}} \Big|_{5.2} + \dot{M}\sqrt{\frac{\gamma R T_T'}{\gamma-1}} \Big|_{14.0} \right]^2}{(\dot{M}_{5.2} + \dot{M}_{14.0})(\dot{M}\frac{\gamma R}{\gamma-L} \Big|_{5.2} + \dot{M}\frac{\gamma R}{\gamma-1} \Big|_{14.0})}$$

$$APRIME = \sqrt{494348 \left(\frac{\gamma 5.2}{\gamma 5.2 + 1}\right) T_{T5.2}'}$$

$$PSTG = (\dot{M}_{5.2} P_{T5.2}' + \dot{M}_{14.0} P_{T14.0}')/(\dot{M}_{5.2} + \dot{M}_{14.0})$$

$RGAS = 247174.0$ in.^{2}/sec^2 °R

$$TMIX = \frac{\frac{\dot{M}\gamma R T_T'}{\gamma-1}\Big|_{5.2} + \frac{\dot{M}\gamma R T_T'}{\gamma-1}\Big|_{14.0}}{\frac{\dot{M}\gamma R}{\gamma-1}\Big|_{5.2} + \frac{\dot{M}\gamma R}{\gamma-1}\Big|_{14.0}}$$

$TREF = T_{T5.2}'$

NOTE: Prime values correspond to 1st rake setting.

Units are as follows:

      TEMP $\sim$ °R   VELOCITY $\sim$ IN/SEC

      PRESS $\sim$ #F/IN^2

      LENGTHS $\sim$ IN.

*REQUIRED X NUMBER OF TIMES PER SURVEY RUN WHERE X = ICNT

    DO 200 (J = 2, NY) $\sim$ (RADII IN INCREASING ORDER)

    DO 200 (I = 2, NX) $\sim$ (THETA'S IN INCREASING ORDER WHERE
                                 INITIAL THETA IS SET TO 0.0)

    WRITE (200) L, I, J, RAD, THETA, Z, Y, X, CRMN, VELRAT, PS,
             PTRAT, TTRAT

    200 FORMAT (3I3, 7F6.3, F7.3, 2F7.4)
           See Page 7 of this Attachment for sample)

Where: L = 1
               I = 2, NX
               J = 2, NY
            RAD = PROBE RADIUS $\sim$ IN.
         THETA = RAKE ANGLE $\sim$ RADIANS
              Z = SURVEY PLANE STATION
                 (See Page 6 of this Attachment)
              Y = RAD cos θ
              X = RAD sin θ
           CRMN = V/V*

Where:
$$V = \sqrt{\frac{2\gamma}{\gamma-1} R_{GAS} T_T [1 - (\frac{P_S}{P_T})^{(\gamma-1)/\gamma}}$$

$$V^* = \sqrt{2(R_{GAS})\frac{\gamma}{\gamma+1} T_T}$$

and $\gamma = f$ (TEMP)

$$VELRAT = V/V^*_{5.2}$$

where: $V^*_{5.2} = \sqrt{2}(R_{GAS}) \frac{\gamma 5.2}{\gamma 5.2 + 1} T'_{T5.2}$

PS = Probe Static pressure as defined on Page 1 of this attachment.

$$PTRAT = P_T/P'_{T5.2}$$

where P_T is determined from measurement and interpolation as defined on Page 1 of this attachment.

$$TTRAT = T_T/T'_{T5.2}$$

where T_T is measured temperature from thermocouples TT1 through TT11.

232

APPENDIX B

REFERENCES

APPENDIX B

REFERENCES

1. Bernstein, A., W. Heiser, C. Hevenior, "Compound-Compressible Nozzle Flow," AIAA Paper No. 66-663.

2. Fage, E. L., "Apparent Subsonic Chocking in Dual Stream Nozzles and Practical Consequences," AIAA Paper No. 74-1176.

3. L'Eluyer, M. R., J. J. Morrison, W. E. Mallet, "Correlation of Turbofan Engine Thrust Performance with Compound Nozzle Flow Theory," AIAA Paper No. 70-612.

4. Thompson, C. E., "Aeronca Tests of a 1/6 Scale Model Compound Exhaust Nozzle and Cascade Thrust Reverser," AiResearch Report 21-2943.

5. Grochowsky, L., W. Blackmore, "Estimated Performance of the ATF3-6 Exhaust System," AIAA Paper No. 70-612, AiResearch Report 76-212212.

6. Blackmore, W., C. Thompson, "IR&D Mixer Compound Exhaust System 1/6 Scale Model Tests," AiResearch Report 22-0003, 1976.

7. Postlewaite, J., "Thrust Performance of Suppressor Nozzles," J. Aircraft Vol. 3, No. 6, Nov.-Dec. 1966, pp 587-588.

8. Frost, T., "Practical Bypass Mixing Systems for Fan Jet Aero Engines," The Aeronautical Quarterly, May 1966.

9. Von Glahn, U., D. E. Groesbeck, R. G. Huff, "Peak Axial-Decay with Single- and Multi-Element Nozzles," AIAA Paper No. 72-48.

10. Von Glahn, U., N. Sekas, D. Groesbeck, R. Huff, "Forward Flight Effects on Mixer Nozzle Design and Noise Consideration for STOL Externally Blown Flap Systems," AIAA Paper No. 72-792.

11. Groesbeck, D., R. Huff, U. Von Glahn, "Comparison of Jet Mach Number Decay Data with a Correlation and Jet Spreading Contours for a Large Variety of Nozzles," NASA TND-8423, June 1977.

12. Blackmore, W. L., "TFE731-2 Turbofan Bypass Duct Model Test Results," AiResearch AD-8065, August 1972.

13. Sovron, G., E. Klump, "Experimentally Determined Optimum Geometries for Rectilinear Diffuser with Rectangular, Conical or Annular Cross-Section," presented at the Symposium "Fluid Mechanics of Internal Flow," Sept. 20-21, 1965.

14. Dodge, Paul R., "3-D Heat Transfer Analysis Program Final Report," AiResearch Report 21-2541(7), August 1977.

15. Dodge, Paul R., "Input Data for Compressible 3-D Viscous", AiResearch Office Memo, January 31, 1977.

16. Dodge, Paul R., "Three-Dimensional Analysis Program Development Results and User's Guide for First Version of Program NANCY - Program J6575Pl," AiResearch Report 75-211691.

17. Caretto, L. S., A. D. Gosman, S. V. Patankar, and D. B. Spalding, "Two Calculation Procedures for Steady, Three-Dimensional Flow with Recirculation," proceedings of the Third Conference on Num. Methods in Fluid Mechanics, Vol. II, 1973.

18. "Studies in Convection Theory, Measurement, and Applications," Vol. 1 edited by B. E. Launder, 1975.

19. Paynter, G. C., S. C. Birch, Spalding, D. G. Tatchell, "An Experimental and Numerical Study of the 3-D Mixing Flows of a Turbofan Engine Exhaust System," AIAA 77-204.

20. Stone, J. R., "Interim Prediction Method for Jet Noise," NASA TMX-71618, 1974.

21. Stone, J. R., "Flight Effects on Exhaust Noise for Turbojet and Turbofan Engines - Comparison of Experimental Data with Prediction," NASA TMX-73552, November, 1976.

22. Gipson, W. M., "Flyover noise Prediction Procedure," AiResearch Report 21-2552, March 30, 1977.

236

APPENDIX C

LIST OF SYMBOLS AND DEFINITIONS

APPENDIX C

LIST OF SYMBOLS AND DEFINITIONS

a_{cr} = Critical Velocity [m/s (IN./SEC)]

A = Area [cm^2 ($IN.^2$)]

A_E = Exit Area [cm^2 ($IN.^2$)]

A_I = Inlet Area [cm^2 ($IN.^2$)]

A_{FS} = Full Scale Area [cm^2 ($IN.^2$)]

AR = Lobe Aspect Ratio

A' = Effective Area ($C_D A$) [cm^2 ($IN.^2$)]

AGW = Aircraft Gross Weight [kg (LBS)]

ALT = Altitude [m (FT)]

B = Compound Choking Criteria

C_D = Flow Coefficient

C_{DE} = Exit Flow Coefficient

C_{DS} = Splitter or Mixing Plane Flow Coefficient

C_F = Thrust Coefficient

CFA = Compound Flow Analysis

C_{FT} = Total Thrust Coefficient

C_L = Centerline

CP = Contact Perimeter [cm (IN.)]

C_p = Pressure Coefficient

C_s = Vacuum Thrust Coefficient

CRDP = Cruise Design Point

dB = Log Unit of Pressure

D = Mixing Duct Diameter [cm (IN.)]

D_E = Diameter of Equivalent Area Circle [cm(IN.)]

D_H = Hydraulic Diameter [cm(IN.)]

D_{HE} = Equivalent Hydraulic Diameter [cm(IN.)]

DDR = Detailed Design Review

EPNdB = Effective Perceived Noise Level, dB

EPNL - **Effective Perceived Noise Level Measured in EPNdB**

F = **Actual Gross Thrust** [N(LB)]

F_N = Net Thrust [N(LB)]

F_{ID} = Ideal Thrust [N(LB)]

f = Interface Function

f/a = Fuel-Air Ratio

f = Friction Factor

f( ) = Functional Parameter

h = Lobe Height [cm(IN.)]

HZ = Unit of Frequency (Cycles/Second)

K = Constant

K_R = Loss Ratio

L = Length [cm(IN.)]

M = Mach Number

m = Mass Flow Rate [kg/s(LB/SEC)]

N = Number of Lobes

N_1 = Low Rotor Speed [rad/s(rpm)]

N_2 = High Rotor Speed [rad/s(rpm)]

NM = Nautical Miles

P = Pressure [Pa(psi)]

PDR = Preliminary Design Review

PEN = Penetration Ratio

240

$PNdB_t$ = Tone Corrected Perceived Noise Level, dB

PR = Pressure Ratio

P_S = Static Pressure [Pa(psi)]

P_{SCL} = Static Pressure at Centerline [Pa(psi)]

P_T = Total Pressure [Pa(psi)]

P_{TR} = Rating Station Total Pressure [Pa(psi)]

q = Dynamic Pressure [Pa(psi)]

R = Radius [cm(IN.)]

R_1 = Plug Radius [cm(IN.)]

P_∞ = Ambient Pressure [Pa(psi)]

R_{eD} = Reynolds Number Based on Diameter

s = Lobe Spacing [cm(IN.)]

SLS = Sea Level Static

SPL = Sound Pressure Level re 2×10^{-5} N/m^2

SPL_{FF} = Far-Field Sound Pressure Level, dB

SPL_{FS} = Full-Scale Sound Pressure Level, dB

SPL_M = Scale Model Sound Pressure Level, dB

SR = Spacing Ratio

STA = Station

T_T = Total Temperature [°K(°R)]

$T_{T4.1}$ = Turbine Inlet Temperature [°K(°R)]

T_{T5} = Total Temperature at Rig Measurement Station [°K(°R)]

T/O = Takeoff

TR = Lobe Taper Ratio

TSFC = Thrust Specific Fuel Consumption [kg/hr/N(lb/hr/lb)]

V = Velocity [m/s(FT/SEC)]

VR	=	Velocity Ratio
w	=	Lobe Width [cm(IN.)]
W	=	Total Air Weight Flow [kg/s(lb/sec)]
WP	=	Wetted Perimeter [cm(IN.)]
X	=	Mixing Duct Length [cm(IN.)]
Z	=	Axial Station Location
Z_C	=	Characteristic Length at Onset of Coalescing Core Region
$(\ )_1$	=	Core Stream Properties
$(\ )_2$	=	Bypass Stream Properties
$(\ )_{5.2}$	=	Core Nozzle Rating Station
$(\ )_{14.0}$	=	Bypass Nozzle Rating Station
3-D	=	Three Dimensional
α	=	Angle [rad(°)]
β	=	Inlet Blockage Factor
γ	=	Ratio of Specific Heats
Δ	=	Difference
δ	=	Pressure Divided by Standard Sea Level Static Day Pressure
η_{mix}	=	Percent Mixing (Mixing Efficiency)
θ	=	Temperature Divided by Standard Sea Level Static Day Temperature
λ	=	Pressure Ratio
π	=	A Constant (3.14159265)
τ_w'	=	Wall Shear Stress [Pa(psi)]
ϕ	=	Plug Half Angle [rad(°)]
$\bar{\omega}$	=	Loss Coefficient

242

APPENDIX D

QCGAT 0.35 SCALE MODEL NOZZLE ACOUSTIC DATA
MEASURED NOISE LEVELS
FOR
SIX NOZZLE CONFIGURATIONS

APPENDIX D

QCGAT 0.35 SCALE MODEL NOZZLE ACOUSTIC DATA
MEASURED NOISE LEVELS
FOR
SIX NOZZLE CONFIGURATIONS

TABLE OF CONTENTS

D-1 Introduction

Six separate configurations of the QCGAT 0.35 scale-model nozzle were tested at the Fluidyne Engineering Corporation's Medicine Lake hot-flow test facility. The acoustic tests were conducted to provide information on the relative noise levels and directivities of the six nozzle configurations under consideration. The resultant information was used, along with the aerodynamic performance of each nozzle, in the selection of the final nozzle configuration for the QCGAT engine.

The acoustic test procedure and test setup were previously defined in Section 4.1.3. In summary, six microphone locations were utilized. The microphones were located at azimuth angles of 0.26, 0.34, 0.52, 0.69, 0.87 and 1.04 radians (15, 20, 30, 40, 50 and 60 degrees) from the nozzle-exhaust centerline at a radius of 2.44 meters (eight feet) from the nozzle-exit plane. These microphone locations were denoted as microphone locations 1 through 6 respectively. A schematic diagram of the acoustic test setup was previously presented as Figure 4-4 in Section 4.1.3.

D-2 Summary of Nozzle Operating Conditions

Acoustic testing was conducted at two different core- and bypass-pressure-ratio settings. These pressure-ratio settings simulated the sea level static takeoff and cruise-design-point operating conditions.

A summary of the core- and bypass-pressure ratios and temperature ratios measured at the nozzle rating station for the sea level static takeoff and cruise operating conditions is presented in Table D-1 for each nozzle configuration tested.

D-3 Tabulated Noise Levels for Each Nozzle Configuration

One-third octave band sound pressure levels measured at each microphone location are presented in Tables D-2 through D-7 for nozzle Configurations I through VI respectively. Measured levels for both the sea level static takeoff and cruise conditions are presented for each nozzle configuration.

The relative noise levels for each configuration were compared on a relative basis to determine the configuration producing the lowest noise levels.

Previous flyover-noise estimates for the full scale QCGAT engine indicated that the maximum tone-corrected perceived noise level for the jet noise occurred at an angle of approximately 1.08 radians (62 degrees) from the jet-exhaust axis.

245

TABLE D-1. SUMMARY OF SCALE MODEL NOZZLE OPERATING
CONDITIONS DURING ACOUSTIC TESTS.

Config.	Run No.	Operating Condition	Core P.R.	Bypass P.R.	$T_{T5.2}/T_{T14}$
I	9	S.L. Static T.O.	1.415	1.452	2.509
	10	Cruise	2.400	2.415	2.634
II	18	S.L. Static T.O.	1.387	1.414	2.487
	19	Cruise	2.409	2.471	2.620
III	27	S.L. Static T.O.	1.403	1.432	2.460
	28	Cruise	2.401	2.419	2.529
IV	36	S.L. Static T.O.	1.400	1.424	2.491
	37	Cruise	2.393	2.409	2.626
V	42	S.L. Static T.O.	1.389	1.424	2.522
	43	Cruise	2.400	2.425	2.681
VI	48	S.L. Static T.O.	1.390	1.429	2.532
	49	Cruise	2.412	2.434	2.663

246

TABLE D-2. MEASURED NOISE LEVELS - CONFIGURATION I.
QCGAT 0.35 SCALE MODEL NOZZLE ACOUSTIC TEST.
ONE-THIRD OCTAVE SOUND PRESSURE LEVELS*, dB re 2 x 10^{-5} N/M^2

RUN 9
SEA LEVEL STATIC CONDITION

MICROPHONE LOCATION

RUN 10
CRUISE CONDITION

MICROPHONE LOCATION

*2.4 m (8 ft) radius from nozzle exit.

TABLE D-3.   MEASURED NOISE LEVELS - CONFIGURATION II.

QCGAT 0.35 SCALE MODEL NOZZLE ACOUSTIC TEST

ONE-THIRD OCTAVE SOUND PRESSURE LEVELS*, dB re 2 x 10^{-5} N/M^2

RUN 18

SEA LEVEL STATIC CONDITION

MICROPHONE LOCATION

FREQUENCY	1.	2.	3.	4.	5.	6.
25.	114.	107.2	102.8	101.8	102.	98.8
31.5	116.	112.4	104.6	105.4	104.	105.2
40.	117.	111.4	104.8	104.	105.6	104.4
50.	115.2	110.8	105.	104.	105.6	105.2
63.	115.6	108.4	101.	98.	98.4	99.4
80.	114.6	106.6	102.4	97.2	93.2	95.2
100.	113.2	107.8	104.2	101.8	98.	94.
125.	113.6	109.8	106.	104.	100.8	96.8
160.	112.8	108.8	105.2	102.4	102.	100.8
200.	111.6	108.4	104.	104.2	104.6	106.2
250.	112.	110.	108.6	106.	107.4	108.2
315.	113.4	112.	111.4	110.6	110.6	107.2
400.	111.6	109.8	107.	105.	104.6	102.8
500.	110.2	108.4	105.8	104.	103.	101.4
630.	109.2	107.	105.2	103.2	101.8	99.8
800.	108.6	106.8	105.6	105.	103.2	101.4
1000.	107.4	106.4	105.2	104.6	104.6	102.8
1250.	106.	105.8	105.6	104.6	105.2	103.6
1600.	104.8	104.4	103.6	104.6	106.8	103.8
2000.	103.2	103.6	103.2	105.6	107.	104.4
2500.	103.	102.6	104.6	105.	107.	105.2
3150.	102.2	102.6	103.8	103.8	106.4	105.
4000.	101.4	102.2	102.6	103.6	106.4	105.4
5000.	101.4	101.2	101.8	102.8	107.	105.6
6300.	101.4	101.2	100.8	102.	107.2	106.
8000.	100.2	100.8	100.6	101.6	106.6	106.6
10000.	100.2	98.2	99.8	100.2	106.	106.8
12500.	99.	99.8	99.8	100.4	106.8	107.6
16000.	99.6	98.8	99.4	100.4	106.2	106.6
20000.	98.2	97.8	98.	100.6	106.2	106.
25000.	96.4	96.8	97.	100.6	105.4	105.
31500.	96.8	98.8	96.	93.8	99.	98.4
40000.						
OASPL	125.1	122.4	119.7	119.1	120.5	119.3
A-SCALE	118.	116.8	116.2	116.4	118.	116.4
D-SCALE	123.9	122.9	122.7	123.4	125.5	123.9
PNL	132.1	130.2	130.5	132.	132.	130.2
PNLTC	132.1	130.7	130.8	131.4	132.7	130.9

RUN 19

CRUISE CONDITION

MICROPHONE LOCATION

FREQUENCY	1.	2.	3.	4.	5.	6.
25.	113.8	108.2	106.8	106.2	107.2	105.8
31.5	119.	115.2	112.4	113.8	113.	114.
40.	117.	116.4	114.4	114.6	114.6	117.2
50.	120.8	116.8	116.4	115.8	116.2	118.6
63.	121.2	113.6	112.	111.8	113.	115.4
80.	123.4	105.8	112.6	110.2	107.	105.2
100.	123.6	107.8	112.6	113.8	109.8	106.4
125.	125.	112.6	115.2	113.4	112.8	109.4
160.	126.2	113.2	113.4	115.8	114.4	113.2
200.	126.6	116.	119.	119.4	116.	115.2
250.	128.6	116.	115.6	119.2	118.4	119.4
315.	131.2	124.	122.	122.	124.8	118.
400.	130.6	119.6	124.2	125.	121.8	119.
500.	131.2	119.2	122.	122.2	120.4	118.8
630.	132.2	118.	120.2	119.2	118.4	115.6
800.	131.2	117.2	120.4	119.	117.	116.
1000.	130.4	118.	122.2	120.2	117.	118.4
1250.	128.6	120.8	121.6	120.2	120.2	120.6
1600.	127.	125.4	122.8	124.8	125.2	122.6
2000.	125.	126.6	123.2	125.	127.2	125.6
2500.	124.8	126.4	124.	125.4	127.4	125.4
3150.	124.2	127.4	125.4	126.	127.8	125.2
4000.	124.2	128.8	124.6	125.4	127.8	125.4
5000.	125.2	127.	124.2	126.2	127.8	124.
6300.	124.8	126.	123.8	124.2	126.	124.
8000.	122.8	125.	121.4	122.2	125.4	123.4
10000.	121.2	124.	120.4	120.2	124.	123.
12500.	120.	123.6	120.	120.	123.4	123.
16000.	118.4	122.2	118.8	119.8	122.	121.2
20000.	116.2	121.	117.4	118.6	120.8	120.
25000.	113.2	119.6	116.	117.4	119.4	118.
31500.	110.	113.4	109.	111.	113.2	112.2
40000.						
OASPL	141.7	138.	135.2	137.	139.2	136.2
A-SCALE	130.4	137.4	135.1	135.4	137.	135.0
D-SCALE	144.9	145.8	142.9	144.6	145.	144.3
PNL	152.	151.	149.4	150.3	151.2	149.5
PNLTC	152.	151.5	154.	151.3	151.2	149.5

*2.4m (8 ft) radius from nozzle exit.

TABLE D-4. MEASURED NOISE LEVELS - CONFIGURATION III.
QCGAT 0.35 SCALE MODEL NOZZLE ACOUSTIC TEST

ONE-THIRD OCTAVE SOUND PRESSURE LEVELS*, dB re 2×10^{-5} N/M^2

RUN 27
SEA LEVEL STATIC CONDITION

RUN 28
CRUISE CONDITION

*2.4m (8 ft) radius from nozzle exit

TABLE D-5. MEASURED NOISE LEVELS - CONFIGURATION IV.

QCGAT 0.35 SCALE MODEL NOZZLE ACOUSTIC TEST

ONE-THIRD OCTAVE SOUND PRESSURE LEVELS*, dB re 2 x 10^{-5} N/M^2

RUN 36
SEA LEVEL STATIC CONDITION

RUN 37
CRUISE CONDITION

MICROPHONE LOCATION

FREQUENCY	1.	2.	3.	4.	5.	6.
25.	118.8	105.	102.6	101.2	98.8	100.6
31.5	122.2	107.8	102.6	103.6	101.4	102.
40.	124.6	106.2	104.4	104.8	103.6	105.6
50.	120.6	108.2	103.2	102.4	103.	106.6
63.	121.	108.	102.4	97.4	99.2	99.6
80.	120.4	107.6	101.8	96.8	92.2	93.
100.	118.	106.6	102.8	100.8	98.6	95.8
125.	116.6	107.	106.2	103.	101.2	97.8
160.	116.6	107.	105.4	103.	102.	99.8
200.	116.2	108.6	105.	104.	102.6	101.4
250.	117.	109.4	104.6	107.2	107.8	103.8
315.	116.	112.8	111.6	110.8	110.4	103.
400.	115.6	109.8	107.4	105.6	104.8	101.2
500.	114.4	108.2	106.6	105.	103.4	100.6
630.	117.	107.8	107.	104.2	103.	102.2
800.	113.8	107.4	106.4	106.2	104.8	102.8
1000.	113.	107.6	106.	106.4	106.8	104.6
1250.	112.	107.8	107.	107.8	106.2	103.8
1600.	110.6	106.6	106.6	106.4	106.6	105.4
2000.	110.8	105.2	106.2	106.4	107.4	105.2
2500.	110.4	104.8	106.4	105.4	107.2	107.2
3150.	108.8	104.8	105.2	105.	107.2	107.2
4000.	108.	103.4	104.4	104.8	107.4	107.2
5000.	107.2	102.4	102.6	103.	106.6	107.2
6300.	106.	101.2	102.4	101.4	106.8	107.
8000.	105.6	101.	101.6	101.4	106.2	107.
10000.	104.6	100.6	100.8	101.	106.6	107.
12500.	104.	99.8	100.4	101.2	106.2	107.2
16000.	103.	98.6	100.2	101.4	107.	107.8
20000.	101.8	98.8	99.8	101.4	106.6	107.2
25000.	100.8	97.8	98.	101.	106.2	106.8
31500.	99.6	96.6	94.6	95.2	100.6	105.6
40000.	93.6	91.2	83.	85.2	100.8	100.8
OASPL	131.5	121.7	120.3	119.8	120.7	120.
A-SCALE	123.3	117.8	117.7	117.8	118.6	117.6
D-SCALE	129.4	123.9	124.2	124.7	125.2	125.5
PNL	137.6	131.7	131.4	131.6	132.5	131.6
PNLTC	137.6	132.	132.	132.4	133.2	132.2

MICROPHONE LOCATION

FREQUENCY	1.	2.	3.	4.	5.	6.
25.	119.2	115.8	112.6	110.6	109.2	111.8
31.5	117.2	117.2	114.	115.8	116.	113.8
40.	122.	120.6	116.4	118.6	118.	118.
50.	122.8	120.	114.6	113.4	112.8	114.
63.	124.2	118.6	112.6	111.	113.	114.
80.	122.8	119.2	112.6	109.8	106.6	109.2
100.	124.8	120.	113.8	112.8	110.2	107.2
125.	126.	122.8	116.	115.8	114.	111.2
160.	125.8	122.8	118.4	115.8	116.2	113.2
200.	127.	123.8	117.	118.8	117.6	116.2
250.	129.8	127.2	122.6	120.	123.	119.8
315.	130.8	130.	124.6	125.6	122.6	120.6
400.	131.4	128.2	121.8	121.6	121.	121.2
500.	132.6	120.2	121.8	120.	119.	117.2
630.	132.6	120.2	120.6	120.8	119.	116.2
800.	132.2	129.	121.6	120.8	117.	117.
1000.	130.4	120.	124.	122.8	118.4	119.
1250.	120.	127.8	123.	121.2	118.4	123.
1600.	128.	127.	124.	124.6	120.8	123.
2000.	126.6	126.6	123.6	125.4	127.6	125.8
2500.	125.8	126.6	125.2	125.8	127.2	127.2
3150.	125.6	126.2	126.	126.8	128.2	126.8
4000.	125.6	125.4	125.	125.	127.	126.
5000.	124.2	125.	123.4	125.2	125.2	124.6
6300.	122.6	122.	122.	123.	123.8	124.
8000.	120.4	121.	122.	120.6	122.8	123.8
10000.	119.	120.6	120.	120.6	120.2	123.2
12500.	118.	118.8	118.6	119.8	122.8	122.8
16000.	116.4	117.8	117.6	119.	121.4	119.6
20000.	114.8	116.4	116.4	117.8	120.	117.8
25000.	100.8	110.8	110.8	111.6	114.	113.2
31500.	142.6	140.5	137.2	137.2	138.2	135.1
A-SCALE	140.7	139.1	136.	136.5	137.6	135.1
D-SCALE	146.2	145.6	144.2	144.6	146.8	144.4
PNL	153.6	152.6	150.4	150.5	151.4	149.7
PNLTC	153.5	152.5	150.4	151.3	152.	149.7

*2.4m (8 ft) radius from nozzle exit

250

TABLE D-6. MEASURED NOISE LEVELS - CONFIGURATION V.

QCGAT 0.35 SCALE MODEL NOZZLE ACOUSTIC TLST

ONE-THIRD OCTAVE SOUND PRESSURE LEVELS*, dB re 2 × 10^{-5} N/M^2

SEA LEVEL STATIC CONDITION
RUN 42

MICROPHONE LOCATION

FREQUENCY	1.	2.	3.	4.	5.	6.
25.	116.6	107.	106.4	103.8	103.8	96.4
31.5	120.8	113.2	107.4	106.4	103.	101.
40.	118.6	113.	109.2	109.2	110.8	108.
50.	117.6	111.8	102.	106.8	102.4	104.
63.	117.	111.	103.	98.2	98.	100.8
80.	118.4	109.2	101.4	93.8	95.6	95.2
100.	117.2	109.4	108.6	104.4	101.2	96.6
125.	117.	112.4	107.2	104.	103.6	99.
160.	114.2	110.2	106.	103.8	100.6	100.
200.	114.	110.2	104.6	105.	103.6	101.
250.	115.4	111.8	108.8	108.4	108.2	103.4
315.	115.8	113.	110.8	109.8	106.2	106.6
400.	113.8	111.	106.8	105.8	103.6	102.4
500.	113.	110.8	106.2	105.2	103.	101.8
630.	111.8	109.6	105.8	104.6	102.8	101.8
800.	110.	109.	107.8	107.2	104.4	103.6
1000.	109.2	108.6	108.	106.8	104.6	105.
1250.	108.2	107.8	107.2	107.2	105.8	102.6
1600.	106.6	106.8	106.4	106.6	105.8	102.6
2000.	105.4	105.6	105.2	106.2	107.6	107.8
2500.	105.4	105.6	106.2	106.6	108.2	105.6
3150.	104.8	104.8	105.	106.8	108.2	106.6
4000.	104.2	104.4	105.	105.8	106.	106.
5000.	104.	104.2	104.6	106.	109.6	106.
6300.	103.4	103.6	104.6	104.6	109.6	106.
8000.	103.4	103.2	103.8	104.8	108.	106.6
10000.	102.6	102.2	102.8	103.8	108.2	106.8
12500.	102.2	102.2	102.8	102.6	107.2	107.8
16000.	102.2	101.8	102.2	103.2	108.4	108.6
20000.	100.6	100.6	101.4	102.8	107.4	107.8
25000.	99.4	100.	100.1	103.	107.6	107.
31500.	97.8	98.4	99.2	102.6	107.2	105.8
40000.	96.	92.2	92.2	95.8	102.	101.2
OASPL	128.6	124.1	121.1	120.6	121.8	119.9
A-SCALE	120.1	118.0	117.9	118.1	119.5	117.2
D-SCALE	126.1	125.	124.5	125.1	127.4	124.7
PML	134.2	132.8	131.8	133.1	133.4	130.8
PNLTC	134.2	132.8	132.5	133.1	134.1	131.4

CRUISE CONDITION
RUN 43

MICROPHONE LOCATION

FREQUENCY	1.	2.	3.	4.	5.	6.
25.	114.2	112.	106.8	108.8	107.8	106.
31.5	121.	117.	115.6	114.2	116.2	114.2
40.	120.8	120.8	117.2	114.6	117.8	121.2
50.	122.	119.2	114.	110.6	111.6	114.
63.	121.2	117.8	114.4	110.6	105.4	111.6
80.	124.2	119.	113.8	110.6	105.	107.
100.	124.	120.	115.	113.6	116.	112.2
125.	126.2	122.8	117.8	116.6	114.	112.6
160.	125.8	122.	118.	116.	115.2	116.
200.	128.	124.	115.8	119.	115.6	116.4
250.	129.6	126.2	120.	119.6	120.6	116.8
315.	130.	128.2	123.2	122.2	117.	117.
400.	131.2	128.2	121.2	118.2	117.	116.8
500.	132.8	130.	123.	120.6	119.8	118.
630.	133.	130.	122.6	120.2	119.6	117.
800.	131.8	129.6	125.2	121.6	119.	116.8
1000.	132.6	127.2	123.2	121.6	120.4	116.2
1250.	128.6	127.2	124.	123.6	121.2	117.
1600.	127.2	124.8	124.8	120.	121.2	121.2
2000.	125.8	124.4	124.	126.2	125.9	125.6
2500.	124.8	124.8	124.	126.2	125.4	125.8
3150.	123.6	123.4	124.4	126.4	124.8	123.6
4000.	125.	125.2	124.6	126.2	124.2	122.2
5000.	125.	125.2	125.2	125.4	124.6	120.1
6300.	124.6	124.	124.6	125.2	127.6	124.6
8000.	124.	124.	124.	123.8	125.2	124.6
10000.	122.2	121.2	122.2	123.6	125.	123.6
12500.	121.4	121.8	121.8	121.6	123.6	122.2
16000.	120.	120.	120.6	121.	123.	120.
20000.	117.8	118.6	118.8	121.	122.	110.1
25000.	115.8	117.2	117.6	119.2	121.	110.6
31500.	113.8	115.6	115.8	112.2	114.4	112.6
40000.	105.8	109.2	106.8	112.8	118.8	110.8
OASPL	146.3	149.1	136.8	137.3	138.6	136.8
A-SCALE	149.1	138.7	135.9	136.6	138.3	135.9
D-SCALE	145.2	144.7	144.3	144.6	146.7	145.
PML	152.	151.8	149.6	159.3	151.7	144.3
PNLTC	152.4	151.8	149.6	151.	152.3	149.3

*2.5 m (8 ft) radius from nozzle exit

TABLE D-7. MEASURED NOISE LEVELS – CONFIGURATION VI.

OCGAT 0.35 SCALE MODEL NOZZLE ACOUSTIC TEST

ONE-THIRD OCTAVE SOUND PRESSURE LEVELS*, dB re 2 x 10^{-5} N/M^2

RUN 48

SEA LEVEL STATIC CONDITION

MICROPHONE LOCATION

FREQUENCY	1.	2.	3.	4.	5.	6.
25.	114.2	106.8	104.8	105.4	101.2	104.2
31.5	117.4	107.4	106.4	105.6	103.4	102.6
40.	118.6	108.4	108.8	108.	107.8	107.
50.	118.6	107.2	103.4	103.4	106.	105.6
63.	120.4	107.2	102.8	95.4	98.8	100.2
80.	118.8	105.8	102.8	96.	93.8	95.6
100.	118.2	105.8	107.	103.8	100.6	96.8
125.	115.8	108.4	108.6	105.	103.	100.6
160.	114.4	108.4	105.6	101.6	103.	101.8
200.	115.	108.2	106.	104.6	101.6	101.6
250.	114.6	108.2	108.6	107.4	106.6	104.
315.	116.2	111.	111.8	111.8	111.4	107.6
400.	114.	110.	105.2	105.8	105.2	102.8
500.	113.8	109.6	107.6	105.6	103.4	101.8
630.	112.4	109.2	107.	106.	103.4	101.2
800.	110.8	108.	107.8	106.2	105.8	102.6
1000.	109.4	108.	107.2	105.6	105.2	103.4
1250.	108.4	107.	106.8	107.	107.	105.4
1600.	106.6	106.6	106.2	106.4	106.2	104.8
2000.	105.4	106.2	106.	106.6	106.	107.6
2500.	105.6	105.	106.	106.2	108.	107.4
3150.	105.	104.6	105.4	106.4	108.8	106.8
4000.	104.4	103.8	104.2	106.	109.	106.6
5000.	104.2	103.4	104.2	105.8	109.4	107.2
6300.	103.4	102.6	103.	104.2	109.6	107.6
8000.	103.	102.8	102.6	104.4	109.	108.2
10000.	102.2	102.	102.	103.8	108.8	108.
12500.	101.8	101.6	102.2	102.8	108.4	108.8
16000.	101.8	101.	102.	102.8	108.4	108.
20000.	100.	99.2	101.	102.4	108.	108.
25000.	98.8	98.6	100.	102.6	107.8	107.6
31500.	97.8	97.8	99.2	102.2	107.4	106.2
40000.	91.6	91.2	92.6	96.	102.1	101.
OASPL	129.	121.8	121.1	120.6	122.1	120.7
A-SCALE	120.4	118.2	117.8	118.1	120.	118.2
D-SCALE	126.4	124.2	124.4	125.2	127.7	125.8
PNL	134.5	131.8	131.8	132.	133.8	131.6
PNLTC	134.5	131.8	132.4	132.9	134.7	132.5

RUN 49

CRUISE CONDITION

MICROPHONE LOCATION

FREQUENCY	1.	2.	3.	4.	5.	6.
25.	112.8	112.	100.	100.2	110.8	108.6
31.5	118.2	117.	114.	112.8	113.8	115.
40.	120.	118.8	116.8	117.	118.2	118.8
50.	121.	118.4	114.6	115.	112.8	120.
63.	120.	118.	114.4	109.8	112.8	115.
80.	122.6	118.6	113.2	110.6	107.2	110.6
100.	124.	119.6	114.4	114.	111.6	110.8
125.	125.2	121.4	116.2	113.	114.4	105.8
160.	125.	122.	117.	116.6	113.8	113.4
200.	128.	124.2	114.8	110.6	114.6	116.6
250.	129.6	125.8	120.2	119.	120.6	117.8
315.	131.	121.4	123.	123.2	122.2	117.
400.	132.2	129.	121.	118.	117.2	115.
500.	132.6	130.2	122.6	121.	119.	118.8
630.	133.2	130.4	122.2	120.6	119.2	115.8
800.	132.2	130.6	121.8	120.8	116.	116.8
1000.	132.2	130.	122.8	122.	119.	118.
1250.	129.	127.	122.8	122.2	120.	122.
1600.	128.	127.2	125.	125.8	125.	125.6
2000.	125.	126.2	125.	125.8	127.	125.6
2500.	125.	125.	124.	125.2	127.8	127.
3150.	124.2	124.4	124.4	127.2	125.2	125.2
4000.	124.8	125.	125.8	127.	121.	125.8
5000.	125.2	125.2	125.8	127.2	120.8	125.6
6300.	124.	125.4	125.2	126.6	120.	125.2
8000.	124.	125.	124.	125.	125.2	125.2
10000.	123.6	123.8	123.	124.2	124.	124.2
12500.	122.2	122.8	122.2	122.4	125.2	124.2
16000.	120.6	120.8	121.2	122.	124.8	123.
20000.	118.2	119.	120.	121.6	123.4	122.2
25000.	116.4	117.8	118.4	120.8	122.2	121.
31500.	114.8	116.4	117.2	119.8	121.	119.2
40000.	106.4	108.6	108.6	112.8	113.	111.
OASPL	142.6	140.7	136.8	137.7	134.9	137.
A-SCALE	140.4	139.1	136.1	137.	138.3	136.2
D-SCALE	145.5	145.	143.8	145.1	144.8	144.6
PNL	152.7	152.	150.	150.8	151.9	149.6
PNLTC	152.7	152.	150.	151.6	152.6	149.6

*2.4m (8 ft) radius from nozzle exit.

As a result, the measured noise levels for each nozzle configuration were initially compared in terms of the tone-corrected perceived noise level occurring at each microphone location, with major emphasis placed on the noise level comparison at microphone location 6, 1.04 radians (60 degrees) from the exhaust centerline.

A summary of the measured tone-corrected perceived noise levels occurring at each microphone location for each nozzle configuration is presented in Table D-8 for the sea level static takeoff operating condition.

The lowest noise levels (tone-corrected perceived noise) for the six nozzle configurations is provided by Configuration II at all microphone locations.

In addition to providing the lowest measured noise levels, configuration II also provided the highest measured thrust coefficient and highest percent mixing at the sea level static takeoff condition for the six nozzle configurations tested (refer to Performance Summary, Table 1.1 of Section 1.4).

D-4. One-Third Octave Spectra Comparisons

The measured one-third octave band spectra levels for scale nozzle configurations I, II, III and IV are plotted for comparison in Figures D-1 through D-6 for the sea level static takeoff operating condition.

Nozzle configuration II generally provides the lowest noise levels across the entire frequency spectra for each microphone location for each of the configurations compared.

The measured one-third octave band spectra levels for scale nozzle configurations I, II, V and VI are plotted for comparison in Figures D-7 through D-12 for the sea level static takeoff operating condition.

Again, configuration II generally provides the lowest consistent noise levels across the entire frequency spectra for each of the configurations compared.

Conclusion

The resultant acoustic data shows conclusively that scale model nozzle configuration II provided the lowest relative noise levels of the six nozzle configurations tested. This fact, combined with the superior sea level static takeoff aerodynamic performance of configuration II, compared to the other nozzles, resulted in the selection of configuration II for the QCGAT engine.

TABLE D-8. SUMMARY OF ACOUSTIC TEST RESULTS.

Six Nozzle Configurations
at Sea Level Static Condition

Nozzle Configuration	Tone Corrected Perceived Noise Level $(PNdB_t)$					
	Angle from Exhaust Center Line					
	0.26 rad. (15°)	0.3? rad. (20°)	0.52 rad. (30°)	0.69 rad. (40°)	0.87 rad. (50°)	1.04 rad. (60°)
I	136.8	135.6	134.7	134.0	134.7	131.9
II	132.1*	130.7*	130.8*	131.4*	132.7*	130.9*
III	135.8	134.2	133.3	133.2	134.4	133.7
IV	137.6	132.2	132.0	132.4	133.2	133.2
V	134.2	132.8	132.5	133.1	134.1	131.4
VI	134.5	131.8	132.4	132.9	134.7	132.5

*Denotes minimum noise level at each angle

254
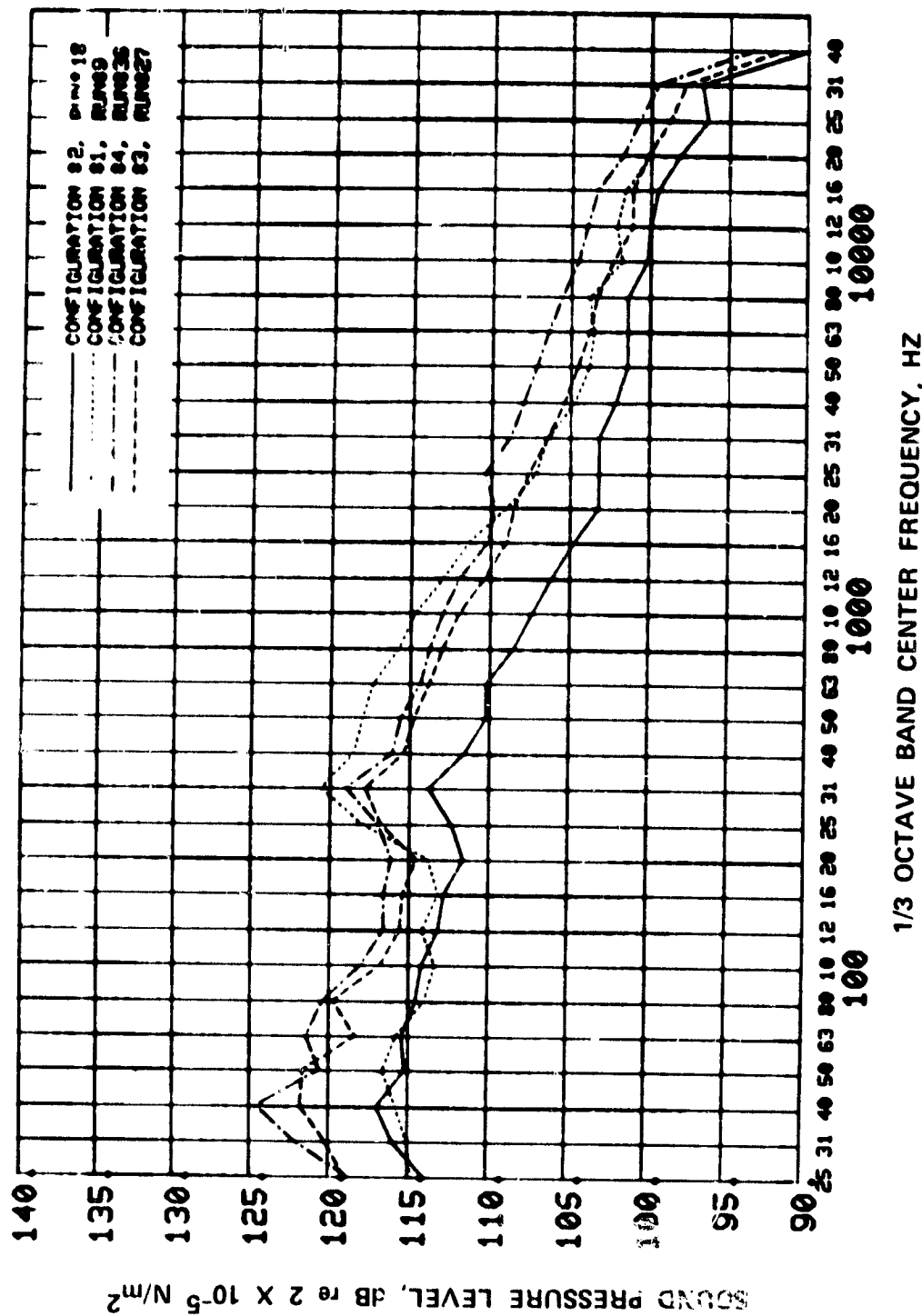
Figure D-1. Noise Spectra Comparison, Microphone Location 1, Configurations I, II, III, and IV.
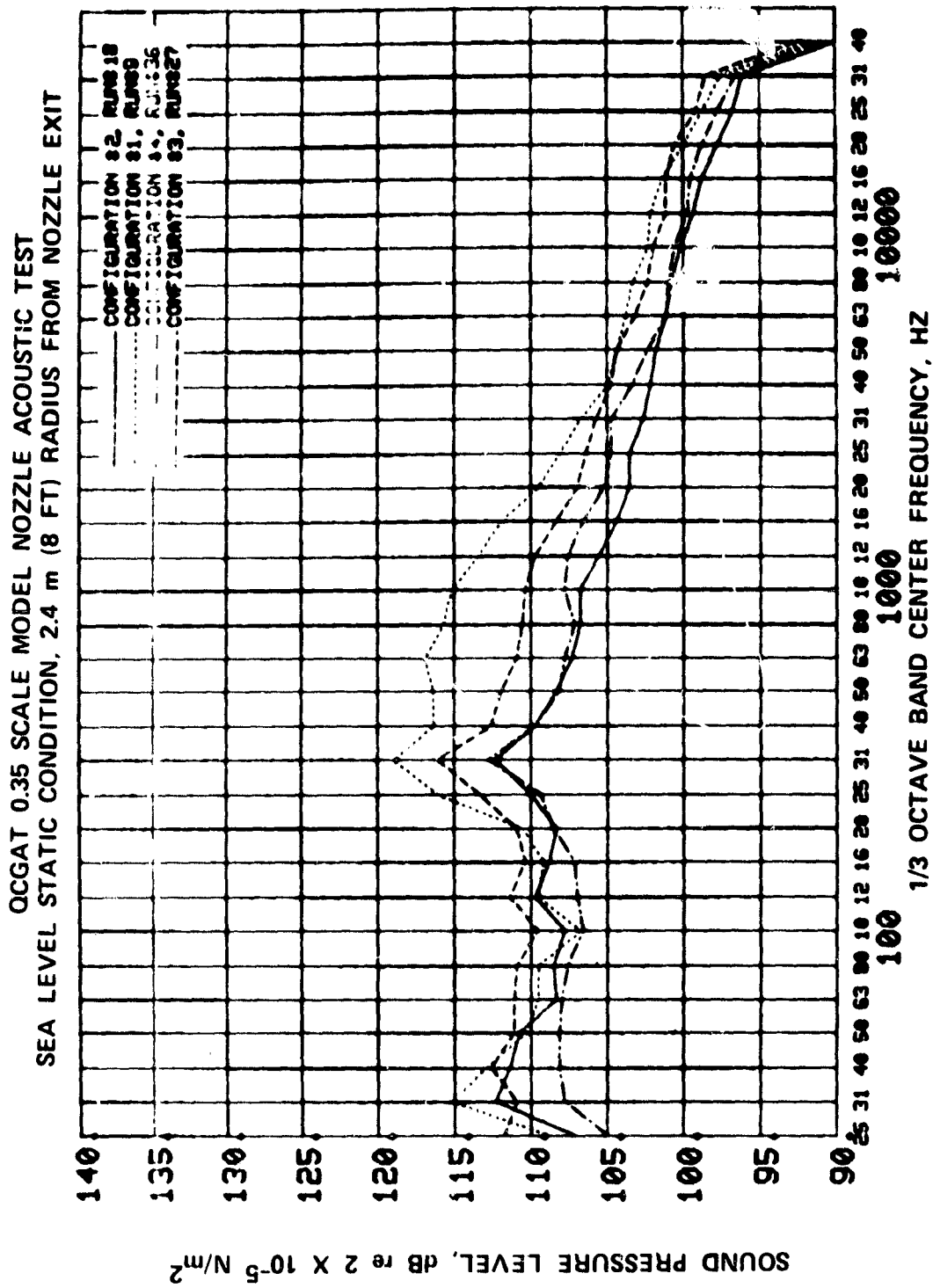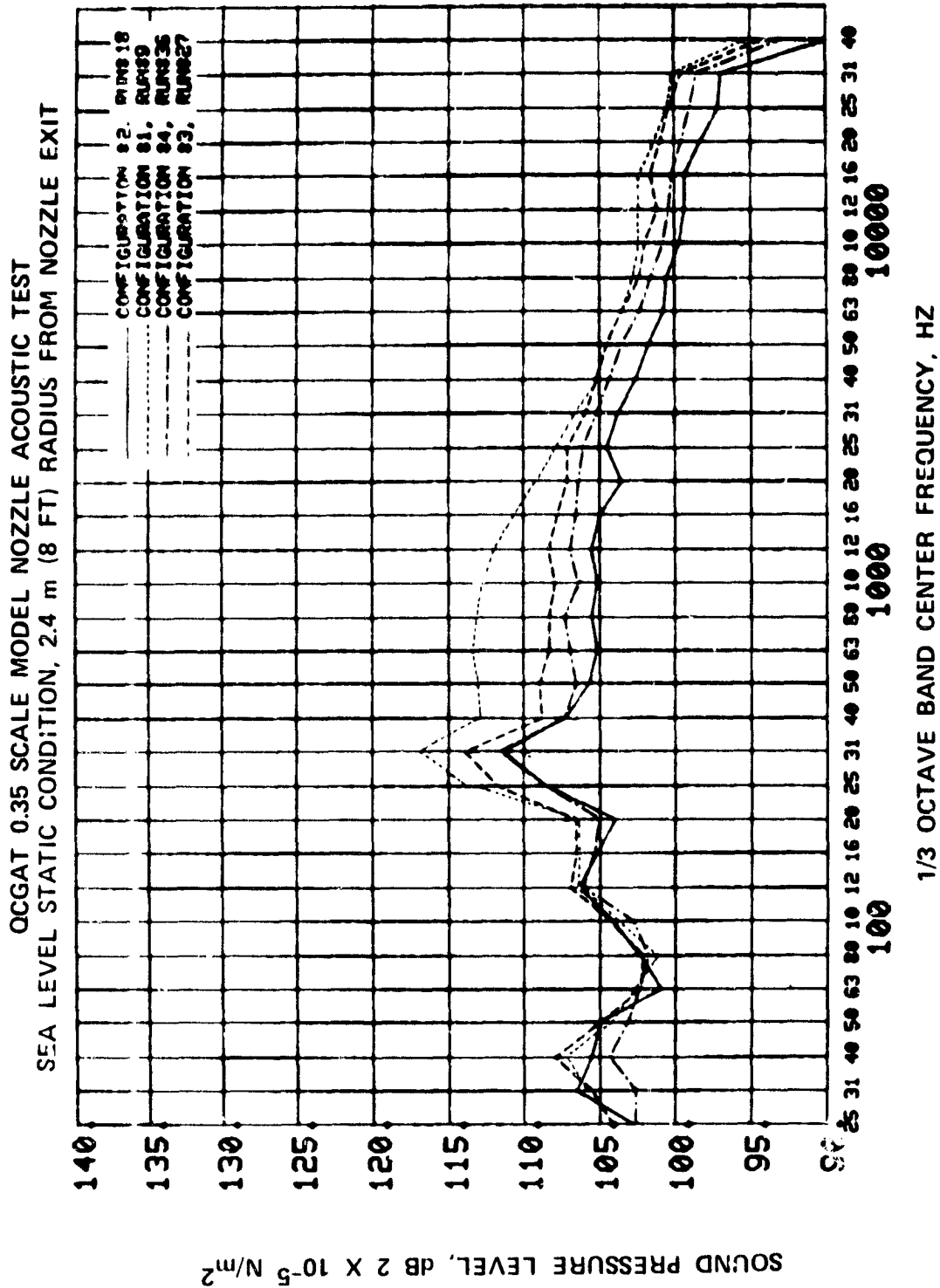
Figure D-2. Noise Spectra Comparison, Microphone Location 2, Configurations I, II, III and IV.

Figure D-3. Noise Spectra Comparison, Microphone Location 3,
Configurations I, II, III and IV.

257

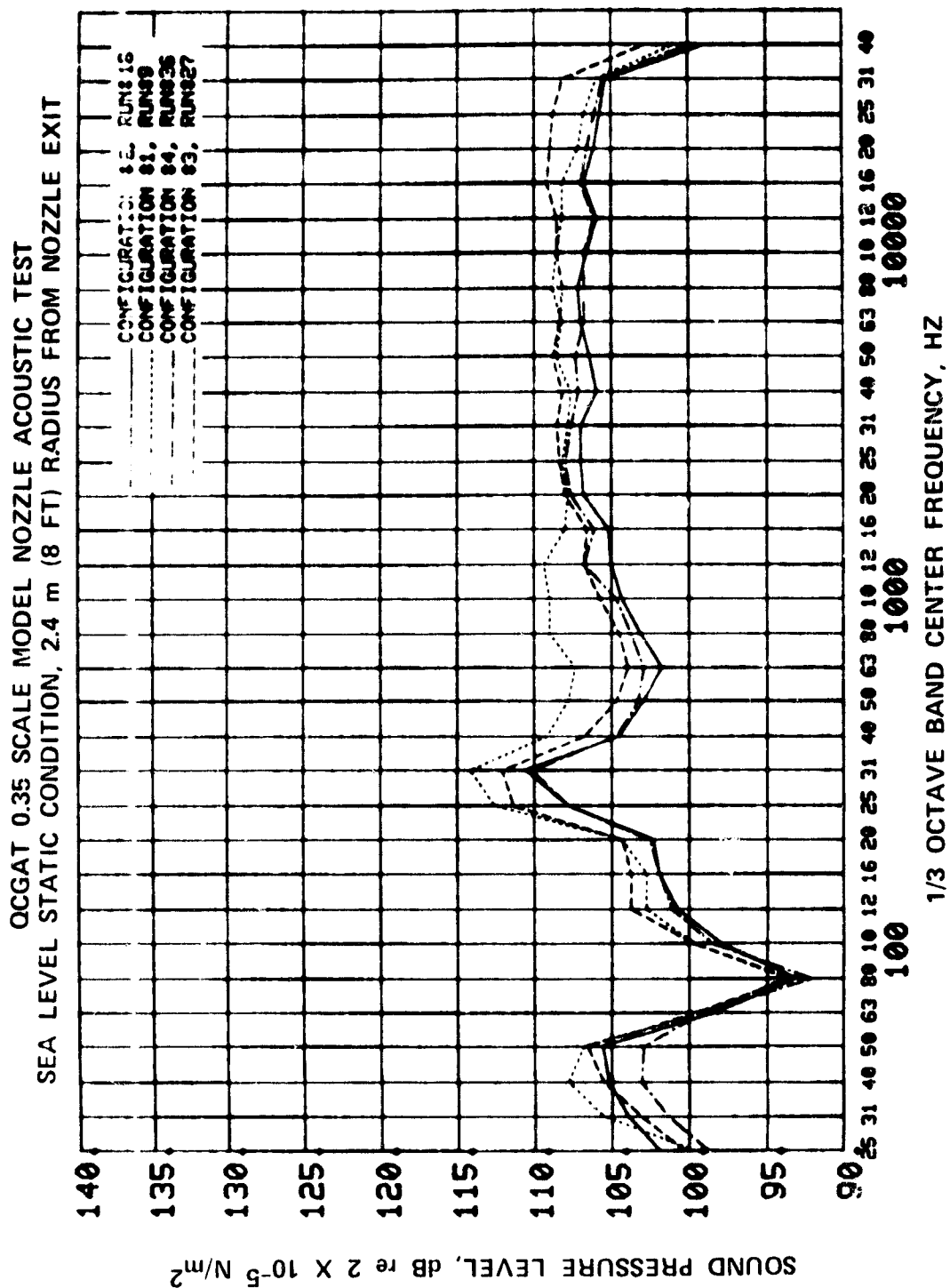Figure D-4. Noise Spectra Comparison, Microphone Location 4, Configurations I, II, III and IV.

258

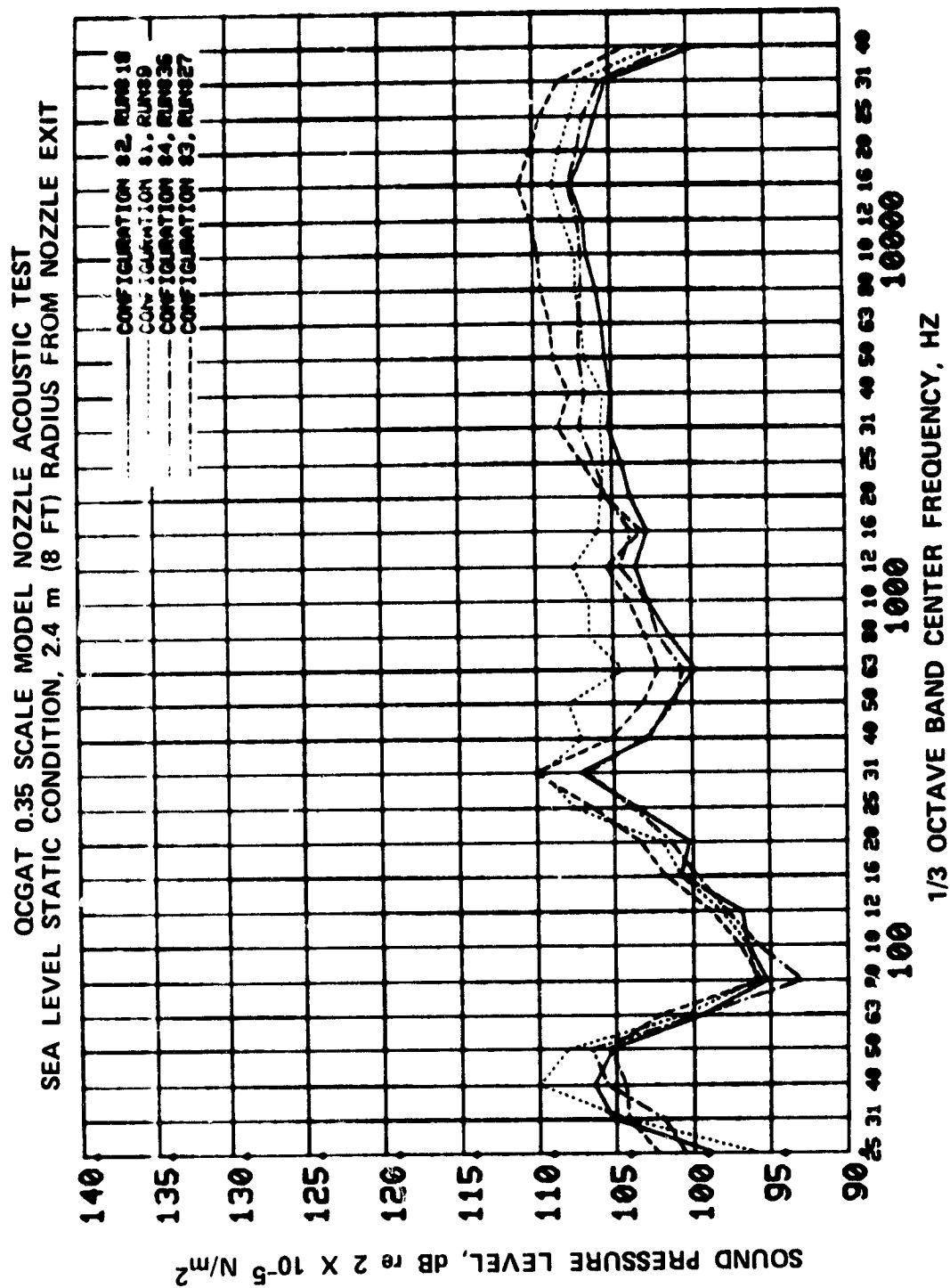Figure D-5. Noise Spectra Comparison, Microphone Location 5,
Configurations I, II, III and IV.

259

Figure D-6. Noise Spectra Comparison, Microphone Location 6, Configurations I, II, III and IV.

260

Figure D-7. Noise Spectra Comparison, Microphone Location 1, Configurations I, II, V and VI.
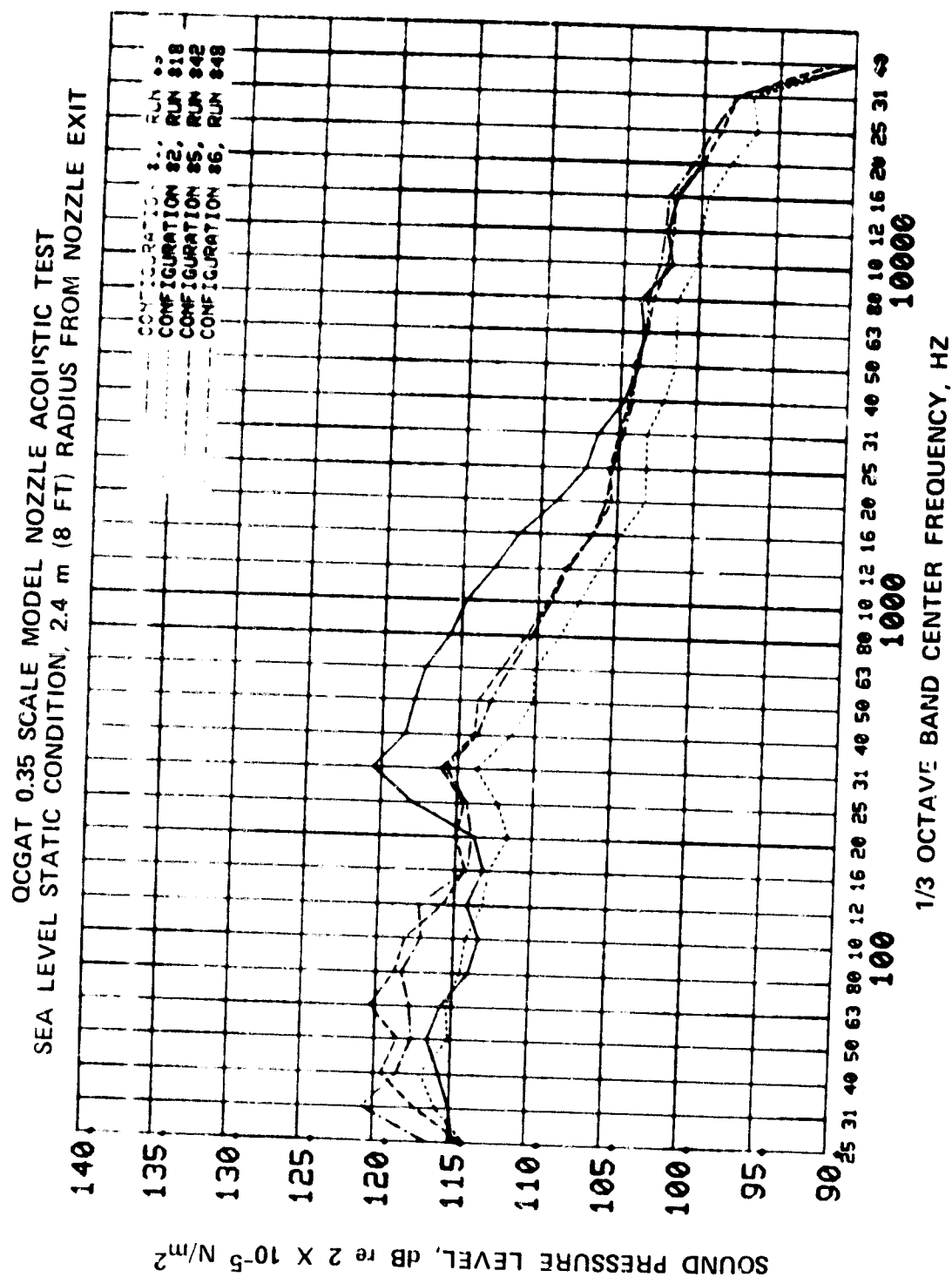
261
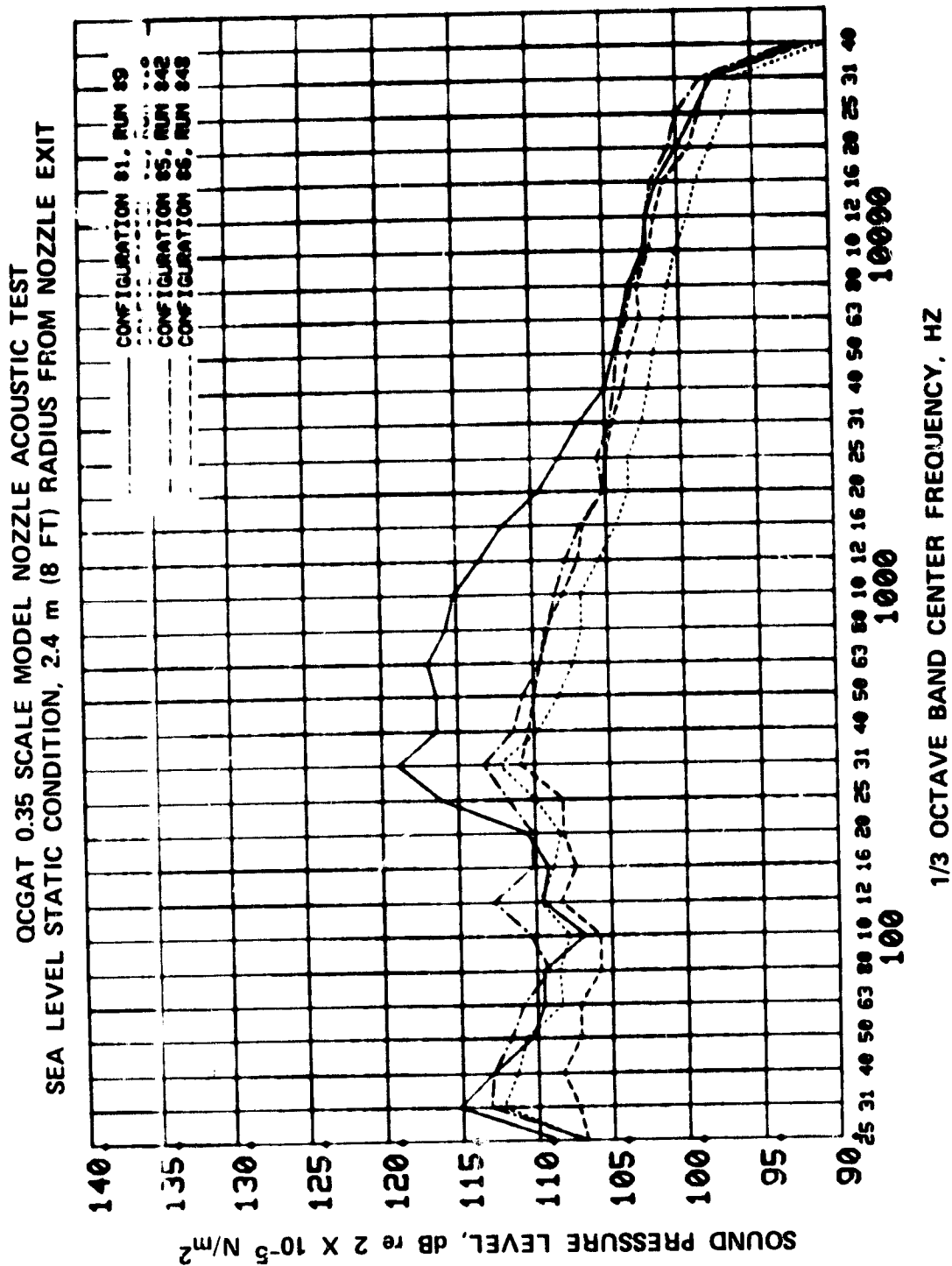
Figure D-8. Noise Spectra Comparison, Microphone Location 2, Configurations I, II, V and VI.

Figure D-9. Noise Spectra Comparison, Microphone Location 3, Configurations I, II, V and VI.
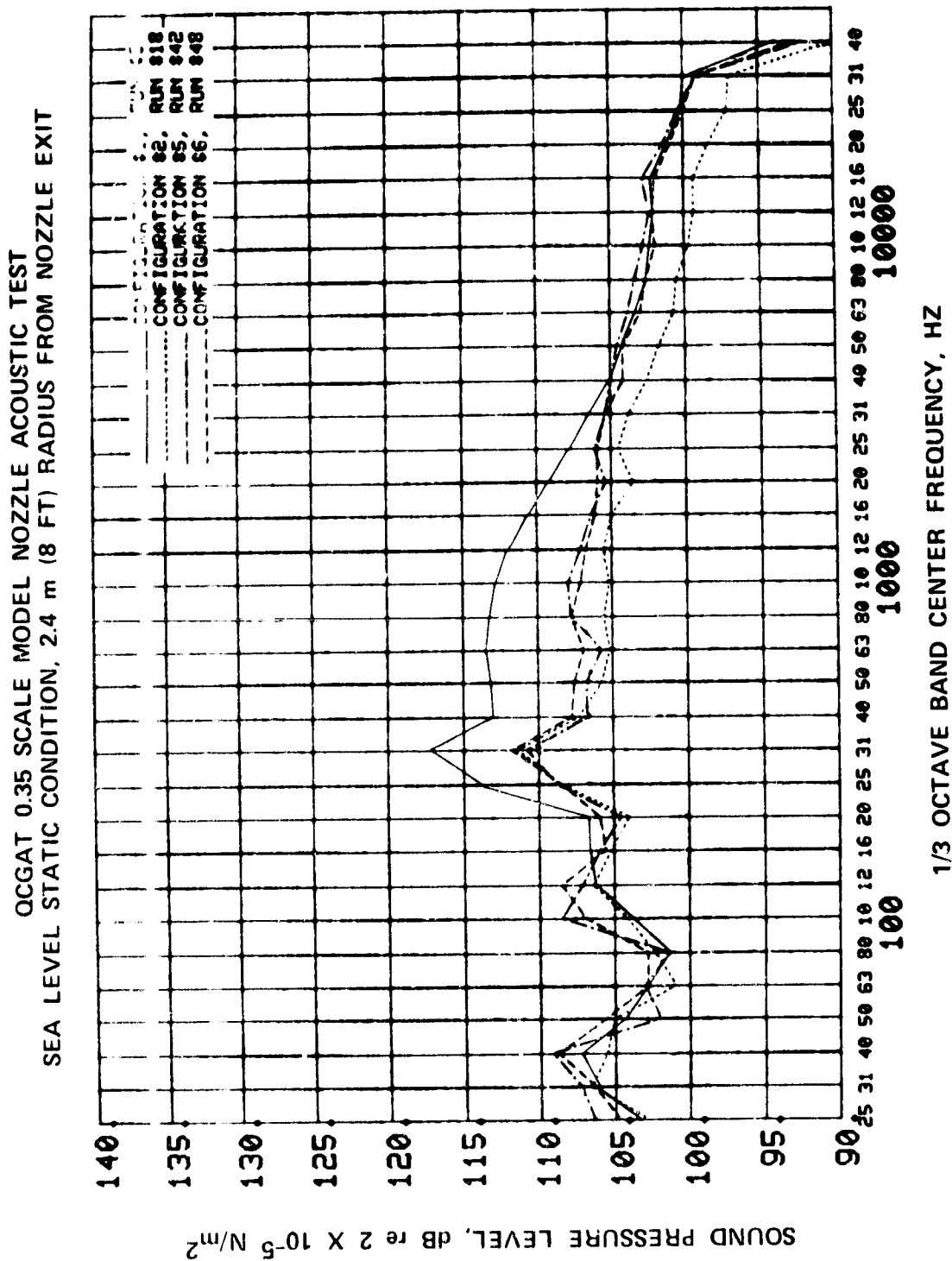
263

Figure D-10. Noise Spectra Comparison, Microphone Location 4, Configurations I, II, V and VI.
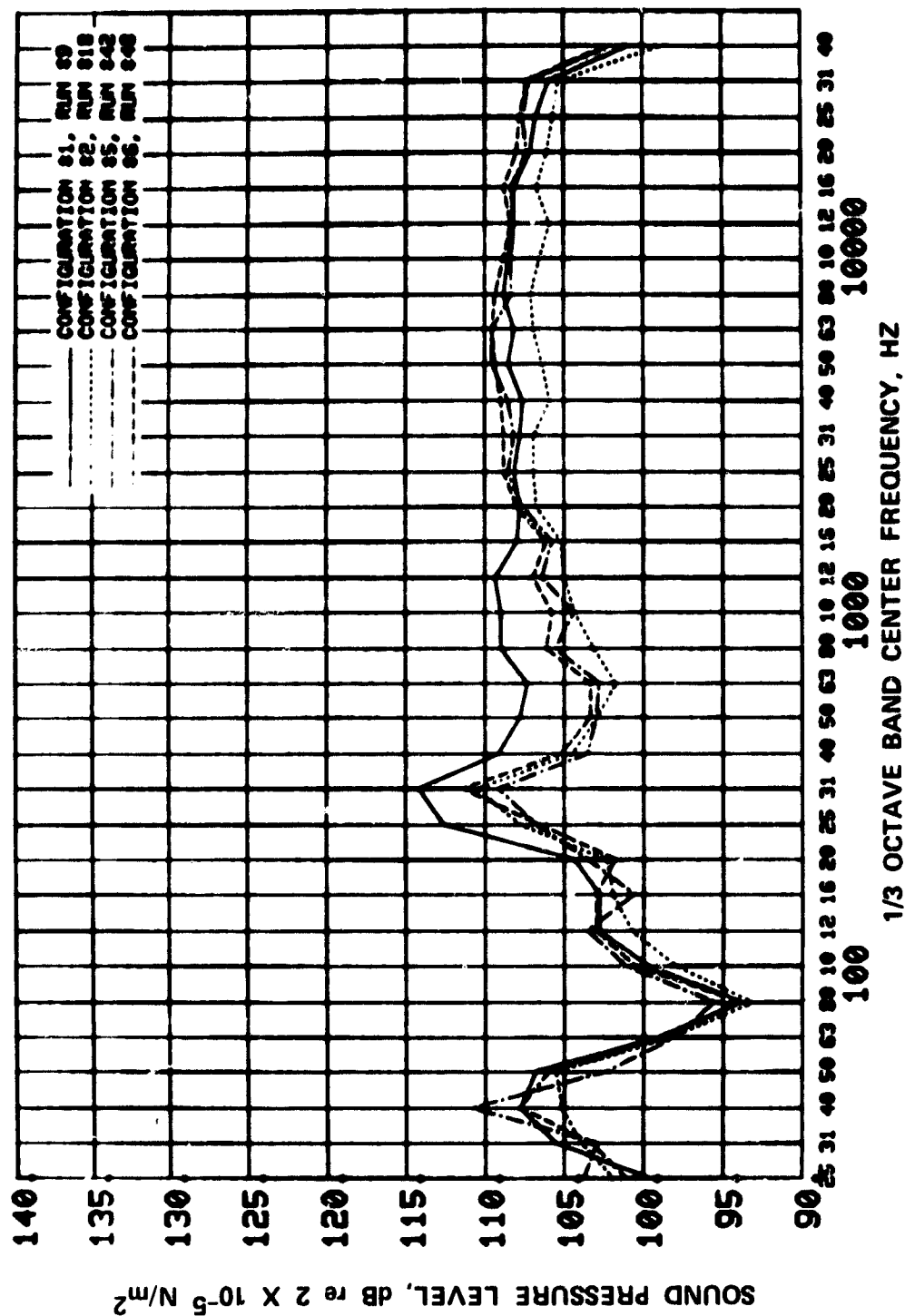
Figure D-11. Noise Spectra Comparison, Microphone Location 5,
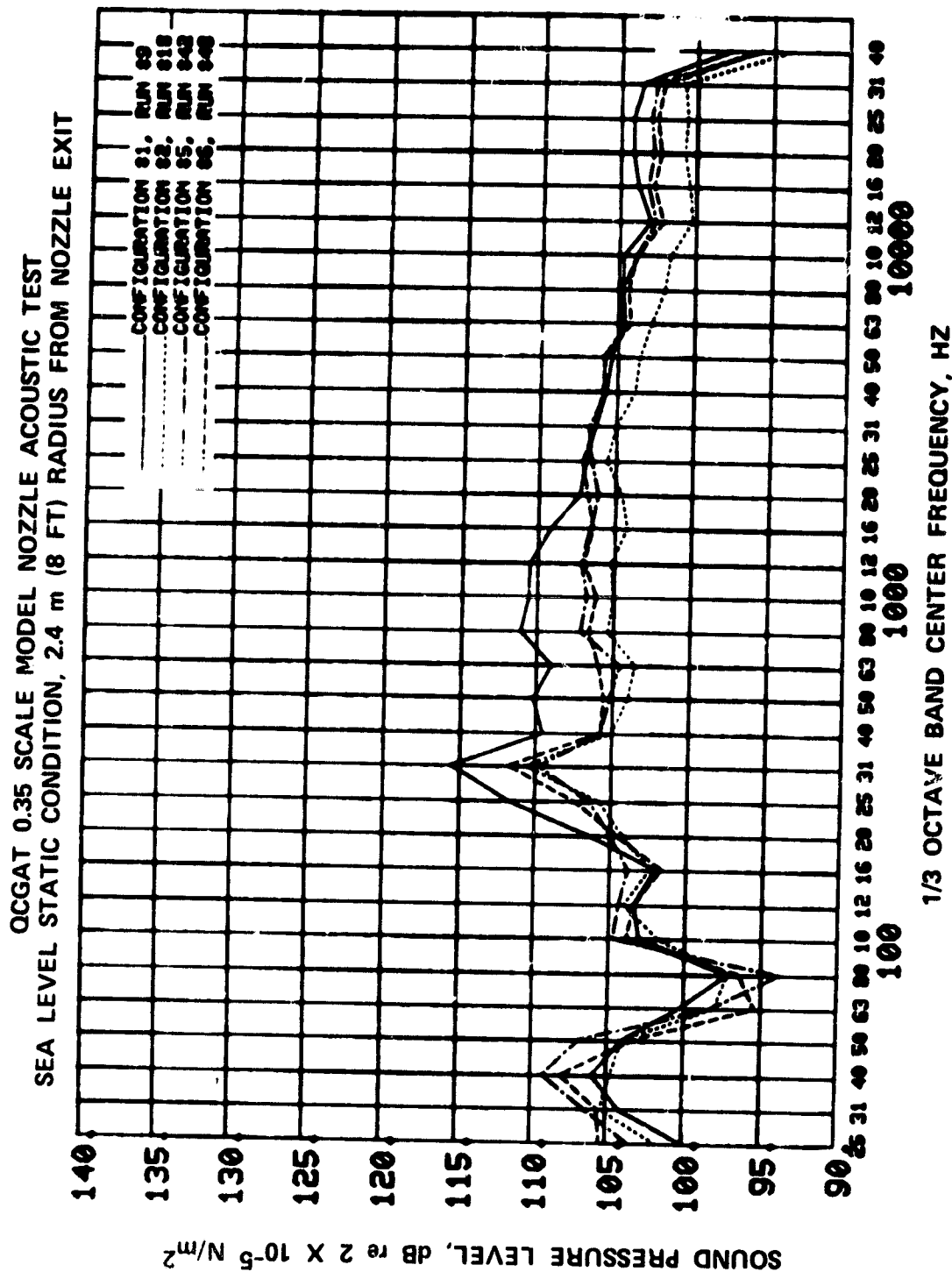Configurations I, II, V and VI.
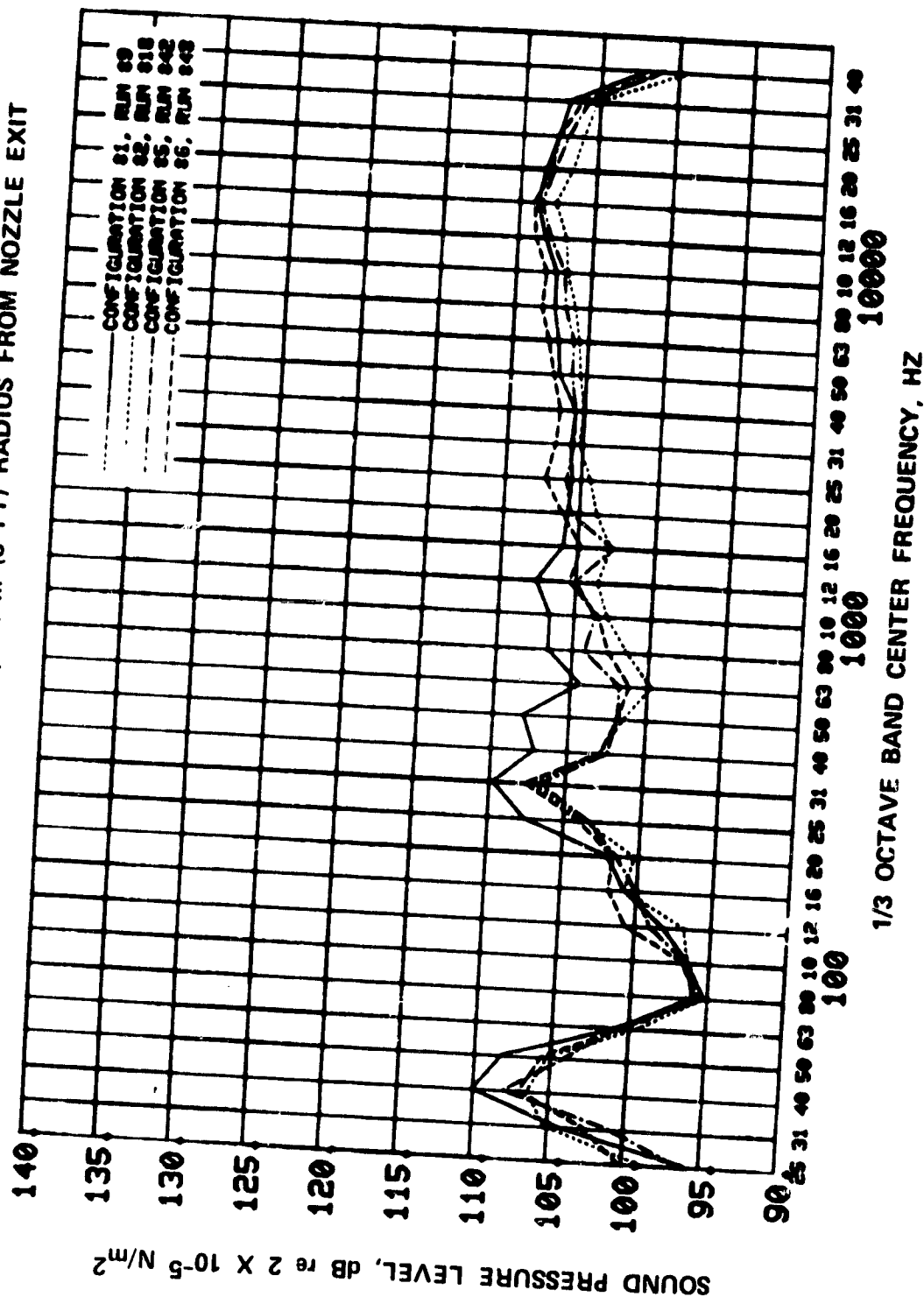
Figure D-12. Noise Spectra Comparison, Microphone Location 6, Configurations I, II, V and VI.

266

ATTACHMENT 1

HOT/COLD FLOW MODEL TESTS
TO DETERMINE STATIC PERFORMANCE
OF 35%-SCALE QCGAT EXHAUST NOZZLES

(FluiDyne Engineering Corporation Report 1123)

FLUIDYNE ENGINEERING CORPORATION

HOT/COLD FLOW MODEL TESTS

TO DETERMINE STATIC PERFORMANCE

OF 35%-SCALE QCGAT EXHAUST NOZZLES

by

John H. Berger
Nebojsa Kovacevic
Richard G. Brasket

Conducted for
AiResearch Manufacturing Company
Phoenix, Arizona 85034

AiResearch Purchase Order No. 1368357
FluiDyne Report 1123
February 1978

Approved: _Richard G. Brasket_
Richard G. Brasket, Group Head
Test Operations

Owen P. Lamb
Owen P. Lamb
Vice President

FLUIDYNE ENGINEERING CORPORATION

SUMMARY

This report presents the results of hot/cold flow model tests
conducted to determine static performance of several candidate
compound-flow exhaust nozzles for the QCGAT engine program. The
model tests were conducted by FluiDyne Engineering Corporation
for AiResearch under Purchase Order No. 1368357. The tests were
performed in the Channel 11 static thrust stand at the FluiDyne
Medicine Lake Aerodynamic Laboratory.

The 35%-scale model simulated the fan and core nozzle passages,
various mixer designs, and a mixed-flow exit duct. The interchange-
able mixers included three 12-lobed mixers and one axisymmetric
splitter (free-mixer). Each of the four mixers was tested with
core-flow-only, and in a dual-flow configuration. One selected
mixer was also tested with two variations in mixing duct length.

Tests made with core-only and dual-flow configurations determined
thrust performance, flow characteristics, and pressure distributions.
In addition, acoustic characteristics and exit pressure and tempera-
ture distributions were measured for the six dual-flow configurations.

Test results include nozzle thrust coefficients, flow rates,
nozzle discharge coefficients, effective throat areas, and pressure
and temperature distributions. Acoustic measurements were recorded
by AiResearch for separate analysis.

i

FLUIDYNE ENGINEERING CORPORATION

TABLE OF CONTENTS

FluiDyne ENGINEERING CORPORATION

LIST OF FIGURES

DEFINITION OF SYMBOLS

A	Cross-section area, in.^{2}
c	Real-gas A/A* correction factor, dimensionless
C_2	Axial balance readout, counts
C_D	Discharge coefficient, dimensionless
C_T	Static thrust coefficient, dimensionless
F	Stream thrust, lb.
G	Real gas stream thrust correction factor, dimensionless
H_x	Net axial thrust, lbs.
H_2	Axial balance force, lbs.
K	Critical weight flow parameter, $^{O}R^{1/2}$/sec.
K_2	Balance force calibration factor, lbs/count
M	Mach number, dimensionless
m	Mass flow rate, slugs/second
P	Pressure, static unless otherwise specified by subscript, psia
ΔP	Static pressure difference across seal, psi
q	Dynamic pressure, psia
R_N	Reynolds number, dimensionless
T	Temperature, ^{O}R
v	Velocity, ft/sec
W	Weight flow rate, lb/sec
W_x	Dead-weight calibration load, lbs
y	Distance from wall
γ	Ratio of specific heats, dimensionless
δ	Boundary layer thickness
Δ	Incremental quantity
λ	Pressure ratio, P_t/P_a, dimensionless
θ	Meridian angle measured clockwise looking upstream, degrees
ρ	Density, slugs/ft^3
Σ	Summation

Subscripts:

a	Ambient
e	Exit
i	Ideal
t	Total conditions
w	Wall
x	Axial
∞	Freestream
1,2,...	See Figure 7

Superscripts:

*	Sonic condition

1.0 INTRODUCTION

This experimental study was conducted to evaluate static performance characteristics, and obtain preliminary acoustic data, for several compound-flow exhaust nozzles for the NASA Quiet, Clean General Aviation Turbofan engine. Model aerodynamic lines and test conditions were specified by AiResearch. The model (except for the lobed mixers) was designed and fabricated by FluiDyne Engineering Corporation. The tests were conducted at the FluiDyne Medicine Lake Aerodynamic Laboratory in a two-temperature-flow static thrust stand.

The basic test program was defined by AiResearch test plan, Report No. 21-2603-A, prepared by Walter L. Blackmore and Craig E. Thompson. Technical liaison for AiResearch was performed by Craig Thompson, who witnessed most of the tests. The acoustic measurements were made by AiResearch personnel (Walter M. Gipson, Al G. Tolman and Robert Hagler) for analysis by AiResearch.

This report describes the test facility, test model, data acquisition and analysis procedures, and presents the test results. Test conditions and major test results are tabulated in Figure 9 and are plotted in Figures 10 - 17. Detailed data and calculations are contained in a separate Data Appendix.

FLuiDYNE ENGINEERING CORPORATION

2.0 FACILITY DESCRIPTION

The tests were performed in Channel 11 at FluiDyne's Medicine Lake Aerodynamics Laboratory. Channel 11 is a two-temperature flow static thrust stand used to determine performance of exhaust nozzles in which the two exhaust flows are at different temperatures. Nozzle thrust is determined from force measurement with strain gage force balances. The general arrangement of Channel 11 is shown in Figure 1. Photographs of test model installations are presented in Figure 6.

The airflows for both the cold and hot passages of a test nozzle are obtained from the facility high-pressure dry air storage system. Air for the cold passage is throttled, metered through a long-radius ASME nozzle, ducted to the cold passage of the test nozzle, and finally exhausted to atmosphere. Air for the hot passage is throttled, passed through a regenerative storage heater, mixed with unheated bypass flow to achieve a desired temperature, metered through a long-radius ASME nozzle, ducted to the hot passage of the test nozzle, and finally exhausted to atmosphere.

The air heater used for the hot flow contains alumina pebbles which are preheated to approximately 1250°F with a combustion heater. The heater capacity is nominally 40 lbs./sec. at 1200°F.

The model assembly is supported by a 3-component strain-gage force balance and is isolated from the facility piping by two elastic seals; see schematic in Figure 7. Calibration of the balance and seals is described in Section 4.6.

The ASME meter at Station 1 is water-cooled to protect the elastic seal from thermal effects. Since the cooling water is confined to the upstream (i.e., non-metric) hardware only, no tare forces are introduced by the water supply lines.

Facility instrumentation is provided to calculate mass flow rates at Stations 1 and 3, and to calculate the exit thrust produced by the test nozzle; details are described in Section 4.0. The data were recorded witn Polaroid cameras and digital printers.

3.0 MODEL DESCRIPTION

The test model was designed by FluiDyne using aerodynamic lines and instrumentation locations specified by AiResearch. The model was fabricated by FluiDyne, except for the lobed mixers which were furnished by AiResearch. The model attached to existing model-to-facility adapters. Figure 2 shows the model assembly, Figure 3 defines the test configurations, and Figure 4 shows the adapters. Photographs of model assemblies are shown in Figure 6.

3.1 Model Adapters

The test models attached to common adapting hardware which supplied separately-metered flows to the fan and core nozzles. The fan air flow was nominally at ambient temperature for all tests. The core air flow was nominally at ambient temperature for the "cold" tests, but was heated to approximately 700-900^OF for the "hot" tests.

The main support member for the adapters is the "spider," Item 4 in Figure 4. Adapters for the core passage consisted of an insulated duct, a choke plate, two screens, a centerbody which supported the interchangeable plugs, and a common core shroud adapter which supported the interchangeable core shrouds (mixers). Charging station instrumentation in the core passage included four 5-tube area-weighted total pressure ($^Pt_5$) rakes, eight area-weighted total temperature probes, one thermocouple for controlling the flow temperature, and static pressure taps on the inner and outer walls.

The adapters for the annular fan passage included a choke plate, two screens, a bellmouth contraction and fan shroud adapter, and six instrumentation plugs. Charging static instrumentation in the fan passage included four 12-tube area-weighted $^Pt_{14}$ rakes, two 4-probe $^Tt_{14}$ thermocouple rakes, one thermocouple for control purposes, and four static taps on the inner and outer walls.

The single control thermocouples at the two charging stations were used to set the desired temperature ratio, $^Tt_{5.2}/^Tt_{14}$. Outputs from these two thermocouples were amplified, divided and displayed on a digital panel meter to provide the facility valve operators with a visual indication of the actual temperature ratio.

3.2 Model Components

Reduced drawings of model components are presented in Figures 5a-k. The two interchangeable plugs (Figures 5a-b) had identical contours except for the addition of a straight section in Plug #2. Plug #1 contained two removable 6-probe rakes ($^Pt_{5.2}$) used to determine pressure drop between Stations 5 and 5.2. Both plugs contained 12 static pressure taps.

Interchangeable mixers attached to the common Core Cowl, Figure 5c. This cowl contained two internal static pressure taps (at Station 5.2) and two o-ring connections for base pressure taps on the mixers. The free-mixer (splitter) and lobed mixers are shown in Figures 5d-g. The splitter and Mixer A ended at engine Station 56, while Mixers C and D were 4-inches (full-scale) longer. The short mixers were used with Plug #1 and the long mixers with Plug #2.

The Forward Fan Duct and Aft Fan Duct, Figures 5h-i, were used with all dual-flow configurations. The Aft Fan Duct contained ten static pressure taps. For Configurations III, IV and VI, a 4-inch (full-scale) spacer was inserted to move the Aft Fan Duct downstream as shown in Figures 2 and 6c. The model assembly was completed by addition of a Duct Exit (Figures 5j or 5k). The Duct Exit contained two base taps and two internal static taps near the exit plane.

4.0   DATA ANALYSIS PROCEDURES

The following subsections describe the data analysis procedures used in the present test program. Station notations are defined in Figure 7. Computer programs written in BASIC language are included in the Appendix.

4.1   Flow Rates

The mass flow rates through the test nozzles were determined using choked ASME long-radius metering nozzles. The core nozzle flow rate was calculated at Station 1 (see Figure 7) and the fan nozzle flow rate was calculated at Station 3, using the following equations.

$$W_1 = W_{5.2} = \frac{K_1 C_{D_1} A_1 P_{t_1}}{\sqrt{T_{t_1}}}$$

$$W_3 = W_{14} = \frac{K_3 C_{D_3} A_3 P_{t_3}}{\sqrt{T_{t_3}}}$$

The critical flow factor, K, was calculated as a function of total pressure and total temperature.

$$K = 0.5280 + a\,T_t + b\,T_t^2 + c\,T_t^3 + 0.186 \times 10^{-4} \times P_t \times e^{-.0067(T_t-500)}$$

where: $a = 0.1654 \times 10^{-4}$
$b = -0.2119 \times 10^{-7}$
$c = 0.6008 \times 10^{-11}$
T_t is in $^\circ R$ and P_t is in psia.

- 6 -

This equation was obtained by curve-fitting tabulated values in Reference 1; the curve-fit is accurate to within $\pm$ 0.03% for $0 < P_t < 30$ atmospheres and $460 < T_t < 700°R$, and is accurate to within ± 0.1% for $0 < P_t < 40$ atmospheres and $460 < T_t < 1800°R$.

C_{D_3} was calculated using a semi-empirical equation

$$C_{D_3} = 1 - 0.184 \; R_{N_3}^{-0.2}$$

and varied from 0.990 to 0.993 for the present tests.

C_{D_1} was calculated from a similar equation, modified to account for a thermal boundary layer. This thermal boundary layer results from water-cooling of the Station 1 meter.

$$C_{D_1} = 1 - (0.184 \; R_{N_1}^{-0.2}) \; (1.574 - 0.574 \; T_{t_1}/T_W)$$

The above equation was derived assuming constant static pressure in the boundary layer, a 1/7 power velocity profile, thermal boundary layer thickness equal to velocity boundary layer thickness, and a density distribution in the boundary layer defined by

$$\frac{\rho}{\rho_\infty} = \frac{T_\infty}{T_W} - \left(\frac{T_\infty}{T_W} - 1 \right) \; \left(\frac{y}{\delta} \right)^{1/7}$$

T_W, the wall temperature at the nozzle throat, was estimated from heat-balance calculations of heat transfer from the air stream to the cooling water. T_W values calculated for the present tests varied from $99°$ to $169°F$. R_{N_1} was calculated using a mean temperature, $(T_W + T_{t_1})/2$. C_{D_1}, calculated using the above equation, varied from 0.990 to 0.998 for the present tests. Given sufficient wall cooling, C_{D_1} may exceed unity (Reference 2).

FLUIDYNE ENGINEERING CORPORATION

The above equation for C_{D_1} is believed to be correct within $\pm$ 0.0025, on the basis of results from facility demonstration tests. These demonstration tests included test series with either a 2.5-inch or a 4-inch diameter ASME nozzle located downstream of the water-cooled Station 1 meter. The downstream nozzle was essentially at adiabatic conditions (thin-wall construction, backside insulated). Flow rates calculated at Station 1 (using the above C_{D_1} equation) agreed within $\pm$ 0.25% with flow rates calculated at the downstream nozzle (using adiabatic wall C_D), thereby indicating the adequacy of the C_{D_1} equation.

A_3, the geometric throat area of the Station 3 meter, was 11.0358 in^2. A_1, the geometric throat area of the Station 1 meter, was calculated assuming thermal expansion from $70^{\circ}F$ to T_W. The largest value of A_1 calculated for the present tests was 3.8202 in^2, representing a thermal expansion area change of 0.18% from the nominal area of 3.8134 in^2.

P_{t_1} and P_{t_3} were measured with Statham differential pressure transducers. T_{t_1} and T_{t_3} were measured with shielded chromel/alumel thermocouples and recorded on the facility Vidar system (analog to digital converter, printer).

Calculated flow rates (lbm/sec) for the present tests were in the ranges

$$1 < W_1 < 16 \qquad 8 < W_3 < 36 .$$

4.2   Discharge Coefficients and Effective Throat Areas

Discharge coefficient is defined as the ratio of actual flow rate through a nozzle to the ideal isentropic flow rate at the over-all nozzle pressure ratio. Core nozzle pressure ratio is defined as $\lambda_{5.2} = P_{t_{5.2}}/P_a$, and fan nozzle pressure ratio is $\lambda_{14} = P_{t_{14}}/P_a$. For the present tests (exhausting to atmosphere), P_a equals barometric pressure.

$$C_{D_{5.2}} = W_1/W_{5.2_i} \quad \text{and} \quad C_{D_{14}} = W_3/W_{14_i}$$

where

$$W_{5.2_i} = \frac{K_{5.2} A_{5.2} \, P_{t_{5.2}} \, (A^*/A)_{5.2}}{\sqrt{T_{t_{5.2}}}} \quad \text{and} \quad W_{14_i} = \frac{K_{14} A_{14} \, P_{t_{14}} \, (A^*/A)_{14}}{\sqrt{T_{t_{14}}}}$$

$K_{5.2}$ and K_{14} were evaluated using a previous equation, as functions of $P_{t_{5.2}}$, $T_{t_{5.2}}$ and $P_{t_{14}}$, $T_{t_{14}}$. $P_{t_{5.2}}$ was determined by measuring P_{t_5} and applying a correction for the pressure drop between Stations 5 and 5.2 as described in Section 5.0. P_{t_5} and $P_{t_{14}}$ were measured with mercury manometers and were defined as the averages from area-weighted probes (20 tubes for P_{t_5}, 48 tubes for $P_{t_{14}}$). $T_{t_{14}}$ was measured with 8 area-weighted thermocouples. $T_{t_{5.2}}$ was defined as T_{t_5} (measured with 8 area-weighted thermocouples) minus an estimated ΔT due to heat transfer to the inner core cowl between Stations 5 and 5.2. The calculated ΔT values varied between 0° and $16^O F$.

For the present tests, effective throat areas $C_{D_{5.2}} A_{5.2}$ and $C_{D_{14}} A_{14}$ were calculated instead of discharge coefficients $C_{D_{5.2}}$ and $C_{D_{14}}$. In addition, an overall nozzle discharge coefficient was calculated as $C_{D_8} = (C_{D_{5.2}} A_{5.2} + C_{D_{14}} A_{14})/A_8$, where A_8 is the geometric area of the duct exit. The inspected area for both Exits #1 and #2 was $A_8 = 49.747$ in^2.

A^*/A, the isentropic area ratio, is used to correct the ideal flow rate when the nozzle is unchoked. A^*/A for the fan nozzle was calculated using equations valid for $\gamma = 1.4$, obtained from Reference 3.

$$A^*/A = 3.86393 \lambda^{-0.71429} \sqrt{1 - \lambda^{-0.28571}} \quad \text{for } \lambda \leq 1.8929$$

and

$$A^*/A = 1 \text{ for } \lambda \geq 1.8929.$$

A*/A for the core nozzle was obtained by correcting the $\gamma = 1.4$ value for "real gas effects," to account for $\gamma_{5.2}$ being significantly less than 1.4. The correction was derived by curve-fitting tabulated values from Reference 4; no corrections are indicated for $T_t < 900^\circ R$. First, the critical pressure ratio was expressed as a function of total temperature:

$$1/\lambda^* = 9.667 \times 10^{-6} \times T_t \ (^\circ R) + 0.5196$$

if $\lambda \geq \lambda^*$, then A*/A = 1. If $\lambda < \lambda^*$ and $900 < T_t < 1260^\circ R$,

$$c = 1 + (\tfrac{1}{\lambda} - \tfrac{1}{\lambda^*}) \ 5.728 \times 10^{-5} \ (T_t - 900).$$

if $\lambda < \lambda^*$ and $1260 < T_t < 1800^\circ R$,

$$c = 1 + (\tfrac{1}{\lambda} - \tfrac{1}{\lambda^*}) \left[2.615 \times 10^{-5} \ (T_t - 1260) + 0.020621 \right].$$

Finally,

$$A^*/A = c \times \left[(A^*/A) \ \text{at} \ \gamma = 1.4) \right].$$

For the present tests, c (denoted c* on computer output sheets) varied from 1.000 to 1.0063.

4.3   Thrust Measurement

The net static axial thrust of an exhaust nozzle is defined as the axial exit momentum of the exhaust flow, plus the excess of exit pressure over ambient pressure times the exit area.

$$_x = m v_{e_x} + (P_e - P_a) A_{e_x}.$$

The net static thrust of an exhaust nozzle model was determined in the present test program by applying the momentum equation to the control volume shown in Figure 7. The analysis of axial forces applied to the control volume includes entering stream thrusts

- 10 -

(F_1 and F_3), a balance force (H_2), various pressure-area terms and the axial exit stream thrust, ($H_x + p_a A_{e_x}$). The axial balance force, H_2, as used here, includes seal tare forces. Summing axial forces,

$$H_x = F_1 + F_3 + p_2 (A_2 - A_1) + p_4 (A_4 - A_3) - p_a (A_2 + A_4) - H_2.$$

The stream thrust at Station 3 is the exit stream thrust of a choked long-radius ASME nozzle, and was calculated as:

$$F_3 = G_3 (1 + 1.4 \; C_{D_3} C_{T_3}) \; .52828 \; P_{t_3} A_3.$$

Use of $\gamma = 1.4$ and $P*/P_t = .52828$ in the above equation imply an ideal gas. The factor G, derived from tabulated values in References 1 and 4, corrects the stream thrust from that of an ideal gas to that of a real gas.

If $T_t < 560^O R$, $G = 1.00012 + 6.8338 \times 10^{-6} \times P_t$ (psia).

If $T_t > 560^O R$, $G = 1.0044 - (4.196 - .0059 \; P_t)(T_t + 460) \times 10^{-6}$.

C_{D_3} has already been discussed; C_{T_3} was calculated in an analogous manner,

$$C_{T_3} = 1 - 0.109 \; R_{N_3}^{-0.2} \quad .$$

This equation is a semi-empirical expression of the thrust coefficient of an ASME nozzle at a pressure ratio of $\lambda = 1.8929$ (corresponding to $P*/P_t = .52828$). For the present tests, G_3 varied from 1.000 to 1.0010, and C_{T_3} varied from 0.994 to 0.996.

The stream thrust at Station 1 was calculated as:

$$F_1 = G_1 (1 + 1.4 \; C_{D_1} C_{T_1}) \; .52828 \; P_{t_1} A_1.$$

Each variable in this equation has been previously described, except C_{T_1}. C_{T_1} was calculated in a similar manner as C_{T_3}, but was modified to account for the thermal boundary layer described in the discussion

of C_{D_1} in Section 4.1:

$$C_{T_1} = 1 - (0.109 \ R_{N_1}^{-0.2}) \ (0.828 + 0.172 \ T_{t_1}/T_W).$$

The above equation was derived using the same assumptions as in the derivation of C_{D_1}. C_{T_1} for the present tests varied from 0.991 to 0.996.

Static pressures p_2 and p_4 were measured with Statham differential pressure transducers. Ambient pressure (p_a) was measured on a Hass mercury manometer (barometer). A_2 and A_4, the geometric reference areas for the seals, were 7.0686 and 12.5664 in^2, respectively.

4.4 Thrust Coefficient

The static thrust coefficient of an exhaust nozzle is defined as the ratio of the measured nozzle net thrust, to the ideal thrust of the actual mass flow when expanded isentropically from P_t to P_a.

$$C_T = \frac{H}{m \ v_i}$$

For the dual-flow tests, the ideal thrust was calculated as the sum of the fan nozzle ideal thrust and the core nozzle ideal thrust:

$$C_T = \frac{H}{m_{5.2} v_{i_{5.2}} + m_{14} v_{i_{14}}}$$

Ideal thrust was calculated using a dimensionless ideal thrust function, $m_i v_i/P_t A^*$, which is a function of both λ and γ .

$$m_{5.2} v_{i_{5.2}} = (A^*/A)_{5.2} \ C_{D_{5.2}} A_{5.2} P_{t_{5.2}} \ (m_i v_i/P_t A^*)_{5.2}$$

$$m_{14} v_{i_{14}} = (A^*/A)_{14} \ C_{D_{14}} A_{14} P_{t_{14}} \ (m_i v_i/P_t A^*)_{14}$$

where

$$(m_i v_i / P_t A^*) = \gamma \left[\frac{2}{\gamma+1} \right]^{\frac{\gamma}{\gamma-1}} \sqrt{\frac{\gamma+1}{\gamma+2}} \sqrt{1 - \lambda^{\frac{1-\gamma}{\gamma}}}$$

$$= 1.81162 \sqrt{1 - \lambda^{-0.28571}} , \quad \text{for } \gamma = 1.4.$$

For the present tests, γ_{14} was taken to be 1.400. However, $\gamma_{5.2} \neq 1.4$ and, therefore, $(m_i v_i / P_t A^*)_{5.2}$ obtained from the above equation was corrected to account for "real gas effects" by multiplying by the ratio

$$\frac{(m_i v_i / P_t A^*) \text{ for real gas}}{(m_i v_i / P_t A^*) \text{ for } \gamma = 1.4} .$$

This ratio was calculated from tabulated values in Reference 4; for the present range of test conditions this factor was obtained from a curve-fit expression:

$$.9957 - 5.81 \times 10^{-6} \times (T_t, {}^{O}R - 1000) + 1.25 \times 10^{-3} \times (\lambda - 1)$$

and varied between .9943 and .9962.

4.5   Pressure and Temperature Data

Pressure instrumentation for facility pressures and charging station pressures were described previously. All other pressures in the model were measured using multiple-tube mercury manometers. Model pressure data were reduced to absolute pressures (psia). The results are tabulated on computer output sheets, contained in the Appendix.

Facility and charging station temperature data were obtained using shielded chromel/alumel thermocouples, and were recorded on the facility Vidar system. Temperatures were expressed in ${}^{O}F$ or ${}^{O}R$, or both.

- 13 -

4.6   Force Balance Calibration

The force balance calibration determined the output character-
istics of both the force balance flexure and the two elastic seals
between the metric model assembly and the non-metric facility
structure.   The elastic seals produce a small tare force, largely
due to radial seal deflections necessary to support the static pres-
sure differential across the seal.   The seal and balance assembly are
calibrated under simulated operating conditions of loads and seal
differential pressures.

The balance assembly was first calibrated with the internal
seals unpressurized.   Known loads (dead-weight) were applied to
obtain a balance calibration coefficient, $K_2 = H_2/C_2$, where H_2 is
the axial load and C_2 is the balance output.

Calibration of the elastic seals was accomplished as follows.
Blank-off plates were installed downstream of the seals, and the
seals were pressurized to selected values of pressure differentials,
ΔP.   This pressure loading produces a downstream force on the balance.
Additional axial loads, W_x, were then applied to increase or decrease
the net load to simulate test conditions of axial load and ΔP.   Summing
forces, the axial balance force (which is calculated from the balance
output) must equal the applied load plus the pressure-area forces at
the two seals, i.e.,

$$H_2 = W_x + \Delta P_2 \ (A_2 + \Delta A_2) + \Delta P_4 \ (A_4 + \Delta A_4)$$

from which the apparent change in seal area (ΔA) may be calculated.
ΔA was then curve-fit as a function of H_2 and ΔP, and included as a
correction term in the balance force calculation.   When used to reduce
test data, ΔA for each seal was defined by H_2 and the ΔP at each
seal.

4.7   Supplementary Calculations

Supplementary calculations were made to present the test results in additional nondimensional forms. The results are contained in the Appendix, and include the following items.

Flow rates corrected to standard conditions:

$$\theta_{5.2} = {}^T t_{5.2}/518.69 \qquad\qquad \theta_{14} = {}^T t_{14}/518.69$$

$$\delta_{5.2} = {}^P t_{5.2}/14.696 \qquad\qquad \delta_{14} = {}^P t_{14}/14.696$$

$$W_{5.2_{corrected}} = \frac{W_{5.2}\sqrt{\theta_{5.2}}}{\delta_{5.2}}$$

$$W_{14_{corrected}} = \frac{W_{14}\sqrt{\theta_{14}}}{\delta_{14}}$$

Core nozzle flow coefficient referenced to mixer base pressure (taps #27, 37) and fan nozzle flow coefficient referenced to match plane static pressure (taps #151, 152):

$$CD\ (J1) = W_{5.2}/W_{6_i} \qquad \text{and} \qquad CD\ (J2) = W_{14}/W_{16_i}$$

These coefficients are similar to $C_{D_{5.2}}$ and $C_{D_{14}}$ defined earlier, except that ideal flows were evaluated assuming isentropic expansion from P_t to the appropriate static pressures, rather than from P_t to P_a. Reference areas used were:

	A_6, in^2	A_{16}, in^2
Splitter	25.502	59.798
Mixer A	25.422	58.781
Mixer C	26.168	58.035
Mixer D	26.162	58.037

the nozzle flow coefficient:

$$CD \ (E) \ = \ (W_{5.2} + W_{14})/W_{8_i}$$

where W_{8_i} was evaluated using mass-flow-weighted averages (of $P_{t_{5.2}}$, $P_{t_{14}}$ and $T_{t_{5.2}}$, $T_{t_{14}}$), isentropic expansion to exit base pressure (taps #161, 162), and $A_8 = 49.747 \ in^2$.

4.8   Exit Survey Data

Pressure and temperature surveys at the nozzle exit were obtained using a survey rake, rake support, and drive mechanism furnished by AiResearch. The survey hardware is shown in place at the nozzle exit in Figure 6d.

The survey rake assembly was supported from the floor by an adjustable platform which provided accurate locating of the rake relative to the nozzle exit. The rake assembly was non-metric, i.e., did not touch the metric model.

Survey data were obtained with the rake located in 3° increments over a 30° arc. Measurements consisted of 15 temperatures, 6 total pressures, centerline static pressure, and 2 wall static pressures (taps #161, 162). Temperatures were recorded with a digital printer, and pressures were recorded by photographing mercury manometers. The data were reduced as specified, and transmitted to AiResearch for plotting and analysis. Computer program and output sheets are contained in the Appendix.

4.9   Acoustic Data

Acoustic measurements were obtained during 12 dual-flow tests using microphones and tape recording equipment supplied and operated by AiResearch. Analysis of the tapes was performed by AiResearch. Arrangement of the microphones is illustrated in Figures 6d and 8.

5.0 PRESENTATION OF RESULTS

Test conditions and major test results are tabulated in
Figure 9 and are plotted in Figures 10 - 17. Detailed data and
calculations, including tabulated static pressure distributions and
exit survey results, are contained in a separate Data Appendix.

The tabulation in Figure 9 includes: configuration number, run
number and type of data obtained, actual values of the independent
variables $(\lambda_{5.2},\ \lambda_{14},\ {}^{T}t_{5.2}/{}^{T}t_{14})$, and major test results $(C_T,\ C_D A$
for the core and fan passages, $W_{14}/W_{5.2})$.

The first test series (Runs 1.0 - 6.0) was made to determine
the total pressure loss between Stations 5 and 5.2. The results
are plotted in Figure 10 as ${}^{P}t_{5.2}/{}^{P}t_5$ versus M^2_5, where M_5 is
the isentropic flow Mach number (Reference 3) indicated by the static
to total pressure ratio at Station 5. The data points fall close to
a straight line, since the pressure loss in the passage is nearly
proportional to the dynamic pressure, $q = .7pM^2$. After these initial
tests, the pressure rakes at Station 5.2 were removed; ${}^{P}t_{5.2}$ for all
remaining tests was calculated as ${}^{P}t_5\ (1-.02\ M^2_5)$.

Tests with core-flow-only were made with the four core nozzle
configurations shown in Figure 6b. These tests determined thrust
coefficients, effective throat areas, and static pressure distribu-
tions of the core nozzles when exhausting to atmosphere (i.e., with-
out the restraints imposed by the fan duct and fan flow). Thrust
coefficients and effective throat areas from the core-only tests
are plotted in Figures 11a-b.

Dual-flow tests were made with each of the four configurations
shown in Figure 6a and with two additional configurations (V, VI)
obtained by using the short duct exit with Configuration II. Each
dual-flow configuration was tested both with cold-flow and hot-flow

- 17 -

$(^{T}t_{5.2}/^{T}t_{14} \simeq 1.0$ and $2.5)$. Figure 12 presents thrust coefficients for all six configurations. With cold-flow, the highest C_T level was obtained with the splitter (Configuration I). Increasing temperature ratio with Configuration I produced a slight C_T increase. Increasing temperature ratio with the lobed mixers produced substantial C_T increases. These increases are dependent on the extent of temperature mixing (Reference 5).

Thrust measurements were also obtained for all six dual-flow configurations during exit survey tests. C_T values from these tests are tabulated in Figure 9, and are identified by the note "with survey data," but have not been plotted due to the apparent interference of the rake on the thrust measurement. C_T values with the rake are higher than those without (the largest difference is .0056, the average is .004).

Another indication of rake interference is the effect of the rake on effective throat areas. The combined effective throat area, $C_{D_{5.2}}A_{5.2} + C_{D_{14}}A_{14}$, decreased 0.8% (average from six pairs of data) due to the presence of the rake.

Configurations I and II were selected for a larger mapping of nozzle performance. Results are presented in Figures 13 and 14, as C_T versus $\lambda_{5.2}$ with lines of constant λ_{14}.

Effective throat areas for the core and fan passages are plotted in Figures 15-17. Figure 15 shows results for all six configurations, and Figures 16 and 17 show the larger mapping for the two selected configurations.

FLUIDYNE ENGINEERING CORPORATION

REFERENCES

1.   Johnson, R. C., "Real-Gas Effects in Critical-Flow-Through
     Nozzles and Tabulated Thermodynamic Properties." NASA TN
     D-2565. 1965.

2.   Massier, P. F., Back. L. H., Noel, M. B., and Saheli, F.,
     "Viscous Effects on the Flow Coefficient for a Supersonic
     Nozzle." AIAA Journal, Volume 8, No. 3, March 1970,
     pp. 605-607.

3.   Ames Research Staff, "Equations, Tables and Charts for
     Compressible Flow." NACA Report 1135. 1953.

4.   Jordan, D. P., and Mintz, M.D., "Air Tables."
     McGraw-Hill Book Company, New York. 1965.

5.   Stratford, B. S., and Williams, J. G., "A Simplified Treat-
     ment for the Loss of Total Pressure, and Gain of Total
     Thrust, Resulting from the One-Dimensional Mixing Between
     Hot and Cold Gas Streams." National Gas Turbine Establish-
     ment (England) Report NT 496; ARC 23899. June 1962.

FIGURE 4. ADAPTER ASSEMBLY

FIGURE 2. MODEL ASSEMBLY

Config.	Splitter or Mixer	Plug	Duct Spacer (17172)	Exit
I	Splitter (SKP17162)	#1 (SKP17160)		Long (SKP17167)
II	Mixer A (17163)	#1 (17160)		Long (17167)
III	Mixer C (17168)	#2 (17169)	Yes	Long (17167)
IV	Mixer D (17170)	#2 (17169)	Yes	Long (17167)
V	Mixer A (17163)	#1 (17160)		Short (17166)
VI	Mixer A (17163)	#1 (17160)	Yes	Short (17166)

FIGURE 3.   DEFINITION OF TEST CONFIGURATIONS
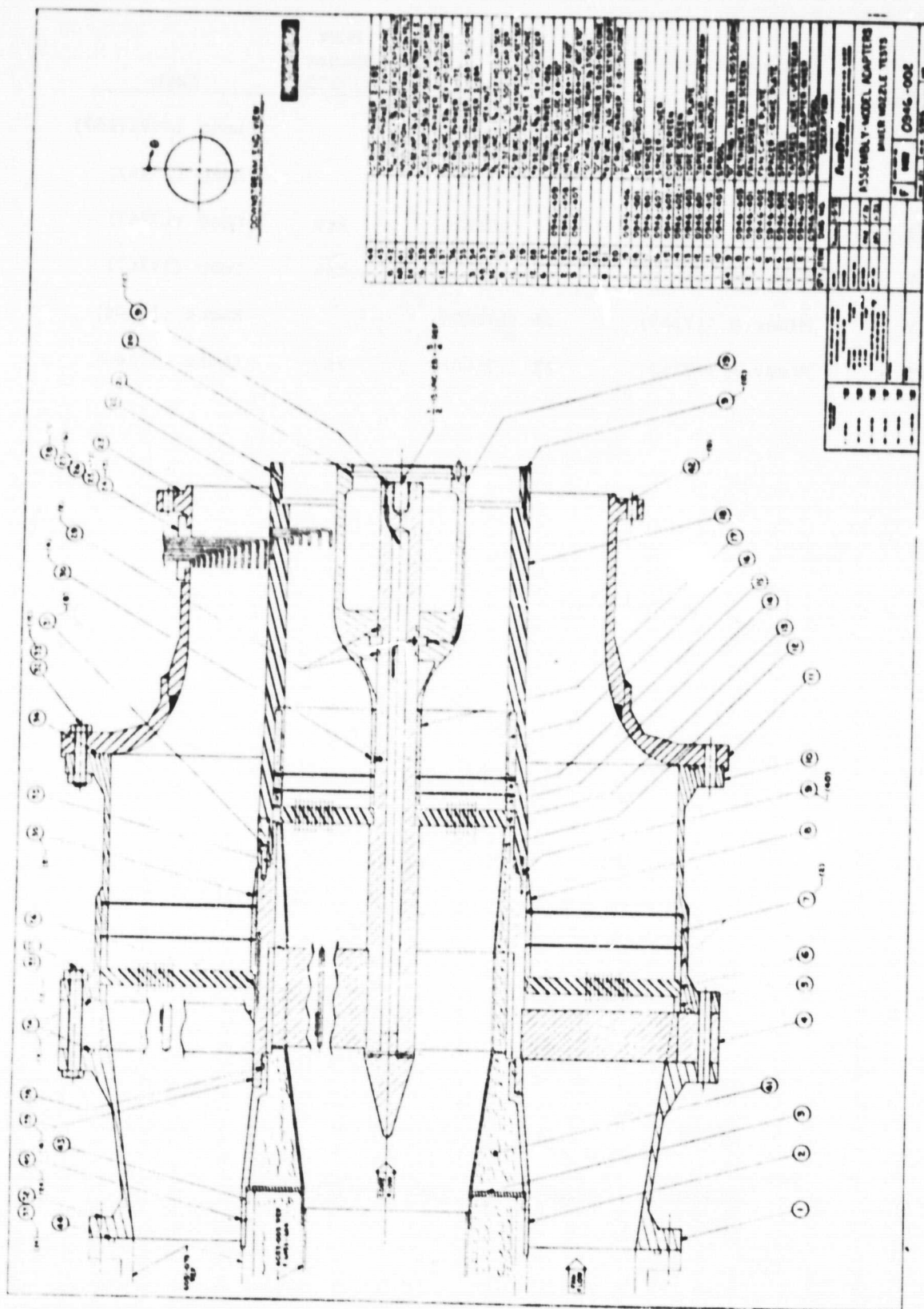
FIGURE 4. ADAPTER ASSEMBLY

FLUIDYNE ENGINEERING CORPORATION

FIGURE 5a. PLUG #1
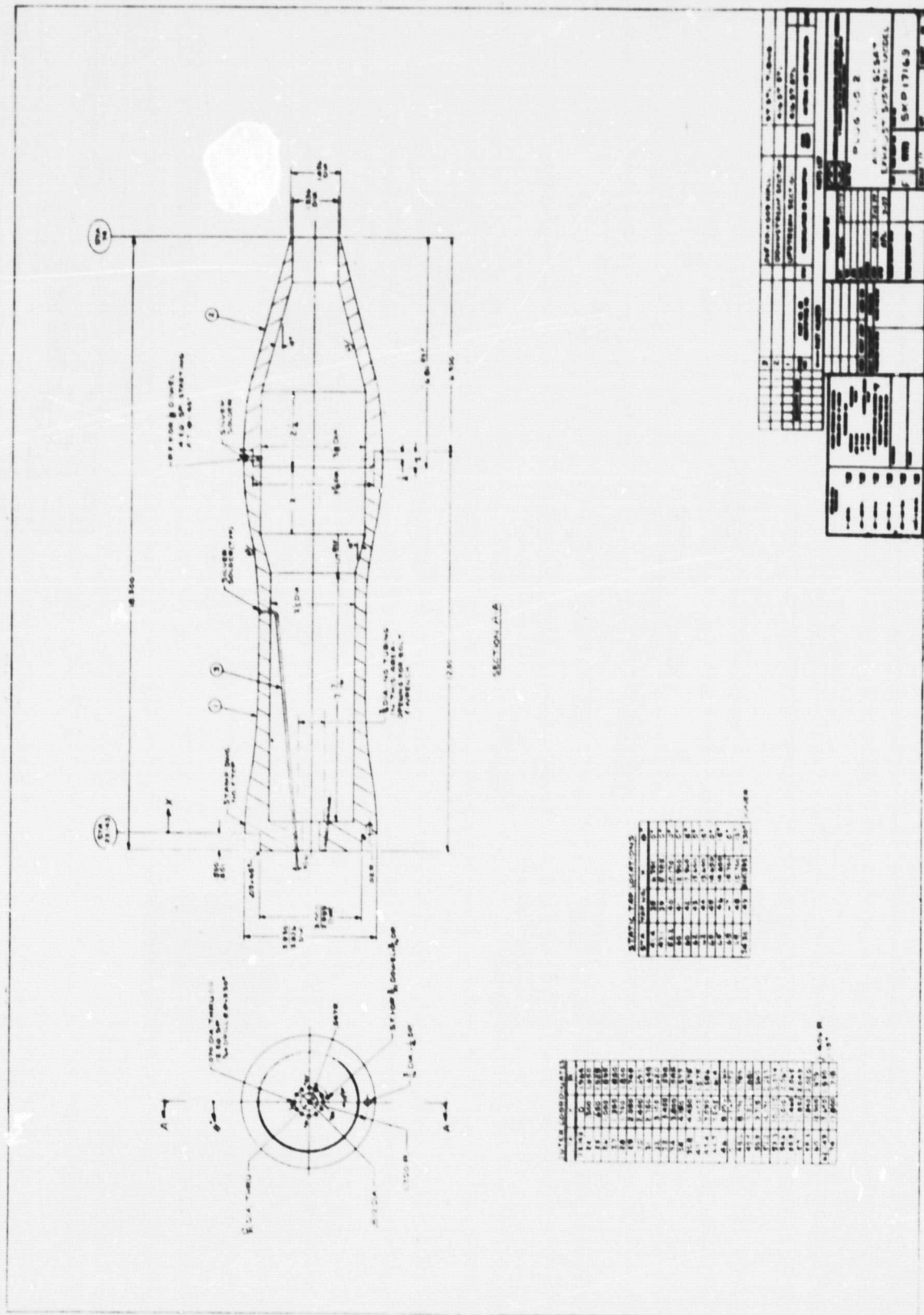
FIGURE 5b. PLUG #2

FluiDyne ENGINEERING CORPORATION

FIGURE 5c. CORE COWL
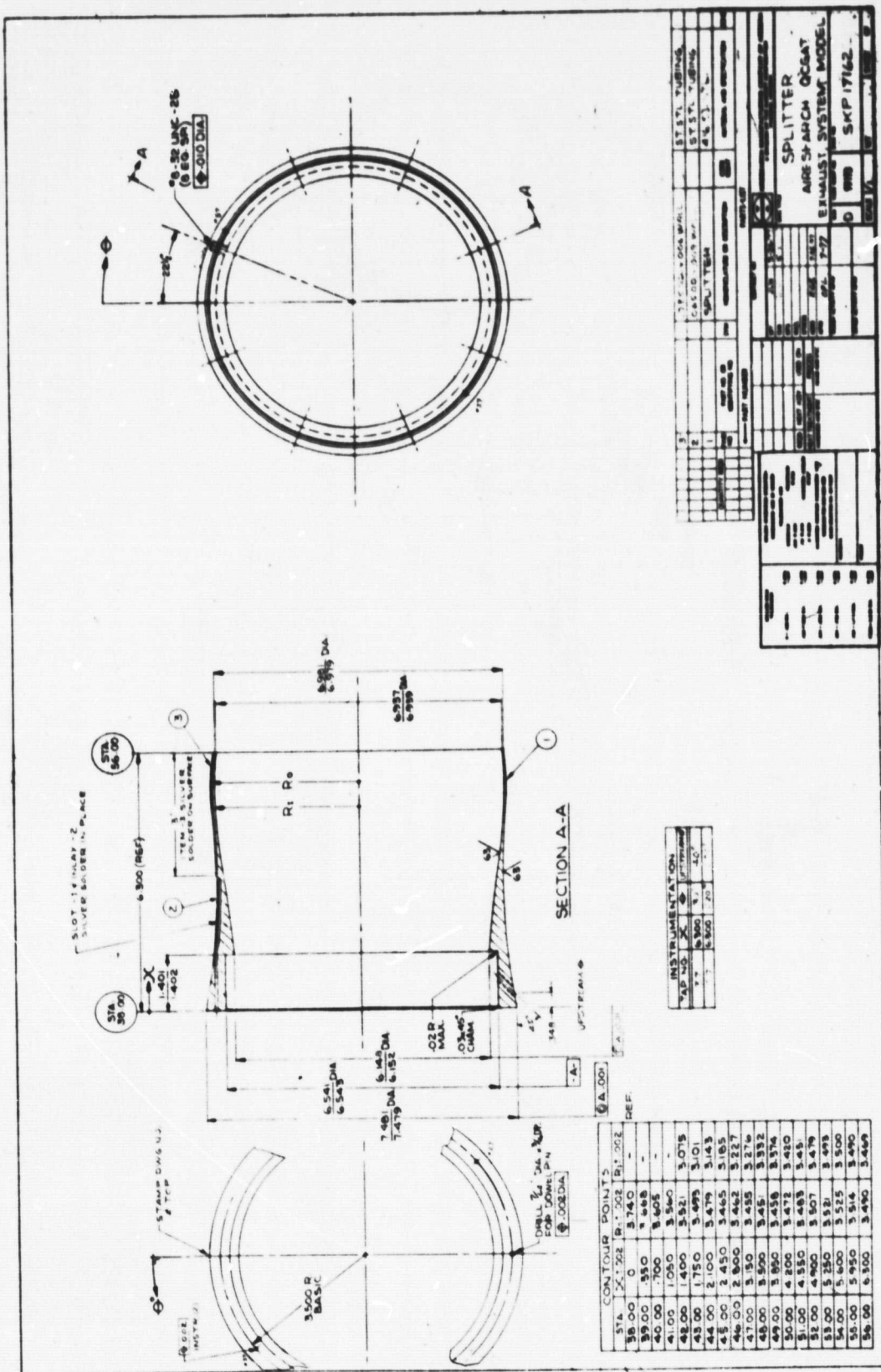
FIGURE 5d. SPLITTER

ORIGINAL PAGE IS
OF POOR QUALITY

FIGURE 5e.   MIXER A

FIGURE 5f. MIXER C

ORIGINAL PAGE IS
OF POOR QUALITY

FIGURE 5g. MIXER D
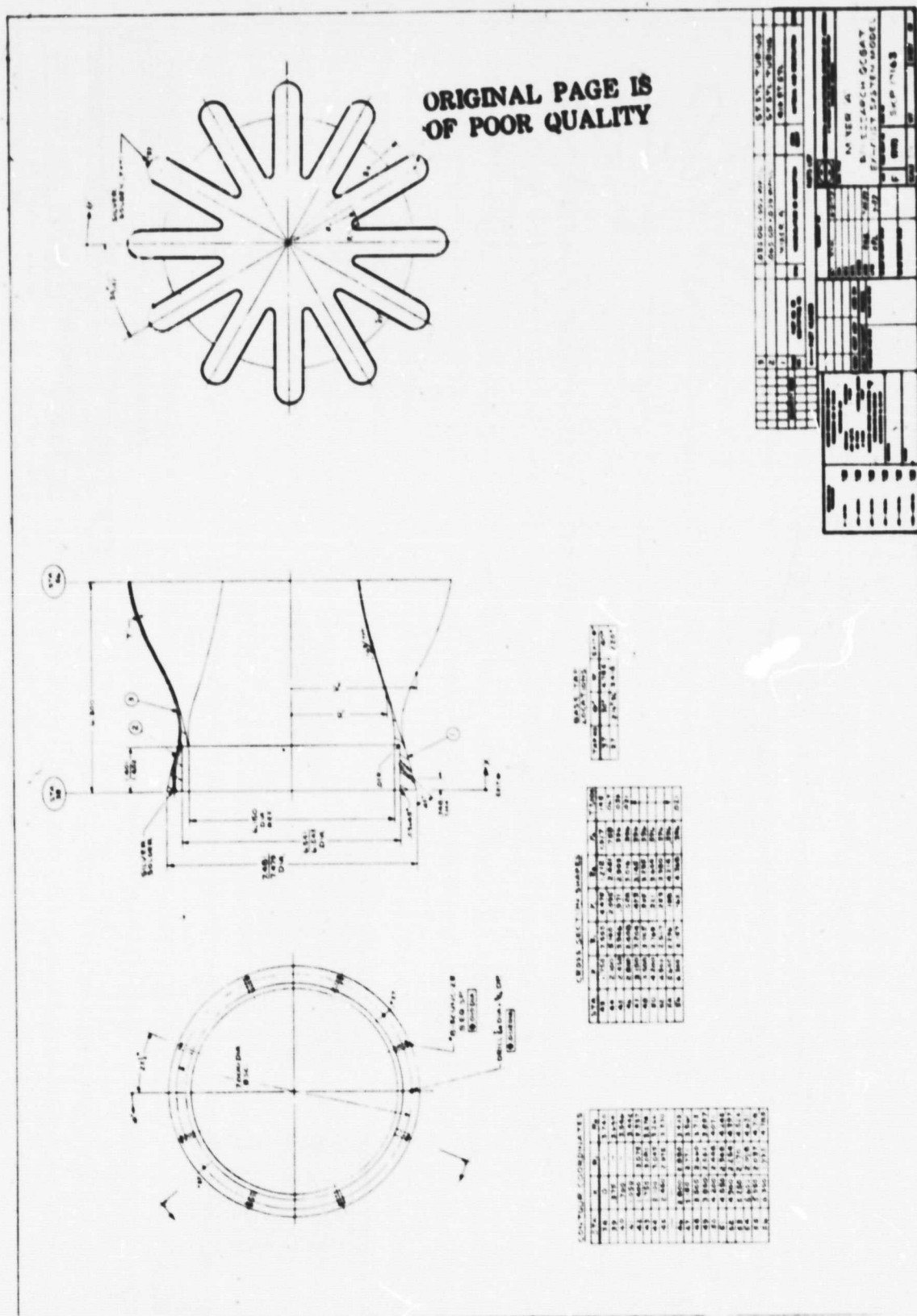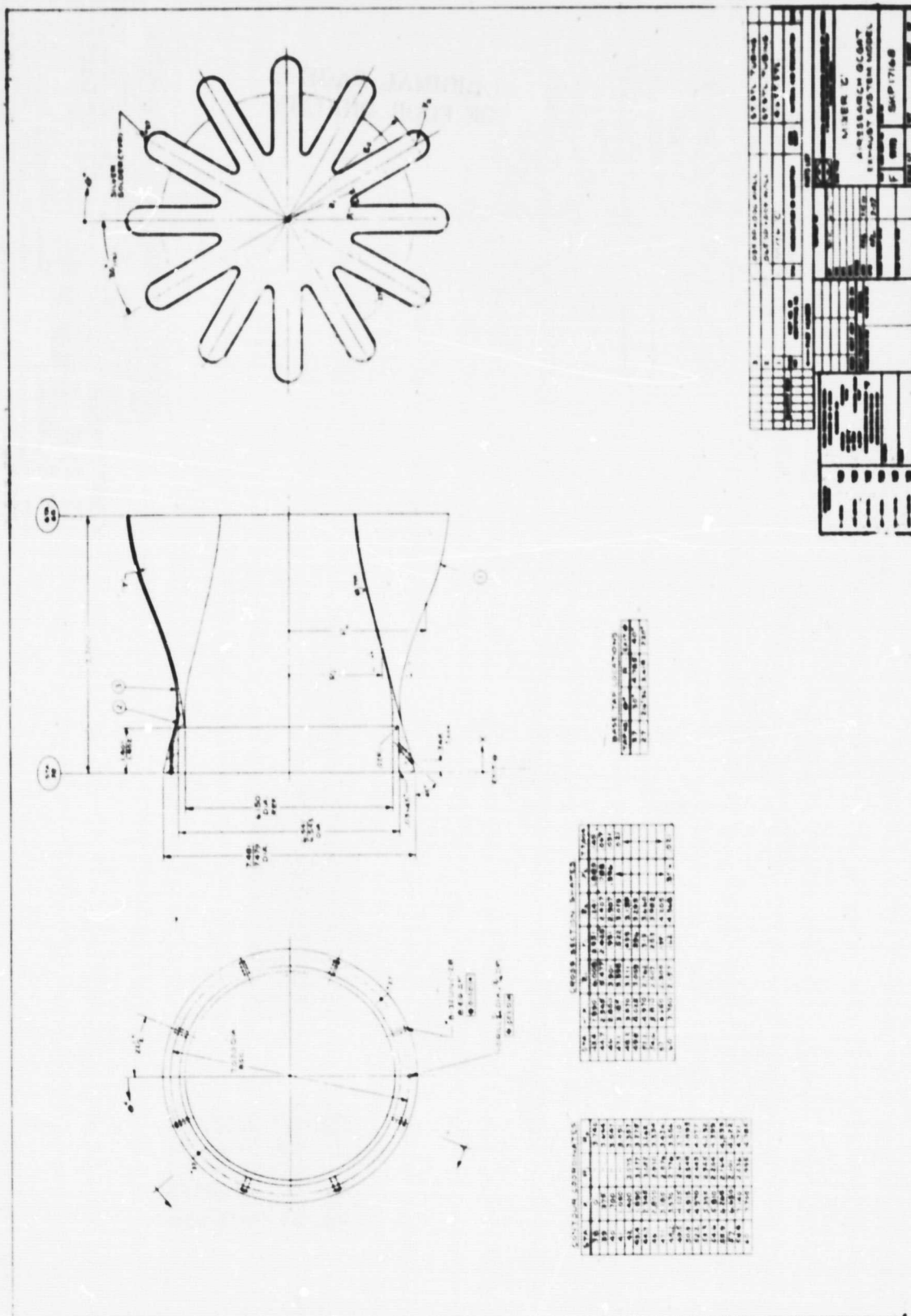
FIGURE 5h. FAN DUCT - FORWARD
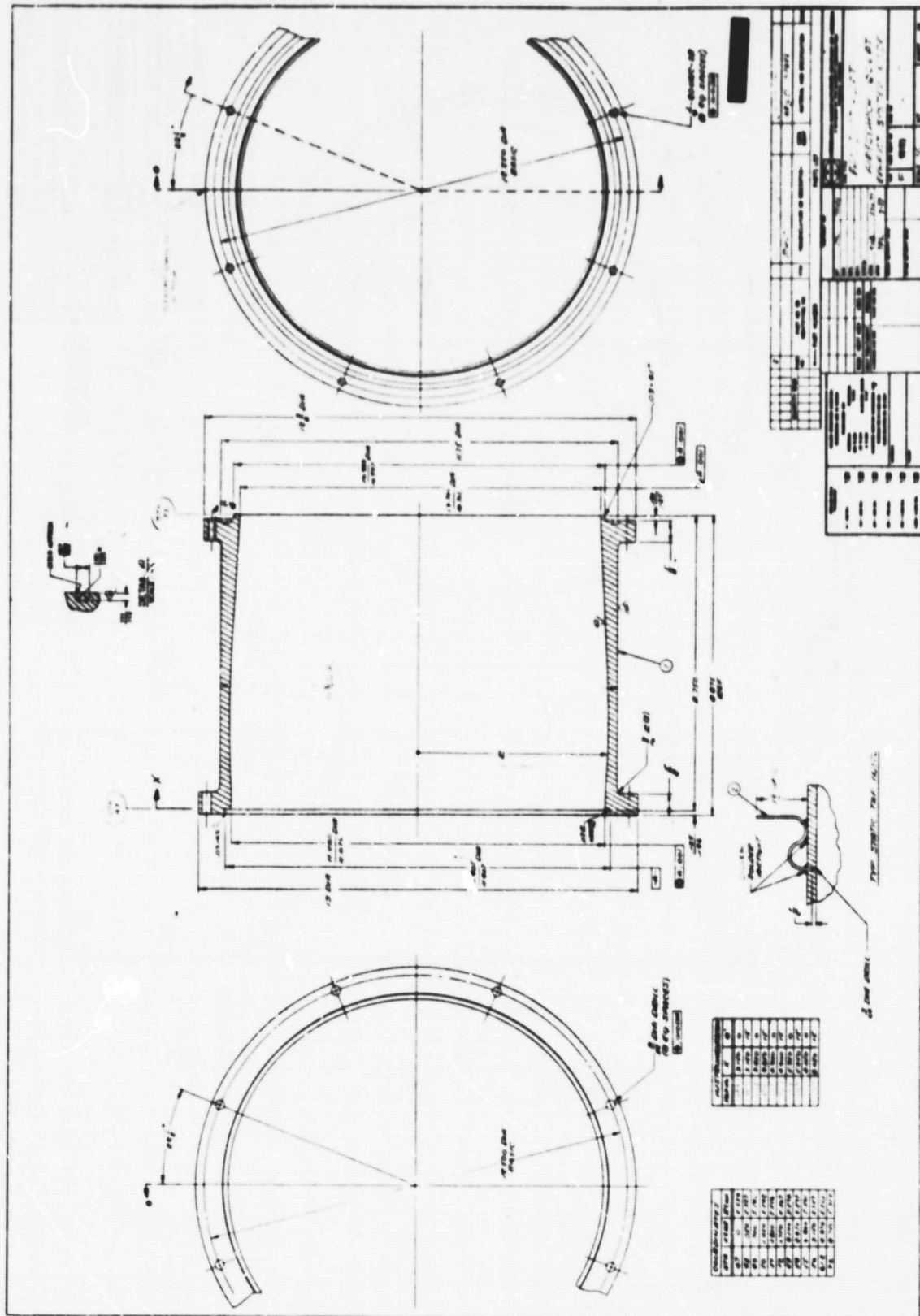
FluiDyne ENGINEERING CORPORATION

FIGURE 5i. FAN DUCT - AFT
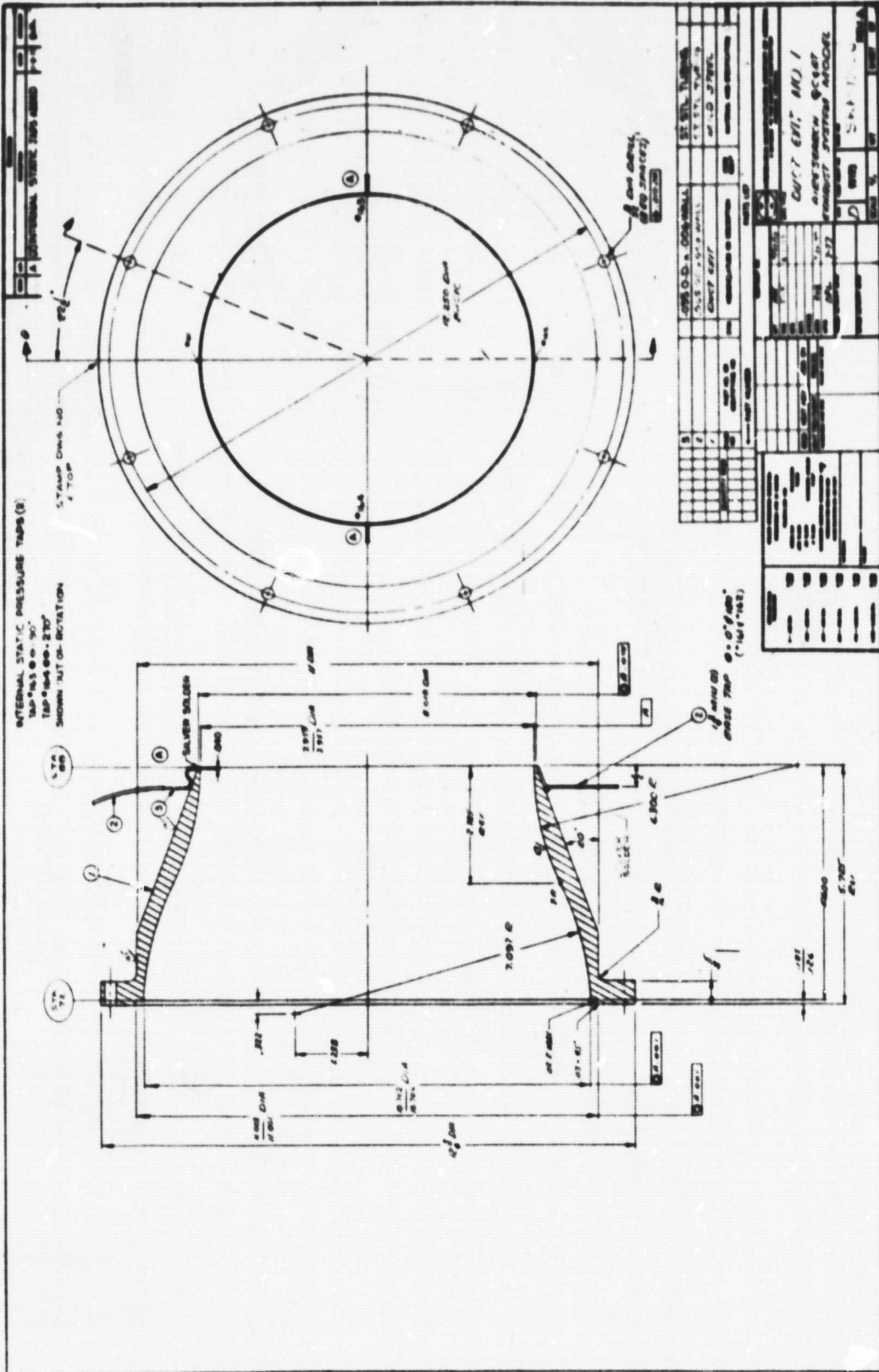
FIGURE 5j. DUCT EXIT #1

FLUIDYNE ENGINEERING CORPORATION

FIGURE 5k. DUCT EXIT #2
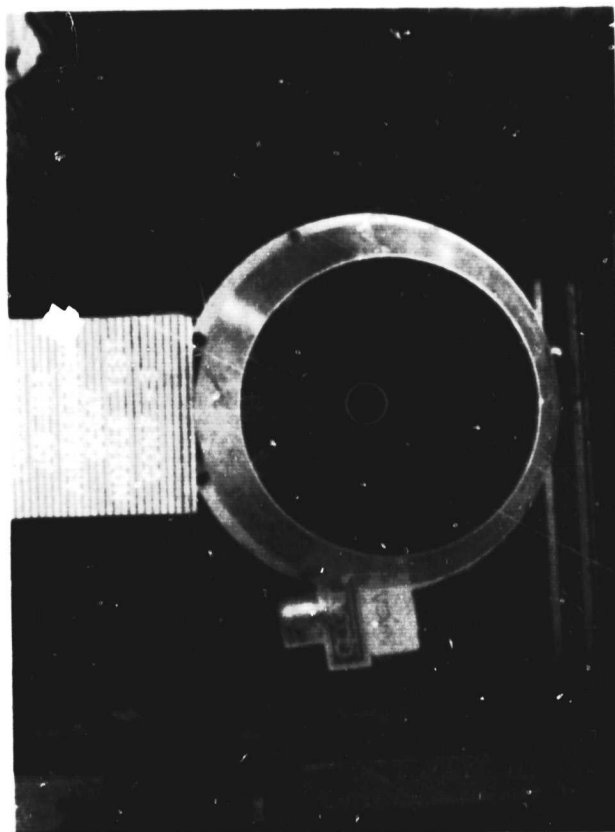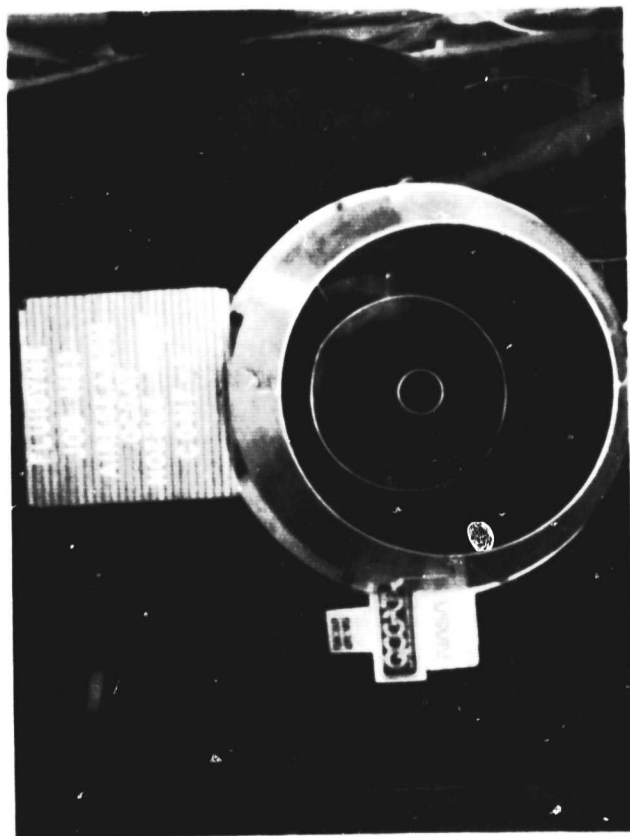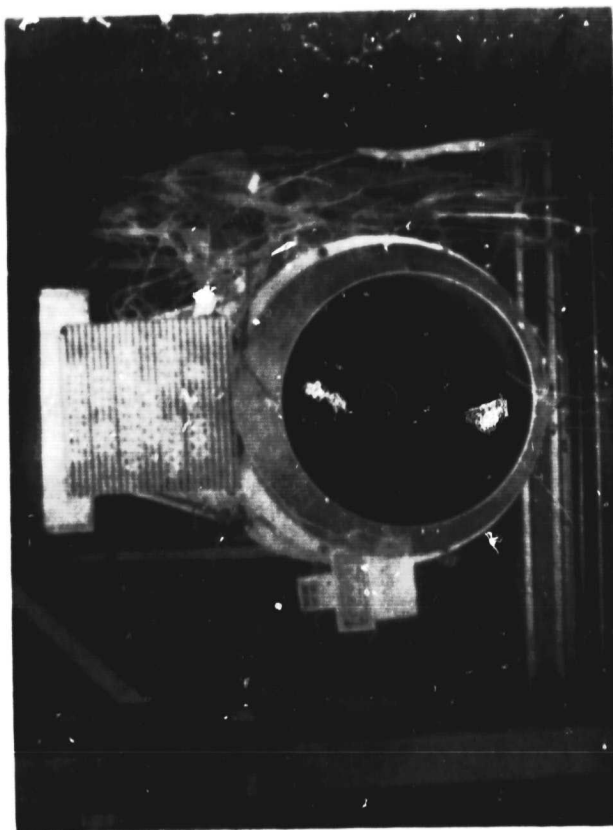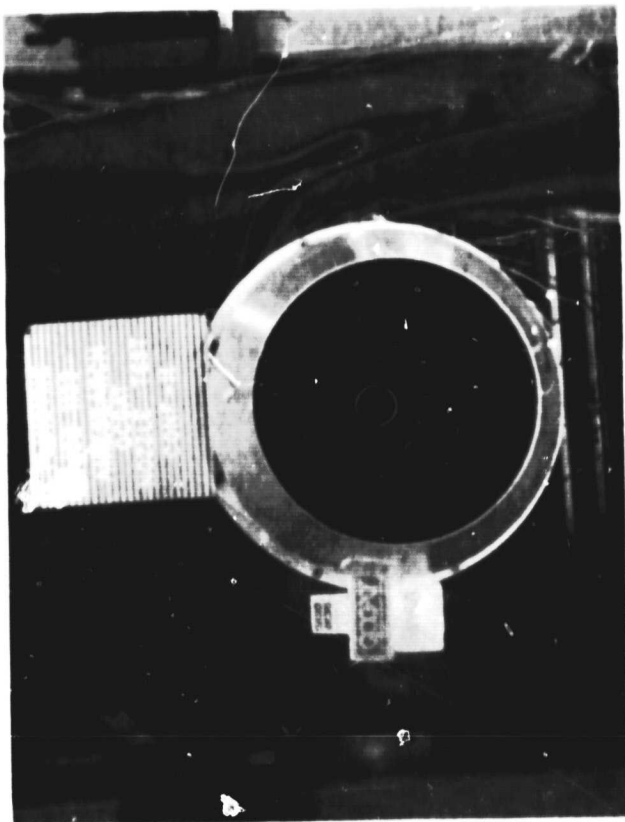
FIGURE 6a. MODEL PHOTOGRAPHS

FIGURE 6b. MODEL PHOTOGRAPHS

FluiDyne ENGINEERING CORPORATION
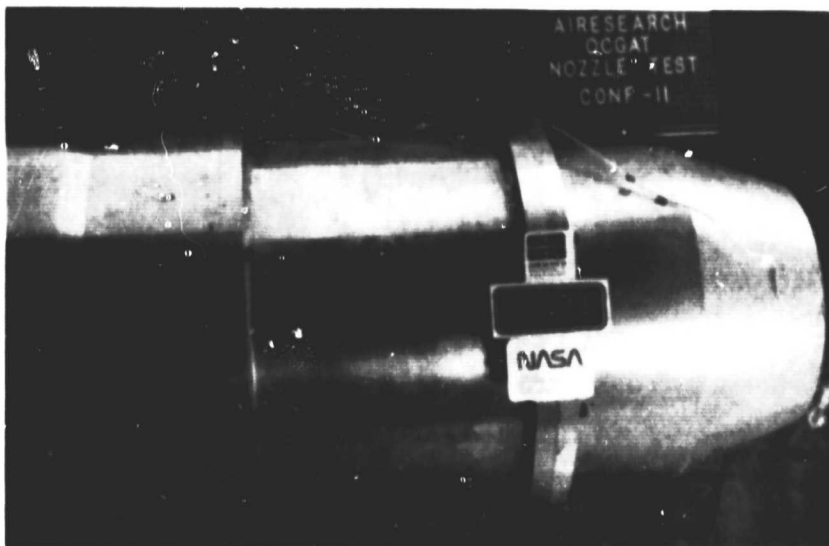
no spacer
long exit
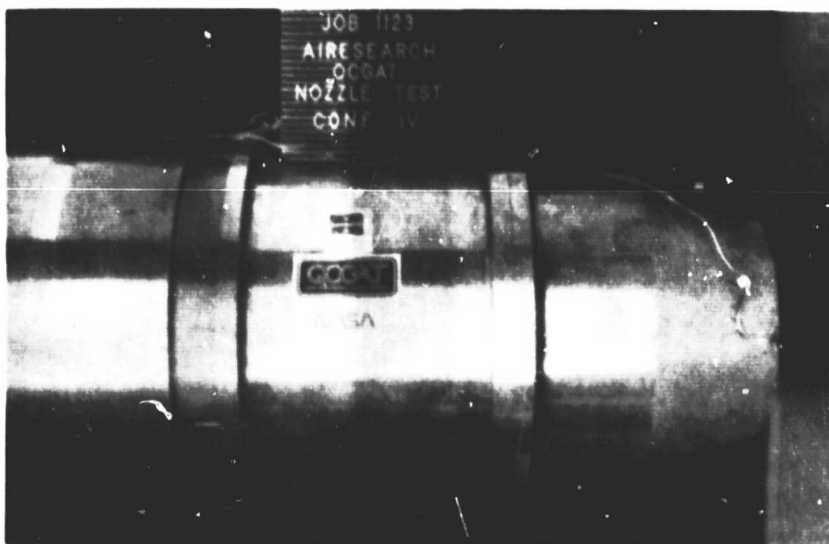
spacer
long exit
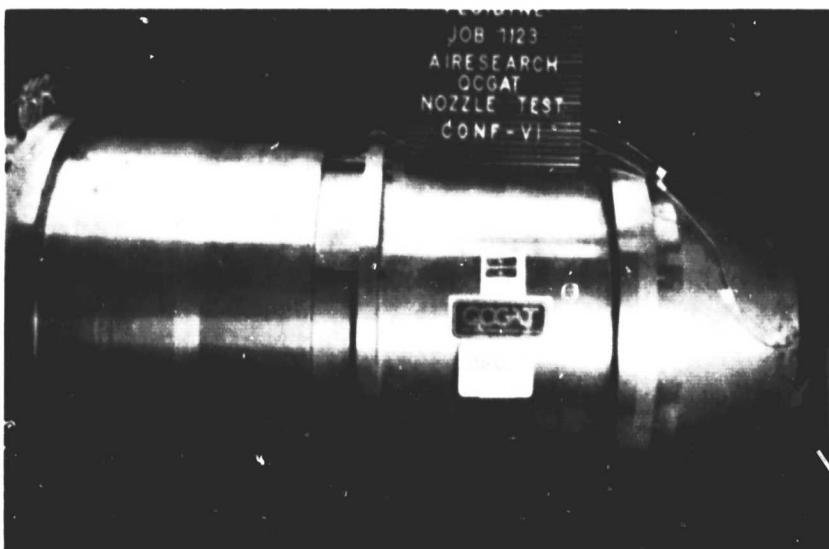
spacer
short exit

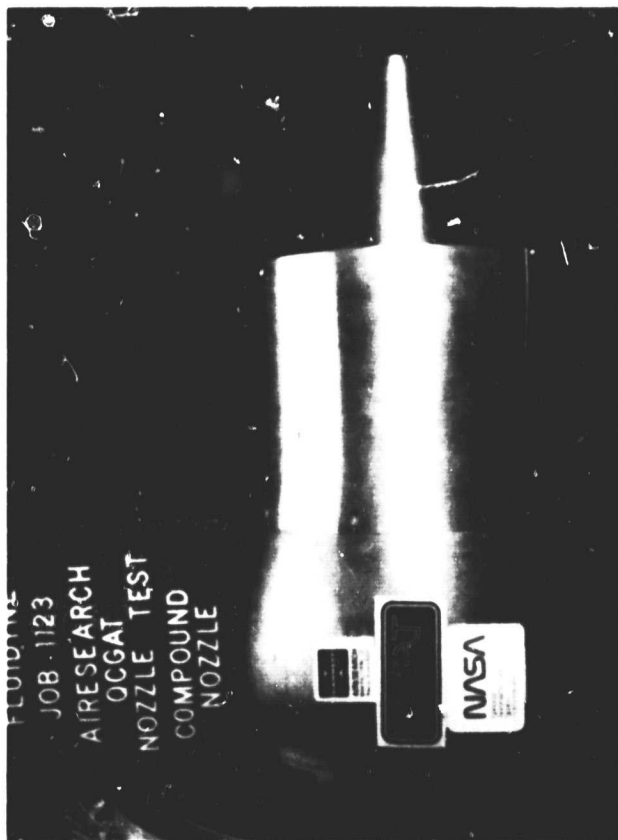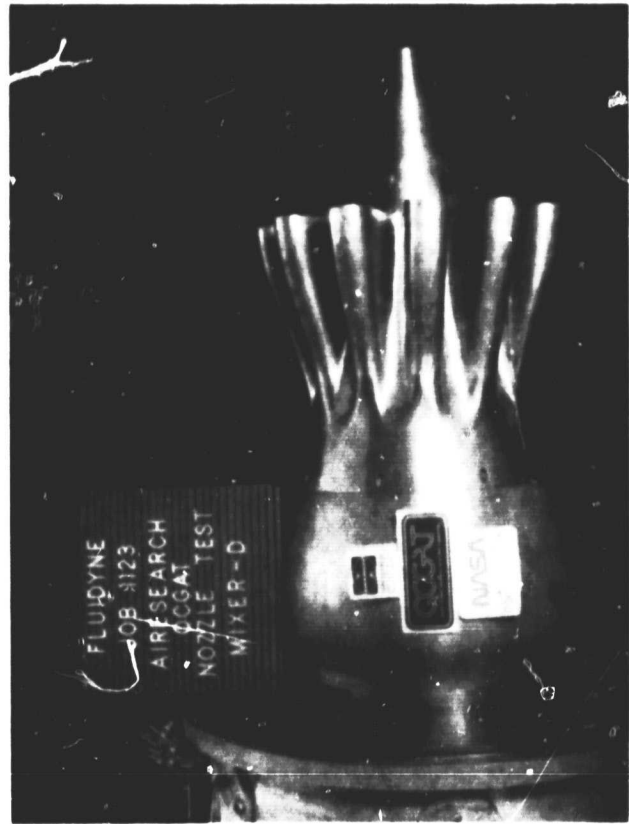FIGURE 6c. MODEL PHOTOGRAPHS
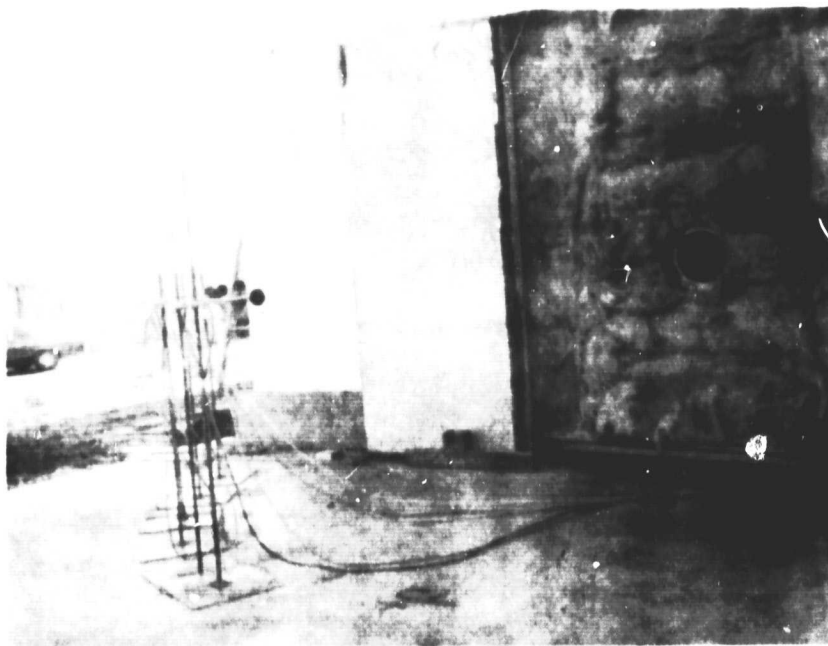
acoustic test setup
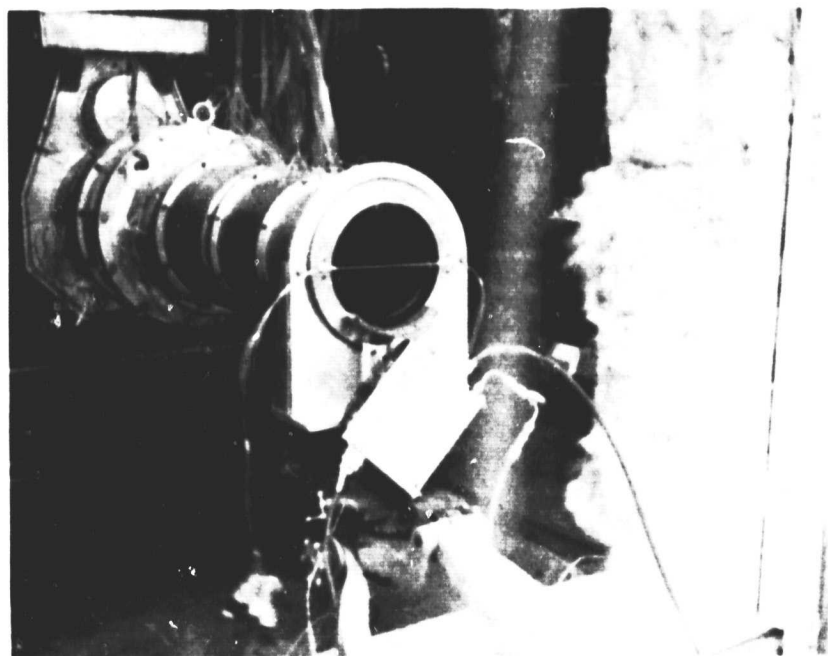
survey test setup

FIGURE 6d. MODEL PHOTOGRAPHS

Station	Description
1	ASME meter throat (core flow)
2	Flexible seal (core flow)
3	ASME meter throat (fan flow)
4	Flexible seal (fan flow)
5	Instrumentation station in adapters
5.2	Core nozzle entrance
6	Core nozzle exit
8	Mixed flow nozzle exit
14	Fan nozzle entrance
16	Fan nozzle exit

FIGURE 7. STATION NOTATION

FIGURE 8. ACOUSTIC TEST SETUP

FLUIDYNE ENGINEERING CORPORATION

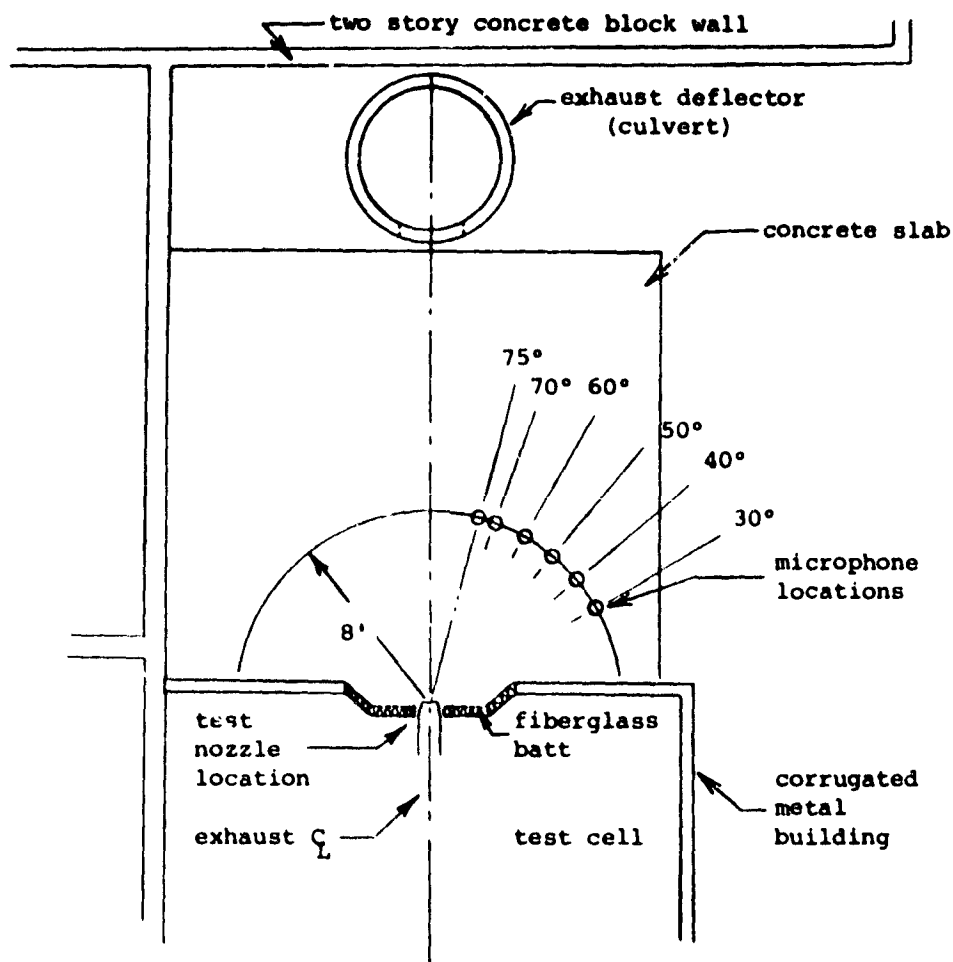| Config.	Run No.	Note	$\lambda_{5.2}$	λ_{14}	$\lambda_{14}/\lambda_{5.2}$	$T_{t_{5.2}}/T_{t_{14}}$	C_T	$C_{D_{5.2}}A_{5.2}$	$C_{D_{14}}A_{14}$	$W_{14}/W_{5.2}$
I	1.0	Core-only (cold flow with $P_{t_{5.2}}$ rakes)	1.048				.9425	25.09		
	2.0		1.097				.9486	24.93		
	3.0		1.147				.9495	24.88		
	4.0		1.196				.9508	24.74		
	5.0		1.242				.9502	24.57		
	6.0		1.290				.9441	24.34		
	1	Core-only (cold-flow)	1.062							
	2		1.095							
	3		1.136							
	4		1.190							
	5		1.247							
	6		1.295							
	7		1.386	1.430	1.032	1.034	.9845	12.97	35.23	2.909
	8		2.391	2.421	1.013	1.020	.9919	14.42	34.71	2.461
	9	With acoustic data	1.415	1.452	1.027	2.509	.9897	13.28	34.56	4.323
	10		2.400	2.415	1.006	2.634	.9940	14.88	34.18	3.792
	11	With survey data	1.405	1.429	1.017	2.506	.9896	13.97	33.71	3.951
	12		2.264	2.419	1.069	2.643	.9961	11.59	36.94	5.594
II	13	Core-only (cold-flow)	1.204				.8912	21.36		
	14		1.338				.8819	20.41		
	15		1.498				.8650	19.03		
	16		1.385	1.420	1.026	1.021	.9815	12.47	35.53	3.006
	17		2.404	2.421	1.007	1.012	.9896	13.50	35.49	2.663
	18	With acoustic data	1.387	1.414	1.019	2.487	.9932	13.03	33.93	4.267
	19	data	2.409	2.471	1.026	2.620	1.0050	13.23	34.76	4.410
	20	With survey data	1.386	1.425	1.028	2.499	.9978	12.46	34.14	4.562
	21	data	2.405	2.417	1.005	2.629	1.0106	13.83	33.81	4.027

These runs made to determine $F_{t_{5.2}}/P_{t_5}$ versus Mach number, M_5.

FIGURE 9. RUN SCHEDULE AND MAJOR TEST RESULTS
(Sheet 1 of 4)

FLUIDYNE ENGINEERING CORPORATION

Config. No.	Run No.	Note	$\lambda_{5.2}$	λ_{14}	$\lambda_{14}/\lambda_{5.2}$	$T_{t_{5.2}}/T_{t_{14}}$	C_T	$C_{D_{5.2}}A_{5.2}$	$C_{D_{14}}A_{14}$	$W_{14}/W_{5.2}$
III	22	Core-only	1.205				.8666	22.27		
	23	(cold flow)	1.348				.8663	20.96		
	24		1.494				.8596	19.64		
	25		1.390	1.424	1.024	1.038	.9836	13.05	34.99	2.846
	26		2.404	2.405	1.001	1.027	.9906	11.39	34.72	2.447
	27	With acoustic	1.403	1.432	1.021	2.460	.9902	13.42	33.59	4.085
	28	data	2.401	2.419	1.007	2.529	1.0032	14.35	33.67	3.798
	29	With survey	1.397	1.420	1.017	2.485	.9957	13.46	33.20	4.018
	30	data	2.401	2.418	1.007	2.638	1.0084	14.33	33.34	3.846
IV	31	Core-only	1.209				.8809	22.09		
	32	(cold flow)	1.354				.8518	20.39		
	33		1.493				.8354	19.19		
	34		1.386	1.425	1.029	1.026	.9829	12.72	35.26	2.945
	35		2.402	2.415	1.006	1.018	.9908	14.07	34.98	2.522
	36	With acoustic	1.400	1.424	1.017	2.491	.9918	13.64	33.48	4.009
	37	data	2.393	2.409	1.007	2.626	1.0075	14.20	33.62	3.907
	38	With survey	1.399	1.429	1.021	2.497	.9932	13.21	33.19	4.135
	39	data	2.395	2.421	1.011	2.637	1.0087	14.04	33.50	3.959
V	40		1.384	1.427	1.031	1.018	.9834	12.33	35.58	3.067
	41		2.394	2.411	1.007	1.013	.9906	13.58	35.60	2.657
	42	With acoustic	1.389	1.424	1.025	2.522	.9902	12.87	34.10	4.409
	43	data	2.400	2.425	1.010	2.681	1.0068	13.70	34.22	4.174
	44	With survey	1.403	1.425	1.016	2.516	.9959	13.00	33.52	4.219
	45	data	2.417	2.420	1.001	2.657	1.0091	14.07	33.56	3.936
VI	46		1.375	1.421	1.034	1.032	.9831	11.96	35.89	3.228
	47		2.394	2.407	1.006	1.020	.9906	13.63	35.35	2.636
	48	With acoustic	1.390	1.429	1.029	2.532	.9908	12.80	34.24	4.488
	49	data	2.412	2.434	1.009	2.663	1.0066	13.79	34.15	4.123

FIGURE 9. RUN SCHEDULE AND MAJOR TEST RESULTS
(Sheet 2 of 4)

Config.	Run No.	Note	$\lambda_{5.2}$	λ_{14}	$\lambda_{14}/\lambda_{5.2}$	$T_{t_{5.2}}/T_{t_{14}}$	C_T	$C_{D_{5.2}}A_{5.2}$	$C_{D_{14}}A_{14}$	$W_{14}/W_{5.2}$
VI (cont.)	50	With survey	1.392	1.422	1.022	2.610	.9944	12.83	33.78	4.438
	51	data	2.397	2.419	1.009	2.657	1.0102	13.69	33.91	4.117
I	52		1.205	1.202	.998	2.543	.9832	14.64	33.10	3.590
	53		1.298	1.196	.922	2.536	.9843	18.76	28.69	1.992
	54		1.398	1.200	.858	2.523	.9855	20.57	26.78	1.484
	55		1.499	1.400	.934	2.503	.9850	17.55	30.47	2.483
	56		1.590	1.399	.880	2.521	.9837	19.42	28.54	1.946
	57		1.458	1.599	1.097	2.522	.9924	9.44	38.60	7.444
	58		1.601	1.599	.999	2.503	.9904	14.94	33.55	3.571
	59		1.808	1.604	.887	2.517	.9864	19.20	29.10	2.110
	60		1.812	1.998	1.103	2.546	.9946	9.66	39.0?	7.180
	61		2.009	1.999	.995	2.505	.9916	15.16	33.79	3.543
	62		2.202	1.999	.908	2.533	.9925	18.59	30.22	2.370
	63		2.010	2.398	1.194	2.547	.9954	4.15	44.02	20.408
	64		2.200	2.402	1.092	2.553	.9939	10.28	38.36	6.578
	65		2.592	2.405	.928	2.537	.9943	18.06	30.93	2.555
II	66		1.211	1.198	.989	2.513	.9922	14.19	32.14	3.491
	67		1.299	1.195	.920	2.516	.9832	16.99	28.77	2.184
	68		1.509	1.407	.932	2.513	.9914	16.02	30.57	2.731
	69		1.600	1.402	.876	2.521	.9796	17.45	28.76	2.172
	70		1.465	1.602	1.093	2.526	.9931	9.67	37.71	7.060
	71		1.603	1.599	.998	2.491	.9956	13.98	33.30	3.776
	72		1.791	1.602	.895	2.526	.9950	16.88	29.79	2.485
	73		2.007	1.600	.797	2.523	.9786	18.59	27.44	1.848
	74		1.804	2.006	1.112	2.564	.9964	9.29	38.79	7.517
	75		2.000	1.998	.999	2.511	1.0016	14.16	33.78	3.816
	76		2.507	2.003	.799	2.526	.9911	18.57	27.66	1.910
	77		2.214	2.401	1.085	2.529	1.0020	10.45	37.69	6.282
	78		2.589	2.396	.925	2.538	1.0076	16.32	31.31	2.857
	79		2.930	2.398	.818	2.541	.9992	18.37	28.05	2.012
	80		2.502	1.999	.799	1.014	.9707	17.99	29.51	1.319

FIGURE 9. RUN SCHEDULE AND MAJOR TEST RESULTS (Sheet 3 of 4)

Config.	Run No.	Note	$\lambda_{5.2}$	λ_{14}	$\lambda_{14}/\lambda_{5.2}$	$T_{t_{5.2}}/T_{t_{14}}$	C_T	$C_{D_{5.2}}A_{5.2}$	$C_{D_{14}}A_{14}$	$W_{14}/W_{5.2}$
II (cont.)	80.1	Survey rake present	2.498	1.996	.799	1.006	.9727	17.98	29.16	1.299
	81	with	2.501	2.000	.800	1.531	.9772	18.26	28.58	1.552
	82	survey	2.496	1.998	.801	2.034	.9860	18.48	27.91	1.734
	83	data	2.501	2.001	.800	2.527	.9922	18.57	27.10	1.874

FIGURE 9. RUN SCHEDULE AND MAJOR TEST RESULTS
(Sheet 4 of 4)
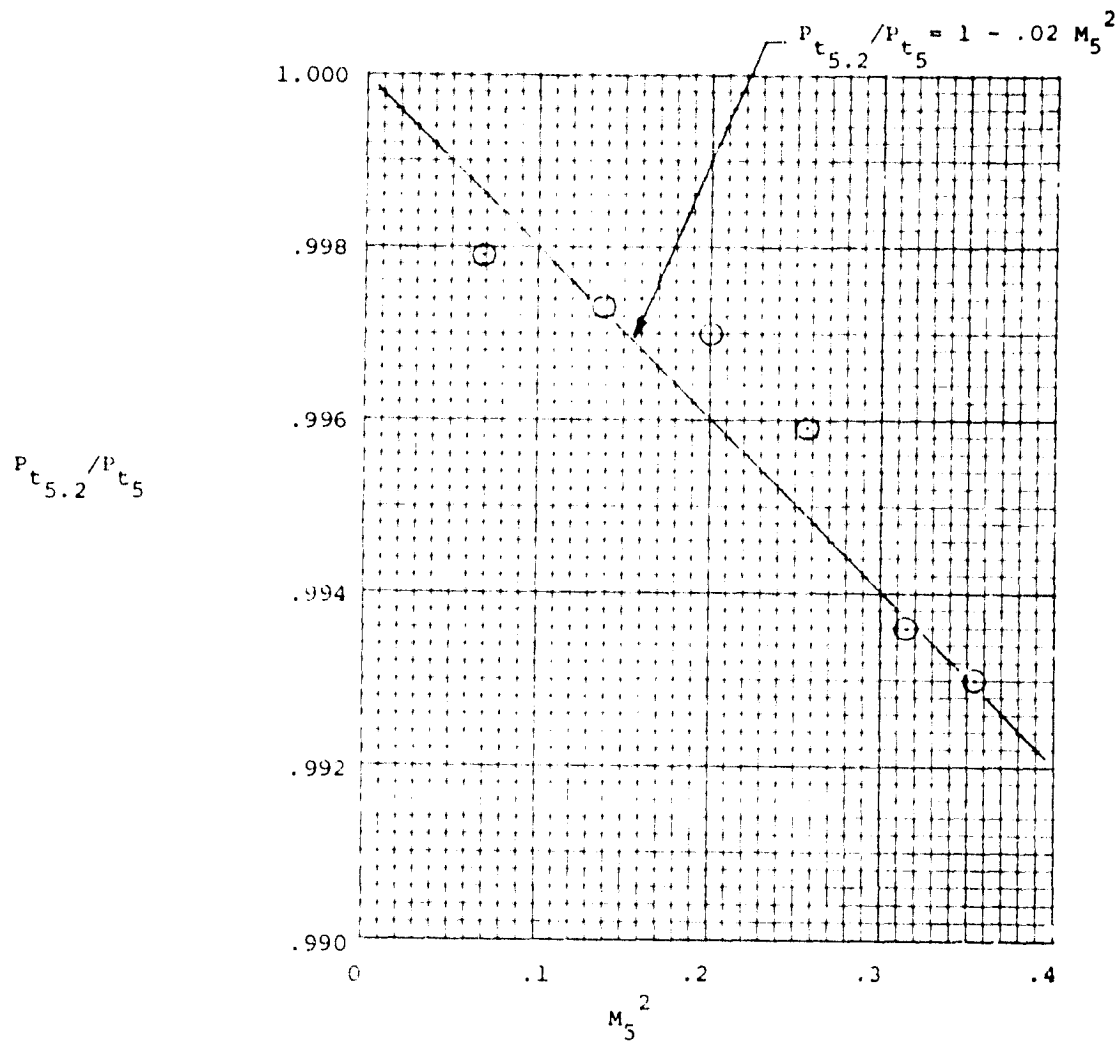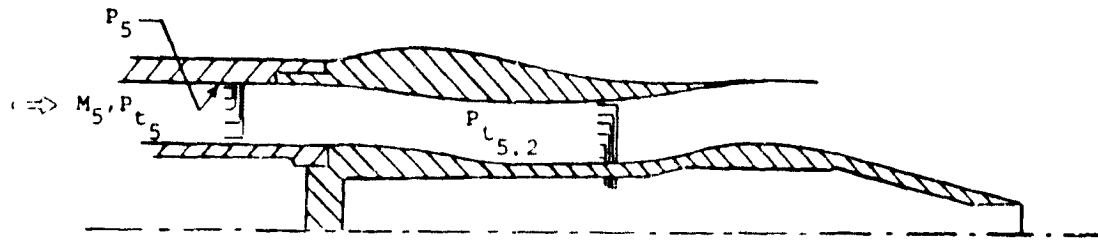
FIGURE 10. CORE PASSAGE TOTAL PRESSURE CORRELATION

Symbol	Config.	Run No.
○	I	1-6
□	II	13-15
◇	III	22-24
△	IV	31-33
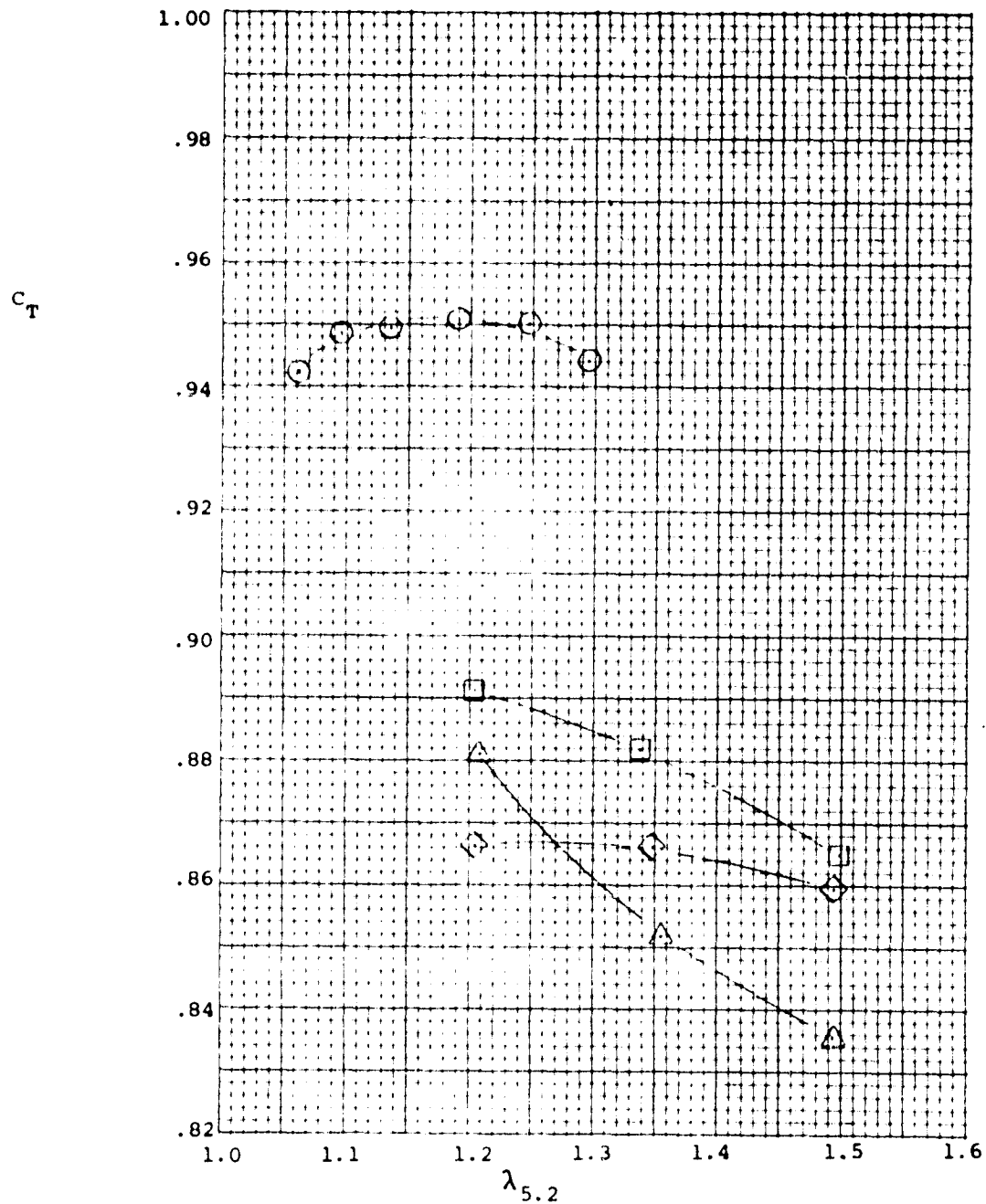
FIGURE 11a. THRUST COEFFICIENTS, CORE-ONLY

Symbol	Config.	Run No.
◯	I	1-6
[ ]	II	13-15
◇	III	22-24
△	IV	31-33

$C_{D_{5.2}} A_{5.2}$, in^2

$\lambda_{5.2}$
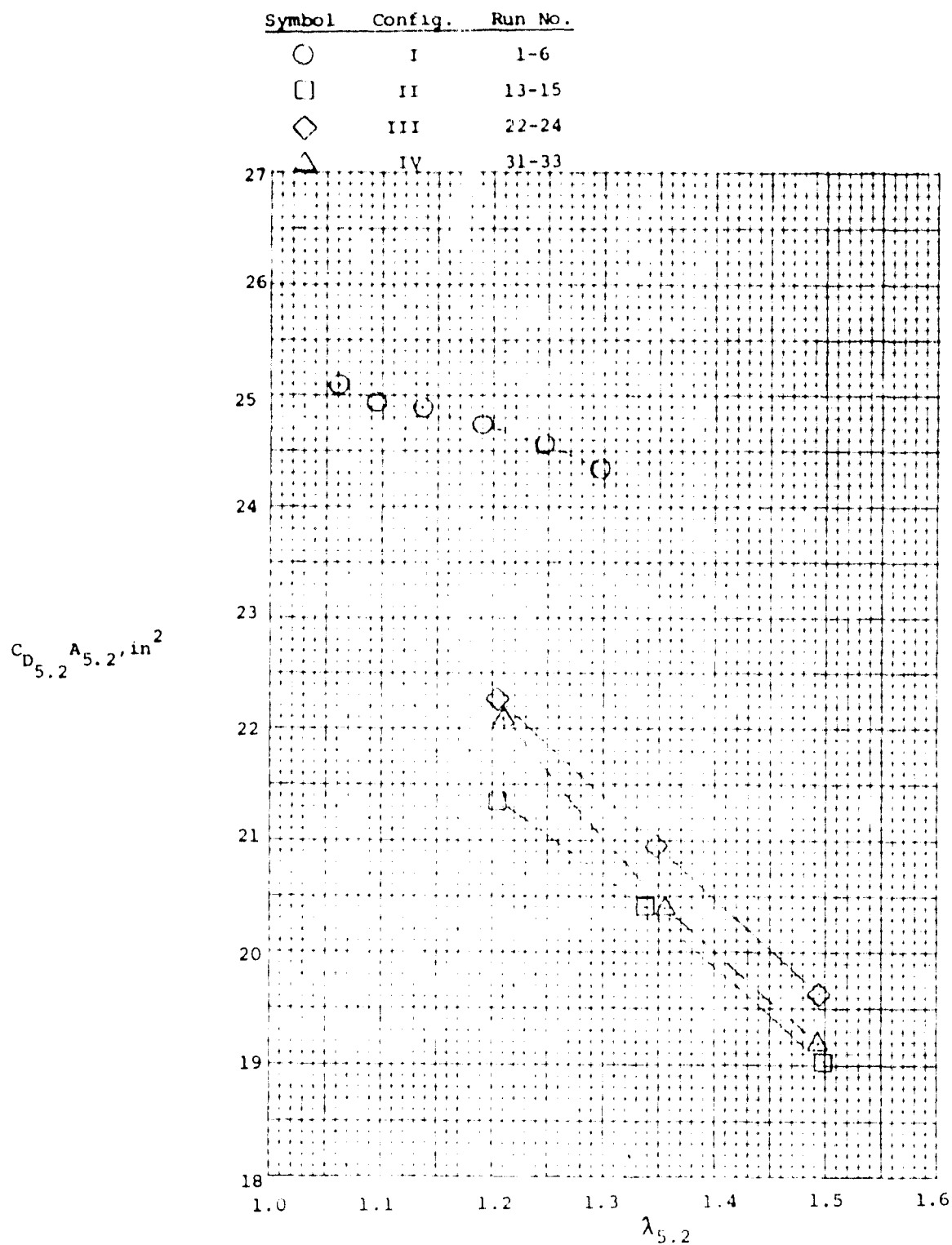
FIGURE 11b. EFFECTIVE THROAT AREAS, CORE-ONLY

FLUIDYNE ENGINEERING CORPORATION
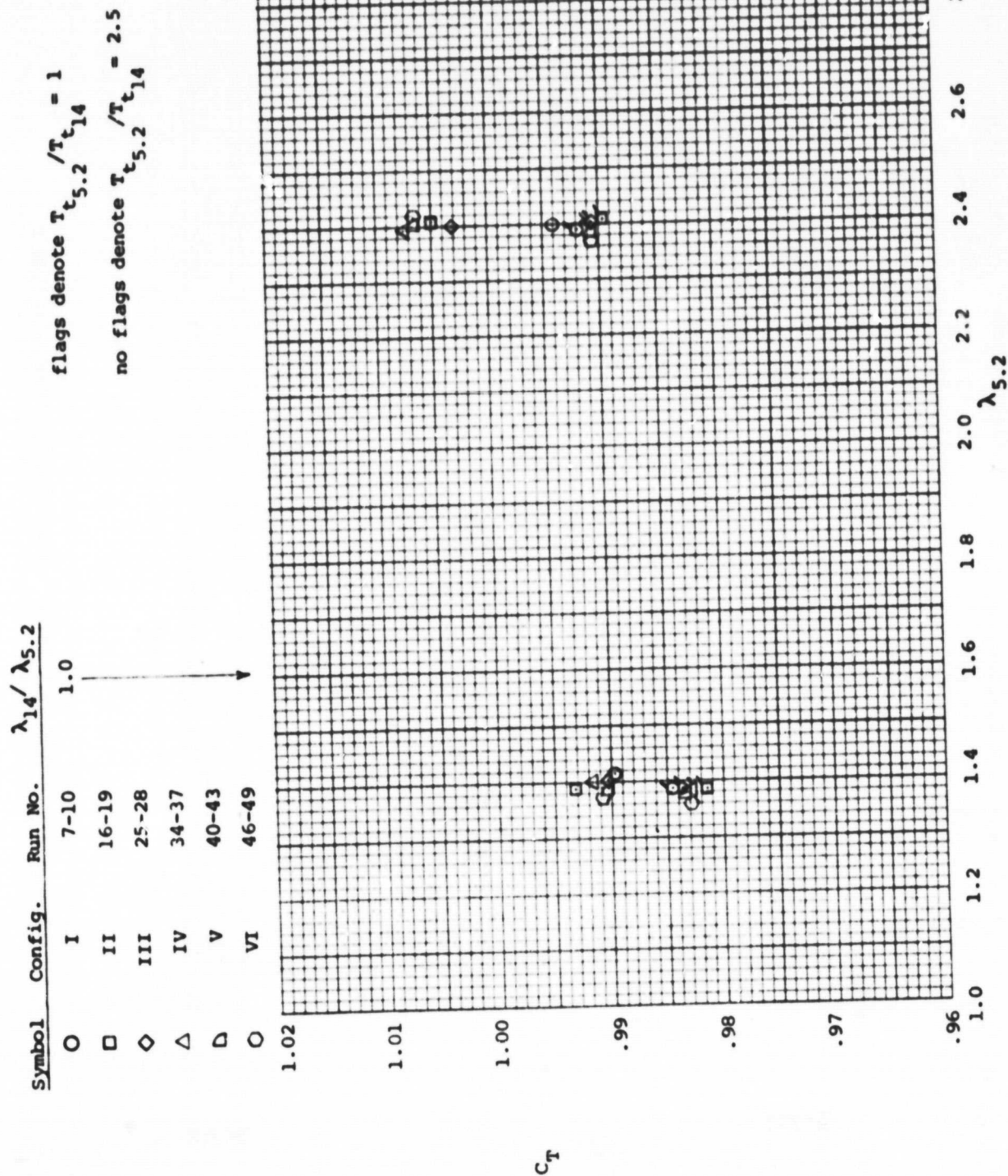
FIGURE 12. THRUST COEFFICIENTS, CONFIGURATIONS I-VI

FIGURE 13.   THRUST COEFFICIENTS, CONFIGURATION I

FIGURE 14. THRUST COEFFICIENTS, CONFIGURATION II
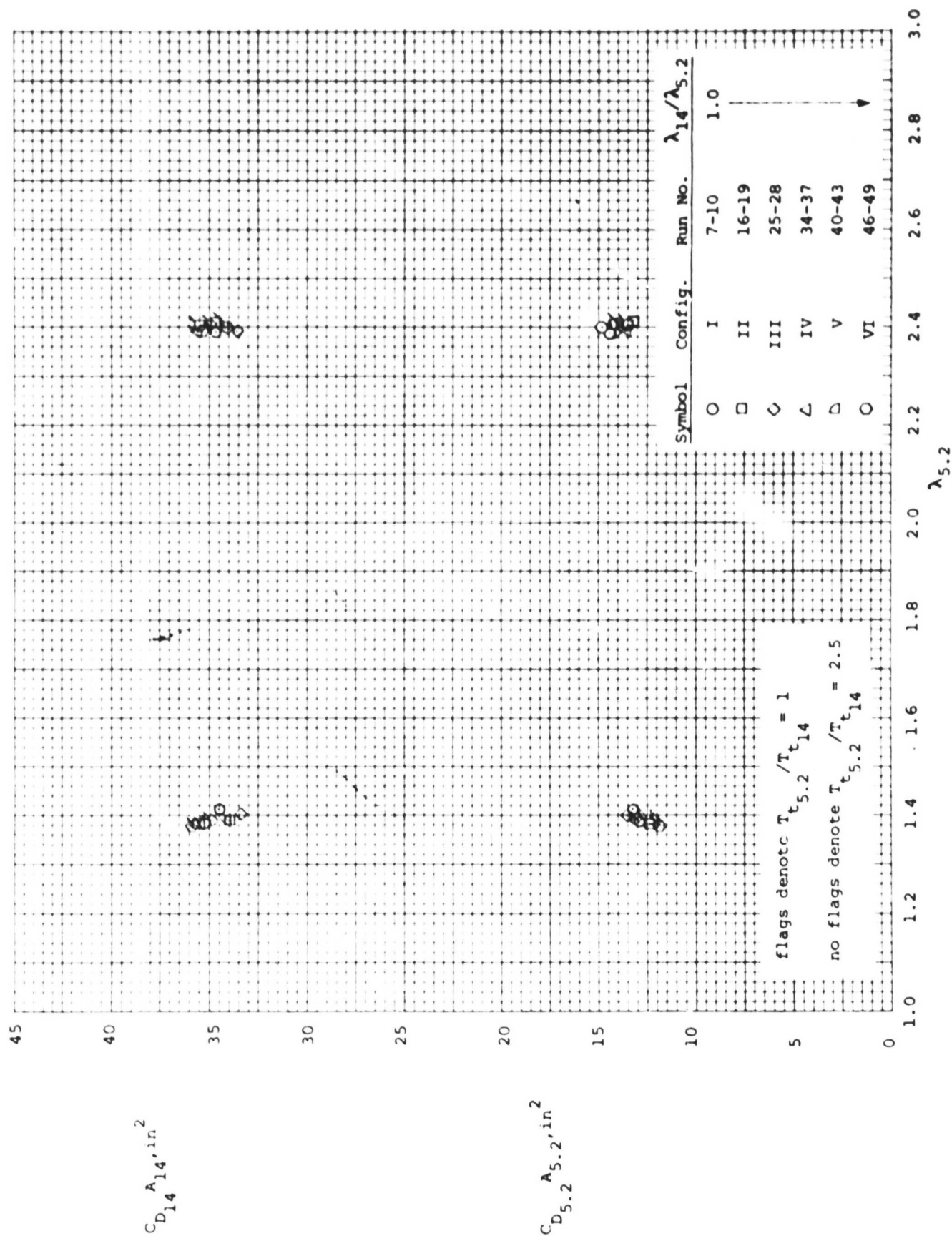
FIGURE 15. EFFECTIVE THROAT AREAS, CONFIGURATIONS I-VI
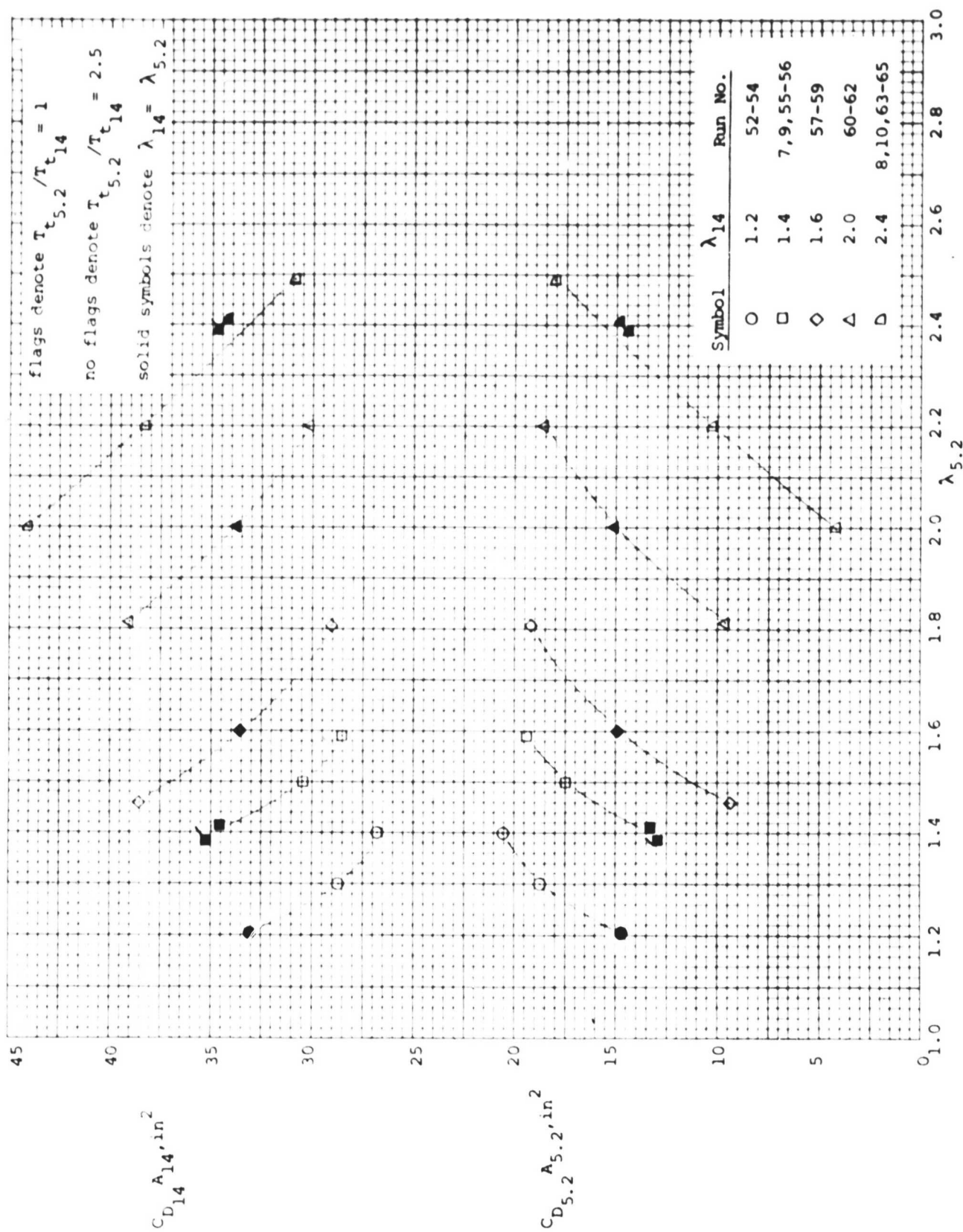
FIGURE 16. EFFECTIVE THROAT AREAS, CONFIGURATION I
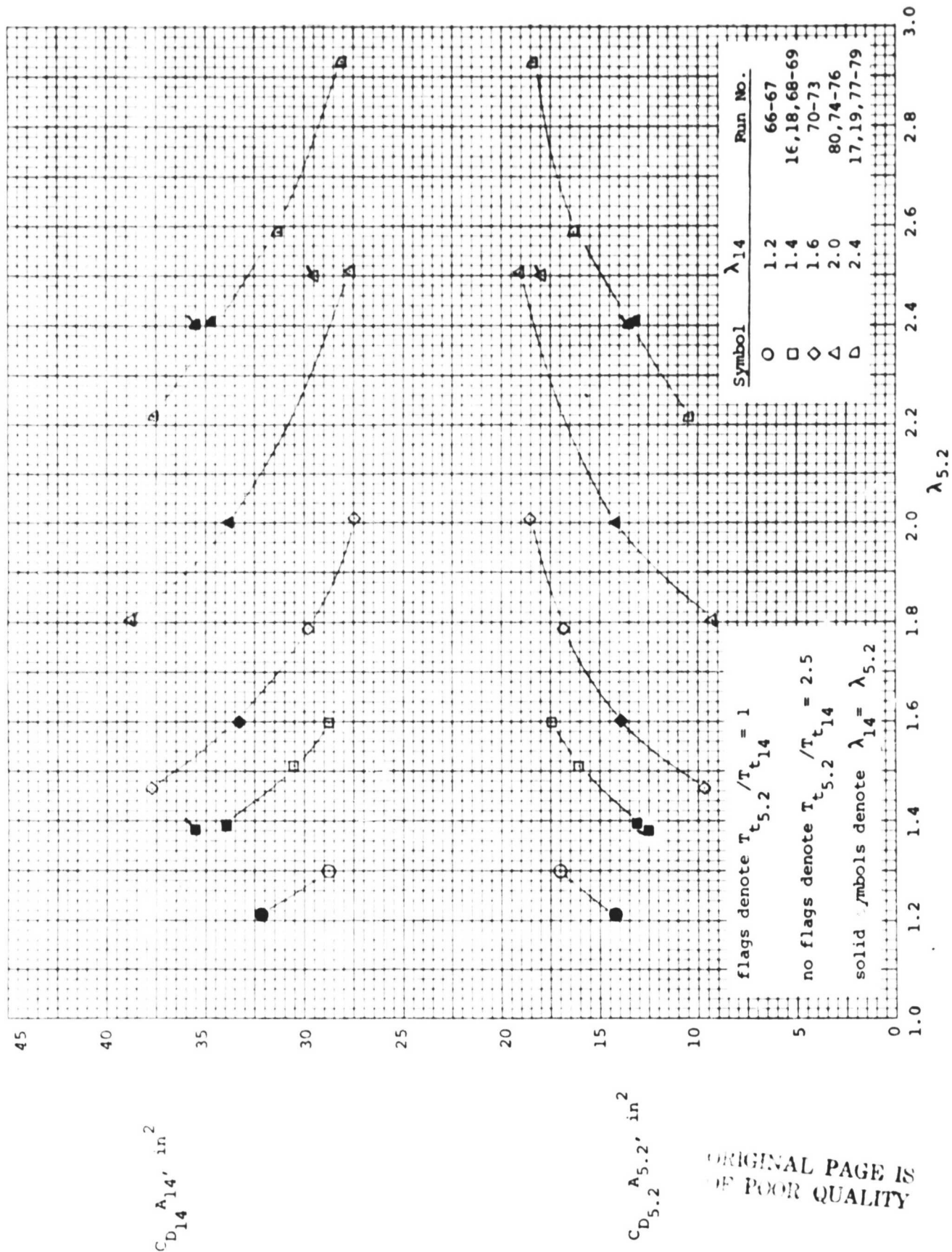
FIGURE 17. EFFECTIVE THROAT AREAS, CONFIGURATION II

Symbol	λ_{14}	Run No.
○	1.2	66-67
□	1.4	16,18,68-69
◇	1.6	70-73
△	2.0	80,74-76
◻	2.4	17,19,77-79

flags denote $T_{t_{5.2}}/T_{t_{14}} = 1$

no flags denote $T_{t_{5.2}}/T_{t_{14}} = 2.5$

solid symbols denote $\lambda_{14} = \lambda_{5.2}$

$C_{D_{14}} A_{14}$, in^2

$C_{D_{5.2}} A_{5.2}$, in^2

$\lambda_{5.2}$